

Absolute Infrared Calibration of Standard Stars by the Midcourse Space Experiment

**S. D. Price
C. Paxson
E. Engelke
T.L. Murdock
K.E. Kraemer**

April 2004

Approved for Public Release; Distribution Unlimited

20060831019



**AIR FORCE RESEARCH LABORATORY
Space Vehicles Directorate
29 Randolph Rd
AIR FORCE MATERIEL COMMAND
Hanscom AFB, MA 01731-3010**

AFRL-VS-HA-TR-2004-1109

When Government drawings, specifications, or other data included in this document are used for any purpose other than Government procurement, this does not in any way obligate the U.S. Government. The fact that the Government formulated or supplied the drawings, specifications, or other data does not license the holder or any other person or corporation; or convey any rights or permission to manufacture, use, or sell any patented invention that may relate to them.

This technical report has been reviewed and is approved for publication.

/ signed /
Stephan D. Price
Author

/ signed /
Robert R. Beland, Chief
Battlespace Surveillance Innovation Center

/ signed /
Robert A. Morris, Chief
Battlespace Environment Division
Space Vehicles Directorate

This report is published in the interest of scientific and technical information exchange and its publication does not constitute the Government's approval or disapproval of its ideas or findings.

This report has been reviewed by the ESC Public Affairs Office (PA) and is releasable to the National Technical Information Service (NTIS).

Qualified requestors may obtain additional copies from the Defense Technical Information Center (DTIC). All other requestors should apply to the National Technical Information Service (NTIS).

If your address has changed, if you wish to be removed from the mailing list, or if the addressee is no longer employed by your organization, please notify AFRL/VSIM, 29 Randolph Rd., Hanscom AFB, MA 01731-3010. This will assist us in maintaining a current mailing list.

Do not return copies of this report unless contractual obligations or notices on a specific document require that it be returned.

REPORT DOCUMENTATION PAGE				Form Approved OMB No. 0704-0188	
<small>data needed, and completing and reviewing this collection of information. Send comments regarding this burden estimate or any other aspect of this collection of information, including suggestions for reducing this burden to Department of Defense, Washington Headquarters Services, Directorate for Information Operations and Reports (0704-0188), 1215 Jefferson Davis Highway, Suite 1204, Arlington, VA 22202-4302. Respondents should be aware that notwithstanding any other provision of law, no person shall be subject to any penalty for failing to comply with a collection of information if it does not display a currently valid OMB control number. PLEASE DO NOT RETURN YOUR FORM TO THE ABOVE ADDRESS.</small>					
1. REPORT DATE (DD-MM-YYYY) 15-04-2004		2. REPORT TYPE Scientific, Interim		3. DATES COVERED (From - To)	
4. TITLE AND SUBTITLE Absolute Infrared Calibration of Standard Stars by the Midcourse Space Experiment				5a. CONTRACT NUMBER	
				5b. GRANT NUMBER	
				5c. PROGRAM ELEMENT NUMBER 63173C	
6. AUTHOR(S) S. D. Price, C. Paxson*, C. Engelke**, T.L. Murdock*, and K. E. Kraemer				5d. PROJECT NUMBER 1182	
				5e. TASK NUMBER BD	
				5f. WORK UNIT NUMBER A2	
7. PERFORMING ORGANIZATION NAME(S) AND ADDRESS(ES) Air Force Research Laboratory 29 Randolph Road Hanscom AFB, MA 01731-3010				8. PERFORMING ORGANIZATION REPORT NUMBER AFRL-VS-HA-TR-2004-1109 E. R. P., No. 1259	
9. SPONSORING / MONITORING AGENCY NAME(S) AND ADDRESS(ES)				10. SPONSOR/MONITOR'S ACRONYM(S) AFRL/VSBYB	
				11. SPONSOR/MONITOR'S REPORT NUMBER(S)	
12. DISTRIBUTION / AVAILABILITY STATEMENT Approved for public release; distribution unlimited					
13. SUPPLEMENTARY NOTES *Frontier Technology, Inc **Institute for Scientific Research, Boston College, Chestnut Hill, MA 02467					
14. ABSTRACT Calibration experiments were conducted with the SPIRIT III infrared instrument on the Midcourse Space Experiment (MSX) against a number of infrared standard stars and five emissive reference spheres that were ejected at various times during the mission. The physical properties of the 2 cm diameter aluminum spheres, such as the Bond albedo and thermal emissivity of the Martin Black coating, were measured in the laboratory. The thermal balance equation between total flux absorbed and that emitted by the sphere was solved to obtain the time dependent temperature of the sphere under the assumption that the sphere radiates as a blackbody at this temperature with a mean infrared emissivity. The estimated uncertainties in the modeling of the sphere are estimated to be about 1K in the thermal component and 3% for the geometry contribution. MSX also measured more than 150 averaged fluxes on eight standard infrared calibration stars during the 10-month mission. The photometric spectral energy distributions of the stars are measured to be within the uncertainties assigned to absolute fluxes adopted for these stars, with a few exceptions. However, the small MSX measurement uncertainties did reveal statistically significant deviations from the recommended values. β Peg was the only calibrations star that was found to be variable. MSX also observed excess fluxes for Vega in the 12.1, 14.7 and 21.3 μ m spectral bands; the excesses in the latter two bands are consistent with the published thermal model for the dust ring around this star. The absolute calibration of the fluxes of the stellar standards based on the average of the measurements of the spheres over all MSX bands and the five experiments agrees with the predictions to within the uncertainties. The zero magnitude absolute fluxes proposed by Cohen et al (1992) are validated if the flux from Sirius is increased by 1%.					
15. SUBJECT TERMS Infrared calibration Infrared stars					
16. SECURITY CLASSIFICATION OF:			17. LIMITATION OF ABSTRACT UNL	18. NUMBER OF PAGES	19a. NAME OF RESPONSIBLE PERSON Stephan D. Price
a. REPORT UNCL	b. ABSTRACT UNCL	c. THIS PAGE UNCL			19b. TELEPHONE NUMBER (include area code)

ERRATA

AFRL-VS-HA-TR-2004-1109

Absolute Infrared Calibration of Standard Stars by the
Midcourse Space Experiment

Please correct the front cover of the report.

The third author's name should be C. Engelke, .

Research Publications
AFRL/VSIP
29 Randolph Road
Hanscom AFB, MA 01731

2006 0831019

A458662

TABLE OF CONTENTS

1	Introduction.....	1
2	Infrared Absolute Calibration Standard Stars.....	4
2.1	The Primary Infrared Calibration Standards: Vega (α Lyr) and Sirius (α CMa).....	5
2.2	The Absolute Zero Magnitude Flux Scale.....	7
2.2.1	The Solar Analog Calibration.....	8
2.2.2	Direct Calibrations.....	10
2.3	Secondary Infrared Calibration Standards.....	12
2.4	A Network of Calibration Stars.....	15
3	MSX Stellar Calibration.....	18
3.1	The MSX SPIRIT III Infrared Telescope.....	18
3.2	Ground Calibration.....	20
3.3	The MSX On-Orbit Calibration Experiments.....	23
3.3.1	MSX Stellar Calibration Measurements.....	23
3.3.1.1	DC44 – Stellar Benchmark Experiment.....	24
3.3.1.2	DC43 – Source Transfer Experiment.....	25
3.3.1.3	DC35 – SPIRIT III Radiometric Calibration.....	25
3.3.1.4	DC33 – Flat Field Calibration Mirror Scan Mode.....	25
3.3.1.5	CB06 – Celestial Radiometric Standards.....	25
3.3.2	Emissive Reference Spheres Experiment – DC22.....	26
3.4	The Effects of On-Orbit Performance on SPIRIT III Calibration.....	26
3.5	Data Processing.....	28
3.5.1	Identification and Photometry of Point Sources in the Mirror Scan Mode.....	29
3.5.2	CB06 Photometry.....	30
4	MSX Mission Averaged Stellar Standard Fluxes.....	31
4.1	Global Mean Fluxes.....	53
4.2	Measurement Precision.....	54
4.3	Results for the Primary and Secondary Standard Stars.....	56
4.3.1	Variability.....	60
4.3.2	Flux Excess.....	62
4.4	Assessment of the Calibration Network Stars with Spectral Templates.....	62
4.5	Bright Stars.....	64
5	Reference Spheres.....	68
5.1	Physical Characteristics of the Emissive Reference Spheres.....	69
5.2	Thermal Input from the Sun.....	71
5.3	Upwelling Radiation from the Earth.....	72
5.4	Measurement Geometry/Orbit of the Sphere.....	76
5.5	Estimated Uncertainty in the Model Predictions.....	77
5.6	Calibration Against the Emissive Reference Spheres.....	79
6	Absolute Calibration of the Standard Stars.....	92
7	Improvement to the Stellar Standards.....	95
7.1	New Calibrated Reference Spectra.....	95
7.1.1	Rationalizing the SWS Spectroscopy.....	97
7.1.2	Splicing the Near-IR data to the SWS Spectra.....	103
7.1.3	Photometric Scaling.....	103

7.2 The Continuum and Spectral Templates	108
7.2.1 Molecular Absorption as a Function of Effective Temperature above 2.36 μm ...	111
7.2.2 Spectra at $\lambda < 2.36 \mu\text{m}$	114
7.2.3 Autoshape and Spectral Templates	114
7.3 Derived Parameters	117
7.3.1 Angular Diameters	117
7.3.1.1 Interferometric Sizes	118
7.3.1.2 Indirect Determinations of Angular Diameters.....	120
7.3.2 Effective Temperatures	121
7.4 Uncertainties and Caveats	123
7.4.1 Estimated Uncertainties	123
7.4.2 Variability	124
7.4.3 Outliers.....	126
8 Summary and Conclusions	127
References.....	129
Appendix A Photometric Scaling of the Calibrated Spectra	143
Appendix B Additional Templated Spectra.....	221

FIGURES

Figure 1: The absolute fluxes derived for Vega in Paper I.....	11
Figure 2: The α Tau composite spectrum from Paper II.....	15
Figure 3: The distribution of stars in the stellar calibration network.	16
Figure 4: The scan geometry used for the DC43 and 44 DCEs.	24
Figure 5: The ratio of the individual measured Band A fluxes of α Boo divided by the DCE mean for six stellar calibration DCEs.....	30
Figure 6: The measured Band D detector biases..	31
Figure 7: DCE averaged fluxes from α Boo in each of the MSX spectral bands plotted as a function of focal plane temperature.	32
Figure 8: The ratio of the fluxes from α Tau to those from α CMa observed on the same DCE plotted as a function of focal plane temperature for that DCE.	33
Figure 9: The irradiance response in Band A normalized to Sirius as a function of focal plane temperature.	35
Figure 10: The B Band irradiance responses normalized to α CMa as a function of focal plane temperature. Band B ₁ is shown on the top and Band B ₂ on the bottom.	36
Figure 11: The Band C irradiance response normalized to Sirius as a function of focal plane temperatures.....	37
Figure 12: The Band D irradiance response normalized to Sirius as a function of focal plane temperatures.....	37
Figure 13: The irradiance response in Band E as a function of focal plane temperature.	38
Figure 14: The responsivity correction as a function of focal plane temperature.	39
Figure 15: The MSX measured response to NGC 6543 compared to the correction curves.....	40
Figure 16: The histogram of the frequency of occurrence in a Band E irradiance bin for γ Cru is shown before (left) and after (right) applying the response correction.....	41
Figure 17: DCE mirror-scan means for α CMa after correcting for temperature dependent responsivity plotted with the standard deviations about the means as error bars.	42
Figure 18: DCE mirror-scan means for α Lyr after correcting for temperature dependent responsivity.....	43
Figure 19: DCE mirror-scan means for α Boo after correcting for temperature dependent responsivity.....	44
Figure 20: DCE mirror-scan means for α Tau after correcting for temperature dependent responsivity.....	45
Figure 21: DCE mirror-scan means for β Gem after correcting for temperature dependent responsivity.....	46
Figure 22: DCE mirror-scan means for β Peg after correcting for temperature dependent responsivity.....	47
Figure 23: DCE mirror-scan means for γ Cru after correcting for temperature dependent responsivity.....	48
Figure 24: DCE mirror-scan means for γ Dra after correcting for temperature dependent responsivity.....	49
Figure 25: Histograms of the mirror scanned measurements on α Boo.....	51
Figure 26: Bias in the ratio of the MSX fluxes measured for the standard stars and for α CMa divided by the ratio of the predicted fluxes from Table 3.....	58

Figure 27: Correlation between MSX magnitude differences with respect to Band D and spectral type.	59
Figure 28: Time variation of the β Peg DCE mean in-band irradiances.	60
Figure 29: COBE/DIRBE 1.25 – 25 μ m photometry of β Peg plotted as a function of Julian day over 10 months in 1993.	61
Figure 30: The brightest infrared stars.	64
Figure 31: Infrared variability of W Hya during the 10 month COBE DIRBE mission (Smith, private communication).	65
Figure 32: MSX photometry in W cm ⁻² of μ Cep as a function of Julian date (minus 2449000).	67
Figure 33: The infrared reflectivity (left) and emissivity (right) of the Martin Black coated sphere as a function of wavelength integrated over a hemisphere.	70
Figure 34: The ground track of the ERS1 is overlain on the AVHRR 11.5 μ m map used to calculate the upwelling thermal radiation from the Earth for this experiment.	72
Figure 35: The spectral radiance from the Earth predicted by MODTRAN (dashed line) is scaled by narrow band measurements from AVHRR (asterisks) obtained near or during the ERS DCE to produce the upwelling spectral radiance from the Earth during the sphere measurements.	73
Figure 36: The time evolution of the predicted infrared spectral radiance from the Earth incident on ERS1.	74
Figure 37: A comparison of the model results for ERS1 (top plots) and ERS5 (bottom plots). ..	75
Figure 38: The reflected spectral flux relative to the total of the first emissive reference sphere just before entering eclipse (a) and just after (b).	78
Figure 39: The in-band irradiances plotted as a function of time for ERS1.	79
Figure 40: Measured irradiances are plotted as a function of time for the ERS5 experiment. ..	80
Figure 41: The ERS1 measurement biases.	81
Figure 42: The ERS2 measurement biases.	82
Figure 43: The ERS3 measurement biases.	82
Figure 44: The ERS4 measurement biases.	83
Figure 45: The ERS5 measurement biases.	83
Figure 46: The weighted mean biases and standard deviations for the individual ERS experiments and the weighted average for all five DCEs (dotted lines and diamonds).	84
Figure 47: Measured ERS1 color ratios with error bars compared to predictions (solid line).	86
Figure 48: Color ratios measured for the second sphere compared to model predictions.	87
Figure 49: Color ratios measured for the third sphere compared to model predictions.	88
Figure 50: Color ratios measured for the fourth sphere compared to model predictions.	89
Figure 51: Color ratios measured for the fifth sphere compared to model predictions.	90
Figure 52: A comparison between various direct absolute infrared calibrations and suggested zero magnitude spectral energy distributions.	93
Figure 53: Comparison of the normalized mid-infrared spectra of α Tau.	99
Figure 54: Comparison of the measured photometry on α Tau with that predicted from the spectra shown in Figure 1.	100
Figure 55: Adjustments to the α Tau SWS spectral segment 2C, which contains the SiO fundamental.	102
Figure 56: Calibrated SWS spectra (solid line) for 12 standard stars normalized to the Engelke function with the parameters given in the box.	105

Figure 57: The percent deviation of the spectral flux from a Kurucz model atmosphere for α Boo (dotted line) from the corresponding Engelke function (dashed line).	109
Figure 58: The inverse of the correction factor ($1/\text{frac}$) to Equation (1) versus the effective temperature of the star.	110
Figure 59: The averaged molecular absorption profiles.	111
Figure 60: The factors needed to scale the profiles in Figure 59 to fit the spectra of the in stars in Tables 20 and 21 plotted as a function of T_{eff} for (a) the CO fundamental, (b) the CO overtone, (c) the SiO fundamental and (d) the SiO overtone bands.	112
Figure 61: The <i>autoshape</i> function at three effective temperatures. The functions are normalized to the appropriate Engelke functions at $\lambda > 1.6$ and by a blackbody with a brightness temperature that varies as a quadratic function in wavelength from the effective temperature at $1.0 \mu\text{m}$ to the temperature of the Engelke function at $1.6 \mu\text{m}$	115
Figure 62: The <i>autoshape</i> spectrum for α Hya (dotted line) compared to the Cohen et al. composite spectrum (solid line).	116
Figure 63: The effective temperatures derived in the present analysis are plotted against spectral index and are compared to those found in the literature.	122
Figure 64: The averaged rms scatter of the deviations of the final calibrated spectra between 2 and $35 \mu\text{m}$ of α Boo, α Tau, γ Dra, β And and γ Cru after they have been normalized by the respective <i>autoshape</i> functions.	124

TABLES

Table 1: The Primary and Secondary Calibration Standard Stars	13
Table 2: Parameters of the MSX SPIRIT III Spectral Bands	19
Table 3: Stellar Standards Measured by MSX.....	23
Table 4: Coefficients for the Response vs. Focal Plane Temperature Correction	40
Table 5: Mirror-Scan Weighted Mission Average Fluxes.....	50
Table 6: CB06 Mission Averaged Fluxes.....	50
Table 7: Global Histogram Averages	53
Table 8: Global DCATT + CB Calibration of the CWW Stars.....	54
Table 9: Reduced χ^2 Goodness of Match between DCATT and CB Scaled Mission Means	54
Table 10: Standard Deviations from Histograms of the Original Data, the Data After Averaging Successive Measurements And After Correcting For The Response	55
Table 11: Precision in Results from Different Processing Procedures	56
Table 12: Measured Divided by the Predicted Fluxes.....	56
Table 13: Results for Stars with Spectral Templates.....	63
Table 14: Bright IR Stars Measured on the DC Calibration Experiments.....	66
Table 15: Percent Biases and Associated Errors for the ERS Experiments.....	85
Table 16: Correction Factors for Model Components from Band Correlated Solution	88
Table 17: The Ratio of the Stellar Fluxes Measured on the DC22s to the Mission Mean Fluxes.....	91
Table 18: Mirror-Scan Corrections For α CMa And Uncertainties	92
Table 19: Corrected Weighted Mean Biases	92
Table 20: Best Secondary Standards.....	96
Table 21: Additional Secondary Standards.....	97
Table 22: Templated Standard Stars.....	116
Table 23: Angular Size Comparison I: Interferometric Values	117
Table 24: Angular Size Comparison II: Indirect Values	118
Table 25: Temperature Comparison	121
Table 26: DIRBE Variability	125

Acknowledgments

The description of the absolute stellar calibration by MSX in this technical report expands on the article by the authors published in the *Astronomical Journal* (Engelke, Price and Kraemer, 2006) in order to provide a detailed step-by-step description of the analysis and includes intermediate benchmark results. The MSX absolute calibration was placed in the wider context of the AFRL Celestial Standards Calibration effort by including sections from a Space Sciences Review article by one of us (SDP). Thus, large sections of the text in this TR appear in these references. We thank Martin Cohen and Russ Walker for providing us with the MSX in-band fluxes they derived from the absolutely calibrated spectra of the CWW primary and secondary standard stars, for the images from the individual CB06 scan legs from which we obtained the photometry in this analysis and the many helpful suggestions. Beverly Smith very kindly allowed us to use the COBE/DIRBE time resolved photometry of the brighter stars observed on the MSX calibration experiments. We used the photometric archive of the mirror scan observations created by Sean Burdick and David Morris who used the Standard CONVERT routine to extract the fluxes from each scan. Michael Baca, James Elgin, Eric Layton and Sara-Anne Taylor were the first to recognize the residual variation in the responsivity in the MSX bands as a function of focal plane temperature from the stellar calibration observations. Wes Cobb, Colleen Hamilton, Joseph Howard and Michael Mavrofrides developed and implemented various routines in the models for the thermal emission from the spheres. We found and corrected errors in the routines that calculated the amount of sunlight reflected by the Earth and the thermal emission from the Earth that was intercepted by the sphere. Don Mizuno provided the NGC 6543 plots. Finally, we acknowledge the original MSX program manager Dr. Barry Katz (deceased) for his efforts in getting MSX flown and placing a high priority on the calibration experiments.

1 Introduction

Accurate calibration of infrared measurements is essential for interpreting the physics of the objects being studied. Although different procedures are used to determine the system responses of space- and ground-based sensors because of the markedly different operating conditions, the sensors responses are, in general, ultimately tied to absolutely calibrated fluxes of standard stars. Using standard stars to calibrate space- and ground-based observations of astronomical sources and Earth satellites has the advantage that such sources are stable, that is, their brightness does not change over the lifetime of the sensor, and they, themselves, can be well calibrated. Also, since the response of a space-based sensor will likely change during the mission due to aging of detectors and (cryo-) deposition on the optics, for example, celestial standards are the in-orbit resources of choice since they calibrate and monitor the entire throughput of the system. Establishing a ladder of primary and secondary infrared calibration stars across the sky is a natural extension of the manner in which optical photometry is calibrated.

The relatively low sensitivity of the pre-1980 space and ground-based instruments required very bright calibration sources and Venus, Mars and Jupiter were proposed (Logan et al., 1973; Becklin et al., 1973; Logan et al., 1974) as were the very brightest stars. The demand for infrared radiometric stellar references in the 1970s with which to compare space-based measurements led Price (1970a) and Hall (1974) to estimate 10 μm fluxes of the bright stars compiled from information in the published literature. The fluxes in these lists were obtained by simply converting the published magnitude for a particular star to fluxes based on the Johnson (1965) photometric zero magnitude fluxes. Since the brightest and most easily measured infrared stars then available are variable, these stars make up a large percentage of the lists. Updated versions of the lists were used to calibrate the AFCRL/AFGL rocket-borne infrared sky surveys (Walker and Price, 1975; Price and Walker, 1976; Price and Murdock, 1983) under the assumption that the variability of the individual stars would be averaged out by observing a large number of sources over the different epochs of the individual experiments. Price and Walker (1978) and Price (1978) determined that the calibration thus derived for the early AFCRL survey instruments agreed to within 10 percent of ground-based calibrations in the Arnold Engineering and Development Center (AEDC) chamber, which was designed and built to calibrate Air Force space-sensors, although the formal uncertainties of the AEDC measurements were lower.

The original infrared calibration of Johnson (1965) used a solar analog method that transferred the measured absolute infrared fluxes from the Sun to Vega using the measured infrared to visual flux differences for solar type stars and the known apparent visual magnitudes of Vega and the Sun. The absolute fluxes of standard stars have also been determined by direct and other indirect means. Indirect methods extrapolate a direct measurement of the flux at one wavelength to the flux at another. A direct calibration compares a certified source, typically a blackbody, with the standard star at various wavelengths, such as was done for Vega in the visual (see Hayes, 1985, for a comprehensive review) and in the near infrared by Walker (1969), Selby et al. (1980) and Mountain et al. (1985, and references therein). The blackbody is placed within, or near, the telescope and account has to be taken for the difference in measurement geometry, the transmissions of the optical paths and the atmospheric attenuation between the blackbody and star. Alternatively, the sensor is used to transfer the laboratory reference to in-flight measurements of a celestial source under the assumption that any instrumental changes between the times of calibration and measurement are tracked and quantified by on-board 'calibration'

sources. This is how Becklin et al. (1973) tied the infrared radiometry of Mars by Mariner 6, 7 and 9 spacecraft to ground-based calibration of the instruments. This calibration was, in turn, transferred through ground-based comparisons between Mars and bright infrared stars. Rieke, Lebofsky and Low (1985) used the same procedure with Viking 7 infrared thermal mapper observations. Subsequently, Witteborn et al. (1999) transferred the laboratory calibration of their airborne spectrometer against a blackbody directly to a spectrum of α Boo obtained from the Kuiper Airborne Observatory (KAO).

Infrared technology has improved considerably since the 1970s. Now, the accuracy of the absolute infrared flux measurements is limited by either the uncertainties in flux from the fundamental standard to which the calibration is referenced or by the difference in the spectral fluxes adopted by various investigators for the same primary standard star. The infrared community has often used the convention that the infrared colors (differences in magnitudes at different wavelengths) are zero for the average A0 V star and that Vega, α Lyr, is the prototypical average A0 V star. But Vega is rather faint in the infrared and more easily measured brighter standards were used initially. This requires that the relative magnitudes of the brighter stars be accurately measured with respect to α Lyr (Vega).

Campins, Rieke and Lebofsky (1985) and Rieke, Lebofsky and Low (1985) critically assessed the near- and mid-infrared flux calibrations of Vega, respectively, as well as the zero magnitude fluxes on the Arizona photometric system. Both studies found systematic differences between the Vega infrared fluxes that were extrapolated from the visual absolute calibration and those obtained by either the direct measurements or the solar analog method. The 10 percent difference they found at 10 μ m is significant, as Rieke, Lebofsky and Low cite a probable error of 3 percent for their 10.6 μ m calibration which was based on a weighted average of their direct and solar analog determinations. The abstract of a XONTECH 1988 report to the Army summarized the situation as: "Progress in the field of sensor calibrations has been mixed and uncalibrated. A literature review revealed that no one published document provides the complete visual and infrared (IR) spectrum of a given star. ... The collection and comparison of the stellar data base in one handbook over a wide waveband range is necessary to establish the accuracy of the existing stellar data base and provide standards for comparisons of sensor observations." Hayes (1985) was of a similar opinion in his detailed review of the absolute visual flux calibration of Vega as he assessed the state of the absolute stellar calibration in the infrared as "immature."

In response to this uncertain state of affairs in the mid-1980s, the Air Force Geophysics Laboratory convened a Stellar Atlas Panel with the goal of improving the accuracy of the calibration for military sensors and to provide a single set of standards for universal use. The common practice at the time was for each military experiment to fund its own ground-based calibration measurements. Representatives from the Air Force, Army, Naval Research Lab and Strategic Defense Initiative Organization served on the panel with contributions from the civilian astronomical community. The objectives of the Stellar Atlas Panel were to:

1. Define a zero magnitude primary standard star and its absolute spectral energy distribution. The zero magnitude fluxes for any spectral band are derived from the standard, and accurate fluxes can be calculated for any star from infrared photometry in a given infrared photometric system relative to the standard.
2. Establish absolute infrared spectral energy distributions for secondary standard stars.
3. Create a network of infrared calibration stars with absolute infrared spectra.

The Panel recommended that α Lyr be defined as zero magnitude at all infrared wavelengths. A realistic spectral energy distribution derived from stellar atmospheric model calculations was adopted for the star. The spectral energy distribution of this model is scaled to absolute visual flux measured by direct comparisons against National Institute of Standards and Technology (NIST) certified laboratory standards (see Hayes, 1985). The zero magnitude infrared fluxes for a photometric system are defined by weighting the absolute spectral energy distribution of α Lyr thus derived by the spectral responses of the bands at the operating temperature of the instrument and integrating the result over wavelength. The second objective is to create secondary stellar standards with well-measured infrared spectra that are scaled to absolute flux levels by reference to the primary standards. The last objective addresses the need of a space-based sensor for *in-situ* calibration in non-astronomical bandpasses with calibration stars near any line of sight. The absolute flux of a standard star in a specific system band is derived by integrating over wavelength the absolute spectrum for that star weighted by the relative spectral response of the system. The system spectral response includes the spectral reflectivity/transmission of the optical train and spectral filters, the relative spectral response of the detectors and, for ground based systems, the atmospheric transmission.

Although many steps were necessary to create the absolute spectral energy distributions for the secondary calibration stars with a pedigree traceable to internationally recognized blackbody standards, the estimated formal uncertainty of the monochromatic spectral irradiance is usually < 2 percent for the stars in the network. However, it may be as much as 8–10 percent in the nearly opaque $4.3 \mu\text{m}$ CO_2 band (Cohen, Walker and Witteborn, 1992). Since this calibration was indirect and relied on extrapolating an absolute visual calibration into the infrared, it too produced values that were consistently lower than those contemporaneously derived by direct calibrations or by the solar analog method (Mégessier, 1995, for example). A synthesis by Bersanelli, Bouchet and Falomo (1991) shows deviations of up to 15 percent between the various infrared calibrations. Mégessier (1995) significantly reduced the discrepancies by considering only the direct calibrations and those based on the solar analog method; she found that half of the Vega calibrations thus selected fell within ± 1.6 percent of the best fitting blackbody curve.

Calibration experiments conducted during the Midcourse Space Experiment (MSX) mission provided the first high quality direct infrared stellar calibration from space. These experiments validated the absolute calibration proposed by Cohen et al. (1992a) to within the stated uncertainties of these authors. However, the high accuracy of the MSX results indicated that detailed revisions of the absolute spectral energy distributions were in order for many of the standards. The most important revision was an increase in the absolute flux from α CMa, Sirius, by one percent. Other measurements indicated that the value of two of the stars as calibrators was limited. The infrared flux from β Peg was measured to vary by ± 4 percent during the 10 month MSX mission. It was determined that Vega, α Lyr, should not be used at wavelengths $> 12 \mu\text{m}$ because of excess emission from the circumstellar shell around this star. Finally, the quality of the MSX results allowed us to adjust the absolute spectral irradiance curves of the calibration stars to improve the accuracy of standards that had MSX measurements. We used the high quality spectra obtained by the Short Wavelength Spectrometer (SWS) on the Infrared Space Observatory (ISO) to create moderate resolution ($\lambda/\Delta\lambda > 400$) absolute infrared spectral energy distributions for all 14 of the secondary standard stars proposed by Cohen et al. We have also improved the spectral resolution of another 20 or so of the Cohen et al. tertiary standards using the SWS observations.

2 Infrared Absolute Calibration Standard Stars

The Air Force Geophysics Lab, and its successor entities, sponsored much of the calibration effort to meet the objective of the Stellar Atlas Panel. This effort and the results are described in a series of published articles:

- Volk and Cohen (1989) corrected the calibration of the Low Resolution Spectrometer (LRS) on the Infrared Astronomical Satellite (IRAS).
- Cohen et al. (1992a; Paper I) derived the absolute infrared flux for α Lyr by extrapolating the recommended visual flux of Hayes (1985) into the infrared using a Kurucz model for the spectral energy distribution. This calibration was transferred to a Kurucz modeled energy distribution for α CMa through accurate photometric scaling with respect to α Lyr.
- Cohen, Walker and Witteborn (1992; Paper II) created a calibrated infrared spectrum of α Tau from spectral measurements and photometry, and then refined the IRAS LRS calibration.
- Cohen et al. (1992b; Paper III) discussed the influences CO and SiO molecular absorptions have on the calibrated spectra of the cooler standard stars.
- Cohen et al. (1995; Paper IV) created 1.2 to 35 μ m calibrated spectra for six stars with spectral types between K0 III and M2.5 III from measured spectra and accurate photometric reference to the primary standards α Lyr and α CMa.
- Cohen and Davies (1995; Paper V) described the care that must be taken to avoid instrumental artifacts in ground-based spectral measurements.
- Cohen et al. (1996a; Paper VI) calibrated three southern hemisphere secondary standard stars.
- Cohen et al. (1996b; Paper VII) derived calibrated composite spectra for four additional stars and updated the α Boo spectrum. They also compared the angular diameters for the seven secondary standard stars with measured values to those obtained by scaling model atmospheres to the calibrated composite spectral energy distributions.
- Cohen et al. (1998; Paper VIII) examined the utility of the large asteroids Ceres, Vesta and Pallas for infrared calibration. This analysis referenced the 5 – 14 μ m spectra of these asteroids to the secondary infrared standards α Tau and/or α Boo and drew conclusions regarding the standard thermal models of asteroids.
- Cohen (1998; Paper IX) assessed the calibration of the Diffuse Background Explorer (DIRBE) instrument on the Cosmic Background Experiment (COBE) against his calibrated spectra of α CMa and 10 secondary standards.
- Cohen et al. (1999; Paper X) created a calibration network of 422 uniformly distributed fainter stars with spectral types from K0 III to M0 III. The representative spectrum for each spectral type was created using the flux distributions of the secondary standards as templates. The appropriate spectral template was assigned to the network star according to its spectral type.
- Witteborn et al. (1999; Paper XI) compared the infrared spectra of Ceres to α Boo and a blackbody.
- Cohen, Hammersley and Egan (2000) checked the calibration of the Egan et al. (1999) MSX Point Source Catalog version 1.2 and examined the MSX photometric colors of ordinary stars.
- Cohen et al. (2001; Paper XII) analyzed the data from one of the MSX calibration experiments.
- Cohen et al. (2003a; Paper XIII) created ‘super-templates’ to extend the spectral templates from the visual through the infrared and proposed a method of generating faint calibration standards for the Spitzer Space Telescope (formerly the Space Infrared Telescope Facility or

SIRTF). They used these super-templates to create 33 stellar calibrators that are 100 – 1000 times fainter than previously published standards.

- Cohen, Wheaton and Megeath (2003b; Paper XIV) assessed the calibration of the Two-Micron All Sky Survey (2MASS).
- Price et al. (2004; Paper XV) directly calibrated the absolute flux from eight of the standard stars through reference to emissive reference spheres on MSX. The analysis presented in that article is expanded upon in considerably more detail in Sections 3 and 4 of this report.
- Price (2004) reviewed the various infrared calibrations that have been done and the different calibration techniques employed. This review places the Cohen et al. work in context of the efforts of others. Section 2 of this report has been adapted and updated from this reference.
- Engelke, Price and Kraemer (2006; Paper XVI) created absolute spectral energy distributions with higher spectral resolution and radiometric precision for all 14 of the Cohen et al. secondary standards and ~20 of the calibration stars that had template spectra.

We denote the calibration and standards produced by Cohen and his colleagues with the generic designation of Cohen et al. We include the date of the specific reference when referring to the details of an explicit analysis.

2.1 The Primary Infrared Calibration Standards: Vega (α Lyr) and Sirius (α CMa)

During the 1970s and 80s, various independent experiments determined the absolute irradiance of Vega (α Lyr) at 0.5556 μm by directly comparing the observed stellar flux to that of various laboratory standards at the telescope. Usually, these sources were either a tungsten strip lamp or a blackbody source operating at the melting point of copper or platinum; the uncertainties associated with the tungsten strip lamps were generally acknowledged to be larger than the blackbodies. The standard sources for the most accurate of these calibrations were, in turn, compared to a gold freezing point blackbody maintained at the National Bureau of Standards or the German equivalent, the Physikalische – Technische Bundesanstalt (PTB). (According to Hayes et al. (1975) “The freezing point of gold, at 1337.58 K, is the highest fundamental temperature on the International Practical Temperature Scale of the 1968 Comité International des Poids et Mesures.”). Hayes (1985) critically evaluated the six independent measurements available at the time of his review article and recommended a 0.5556 μm spectral flux of $3.44 \times 10^{-12} \text{ W cm}^{-2} \mu\text{m}^{-1}$ with a bias uncertainty of 1.45 percent.

Cohen et al. (1992a) derived an absolute infrared zero magnitude flux calibration in Paper I by scaling a Kurucz model spectrum for α Lyr to the absolutely calibrated 0.5556 μm visual flux of $3.44 \times 10^{-12} \text{ W cm}^{-2} \mu\text{m}^{-1}$ for the primary standard, Vega, recommended by Hayes (1985), to extrapolate the flux into the infrared. This analysis assumed that the circumstellar material that gives rise to the far-infrared excess observed for Vega (Aumann et al., 1984) was too cool to contribute at wavelengths less than 20 μm . Actually, Cohen et al. took a conservative approach in subsequent articles by only using the Vega spectrum at wavelengths $< 15 \mu\text{m}$ in creating the secondary standards and templates. In their analysis of the IRAS LRS spectrum of Vega in Paper II, Cohen, Walker and Witteborn (1992) found that there is little or no excess emission below this wavelength, although MSX results indicate possible contamination at $\lambda > 12 \mu\text{m}$.

The absolute infrared spectral flux for the second primary standard star, α CMa, was derived in Paper I by scaling a Kurucz modeled spectral energy distribution representative for Sirius through direct photometric comparisons with Vega in a photometric system that had very well

characterized spectral bands. Cohen et al. (1992a) assigned the 1.45 percent uncertainty derived by Hayes (1985) for the calibration in the visual to the infrared flux of Vega, which means that they assume that the Kurucz model they used is an exact representation. Cohen et al. derived 1.46 percent uncertainties in their absolute infrared fluxes for Sirius. The critical questions are: how valid is the procedure used to create the infrared fluxes of these two primary standard stars and how reasonable are the uncertainty estimates?

The Kurucz model atmosphere for Vega adopted by Cohen et al. in Paper I had effective temperature, gravity, metallicity and microturbulence parameters of $T_{\text{eff}} = 9400\text{K}$, $\log g = 3.9$, $[\text{Fe}/\text{H}] = -0.5$ and $v_{\text{microturb}} = 0\text{ km/sec}$, respectively. Cohen et al. deemed that this model gave the best fit to the observed atomic hydrogen Balmer discontinuity and the Balmer and metal line profiles. In Paper I, Cohen et al. needed a limb-darkened angular diameter of 3.35 milliarcseconds (mas) to scale the Kurucz model to match the $0.5556\text{ }\mu\text{m}$ absolute flux recommended by Hayes (1985). This value is 1.5σ larger than the $3.24 \pm 0.07\text{ mas}$ limb-darkened diameter for Vega measured in the visual by Hanbury-Brown, Davis and Allen (1974) and 4σ larger than the $3.225 \pm 0.032\text{ mas}$ measured by Mozurkewich et al. (2003). This difference between the predicted and measured angular diameters translates into a 7 percent flux discrepancy. Ciardi et al. (2001) determined a value of $3.28 \pm 0.01\text{ mas}$ for Vega with a near-infrared interferometer operating in the K-band atmospheric window, which is in substantial agreement with visual measurements but with a much smaller formal uncertainty. Interestingly, Ciardi et al. also found wavelength dependent residuals in their measurements, which they considered might be interpreted as a wavelength dependent angular diameter. They speculated that, since Vega is known to have an emission excess at longer wavelengths, the residuals could arise from a thin, warm circumstellar disk, which contributes an additional 3 – 6 percent to the flux from the star. Such an interpretation is at odds with the findings of Liu et al. (2004) that the 8 – 13.5 μm emission from the circumstellar ring had to be less than 2 percent of that from the star and those of Su et al. (2005) that indicates that dust has been cleared from the region within $11''$ of the star.

The Ciardi et al. observations qualitatively agree with the conclusions of Gulliver, Hill and Adelman (1994) that Vega is rapidly rotating and is viewed pole on. Gulliver et al. inferred from their models that the equatorial radius of Vega should be 1.28 – 1.4 times larger than the polar radius and that the effective temperature should decrease by $\sim 300\text{K}$ from the pole to the equatorial plane. This implies that the limb-darkening correction for Vega should be larger than that from a spherical body and that, if the standard limb-darkening correction is used, the observed angular diameter should increase with wavelength.

A model atmosphere with an effective temperature of $9500\text{K} < T_{\text{eff}} < 9600\text{K}$ is necessary to bring the measured angular diameters into agreement with the $0.5556\text{ }\mu\text{m}$ flux from Vega. Castelli and Kurucz (1993, 1994) re-examined the sensitivity of the Vega models to observed parameters and concluded that a model with $T_{\text{eff}} \sim 9550\text{K}$ provides a better fit. Subsequently, Kervella et al. (2004) independently derived essentially the same best fitting model with $T_{\text{eff}} = 9522\text{K}$, $\log g = 3.98$, $[\text{Fe}/\text{H}] = -0.33$. Tying the $T_{\text{eff}} \sim 9550\text{K}$ model to the $0.5556\text{ }\mu\text{m}$ absolute flux of Hayes (1985) results in an infrared flux that is about 3 percent lower than that derived in Paper I. As for the absolute visual flux, Mégessier (1995) critically assessed the absolute $0.5556\text{ }\mu\text{m}$ measurements of Vega available as of the early 1990s and recommends an absolute value of $3.46 \times 10^{-12}\text{ W cm}^{-2}\text{ }\mu\text{m}^{-1}$, which is 0.6 percent higher than Hayes' value. Adopting the most recent values of the mean angular diameter as measured by Ciardi et al. (2001), the Castelli and Kurucz (1994) $T_{\text{eff}} \sim 9550\text{K}$ Vega model atmosphere and the Mégessier flux at $0.5556\text{ }\mu\text{m}$ results

in an infrared flux that is about 2.5 percent lower than adopted in Paper I, which is a bit less than twice as large as the 1.45 percent uncertainty Cohen et al. ascribe to their Vega infrared fluxes.

Concern that their direct calibrations indicated that the near-infrared fluxes from Vega were anomalous, led Leggett et al. (1986) to examine the narrow band 1 – 5 μm photometry of 25 B8 – A3 dwarf stars. This J, K, L' and M photometric survey found that the near-infrared colors for Vega are normal for an A0 V star. Similarly, Leggett (1985) determined that the average V – N color for 33 B8 to A2 V stars was essentially the same as that measured for Vega. This is consistent with the Liu et al. (2004) results, which did not resolve N band mid-infrared circumstellar emission from the disk at a distance of > 0.8 AU from the star above 2.1 percent of the stellar flux at the 3σ confidence level. On the other hand, Price et al. (2004) did detect a ~ 4 percent excess at 14 μm , a 6σ result.

Since a single spherically symmetric model atmosphere for Vega is unlikely to reproduce the spectral energy distribution for a distorted rapidly rotating star viewed pole-on, there is some ambiguity as to which model best represents the infrared continuum flux. The excess emission from the circumstellar dust disk around Vega caused Cohen et al. to limit using their Vega absolute infrared spectral irradiances for calibration to wavelengths less than 15 μm , a reasonable restriction given the Leggett (1985) and Liu et al. (2004) measurements. These studies imply that either the infrared fluxes of late B to early A dwarfs predicted by model atmospheres are 3 – 11 percent smaller than that derived by indirect calibrations, which is difficult to reconcile with the general acceptance that the physics within the stellar atmosphere is well understood, or that the models are correct and the optical to infrared photometric colors adopted for these stars are in error.

The Sirius model spectrum in Paper I ($T_{\text{eff}} = 9850\text{K}$, $\log g = 4.25$, $[\text{Fe}/\text{H}] = +0.5$ and $v_{\text{microturb}} = 0$ km/sec) is scaled by the mean infrared flux ratio observed between Sirius and Vega in well-defined photometric systems. These parameters differ little from those adopted by Kervella et al. (2004) for the star. Hanbury-Brown, Davis and Allen (1974) measured a visual limb-darkened angular diameter of 5.89 ± 0.16 mas, a value that was subsequently confirmed by Davis and Tango (1986) but with half the error. Recently, Mozurkewich et al. (2003) obtained a value of 5.993 ± 0.108 , while Kervella et al. (2003a) measured the 2.2 μm limb-darkened diameter of Sirius to be 6.039 ± 0.019 mas. Both values agree within the measurements errors of the 6.04 mas derived in Paper I. Thus, there is no discrepancy between the recent angular diameter measurements for Sirius and the model absolute spectral energy distribution adopted in Paper I times the one percent flux adjustment from the MSX calibration results.

2.2 The Absolute Zero Magnitude Flux Scale

Although the angular diameter derived from the infrared flux predicted for Sirius by Cohen et al. is in excellent agreement with the more recent measured values, the measured physical parameters of angular diameter and absolute visual flux for the fundamental standard, α Lyr, are inconsistent with the absolute infrared fluxes proposed for this star in Paper I. The Cohen et al. Vega fluxes are biased about 3 percent high. The question is: how do the absolute infrared fluxes for Sirius and Vega in Paper I compare to those obtained from other calibration methods.

2.2.1 The Solar Analog Calibration

The absolute infrared fluxes for a zero magnitude star have been calculated by the solar analog method in a number of articles since Johnson's (1965) seminal paper. These include, but are not limited to, articles by Thomas, Hyland and Robinson (1973), Wamstecker (1981), Campins, Rieke and Lebofsky (1985), Rieke, Lebofsky and Low (1985) and Colina and Bohlin (1997). Generally, the steps in this procedure are:

- 1) The infrared colors with respect to the visual magnitude, V , for the Sun are assumed to be the same as the averaged colors for stars similar to the Sun.
- 2) The absolute solar flux in the visual filter, V , and in each infrared bandpass is calculated by integrating the absolute spectral irradiance of the Sun over the wavelength weighted by the spectral response of the respective filters.
- 3) The in-band irradiance for a $V = 0$ star is calculated by either: a) Integrating the absolute spectral energy distribution of Vega (and 109 Vir; Wamstecker, 1981) over wavelength weighted by the spectral response of the respective filters and scaling the result to $V = 0$ by the apparent V magnitude of Vega (and 109 Vir); or b) Adopting the canonical apparent V magnitude of -26.75 for the Sun.
- 4) The zero magnitude fluxes in the infrared bands are obtained by scaling the solar flux in the infrared spectral band in question by the infrared – visual color adopted for the Sun in step 1, that is $V - (V - [IR])$.

All the published infrared solar analog calibrations produce zero magnitude absolute fluxes that are systematically higher with increasing wavelength from those predicted by extrapolating the absolute visual flux measured for Vega into the infrared. Indeed, a blackbody distribution provides a better fit through the solar analog values (Bersanelli, Bouchet and Falomo, 1991; Mégessier, 1995). The exception is an analysis by Hayes, which is included in his 1985 review article (Hayes, 1985). Wamstecker (1981) noted that because Hayes adopted redder colors for a G2 V star than other investigators, his solar analog calibration was closer to the model extrapolations from the visual absolute flux of Vega. However, the discrepancies with respect to the Cohen et al. Vega fluxes are even smaller because these fluxes are biased about 3 percent high with respect to the Vega model extrapolations usually adopted by other investigators.

The solar analog method is predicated on having accurate values for the absolute flux measured for the Sun. All calibrations are ultimately tied to the absolute solar fluxes of Labs and Neckel (1968), as corrected by Labs and Neckel (1970) for a change in the second radiation constant. Note that these values have not been updated for the 1986 refinements radiation constants (Cohen and Taylor, 1994). Labs and Neckel derived 0.33 to 1.25 μm absolute solar fluxes through comparisons with a standard lamp. However, for wavelengths $> 1 \mu\text{m}$, they adopted the spectral energy distribution of a model solar atmosphere, which they 'fit through' the (rather sparse) 3.5 and 12 μm absolute measurements available to them. These measurements are all now quite old. The Saiedy and Goody (1959), Saiedy (1960) and Murcray, and Murcray and Williams (1964) measurements were referenced to standard sources but only the Murcray, Murcray and Williams observations were obtained from a balloon platform above much of the atmosphere. Labs and Neckel also used the Pierce (1954) 1 – 2.5 μm relative measurements to validate the shape of the model spectral energy distribution through the minimum in the solar atmospheric H^- opacity. The 21 to 45 μm infrared measurements of Beers (1966) anchored the shape at longer wavelengths. From the aggregate of these measurements, Labs and Neckel

estimated that the absolute infrared fluxes in their tables had a photometric error of 1 – 2 percent and that the systematic error was 2 – 3 percent. The 3 to 13 μm observations of Kondratyev et al. (1965) are in substantial agreement although the scatter between all the observations is of the order of ~5 percent as may be seen in Figure 11 of Vernazza, Avrett and Loeser (1976).

Labs and Neckel (1968) applied empirically derived correction factors to account for line blanketing and the ratio of the center to disk mean radiance, then scaled the result by the solid angle subtended by the Sun to convert their tabulated radiances for the center of the Sun into irradiances. Subsequently, Neckel and Labs (1981) used the Pierce, Slaughter and Weinberger (1977) wavelength-dependent fifth order polynomial approximations to limb darkening to derive what they consider more accurate 0.33 to 1.25 μm solar irradiances. Although a variety of analytic expressions have been adopted for limb darkening (see the discussion and references in Neckel, 1996, for examples) the fact is that the ratio of mean to central intensity for the Sun is close to unity in the infrared, increasing from 0.885 at 1 μm to 0.98 at 10 μm . Thus, the choice of the expression is of little consequence. Spickler, Benner and Russell (1996) noted that their measurements showed more infrared limb darkening than the limited number of other observations in this wavelength region, by roughly a factor of two at 10 μm . However, such a difference changes the center-to-disk average ratio by only 1 percent.

Aversen, Griffin and Pearson (1969) directly referenced the 0.3 to 2.5 μm solar spectral irradiance against a tungsten standard lamp to a purported accuracy of 3 percent from aircraft altitudes (11.6 to 12.5 km). They alternately measured the integrated solar irradiance and that of the lamp by means of a rotating integrating sphere. Their 1.25 – 2.5 μm solar irradiance agrees well, to ~1.5 percent, with that calculated by Neckel and Labs (1981) from absolute radiances at the center of the Sun. However, Colina, Bohlin and Castelli (1996) questioned the quality of the Aversen, Griffin and Pearson near-infrared solar spectrum, finding it is too blue in J – K and J – H by 0.07 – 0.10 magnitudes compared to photometry on solar analog stars. Instead, Colina et al. adopted the 1993 Kurucz solar model for the energy distribution in this region for their absolute zero magnitude flux calibration.

Thuillier et al. (2004) synthesized the absolute solar spectra to 2.4 μm for two levels of solar activity (Thuillier et al., 2003) from space-based observations that were referenced to direct calibrations in the laboratory. These spectra show 3 – 4 percent larger near-infrared fluxes compared to Labs and Neckel spectra, while the visible fluxes are about the same. The Thuillier et al. absolute solar fluxes are more discrepant compared with extrapolations used in Paper I than the absolute zero magnitude infrared fluxes derived by the solar analog method.

Thus, there are only a small number of directly calibrated absolute infrared solar irradiance measurements and they agree to within 5 – 10 percent. The standard absolute infrared spectral irradiances of the Sun are based on a solar model atmosphere tied to various infrared measurements. So, the question is: which solar atmosphere model is the best? We surveyed the literature and found little difference between solar models. The far-infrared fluxes ($\lambda > 25 \mu\text{m}$) differ by about 5 percent with better agreement at the shorter infrared wavelengths.

Equally ancient are the references used by Hayes (1985) to derive the –26.75 apparent V magnitude for the Sun that is commonly adopted. Hayes lists the three references between 1949 and 1964 that he used for his derivation. The indirect solar analog method scales the synthetic absolute solar flux in the spectral bands by the apparent visual magnitude of the Sun to derive the zero magnitude fluxes in a given photometric system. Lockwood, Tüg and White (1992)

attempted to do this scaling directly by comparing the attenuated spectrum of the Sun directly with Vega and the Tüg, White and Lockwood (1977) measurements of the absolute flux for Vega to derive the absolute solar irradiance between 0.33 and 0.85 μm . Unfortunately, they did not provide the scale factors between Vega and the Sun.

We conclude that the uncertainties in the absolute infrared irradiance from the Sun and the colors of stars chosen as representative solar analogs are as large as the differences between the absolute fluxes derived by the solar analog method and those obtained by extrapolating a model atmosphere tied to the absolute visual flux measured for Vega.

2.2.2 Direct Calibrations

Hall (1961) was the first to directly calibrate near-infrared stellar measurements against a blackbody source at the telescope. Later, Walker (1969) derived the absolute 1.06, 1.13, 1.63 and 2.21 μm fluxes of 61 stars by directly referencing them to a blackbody source maintained at a constant temperature of 402K at the telescope. A research team from Imperial College and Oxford University carried out the most extensive set of direct near-infrared calibration of the absolute fluxes from Vega against laboratory blackbodies throughout the 1980s. Selby et al. (1980) referenced their 2.20 μm irradiance measurements of Vega to that from a 1253.6K furnace operated at the telescope. Various improvements in the experimental configuration followed. Selby et al. (1983) used a narrower filter and extended the observations to 3.8 μm while Blackwell et al. (1983) used transmission attenuators to reduce the flux on the detector from the furnace to a level comparable to that from Vega. This group extended the comparisons to 1.26 μm and 4.6 μm using α Her, an M5 II star, as a transfer source for the 4.6 μm measurements. Mountain et al. (1985) then used a grating spectrometer to select a 0.006 μm wide band at 4.92 μm that was free of the atmospheric water vapor absorption lines for comparing Vega to the furnace. Finally, Booth et al. (1989) adapted the furnace and grating spectrometer to a different telescope to validate the previous calibrations with a 0.001 μm wide narrow-band comparison at 2.25 μm . These references cite probable errors between 4 and 8 percent. Mountain et al. (1985) concluded that the absolute near infrared measurements of the Imperial College/Oxford University team systematically diverged as a function of wavelength by as much as 10 percent from the model atmosphere extrapolation for Vega, and that a 10000K blackbody function provided a better fit. This wavelength dependent discrepancy also applies to the extrapolation of Cohen et al. (1992a) as is evident in Figure 1.

Low (1973) directly calibrated α Aur, α Tau and β And in a narrow mid-infrared filter centered at 11.34 μm against a blackbody using Mars as a transfer. He concurrently used two telescopes: a 30 cm instrument that measured the fluxes from Mars and a 600C blackbody on a tower located 515 m from the telescope while a 71 cm instrument compared Mars with the three stars. The stellar values were extrapolated along a 4000K blackbody to the 10.6 μm effective wavelengths of the Arizona standard N band. The results were scaled by the apparent N magnitudes of the three stars to derive the zero magnitude flux to an estimated accuracy of ± 10 percent.

The 10 and 20 μm calibrations of Becklin et al. (1973) were less direct. They measured the 8 – 13 μm and 17 – 26 μm absolute fluxes over portions of the Martian surface during the Mariner 6, 7 and 9 missions and created a thermo-physical model to convert these measurements into Martian disk-integrated in-band infrared fluxes. The absolute scale of the radiometry was

based on preflight laboratory calibration of the instruments against blackbody references. This was transferred to the observations at Mars by tracking the stability of the instruments through measurements against a reference plate. Ground-based observations transferred the Martian disk-integrated fluxes to α Ori and α Sco. Then, the observed in-band fluxes were converted to 10 and 20 μm spectral fluxes under the assumption that Mars radiated like a 300K blackbody and that the spectral energy distributions of the stars followed a Rayleigh-Jeans law. The zero magnitude fluxes at these wavelengths were derived from the adopted 10 and 20 μm broadband magnitudes for α Ori. Similarly, Rieke, Lebofsky and Low (1985) derived the disk integrated flux from Mars based on observations from the Viking Orbiter Infrared Thermal Mapper and transferred the result to β Gem with concurrent ground-based measurements. The result was converted into a zero magnitude flux through the adopted magnitudes of β Gem.

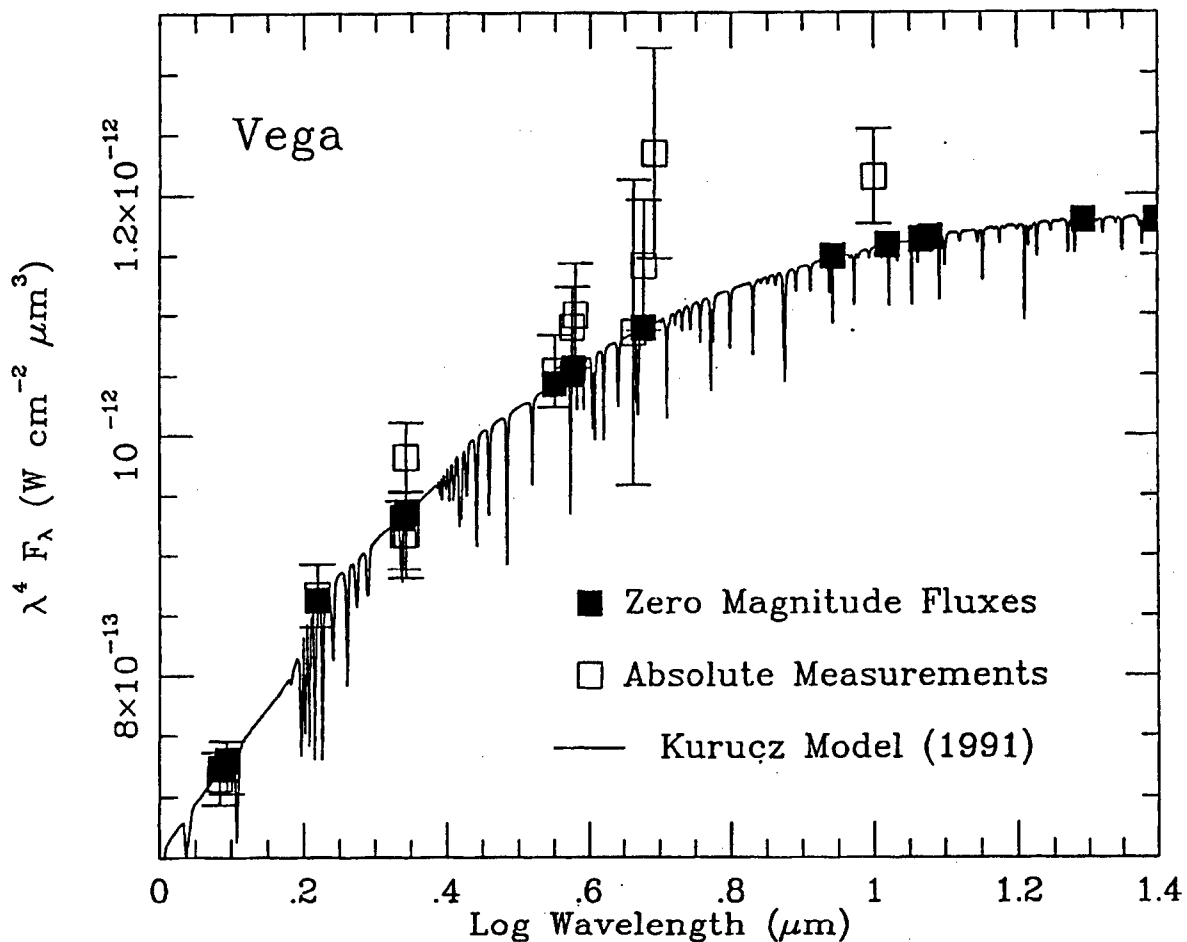


Figure 1: The absolute fluxes derived for Vega in Paper I. The solid line is the infrared from a Kurucz model tied to the visual absolute flux recommended by Hayes (1985). The black squares are the zero magnitude fluxes in various photometric systems; the size of the squares is the ± 1.45 percent uncertainty assigned the absolute flux. The open squares with the uncertainty bars are the various direct measurements of the absolute infrared flux of Vega before 1995. As may be seen, these calibrations give larger fluxes than those adopted in Paper I.

Rieke, Lebofsky and Low (1985) recommended a 10 μm zero magnitude flux that was the weighted average of the direct calibrations of Low (1973), Becklin et al. (1973) and themselves. This flux, plotted at $\log \lambda \sim 1$ as the measured value in Figure 1, is ~ 5 percent higher than the value from Cohen et al. The 20 μm value is an average of their 10 μm results extrapolated to 20 μm and those of Becklin et al. (1973) based on the latter's Mars observation.

These direct calibrations are quite old. The near-infrared calibrations were made ~ 25 years ago and about 30 years have passed since the mid-infrared calibrations were done. Within the last decade, Witteborn et al. (1999) calibrated the 5 – 30 μm spectrum of α Boo against a laboratory standard. This measurement was obtained using an infrared spectrometer flown on the Kuiper Airborne Observatory (KAO) at an altitude of >12 km, which eliminated much of the atmospheric contamination. Analogous to the approach of Becklin et al. (1973) and Rieke, Lebofsky and Low (1985), Witteborn et al. calibrated the absolute spectral response of their HIFOGS spectrometer against a standard blackbody reference source in the laboratory and relied on transfer sources and monitors to transfer the laboratory calibration to the in-flight measurements. However, Witteborn et al. suspected that systematic biases, which they attributed to slight boresight and other misalignments between the airborne and laboratory measurements, reduced the accuracy of this calibration. In the mid-1990s, the MSX experiment conducted the most precise direct mid-infrared calibration to date, as detailed later in the report.

2.3 Secondary Infrared Calibration Standards

The next step after establishing the absolute flux for Vega and Sirius, the two primary stellar calibration standards, and the zero magnitude flux scale in Paper I, was to transfer this calibration to fourteen bright infrared secondary standard stars. The absolute infrared spectral energy distributions for the twelve secondary infrared standard stars listed in Table 1 were created by scaling their measured spectral fragments by well-validated photometry with respect to Vega and/or Sirius. The procedure is summarized by Cohen et al. (1993) and details of the origin of the source spectra, the photometry and the results are given in Papers II, IV, VI and VII. Since no single 2 – 35 μm spectrum was available for these stars in the early 1990s, a spectrum had to be assembled from high signal-to-noise infrared spectral fragments that have a known 'calibration pedigree.' These fragments were culled from various archives and from measurements specifically obtained for this program. The ratio is taken between the spectral fragments of the star and that of Sirius or Vega obtained with the same system. The secondary stars, α Tau and α^1 Cen, were also used in the direct ratios in Papers IV and VI, respectively. The weighted average is then taken of the good quality spectra over the same wavelength interval, if more than one spectral fragment exists. The weights are the inverse of the observed monochromatic variances. Multiplying by the calibrated spectrum of the primary star normalizes out the spectrometer response. The in-band fluxes for spectral bands that are completely contained within the spectral fragments are obtained by integrating over wavelength the well-defined spectral response curves of the photometric system multiplied by the spectral energy distribution over the spectral fragment. The measured flux ratio with respect to a primary standard star scales the spectral fragment to an absolute flux. The normalized overlapping spectra are then spliced together to create a composite spectrum.

Thirteen of the secondary standard stars are relatively cool, K0 through early M giant stars and are brighter than Vega in the infrared. These stars have molecular features in their infrared spectra: the fundamental and first overtone bands of CO and SiO and the infrared water vapor

and OH lines (for example: Paper III; Heras et al., 2002). However, only the SiO and CO bands are important at the resolution of the spectral composites (Paper III). Stars with spectral classification of M4 and later were not considered for secondary standards even though they are among the brightest infrared sources because stars of these spectral types tend to be variable and many of them possess circumstellar dust shells that distort their infrared spectral energy distributions (Sloan and Price, 1998).

Table 1: The Primary and Secondary Calibration Standard Stars

Star	Sp. T.	T_{eff}		Star	Sp. T.	T_{eff}
α CMa (Sirius)*	A1 V	9850 K		ϵ Car	K3 III	4064 K
α Lyr (Vega) *	A0 V	9400 K		β UMi	K4 III	4150 K§
α^1 Cen #	G2 V	5770 K		γ Dra	K5 III	3986 K
β Gem	K0 III	4844 K		β And	M0 III	3839 K
α Boo	K1.5 III	4362 K		μ UMa	M0 III	3735 K
α Hya	K3 III	4141 K		α Cet	M1.5 III	3745 K
α Tau	K5+ III	3898 K		β Peg	M2.5 II-III	3600 K
α TrA	K2 III	4140 K		γ Cru	M3.4 III	3626 K

* Primary Standards

Secondary Standard with modeled infrared spectral radiance

§ Effective temperature adopted in order to derive the K4 III template for this star. The template is replaced by a measured spectrum in the present analysis as is the model infrared flux for α^1 Cen.

The composite spectra were created from spectral fragments obtained by the KAO, the IRAS LRS and ground-based observations. The KAO spectra were extracted from the literature and/or culled from the NASA Ames Research Center archive, while other KAO spectra and ground-based observations were obtained specifically for this effort. The KAO and ground-based spectra measured for this program were in the form of ratios between the spectral fragment for the star being studied and a primary standard star, either Vega or Sirius, or an intermediary that, in turn, had a measured spectral ratio with Vega or Sirius. The LRS spectra span the mid-infrared wavelength range from 7.7 to 22.7 μm and include the 15 μm terrestrial atmospheric CO₂ band, which is opaque to ground, aircraft and balloon platforms. Before the ISO mission, the LRS data were often the only available spectra at wavelengths longer than the 10 μm atmospheric window.

The original IRAS LRS spectral calibration of Olmon and Raimond (1986) demonstrates the pitfalls of assuming a blackbody or pseudo-continuum for the infrared spectral energy distribution and ignoring the rather significant infrared absorption features present in cool giants. The original LRS spectral irradiance calibration assumed that the K5 giant star α Tau radiates as a 10,000K blackbody. As may be seen from Table I, the effective temperature of α Tau is about 3900K. The error in the calibration introduced by adopting the 10,000K blackbody for the continuum was fortuitously not large, as it turns out that the infrared continuum from a star as cool as α Tau in which the opacity is dominated by H⁻ free – free absorption is reasonably well represented by a blackbody with an up to a factor of two higher temperature than the effective temperature. However, the continuum-only assumption produced an excess of emission in the LRS spectra of hot stars (Volk and Cohen, 1989; Paper II) and for very cool Mira variable stars

spectra described in Section 7 use the space-based SWS observations to eliminate these uncertainty spikes.

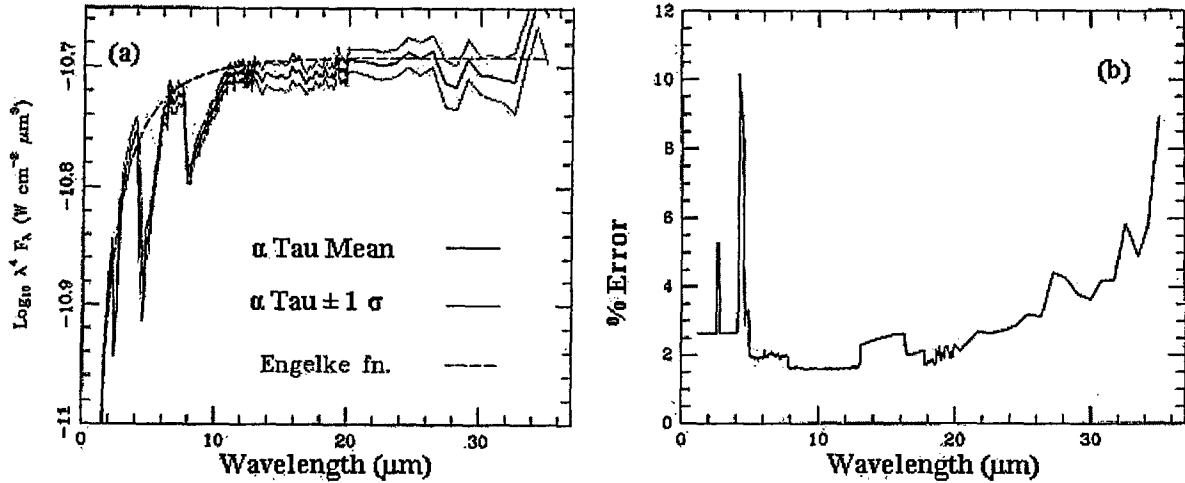


Figure 2: The α Tau composite spectrum from Paper II. The composite spectrum is the heavy line in (a) while the lighter lines are the $\pm 1 \sigma$ deviations. The dashed line is the Engelke function. The uncertainties in terms of percentage of the flux are shown in (b). The spikes in the uncertainty plot at the shorter wavelengths are influenced by the strong atmospheric absorption.

2.4 A Network of Calibration Stars

Some space- and ground-based infrared measurements require 'calibration on the fly', in which the sensor is calibrated by a source in the field of regard during the time the object of interest is being measured or the calibrator is near enough to the line of sight to take only a brief time to move to it. A horizon-to-horizon ground based measurement of an Earth orbiting satellite is an example of how such a network is used. Pre- and post-satellite passage measurements of calibration stars near the apparent track of the object provide a much more accurate estimate of the atmospheric transmission than measuring one or two stars at various zenith angles during the course of the night.

Cohen and his colleagues created a network of 619 calibration stars across the sky; the distribution of these stars on the sky is shown in Figure 3. This network included the modeled spectra for Vega and Sirius, the two primary calibrators, the model spectra of α^1 Cen and the 13 secondary stars with composite spectra. The remaining 603 stars in the network were selected using the criteria that:

- (1) A source should be non-variable in the infrared and not have a circumstellar dust shell. This criterion eliminates extended objects and stars of spectral type M4 III and later.
- (2) The star is isolated with no other source within 6 arcminutes.
- (3) There is no mid-infrared emission from extended sources or interstellar dust within several tens of arcminutes of the star.
- (4) High quality photometry on a well-characterized photometric system is available for the star with which to scale the spectrum.
- (5) The stars are uniformly distributed across the sky with an average spacing of less than 10° between the stars.

(6) The dynamic range of the network is reasonably large with stars with fluxes between $\sim 10^{-15}$ and 10^{-18} W/cm²/μm or a magnitude range of $-3 < m_{\text{IR}} < +5$.

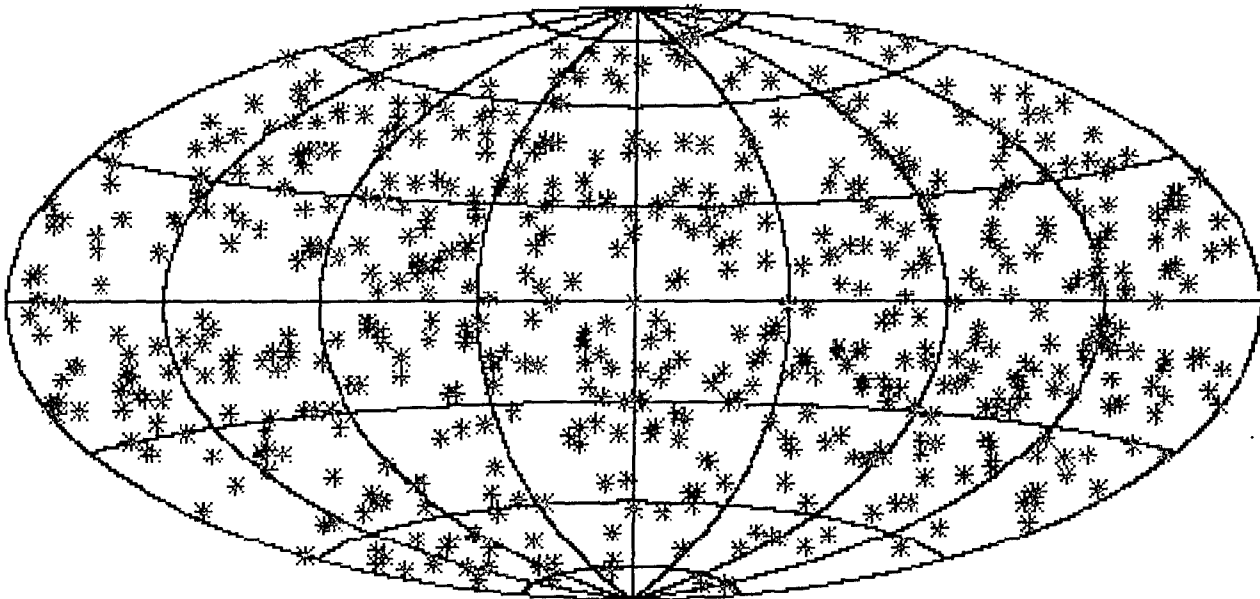


Figure 3: The distribution of stars in the stellar calibration network. The plot is in Galactic coordinates. The locations of the three stars with model spectra are shown in green, the thirteen stars with composite spectra are in red, and stars with spectral templates are blue.

In paper X, Cohen et al. (1999) describe how Version 2 of the network with 422 stars was created; Version 1 was a proof-of-concept that contained 183 stars. Originally, it was intended to give preference to stars that had good quality archival spectral fragments in the near- to mid-infrared ($\lambda < 14$ μm), which could be seamed to an appropriate Engelke function for the longer wavelengths. Unfortunately, the available good quality spectral fragments were inadequate to create a hybrid spectrum for a given star, if the fragments were available at all. Instead, a spectral template was created for each spectral type for which a composite spectrum was available. The composite spectrum at wavelengths shorter than 13 μm from one of the secondary standards was seamed to an Engelke function with the effective temperature assigned to the spectral class of the secondary standard and the result adopted as the template for the spectral class of the secondary standard. The Engelke function is scaled to the spectrum of the composite. The 11 – 13 μm wavelength region is beyond the SiO fundamental, so the splicing does not distort this feature. The template for the spectral class of a star in the network is adopted as the spectral energy distribution for the star and reddened, if necessary. The result is placed on an absolute flux scale by the high quality infrared photometry on the star. Only a third of the stars were reddened and only a modest amount of reddening was required for most of those.

Version 3 of the network had 570 stars, while the current network, Version 4 (Walker and Cohen, 2003), contains 619 stars. More accurate spectral types from the Fifth Volume of the Michigan Spectral Types were found for many of the network stars and appropriate template spectra assigned in the Version 3 update. Certain spectral types were not represented by the 13 secondary standards with composite spectra and, consequently, stars with these spectral types

had not been included in Version 2 of the network. A K4 III template was created by interpolating the smoothed K3 III composite spectrum of α Hya and the K5 III α Tau spectrum in the 's' parameter of de Jager and Nieuwenhuijzen (1987). Fifty-six K4 III stars were then added to the network using this template. M0 – M4 III templates were created in an analogous fashion to support the calibration of the Mid-Infrared Spectrometer on the ISAS/NASA Infrared Telescope in Space experiment (IRTS; Onaka et al., 2003), which were used to add another 19 stars. An additional 46 stars were included thanks to the accurate photometry of Hammersley et al. (1998, 2003) that was obtained on a well calibrated photometric system from the ground-based calibration program conducted for ISO. Cohen et al. created another 19 stars with template spectra in order to assess the calibration of the Diffuse Infrared Background Experiment (DIRBE) on the Cosmic Background Explorer (COBE).

The stars in the calibration network were used to calibrate, or validate the calibration of, the major infrared space-based sensors flown during the last decade. Burdick and Morris (1997) chose Vega and four of the Cohen et al. composites as the primary stellar calibrators for MSX and Egan et al. (2003) scaled the MSX photometry in Version 2.3 of the point source catalog to match the mean of that predicted for the calibration network stars that were measured by MSX. The various instruments on the Infrared Space Observatory were calibrated, at least in part, with the Cohen et al. composites (Schulz et al., 2002; Leech et al., 2003). The near- and mid-infrared spectrometers on the Japanese IRTS were calibrated against stars with spectral templates (Onaka et al., 2003). Cohen et al. critically examined the IRAS photometry in Paper I and the spectroscopic calibration in Paper II. The mid-infrared calibrations of DIRBE were based on the Sirius model in Paper I and were verified in Paper IX. The Vega spectral energy distribution was used to define the zero magnitude fluxes for Deep Near-Infrared Survey (DENIS), a ground-based, large scale, near-infrared survey of the southern sky (Fouqué et al., 2000). Cohen, Wheaton and Megeath (2003b) in Paper XIV provided a basis for assessing the calibration of the Two Micron All Sky Survey (2MASS) against the 33 faint stars for which they had created calibrated spectra from templates and accurate photometry. Cohen et al. (2003a) proposed on-orbit calibrators for the Spitzer infrared telescope. The latter two papers extend the network to 100 to 1000 times fainter fluxes.

3 MSX Stellar Calibration

MSX was a Ballistic Missile Defense Organization satellite designed to obtain ultraviolet through infrared measurements on a wide range of natural and man-made phenomena. MSX was launched on 24 April 1996 into a ~900 km, nearly Sun-synchronous orbit. SPIRIT III, the SPatial InfraRed Imaging Telescope III (SPIRIT III), the third in a series of relatively large cryogenic space borne sensors built by the Space Dynamics Laboratory (SDL) of the Utah State University (USU), was the primary instrument during the initial 10 month phase of the mission, which terminated on 20 February 1997 with the depletion of the solid H₂ cryogen. The eight MSX principal investigator (PI) teams were divided by instrument and experimental objectives, and conducted diverse experiments that viewed from space to the hard Earth. Three teams observed man-made objects, three others measured the Earth, atmospheric and celestial backgrounds and two others explored technology issues associated with the spacecraft environment and accurately quantifying the performance of the various instruments. Mill et al. (1994) give an overview of the MSX spacecraft and mission while Price et al. (2001) detail the astronomy experiments.

Accurately calibrating the MSX sensors was of paramount importance to assure that the data analysis of the PI teams had a common calibration pedigree. The MSX calibration experiments not only provided the first direct absolute calibration of infrared primary standards in many years but also significantly improved the uncertainties in their 4.3 to 21.3 μm absolute fluxes. The MSX Data Certification and Technology Transfer Team (DCATT) provided technical guidance and evaluation of the SPIRIT III ground-based calibrations and was responsible for creating and executing on-orbit calibration experiments. The on-orbit calibration experiments included nearly 200 observations on the Cohen et al. primary and secondary standard stars and absolute flux measurements against five emissive reference spheres (ERS) that were ejected at various times during the mission. The physical properties of the reference spheres were well measured and their absolute fluxes were calculated to good precision.

3.1 The MSX SPIRIT III Infrared Telescope

Ames and Burt (1992, 1994) provide details on the SPIRIT III infrared instrument, a 35 cm aperture off-axis telescope cooled by a 944-liter solid H₂ cryostat. A Lyot stop reduced the clear aperture collecting area by about 7 percent to 896 cm². The Lyot stop also reduced the off-axis radiation from the Earth for the experiments that viewed the atmosphere and the zodiacal scans near the Sun that used the Earth as an occulting disk (Price et al., 2003). The SPIRIT III radiometer had five infrared, line-scanned, Si:As blocked impurity band focal plane arrays. Each focal plane array had eight columns with 192 rows of 18.3" square detectors. Except for the B Bands at 4.3 μm , the columns covered nearly a 1° cross-scan field. Half the columns were offset by half a pixel row, providing ~9" sample spacing in the cross-scan direction. The system parameters are given in Table 2. To reduce the telemetry rate, only half the total number of columns were active. As indicated in the Table, all the Band A columns were active and at least one column was active on either side of the stagger in the other bands. Band B was divided in cross-scan by two different filters centered on the 4.3 μm atmospheric CO₂ band; thus each of the B Bands had 76 active detectors. Bands A, D and E were co-aligned by means of dichroic filters as were Bands B and C. The two sets of coaligned columns were offset by about 0.24°.

Table 2: Parameters of the MSX SPIRIT III Spectral Bands

Spectral Bands	Active Pixels in Array	λ_e (μm)	Isophotal $\Delta\lambda$ (μm)	Zero Mag. Irr. (W/cm^2)	Noise Equiv. Irr. (NEI – W/cm^2)	Ω_{prf} (μsr)
A	8×192	8.28	3.36	8.20×10^{-16}	7×10^{-19}	0.0106
B ₁	2×76	4.29	0.104	3.28×10^{-16}	1.9×10^{-17}	0.014
B ₂	2×76	4.36	0.179	5.36×10^{-16}	1.9×10^{-17}	0.014
C	4×192	12.13	1.72	9.26×10^{-17}	2.3×10^{-18}	0.0117
D	4×192	14.65	2.23	5.69×10^{-17}	1.6×10^{-18}	0.0113
E	2×192	21.34	6.24	3.56×10^{-17}	7.5×10^{-18}	0.0126

Bands B and D are centered on the 4.3 and 15 μm CO₂ atmospheric molecular features, respectively. Band A is the most sensitive and covers a spectral region not easily available from the ground. Band C is a narrower analog of the IRAS 12 μm filter and Band 5 of the COBE/DIRBE. Band E is a good analog of the COBE/DIRBE band 6, the latter being commonly taken in comparison with the IRAS 25 μm band. The intensity response is divided by the wavelength to derive the isophotal effective wavelength and bandwidths. The Kurucz model Vega spectrum from Paper I was used to derive the zero magnitude flux for the radiometer bands listed in the Table.

To accommodate the wide range of experimental objectives, SPIRIT III had two data acquisition modes and several gain states. An internal scan mirror could sweep the 1° cross-scan field of the focal plane columns over in-scan amplitudes of 1°, 2° or 3° at a rate of 0.46°/sec, or the mirror could be fixed while the spacecraft motion scanned the arrays across the sky at various scan rates. The data were sampled five times faster in the mirror-scan mode than in the mirror-fixed mode, nominally at five times lower gain. All the DCATT calibration experiments were taken in the mirror-scan mode while the Celestial Backgrounds (CB) observations used the more sensitive mirror-fixed mode and a 0.05°/sec spacecraft scan rate. The 12-bit telemetry word provided a dynamic range of about 3000, taking the dark offset into account. The gain is nominally reduced by about a factor of four between the four mirror-fixed gain states, for a total dynamic range of $\sim 2 \times 10^5$. The three mirror-scan gain states roughly corresponded to the three lowest mirror-fixed gains. The mirror-scan calibration observations used all the available gain states, at least in Band A, to cover the factor of ~ 1000 difference between the faintest star (α And) and the brightest (α Ori and CW Leo) measured during these experiments. The gains were chosen, whenever possible, such that the in-band response of the sensor for a given star was on the linear portion of the response curve (< 1000 counts per readout).

Since nearly 90 percent of the stellar calibration measurements were taken in the mirror-scan mode, the Noise Equivalent Irradiances (NEIs) for this mode after filtering with the system point response function are listed in Table 2; the mirror fixed NEIs are about 2 – 3 times more sensitive. The NEIs also degraded by about a factor of four during the mission due to the increasing noise caused by rising focal plane temperature as the solid cryogen was depleted.

3.2 Ground Calibration

Calibrating the components and subsystems of an infrared sensor in the laboratory is a multi-step process, which, for example, is described for ISO in five volumes titled *The Calibration Legacy of the ISO Mission* (ESA SP-481, 2003). First, component characterization is done, examples of which are: transmission/reflection of the optics and the spectral response of the filter/detector combination. The characterization of filter/detector/optics at the system operational temperature is important as both the transmission of interference filters and their relative spectral response as a function of wavelength depend upon the temperature and optical quality factors (Stierwalt, 1975; Stierwalt and Eisenman, 1978). An infrared space-based telescope may be cooled to the point where self-emission no longer limits the detector sensitivity. Under these conditions, the photo-conducting detectors that are commonly used become orders of magnitude more sensitive but exhibit background and bias-dependent non-linear responses that have multiple time constants (see Arrington et al., 1976; Sclar, 1983). Attempts to model the non-linear behavior have met with various degrees of success (Zachor and Huppi, 1981; Zachor et al., 1982; Coulais and Abergel, 2000; Fouks, 2003), but none of the efforts were able to completely eliminate the non-linearities from the data. Prior to the early 1990s, the Naval Electronics Laboratory Center (NELC), later the Naval Ocean Science Center (NOSC), was the principal US agency that measured the behavior of detectors, filters and focal plane/filter assemblies under realistic background conditions applicable to satellite-based sensors. NELC/NOSC published ~100 technical reports on the properties of various focal plane components including the extensive characterization of the candidate detectors for the IRAS program by Arrington and Eisenman (1977). The results of this effort were used to select the detectors for the mission and to optimize their biases.

Preferably, after component level characterization, the assembled system should be tested to define throughput factors, such as non-linearity of response with flux, flat fielding, and corrections for optical distortions. The distortion-corrected system response is then scaled to absolute values with measurements against calibrated standard laboratory sources, then updated in-flight by ultimate reference to absolutely calibrated primary or secondary standard stars. According to Thurgood, Larsen and Sargent (1998), the ground calibration uniquely provides quantitative information on sensor parameters such as linearity correction as a function of focal plane temperature, gain factors between integration modes as a function of temperature, non-uniformity correction (flat fielding) over the field of regard as a function of temperature, the photon noise model and the relative spectral response both within the filter bandpass and the out-of-band response. Some system parameters, such as spectral response, are impossible to calibrate while the sensor is in orbit. A detailed laboratory characterization of a mid-infrared instrument at the component and integrated system level is more important for space-based sensors than for ground-based instruments as few space experiments have the luxury of being able to be calibrated after the flight. A notable exception was the post-flight CIRRIS 1A calibration by Bingham et al. (1995) that was guided by the actual in-flight performance of the sensor, which highlighted the deficiencies in the pre-flight sensor characterization. However, having an instrument to calibrate after the mission is a rare circumstance.

Ideally, the absolute calibration of the completed instrument should be quantified under realistic conditions in a laboratory calibration facility before being flown. Military sensors are calibrated, whenever possible, before flight in a ground chamber that mimics the conditions of

space. Several ground-based calibration chambers have been built and used in the US to calibrate space-based infrared sensors. The chambers are cryo-cooled to the photon background levels of space and some are able to articulate their calibration sources to mimic the anticipated encounter geometry of the observation. The physical parameters of the chamber sources are well characterized and the blackbody references used to determine the radiance and irradiance responses of the sensor are cross calibrated with standards maintained by the NIST. Two of the chambers that are currently operational are the 7V chamber at the Air Force Arnold Engineering and Development Center (AEDC) in Tennessee and the Multi-Instrument Chamber (MIC-2) at the Space Dynamics Laboratory of the Utah State University (Bingham et al., 1995). The AEDC has been designated as the US Air Force center for space simulation and testing. The AEDC chamber for spectral radiometric calibration is the 7V chamber (Matty et al., 1991, Simpson, 1995) and was used to calibrate the AFCRL infrared sky survey instruments (Price, 1978; Price and Walker, 1978). Other AEDC chambers are used to measure the off-axis response of the system and assess high-energy radiation effects on the sensor (Arnold and Nelms, 1976). AEDC also has a focal plane characterization facility (Nicholson et al., 1992). The SDL MIC-2, which was used to characterize the SPIRIT III sensor, can accept a one-third meter optical system and measure the absolute point and diffuse radiometric responses of the sensor, the spatial response over the field of view of the focal-plane array and the relative spectral response of the system spectral bands.

The SPIRIT III calibration rests on three independent legs: a characterization in the MIC-2 calibration chamber at SDL, an on-orbit irradiance calibration against standard stars and another against emissive reference spheres. The ground chamber uses a variety of standard sources, all of which have precisely measured physical properties at the time of calibration, such as the temperature and spectral emissivity of the flat black extended source plates.

Garlick et al. (1996) modeled the radiometric response of the SPIRIT III sensor as a series of transfer functions. The resulting equation converts telemetry counts into a linear instrument response:

$$r'_d(t) = B_{i,d}(t) \left[\frac{g_{i,a}(T) L_{i,d}(r_d(t) - D_{i,d}(t), T)}{R_{a,d}(t) G_a(T) F_{d,m} N_{i,d}} \right] \quad (2)$$

The components of this equation are:

- $r'_d(t)$ = the corrected radiometer response for detector d as a function of time, t , on the same unitless scale as the radiometer output
- $r_d(t)$ = the radiometer data in telemetry counts
- $B_{i,d}(t)$ = the bad pixel operator for integration mode i that labels a detector as bad or anomalous. A bad pixel designation eliminates data from that detector for the entire observation. Less than 2 percent of the detectors were inoperative besides the 36 that were blocked by the Band B filter mask. An anomalous pixel designation rejects the data from detector d for specified time intervals. Not-a-number was substituted for the rejected CB data values; an average of the surrounding data was substituted in the mirror-scanned observations.
- $g_{i,a}(T)$ = the gain normalization for array a as a function of focal plane temperature T
- $L_{i,d}\{\dots\}$ = the detector non-linear response correction (Larsen and Sargent, 1997)

- $D_{i,d}$ = the dark offset
- $R_{a,d}(t)$ = the correction for time related response trends in detector d , of array a (Larsen, Thurgood and Sargent, 1998)
- $G_a(T)$ = the temperature dependent response in array a (Sargent, 1997)
- $F_{d,m}$ = the correction for variations in response over the field of regard as a function of mirror position m
- $N_{i,d}$ = the non-uniformity response correction (flat fielding)

Garlick et al. (1996) also provide analytic expressions for each of the components in Equation (2) while considerably more detail is available in the reference listed for a particular component. With the exception of the non-linearity correction and the noise model, all of the remaining corrections can be, and were, determined without reference to the absolute radiance of the source.

The radiance is obtained by dividing the corrected counts from Equation (2) by a single responsivity value for each spectral band. That is:

$$L_d(t) = \frac{r'_d(t)}{\mathfrak{R}_a} \quad (3)$$

where $L_d(t)$ is the measured radiance in $\text{W cm}^{-2} \text{ sr}^{-1}$ for detector d and \mathfrak{R}_a is the responsivity in $\text{counts}/(\text{W cm}^{-2} \text{ sr}^{-1})$ for array a .

The responsivity, \mathfrak{R}_a , in Equation (3) was determined by measuring the instrument response to a known radiance from the extended calibration source in the ground-based chamber. The irradiance response in array a , R_a , was obtained by dividing the radiance response by the effective beam size, Ω_{EFOV} , measured during the ground calibration and includes scattering within the filters. The on-orbit determination was derived using:

$$R_a^{-1} = \frac{\Omega_{EFOV}}{\mathfrak{R}_a} P(r'_d(t), PRF_a) \quad (4)$$

$P(\dots)$ is the point response function (PRF) operator used to extract photometry on the source. Here, Ω_{EFOV} is the beam size derived using the operator and the resulting values are listed in the last column of Table 2. Mazuk and Lillo (1998) derived somewhat cross-scan dependent PRFs from one of the MSX calibration experiments while we derived an average response function for each array. Both were used for the PRF fitted photometry for Version 2.3 of the MSX Point Source Catalog (Egan et al., 2003)

The Radiometer Instrument Products (RIPs) contain the parameters for the various functions in Equation (2) and the responsivities in Equation (3). The SPIRIT III performance assessment team determined the RIPs from the pre-flight and on-orbit calibration. RIP files were released episodically during and after the mission as knowledge of the behavior of the instrument improved. The final version of the RIPs was used in the present analyses. The dark offsets and anomaly files were determined uniquely for each observation.

3.3 The MSX On-Orbit Calibration Experiments

MSX executed one CB and five DCATT calibration experiments. Each MSX observation within an experiment is called a data collection event or DCE and is uniquely labeled. The initial two letters in the label identify the PI team responsible for the experiment, DC for the DCATT and CB for the Celestial Background. This is followed by four numbers that define the exact observing profile, the first two digits of which denote the experiment executed while the next two specify the subclass within the experiment, either a distinct measurement or specific measurement geometry. Thus, the experiment designations DC2201 through DC2205 denote that these are the DCATT (DC) DCEs defined in the 22nd DCATT experiment plan, which was designed to measure the reference spheres 1 – 5 (01 – 05). To this is appended a five digit number assigned to a specific observation. Thus, DC430100018 is the 18th DCE of the DCATT Source Transfer Experiment (DC43) with observing parameters specified under the first sub-experiment. Only the PI team and experiment number are necessary for the present analysis.

3.3.1 MSX Stellar Calibration Measurements

Initially, the radiometric responsivities calibrated on the ground were updated to point source irradiance responsivities by an early on-orbit calibration against α Boo, using the Burdick and Morris (1997) MSX in-band fluxes for this star. Observations of four other Cohen et al. standards (α Lyr, α CMa, α Tau and β Gem) were used to independently assess the SPIRIT III calibration against α Boo. A subsequent DCATT assessment by Baca et al. (2002) used observations from all the calibration stars.

The nine Cohen et al. stellar standards that were measured during the MSX calibration experiments are listed in Table 3. The star name is given in the first column and the in-band fluxes used by Cohen et al. (2001) in Paper XII for their CB06 analysis are listed in the next six columns. Due to improvements in the normalized filter response functions, some of these irradiances differ somewhat from the Burdick and Morris (1997) values used in the initial on-orbit calibration. The last column in the Table lists the number of DCEs on which the star was measured; the number of DC DCEs is first and those observed on the CB06 DCEs are given after the slash.

Table 3: Stellar Standards Measured by MSX

Star	BAND A	BAND B ₁	BAND B ₂	BAND C	BAND D	BAND E	No.
α CMa	2.833×10^{-15}	1.146×10^{-15}	1.874×10^{-15}	3.195×10^{-16}	1.959×10^{-16}	1.22×10^{-16}	35/9
α Tau	1.308×10^{-14}	4.628×10^{-15}	7.373×10^{-15}	1.570×10^{-15}	9.529×10^{-16}	6.046×10^{-16}	30/3
α Boo	1.463×10^{-14}	5.566×10^{-15}	8.813×10^{-15}	1.735×10^{-15}	1.059×10^{-15}	6.744×10^{-16}	25/7
α Lyr	8.196×10^{-16}	3.279×10^{-16}	5.364×10^{-16}	9.259×10^{-17}	5.686×10^{-17}	3.555×10^{-17}	19/2
β Gem	2.498×10^{-15}	9.759×10^{-16}	1.576×10^{-15}	2.858×10^{-16}	1.762×10^{-16}	1.098×10^{-16}	15/1
β Peg	7.516×10^{-15}	2.722×10^{-15}	4.365×10^{-15}	9.17×10^{-16}	5.711×10^{-16}	3.596×10^{-16}	14/1
γ Cru	1.827×10^{-14}	6.235×10^{-15}	9.817×10^{-15}	2.224×10^{-15}	1.359×10^{-15}	8.565×10^{-16}	3/1
γ Dra	3.111×10^{-15}	1.080×10^{-15}	1.722×10^{-15}	3.729×10^{-16}	2.281×10^{-16}	1.427×10^{-16}	2/1
β And	5.391×10^{-15}	1.981×10^{-15}	3.153×10^{-15}	6.494×10^{-16}	3.987×10^{-16}	2.496×10^{-16}	0*/1

In-band fluxes predicted by Cohen (private communication) are in units of W cm^{-2}

* α And was measured four times instead of β And due to a transcription error

3.3.1.1 DC44 – Stellar Benchmark Experiment

The large majority, ~88 percent, of the DCATT stellar observations were obtained on two of the DC calibration experiments: the DC43 Source Transfer Experiment and the DC44 Benchmark Experiment. All DCEs in this analysis were preceded and followed by an internal calibration that measured the instrument response to an internal stimulator at three flux levels and dark offsets in each gain state.

The DC44 Stellar Benchmark Experiment was the standard weekly calibration scheduled by the program. This experiment measured two stars on the same DCE with the geometry shown in Figure 4 in which the 1° amplitude mirror scan is used to sweep a star back and forth across the arrays while the spacecraft moves the star 0.4° down the focal plane array columns in the cross-scan direction. The cross-scan traverse was over the center of the MSX arrays. After measuring the first star, the spacecraft was slued to a second star while the SPIRIT III internal shutter was closed and the detectors dark offsets were measured; then the second star was measured. About half the DCEs measured two of the stars listed in Table 3; the other half measured a standard star and a bright infrared star such as α Ori or CW Leo. Measurements on these bright stars probed the full dynamic range of the sensor and the “wings” of the point response function. A total of 53 DC44 DCEs were executed, which produced 101 observations on stars in Table 3. Each of these observations had a nominal 80 individual measurements during a single DCE.

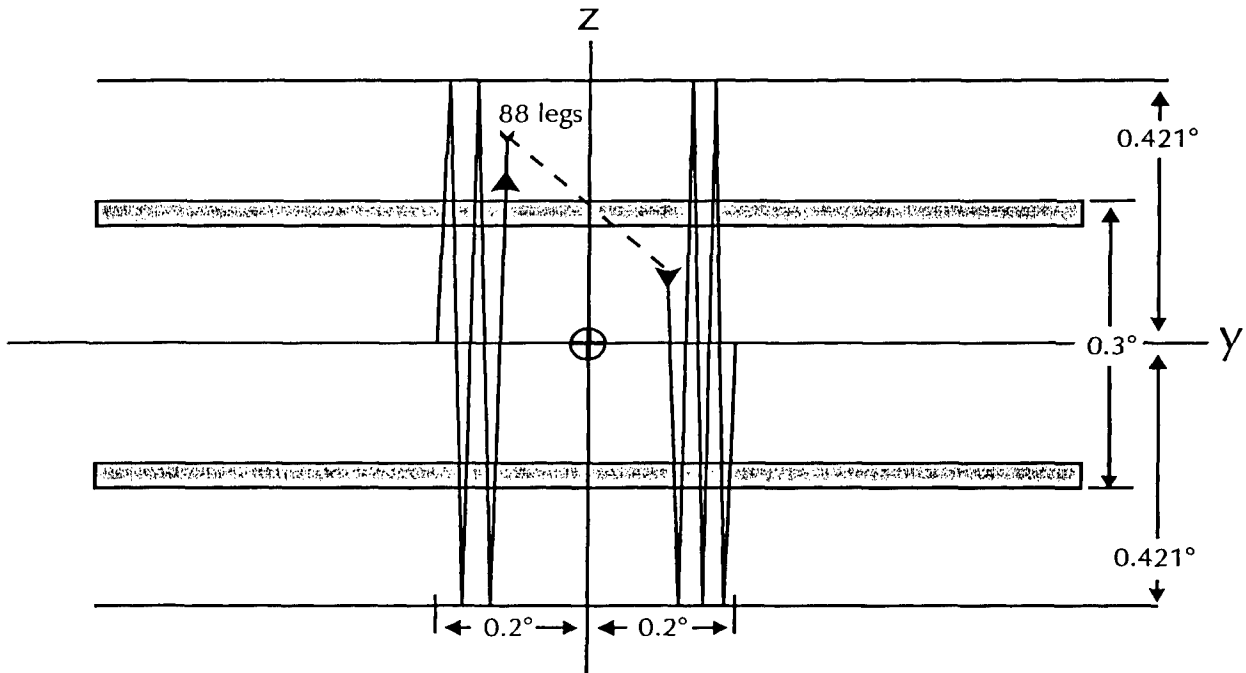


Figure 4: The scan geometry used for the DC43 and 44 DCEs. The spacecraft moves the stars over the central 0.4° in cross-scan while the-mirror scans with a 1° amplitude. The gray rectangles are the two sets of co-aligned columns.

3.3.1.2 DC43 – Source Transfer Experiment

This experiment usually compared two of the stellar calibration standards in Table 3 on the same DCE. The measurement geometry was essentially that of DC44 shown in Figure 4. The difference between the two experiments was that the DC44 dark offset measurement between the two stellar observations was replaced by a long internal stimulator sequence, which was followed by 5 minutes of measuring the dark offset recovery. The stimulator sequence warms the focal plane slightly and the recovery time allows the dark offset to stabilize. Forty-eight stellar observations consisting of 80 individual measurements were made on the twenty-five DC43 DCEs that were executed during the mission.

3.3.1.3 DC35 – SPIRIT III Radiometric Calibration

The radiometric responses for each detector in each SPIRIT III spectral band were calibrated against stellar standards under this experiment. As for the DC43 and DC44s, the spacecraft slowly scanned a star down the center of the field of regard in the cross-scan direction while the star was swept across the arrays using the 1° mirror scan amplitude. The difference is that the entire 1° cross-scan extent of the array was scanned for this experiment and that the $\sim 0.0002^\circ/\text{sec}$ cross-scan motion was slow enough to assure that each detector in the arrays observed the star. Only two sets of observations, one on α Her and the other on α CMa, were made on this experiment but each star had over 220 individual measurements.

3.3.1.4 DC33 – Flat Field Calibration Mirror Scan Mode

This experiment measured the detector-to-detector variations in responses for each of the SPIRIT III infrared arrays over the entire $1^\circ \times 3^\circ$ field of regard. The SPIRIT III point response functions, the scan mirror transfer function and radiometric calibrations of the arrays were derived from these measurements. A single star was observed on each of the nine DC33 DCEs and the number of individual stellar measurements on each DCE varied from about 20 to 180.

For half the DCEs, the spacecraft slowly moved the star along the cross-scan center of the 3° in-scan field of regard swept out by the arrays. For the remainder of the DCEs, the spacecraft executed a sawtooth scan, with ten 1° cross-scan traverses while moving 3° in the in-scan direction. Larsen, Sargent and Tansock (1998) derived the distortion map for the $1^\circ \times 3^\circ$ field scanned by the mirror from the DC33 and DC35 observations. Their Figure 4 shows how these two experiments sampled the response at a number of in-scan and cross-scan positions in the $1^\circ \times 3^\circ$ field of regard.

3.3.1.5 CB06 – Celestial Radiometric Standards

Cohen et al. (2001) described this experiment in detail in Paper XII. Briefly, three stars were observed on each DCE with the mirror fixed while the spacecraft scans the star back and forth across the focal plane arrays. Nominally, 10 scans were executed at the cross-scan centers of the Band B_1 and B_2 arrays; the scans were thus at half the cross-scan distance from the center of the MSX 1° arrays to their edges. Twenty-four CB06 DCEs were executed; each DCE obtained 19 to 20 mid-infrared measurements and 9 to 10 scans in Bands B_1 and B_2 on the three stars. A total of 26 observations were obtained on the stars in Table 3.

3.3.2 Emissive Reference Spheres Experiment – DC22

MSX deployed five emissive reference spheres (ERS) during the cryogenic lifetime of the SPIRIT III sensor. The 1.00 ± 0.01 cm radius spheres were made of solid 6061-T6 aluminum alloy and coated with Martin Black. Thus, the spheres approximated blackbodies with accurately known thermal properties from which instantaneous temperatures could be derived. The in-band irradiances of the spheres were derived from their temperatures and ranges. SPIRIT III was able to observe the spheres for about a third of an orbit after ejection, the DCE duration being limited by capacity of the tape recorders. At least one calibration star was also measured on each ERS DCE. Thus, not only do the emissive reference spheres calibrate the absolute irradiance responsivity of the mid-infrared bands of the SPIRIT III radiometer and, consequently, the mission averaged fluxes for the calibration stars, they also directly calibrate the standard stars measured on the same ERS DCEs.

Nominally, a sphere was deployed in the plane of the MSX orbit at an elevation angle of 15° and a velocity of 14.2 m/sec. Orbital dynamics accelerated the sphere away from and above the spacecraft after release. The sphere passed through the spacecraft zenith at $t \sim 1200$ seconds (~ 1200 seconds after release of the sphere) and reached a range of about ~ 67 km at an elevation angle of approximately 41° behind the velocity vector by the time the experiments terminated at $t \sim 2200$ seconds. The spacecraft was programmed to track and center the sphere in the $1^\circ \times 3^\circ$ field of regard. The highest mirror scan gain was used for the entire DCE since the irradiance of the sphere spanned a dynamic range of only ~ 200 during the measurement period, reaching a signal-to-noise ratio (SNR) of 10 – 15 at the end of the DCE in all radiometer Bands.

The detailed timeline for the ERS measurements varied from DCE to DCE. Nominally, stellar calibration observations of 80 measurements each were obtained 14.5 and 7 minutes before the reference sphere was ejected and a final stellar observation was made at the end of the DCE, some 45 to 60 minutes later. A total of 11 stellar observations were obtained on the five DCEs; the initial two stellar measurements are missing on the ERS2 and ERS3 DCEs. Continuous measurements on ERS1 from $t + \sim 550$ seconds until $t + 2200$ seconds and nearly continuous measurements on ERS5 were obtained over a comparable period with dark offset measurements at about 3 minute intervals. Fewer measurements were made on the ERS 2, 3 and 4 for a variety of reasons. An anomalous deployment azimuth for ERS4 carried the sphere outside the SPIRIT III field of regard until about $t + 1000$ seconds. The sensor was also turned off during the South Atlantic Anomaly passage for ERS3 between ~ 1250 and $t + 2150$; a similar gap appears for ERS4.

3.4 The Effects of On-Orbit Performance on SPIRIT III Calibration

The thermal performance of the sensor complicated the instrument calibration. The cryogen lifetime was about half of what was originally anticipated, which meant that correspondingly fewer on-orbit calibration measurements were made. A higher than expected initial focal plane temperature and a more rapid temperature rise made the system much more dynamic than was originally projected. The focal plane temperatures were expected to change little during most of the mission and rise steeply only near the end. Because of the long period of initial stability, the changes in the temperature dependent corrections in Equation (2) were expected to be small for

most of the data. The larger corrections due to a larger range in focal plane temperature have larger corresponding uncertainties, which are spread over all the calibration measurements.

Ames and Burt (1992) originally estimated the SPIRIT III cryogenic lifetime to be about 20 months. Subsequently, an auto-collimator and a device to measure the bi-directional reflectance of the primary mirror were built into the system, capabilities that were never used but had a ~10 percent negative impact on the cryogen lifetime. Consequently, Ames and Burt (1994) revised their original cryogenic lifetime estimate downward to 18 months. Schick and Bell (1997) attribute the catastrophic cryogenic failure that scrubbed the November 1994 launch and almost terminated the program to a stress corrosion crack in the cryostat. The SPIRIT III "Failure Review Team Final Report" did not agree and ascribed the failure to improper top-off procedures, which implies that if the stress corrosion cracks were the ultimate cause of the failure, any such cracks were likely due to the stresses induced by improperly filling the cryostat. Unfortunately, the uncertainty as to the true cause, and fix, of the failure led program management to the conservative decision not to fill the tank ullage during the final field preparation for the April 1996 launch. As a consequence, the cryotank itself was not completely filled. Schick and Bell estimated that the cryogen life was reduced by another four months owing to the incomplete fill of the tank and that an additional two months of mission time were lost because of degraded performance of the insulation in the rebuilt cryostat. None of these analyses factor in the fact that the parasitic thermal load into the sensor was roughly three times larger than anticipated, which significantly increased the cryogen expenditure rate.

The SPIRIT III optics were thermally tied to the top of the cryotank by means of shrink fitted fixtures as were the focal plane straps. SDL estimated that the beginning of mission focal plane temperature would be as low as ~10K since they had added more copper straps between the dewar cold finger and the focal planes than called for in the original design. During flight, the solid H₂ quickly shrank away from the tank top where all the heat from the sensor was dumped, which raised the operating temperatures of the focal planes. The situation is analogous to what Price, Murdock, and Shivanandan (1983) determined to be the cause of the large focal plane temperature excursions during the Far Infrared Sky Survey Experiment probe rocket flight.

The SPIRIT III focal plane temperatures were ~11.2K at the beginning of mission, about 1K higher than expected, and the subsequent rise in temperature was faster than anticipated. The difference between the actual and anticipated focal plane temperatures ultimately prevented us from combining the ground-chamber calibration with the on-orbit stellar and sphere calibrations in a global calibration. The absolute chamber measurements against the Jones source were the only ones obtained at focal plane temperatures comparable to the 11.2K to 12.5K on-orbit values; the focal planes were at ~10K when all the other chamber sources were used. The large uncertainties in the extended Jones source radiances poorly constrained the global calibration compared to the on-orbit observations and the ground calibration was not used in the final analysis.

Late in the SPIRIT III ground testing, turn-on transients in the dark offsets were noticed which took ~30 minutes to asymptotically stabilize. A settling time of 7 – 12 minutes was programmed into the beginning of each DCE as a compromise between the length of the DCE and available spacecraft power. Three factors exacerbated this problem. One is that the focal plane is warmed slightly as a result of the cycling through the gain states in the initial standard calibration sequence before a DCE, which increased the amplitude of the change. The second was that both the dark offset and change in dark offset during the DCE increased as the focal

plane temperature rose during the mission with the expenditure of cryogen. Third was that the equilibration of the thermal input from stressing observations, such as looking at the hard Earth, took tens of hours. Thus, the data from a DCE executed after a downward looking observation are compromised by having a higher than normal focal plane temperature. A subtle but significant consequence of dark offset error is that it is coupled to the non-linearity and non-uniformity corrections. A dark current error translates into a bias on the sensor response to the background and a distortion of this bias through the non-linearity correction.

The change in dark offset scales with the gain, so the mirror-scan DCEs show about a five times smaller effect than in the mirror-fixed CB DCEs. Price et al. (2001) describe these problems and the steps taken by the CB processing team to mitigate or eliminate them. The various background removal techniques used in the data processing considerably reduced the effects of the changes in dark offset. However, the CB06 experiment was the lowest priority of the regularly scheduled CB experiments and most of the observations were taken late in the mission when the change in dark offset was large, as was the detector noise.

3.5 Data Processing

The telemetry from the MSX satellite to the X-band receiver at the Applied Physics Laboratory (APL) of the Johns Hopkins University in Columbia, MD was recorded as Level 0 data on analog tapes. These analog tapes were de-commutated and formatted into computer compatible Level 1 data tapes. The Level 1 data were stripped out by MSX instrument and ordered in increasing time to create Level 1A tapes, which were sent concurrently to the SPIRIT III Data Processing Center (DPC) at SDL and the Data Analysis Center (DAC) in the Air Force Research Laboratory (AFRL/VSF).

APL also processed the attitude and star tracker information from the spacecraft with the spacecraft ephemeris and the boresight offsets between the various instruments and the spacecraft attitude reference system to create a pointing time history for each instrument for each DCE. The resulting Definitive Attitude File (DAF) describes the pointing evolution in J2000 inertial equatorial coordinates corrected for annual and spacecraft aberration. These files were also sent to the SDL DPC and the VSB DAC.

To assure that the PI teams' analyses have a common pedigree, the MSX program gave SDL the responsibility for calibrating the instrument and creating the software that applies this calibration. This Standard CONVERT software converts Level 1A data by means of Equation (1) into linear, dark-offset subtracted, and flat-fielded Level 2 data. Each DAC was given a copy of Standard CONVERT.

The DPC pipeline processing assesses the data quality of each DCE. It strips out housekeeping information, the dark current observations and the internal stimulator sequence. The mean dark offsets are calculated for each pixel and the results formed a dark offset matrix for each dark measurement. The amplitudes of the stimulator flashes are extracted and used in long term trending of the sensor response (Larsen, Thurgood and Sargent, 1998). The pipeline also flags anomalies such as glitches, dropouts and saturated pixels. The first four standard statistical parameters of each pixel are calculated in blocks of 2400 minor telemetry frames. This is the volume of data generated in the 6.6 seconds it takes for the internal scan mirror to sweep out the maximum 3° field of regard. The same 2400 minor frame sample length is used to assess the data in the mirror fixed mode and spans 33 seconds.

3.5.1 Identification and Photometry of Point Sources in the Mirror Scan Mode

Larsen et al. (1996) describe the Canonical CONVERT processing that identifies point sources in the mirror-scan data and extracts their irradiances (there is no SDL equivalent Canonical CONVERT routine for the mirror-fixed mode). The process parsed the data into scenes 2400 samples in length for each detector beginning at the time the mirror scan monitor marks when the mirror scan reverses direction. If necessary, the scene is subdivided into smaller data blocks that correspond to smaller amplitude mirror scans. The Level 2A SPIRIT III radiances were combined with pointing CONVERT to create time and position tagged radiances for each detector; the result was then formed into a quasi-image in focal plane coordinates for source extraction and photometry.

Averages and standard deviations were calculated for each detector within a moving time interval over the scene. Detector radiances greater than a SNR threshold of 10 were extracted as part of a potential source and those that were less than the threshold were incorporated into the background. Background values were interpolated over and substituted for the data in the gaps left by the radiances that exceeded the threshold criterion. The resulting background values were then averaged and subtracted from the amplitude of the potential sources.

Potential sources consisted of a cluster of extracted radiances that exceeded a signal-to-noise threshold of 10 above the local background. The cluster had to be within a radius of 270 μ rad or three detectors, which was assumed to be typical of a point source. The total intensity and intensity squared, the in-scan and cross-scan centroids and in-scan and cross-scan second moments were calculated for each isolated cluster of radiances. These quantities were used to ascertain how round or point-like the object was as well as provide a rough estimate of position and intensity. Criteria for these statistics were adopted and radiance clusters that met or exceeded these criteria were flagged as potential point sources. The amplitude, or irradiance, and position of the potential source were then simultaneously solved for by minimizing the mean square error between the data and point response function.

Thus, an observation had to pass a two-tier selection criterion: not only did the radiance from a given detector have to exceed a signal-to-noise threshold of 10 but so too must a sufficient number of surrounding values in order to produce moment statistics that were sufficiently point-like. This is the reverse of the usual procedure used in a blind survey in which the data is filtered first and then tested against a signal-to-noise criterion. This criterion introduced a selection bias in the average flux measured for a star on a given DCE by aggressively rejecting measurements near the SNR threshold. Noise will cause some of the stellar measurements that have a true signal-to-noise close to selection threshold value to be rejected. Consequently, the fluxes for the accepted values will average as too high. To compensate for this bias, the DCE averaged flux for any star that had fewer measurements than 0.9 times the total number of opportunities was rejected. Band E is most affected as may be inferred by comparing the NEIs listed in Table 2 with the predicted fluxes in Table 3. For example, there were no valid Band E mirror-scan observations of α Lyr as all of these were obtained well below the SNR > 10 selection criterion. There were few Band E observations within a given DCE on α CMa and β Gem; the small number of non-empty β Gem data sets were rejected, as were all but three of those for α CMa; and those three were ultimately rejected as biased. Approximately a third of the α Tau and α Boo Band E fluxes taken in the second half of the mission were also eliminated. In contrast, only a few DCE average fluxes in the other bands were rejected.

3.5.2 CB06 Photometry

Cohen et al. (2001) described the creation of the stellar images from the CB06 DCEs, which Walker (private communication) provided to us. Analogous to the mirror-scan processing, we extracted the flux of the calibration star from the image of each scan across the star by a least squares fit of the point response function to the stellar values. A mean and standard deviation about the mean were derived from the 19 to 20 mid-infrared irradiances (9 to 10 B Band irradiances) thus extracted for each star on a given DCE. This is in marked contrast to the manner in which Cohen et al. (2001) derived their in-band fluxes. They performed aperture photometry both on the individual scans and on the co-added images. The signal-to-noise of the star was used to weight the individual images to derive the co-added image. Cohen et al. used the co-added irradiance in their analysis but expressed the uncertainties in terms of the range of irradiances from the individual scans. We, on the other hand, found that photometry obtained by a least squares fit of the point response function to the star images from the individual scans produced smaller dispersions than the Cohen et al aperture photometry. Also, the scatter in comparing the average fluxes derived from the mirror-scan DCEs and our photometry is about half that of the comparison using the Cohen et al. means.

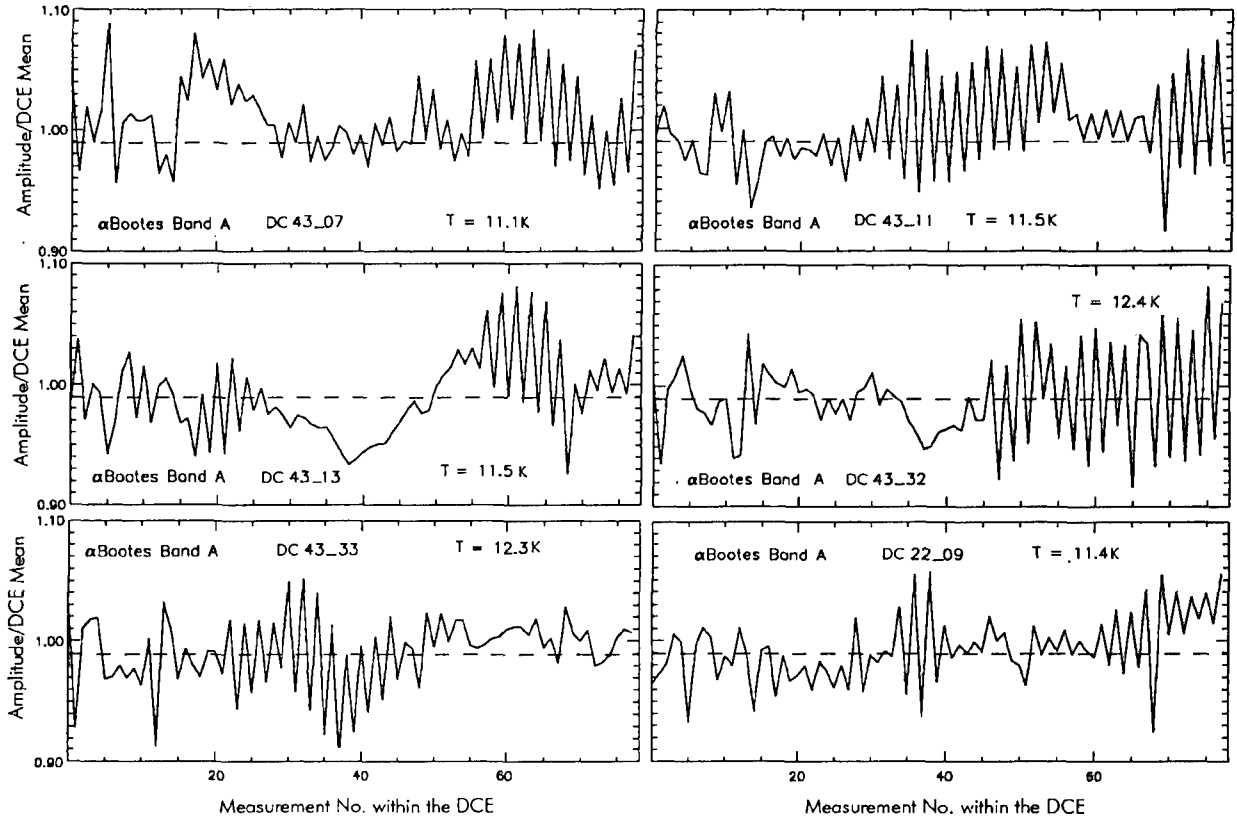


Figure 5: The ratio of the individual measured Band A fluxes of α Boo divided by the DCE mean for six stellar calibration DCEs. The sawtooth variation from one scan to the next is evident.

4 MSX Mission Averaged Stellar Standard Fluxes

Systematic trends were observed in the extracted stellar fluxes on a given DCE; within a DCE, the amplitudes tended to be higher as the mirror scanned in one direction compared to the other, as is apparent in Figure 5. The trend was not universally scan direction specific, that is, the flux is always high in one direction and low in the opposite direction. As shown by the six panels in Figure 5, the sense of which scan direction produced higher values changed from DCE to DCE and within a DCE. A possible explanation for this trending is shown in Figure 6, which plots the histograms for the response of the detectors in the individual Band D columns as well as the sum of all the detectors. The peak or mode in the distributions differs by as much as 2 percent between the columns. Columns 0 and 1 are offset by half a pixel from columns 2 and 3. As the sensor scans the star down the array, the maximum in the point response will, at various times, be closer to the center of the detectors on one side of the offset than the other. The difference in response of the columns may, then, produce the sawtooth pattern. The standard deviation of the DCE mean could be reduced by taking the average of the fluxes from consecutive back and forth scans. This did not significantly change the average stellar irradiance on a given DCE but it did reduce the uncertainty in the mean (σ/\sqrt{N}) by up to 10 percent.

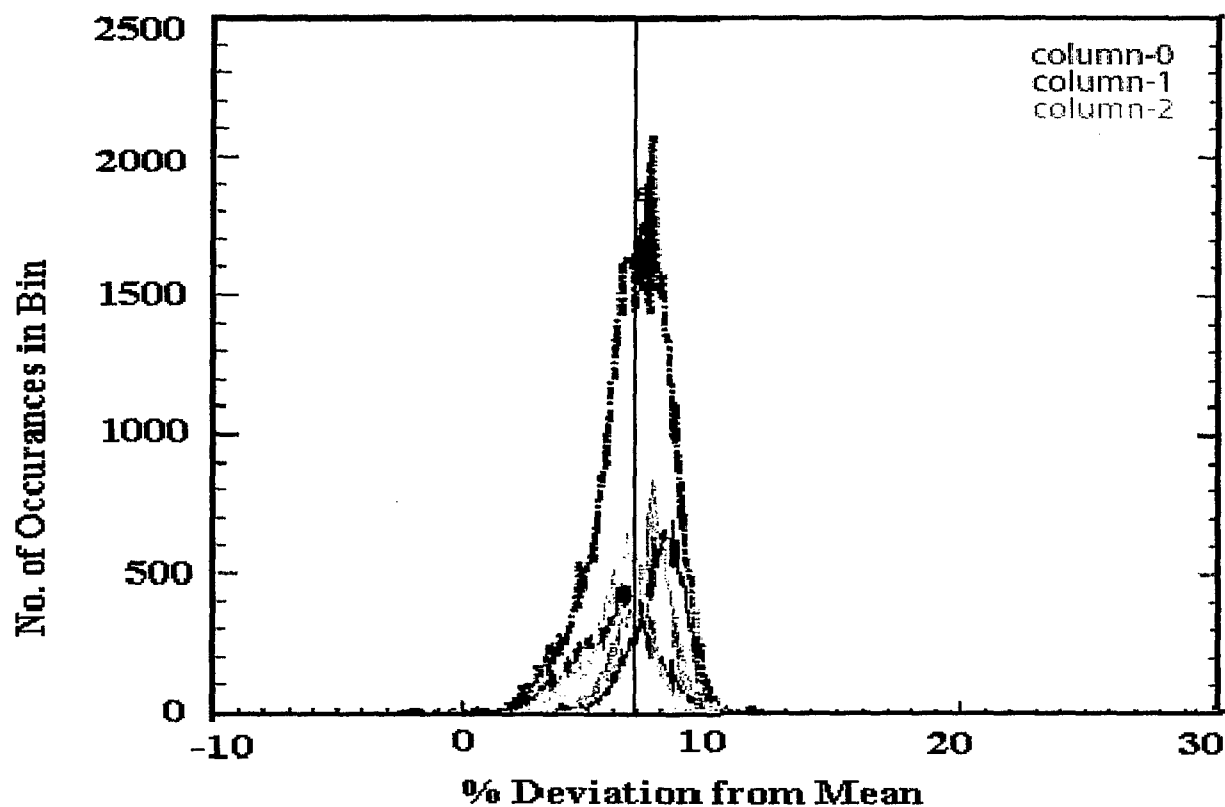


Figure 6: The measured Band D detector biases. The histogram of the frequency of occurrence is plotted against bias for all the detectors as the black line. The various colored lines are the histograms from the individual columns in the array. The maximum bias difference in the peaks of the histograms is 2 percent.

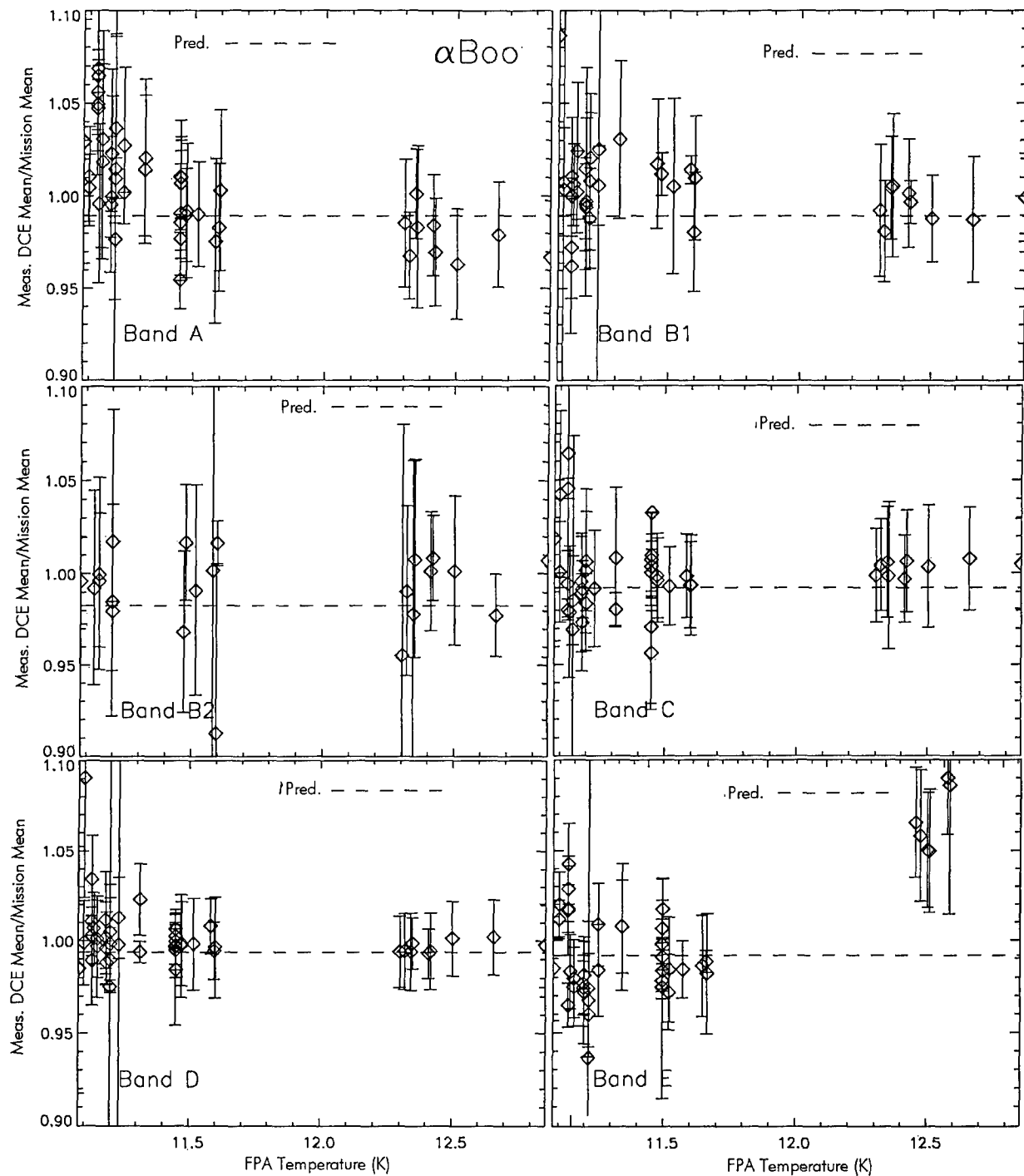


Figure 7: DCE averaged fluxes from α Boo in each of the MSX spectral bands plotted as a function of focal plane temperature. The dashed lines are the ratios predicted by Cohen et al.

The standard deviation of the DCE means about the mission mean is of the order 3 – 5 percent, as may be seen for α Boo from Figure 7. It was inferred that the DCE means had an additional measurement error from the fact that the standard deviation of the DCE means about the global mean was larger than predicted by Gaussian statistics. The DCE mean stellar fluxes indicated that the response varied during the mission and that this variation appeared to correlate either with time or focal plane temperature, since the temperature generally increased with time.

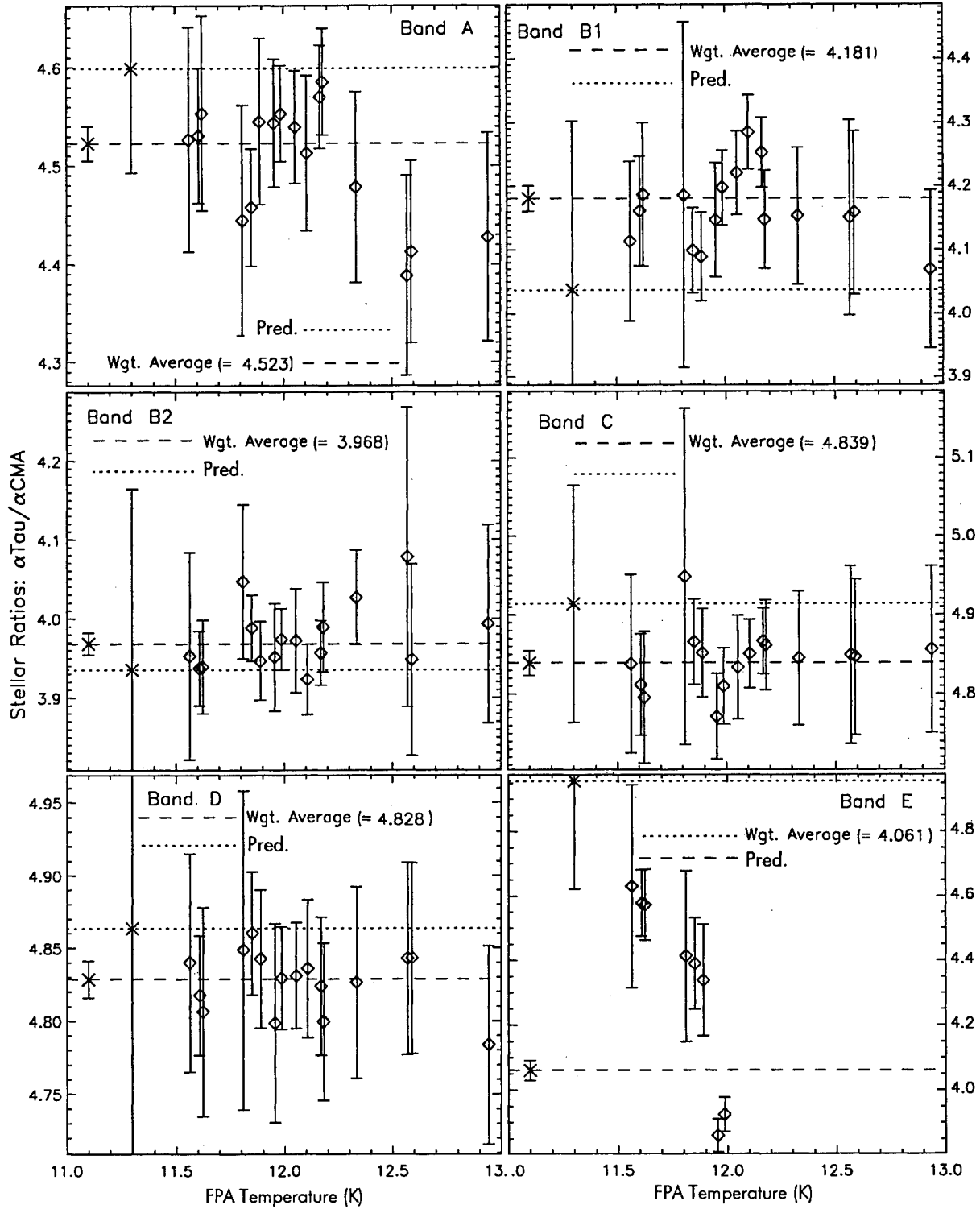


Figure 8: The ratio of the fluxes from α Tau to those from α CMA observed on the same DCE plotted as a function of focal plane temperature for that DCE. The Band E trend is due to the flux overestimation bias in the low signal-to-noise α CMA measurements. The dotted lines are the Cohen et al. predicted ratios. The lines are centered on \times s which shows the estimated error in the prediction. The dashed lines are the straight (equally weighted) averages of the ratios.

The time analysis by Thurgood et al. (1998) of the SPIRIT III sensor response to the internal stimulators indicated that the array responses were constant to within 2 percent and that the responsivity of the individual detectors within an array did not change by more than 3 percent. However, this analysis is not definitive as the uncertainties are within the trends shown in Figure 7. Since many of the components in Equation (2) depend on focal plane temperature (Larsen and Sargent, 1997), a temperature dependent residual would be consistent with what was observed. The trend with respect to temperature was initially masked by the fact that no single star was visible over the entire temperature range.

Baca et al. (2002) first noted that the variations in the DCE averaged SPIRIT III irradiances appeared to correlate with focal plane temperature in their assessment of the final CONVERT 6.0/6.2 responsivity and instrument products. They derived analytic corrections to the SPIRIT III responsivity as a function of focal plane temperature and presented the results in a table in the report. Unfortunately, two aspects of their analysis compromised the results. One was that they did not take into account the flux overestimation biases produced by Canonical CONVERT for sources with irradiances near the signal-to-noise source selection threshold. Less serious was that they adopted the absolute in-band fluxes derived from the spectral energy distributions recommended by Cohen et al. as the independent variable in their analysis without ascribing an error to these values. Cohen et al. assigns an error to each of his spectra, with a minimum error of 1.45 percent for Vega and ~ 2 percent for the other stars.

Since two of the calibration stars in Table 3 were frequently measured on the same DC43 and DC44 experiments, the ratios of the same two stars taken on the same DCEs throughout the mission were examined. The α Tau to α CMa ratios are shown for each MSX spectral band in Figure 8. No systematic trend in the ratios with focal plane temperature is discernable except for Band E and, perhaps, for the higher temperatures in Band A. In both cases, the trends are explained by the flux overestimated bias in the extracted photometry for α CMa.

No single standard star had sufficient measurements over the entire range in focal plane temperature to produce a good solution to the response variation (see Figure 7, for example). Since the standard stellar fluxes determined by Cohen et al. have their own set of uncertainties, scaling factors were derived for the five most frequently observed standard stars and these were used to calculate the trends; measurements on β Peg were rejected, as the star was found to be variable and γ Dra and γ Cru had too few observations to be useful. The observations were normalized to α CMa by taking ratios of the stars and Sirius obtained at the same focal plane temperature. A ratio of a given star to Sirius is obtained whenever these two stars were measured on the same DCE. Since the focal plane temperature changes little during a DCE, this ratio should be free of temperature effects. Another set of scale factors were calculated by averaging the measured irradiances for a given star in 0.5K bins spaced every 0.25K, including Sirius, and then taking the ratio of the averaged irradiances for a given star with those of Sirius within a temperature bin. This procedure doubly weights the α CMa measurements as they appear both individually and in the averages within a temperature bin in the final average. The averaging produces a single scale factor for each star in each spectral band and provides an initial evaluation of the photometric ratios in the calibration network. The measurements are normalized to Sirius and a weighted least squares polynomial is fit through the result where the weights are the inverse variances about the individual DCE means. Selection of the degree of polynomial correction was guided by a χ^2 analysis.

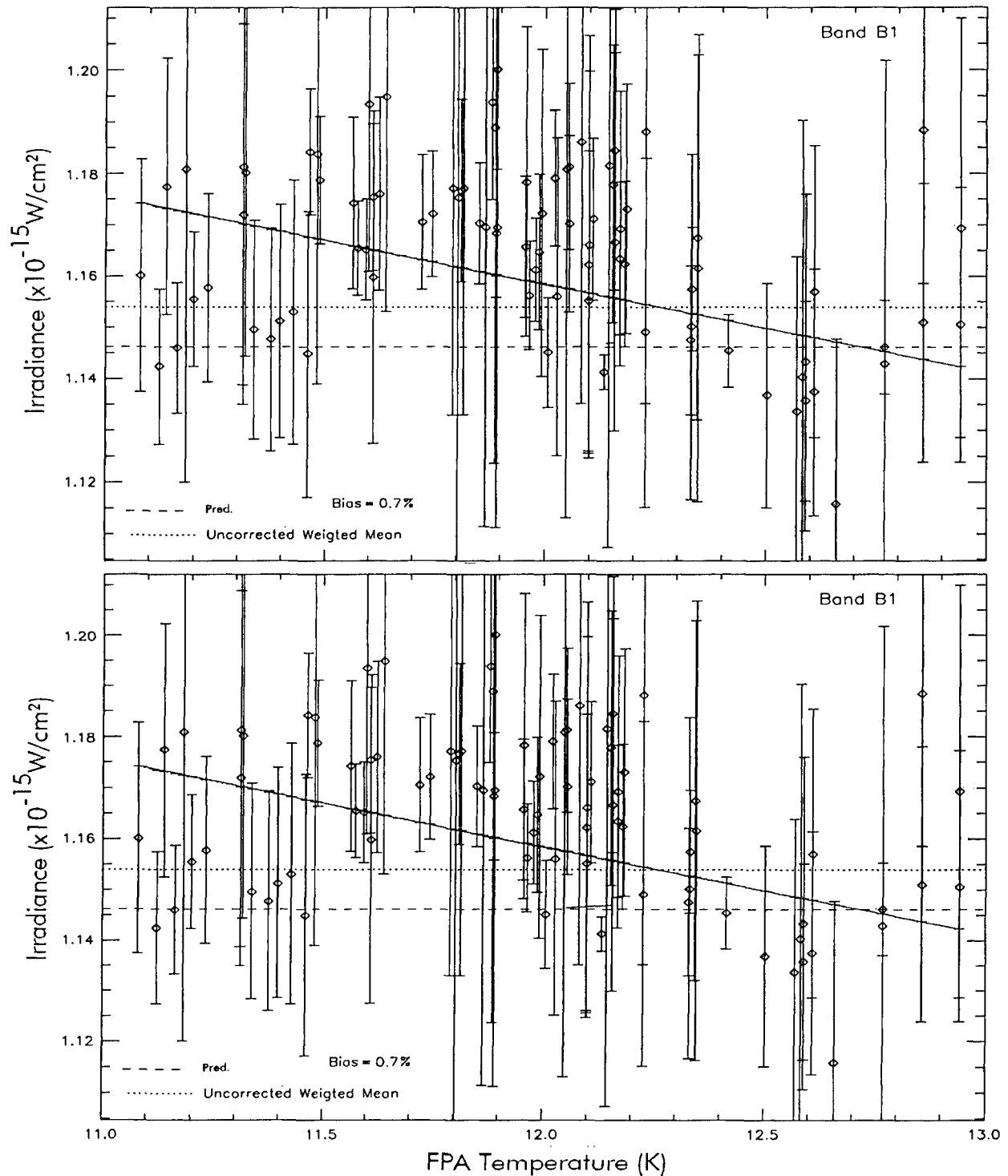


Figure 10: The B Band irradiance responses normalized to α CMa as a function of focal plane temperature. Band B₁ is shown on the top and Band B₂ on the bottom. The solid line is a weighted least squares linear fit of the data as a function of focal plane temperature. The dashed line is the predicted irradiance and the dotted line is the average value of the DCE means before the response is corrected.

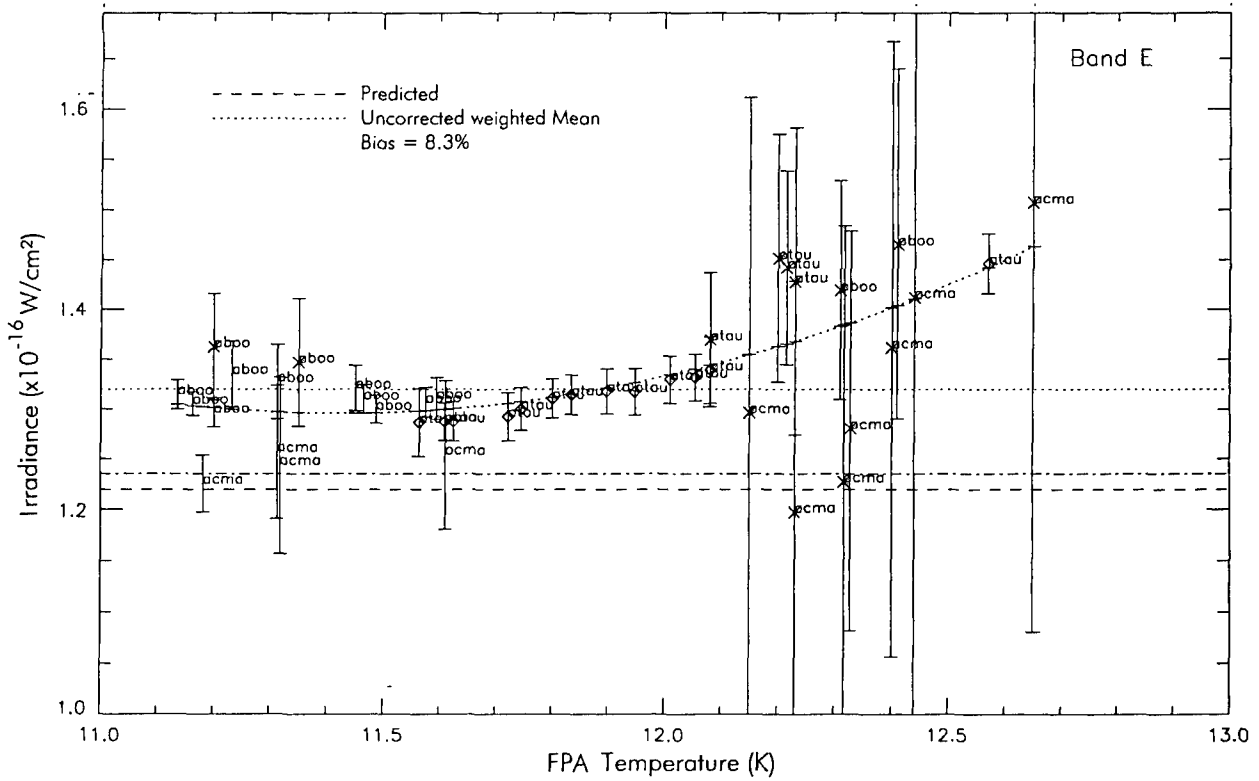


Figure 13: The irradiance response in Band E as a function of focal plane temperature. The CB06 observations are denoted by 'x'. The dotted curve is the parabolic correction term derived for this band.

The normalized DCE means from the CB observations in Band E are designated with an 'x' in Figure 13. The dot dashed line is the straight average of all of the α CMa Band E measurements before response correction. As may be seen, the CB06 values dominate the higher temperature results. The horizontal dotted line is the average of all the scaled measurements. Unfortunately, the α CMa observations are still biased high by the selection effects, even for the aperture photometry Cohen et al. extracted for the CB06 measurement. This bias is reflected in the difference between the two uncorrected means. Fortunately, the solution is dominated by the much higher quality measurements on α Boo and α Tau and the response correction simply needed to be scaled by 1.095. This scale factor was consistent with that needed to adjust the curve shown in Figure 13 to the point response fitted photometry on the CB06 α CMa Band E measurements to anchor it to the predicted values.

The polynomial fits for responsivity corrections are function of the Band B₁ focal plane temperature. Band B₁ was used to derive the fits for the all the bands rather than using the focal temperature readout for each band because the temperature monitors on the Aerojet Bands A and B arrays were more accurate than those on the Rockwell Bands C, D and E arrays. The corrections are used by either as a multiplicative factor to the responsivity, $R_{a,d}(t)$ in Equation (2), or it divides the derived irradiances.

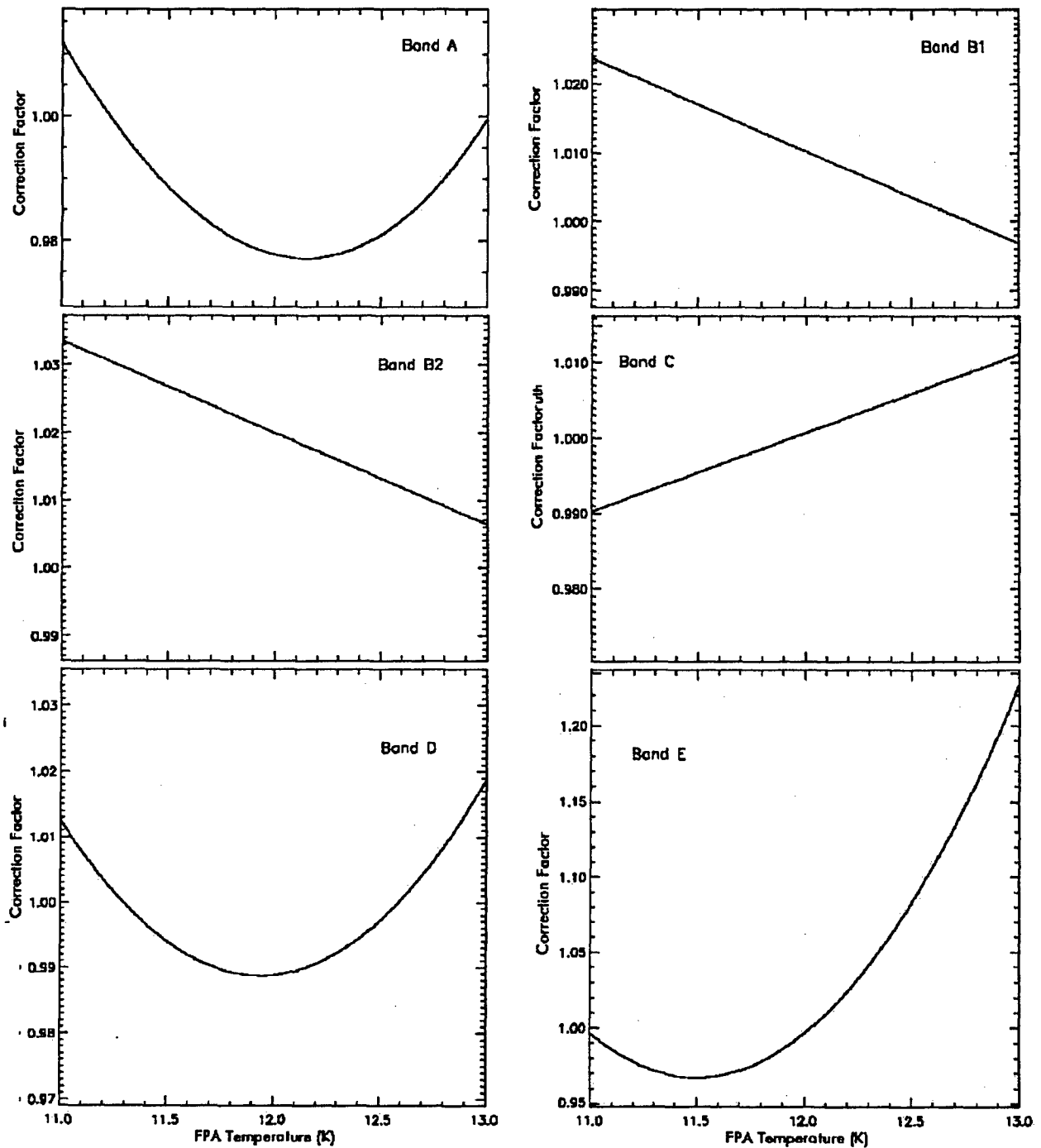


Figure 14: The responsivity correction as a function of focal plane temperature.

The polynomial fits, which have the constants listed in Table 4, are divided by the in-band fluxes predicted for α CMa to obtain the correction factors shown in Figure 14. The response corrections are ≤ 1 percent about a mission average; except for Band E in which it is about ± 10 percent. The responsivity vs. temperature correction also adjusts for the biases in the mission averages provided in Figures 9 through 13.

Table 4: Coefficients for the Response vs. Focal Plane Temperature Correction

Band	Const.	$\times T$	$\times T^2$	$\times T^3$
A	1.403203	0.244561	-0.048938	0.002134
B ₁	1.171592	-0.013441		
B ₂	1.182855	-0.013570		
C	0.874866	0.010486		
D	4.80301	-0.638706	0.026739	
E	16.262953	-2.659675	0.115627	

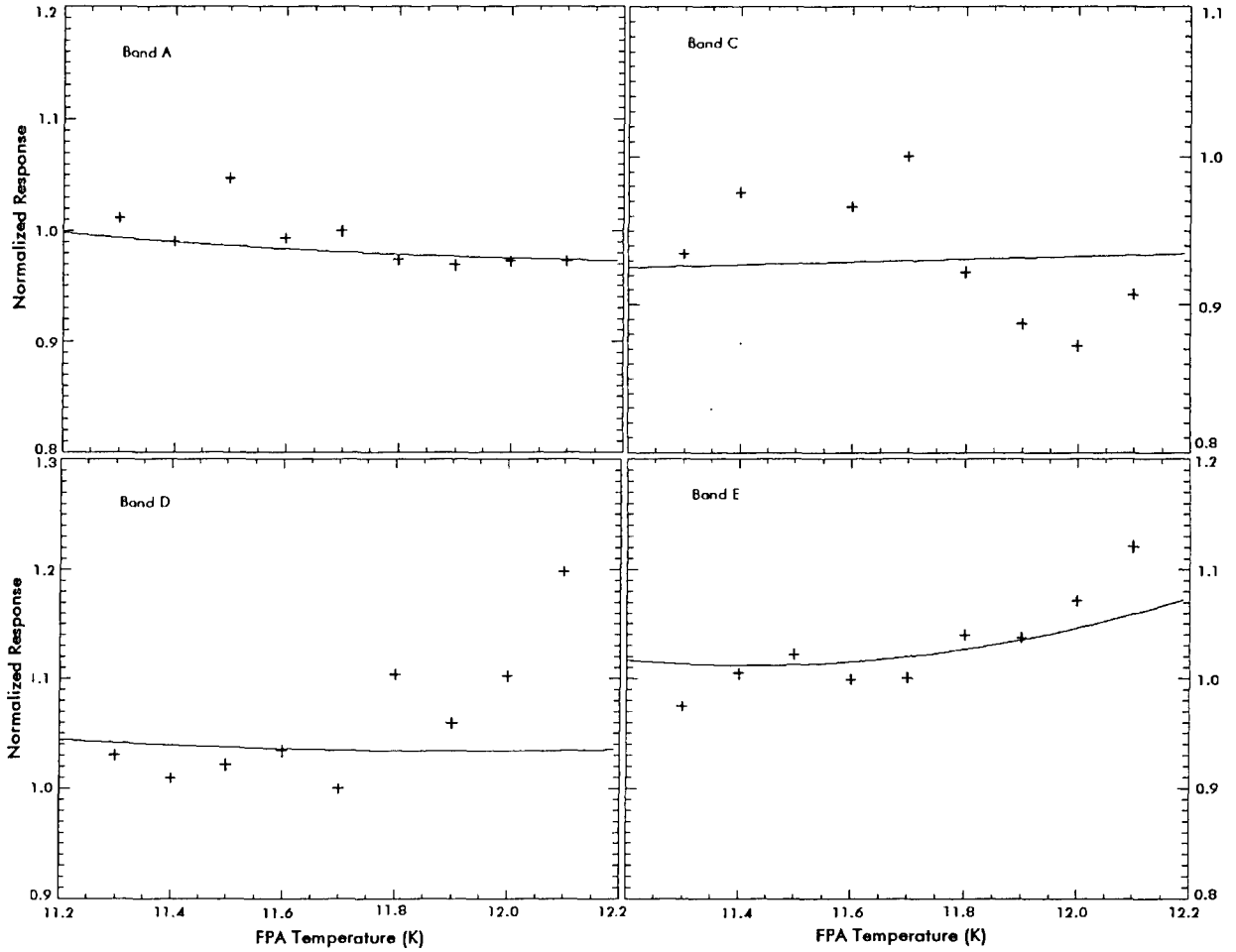


Figure 15: The MSX measured response to NGC 6543 compared to the correction curves. Each plotted value is the average of approximately 5 measurements within a 0.2K temperature bin taken every 0.1K. The correction curves are scaled to the median value in each band.

A crude independent assessment of the correction factors is shown in Figure 15, which plots the MSX measurements of NGC 6543 before correcting the responsivity compared to the polynomial corrections in Figure 14. This small planetary nebula is located very close to the north ecliptic pole, where the scans for the CB04 Areas Missed by IRAS experiment began.

Consequently, this object was observed a number of times in the mirror-fixed mode throughout the mission. Approximately 45 (Band D) to 50 (Band E) MSX measurements were available for this analysis. These measurements were sorted into 0.2K bins every 0.1K in focal plane temperature and averages taken for the measurements in each bin. The SNR for Band D was about 10 and about 20 for the other bands. Although the measurements are noisy for reasons described in Price et al. (2001) the measurements do, generally, follow the temperature correction trend.

A dramatic example of the improvement produced by correcting the response is shown in Figure 16, which plots the histogram of all the individual Band E measurements of γ Cru before and after temperature correction. As may be seen from Figure 23, the observations were taken at 11.5 and 12.5K; the corrections differed by about a 10 percent between these two temperatures. The response correction reduced the standard deviation in this set of observations by almost a factor of three.

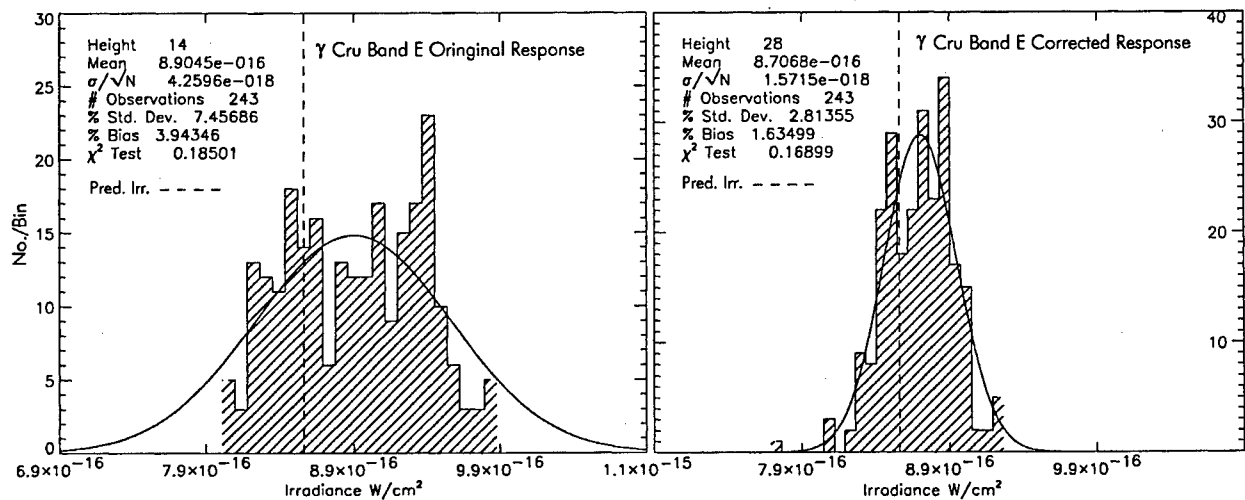


Figure 16: The histogram of the frequency of occurrence in a Band E irradiance bin for γ Cru is shown before (left) and after (right) applying the response correction. The histogram is an aggregate of the 243 individual measurements on the three mirror-scan DCEs that observed this star.

The irradiances averaged over a DCE for the eight standard stars measured in the mirror-scan mode after correcting for the temperature dependent response variation are plotted as a function of focal plane temperature in Figures 17 through 24. The scatter in the α Boo DCE mean irradiances has been reduced as may be seen by comparing Figure 7 with Figure 19, despite the different scale factors for the axes in these plots.

Temperature corrected weighted averaged irradiances for the standard stars measured on the mirror-scanned DCE are listed in Table 5. The temperature corrected mean irradiances for the CB06 experiment are listed in Table 6.

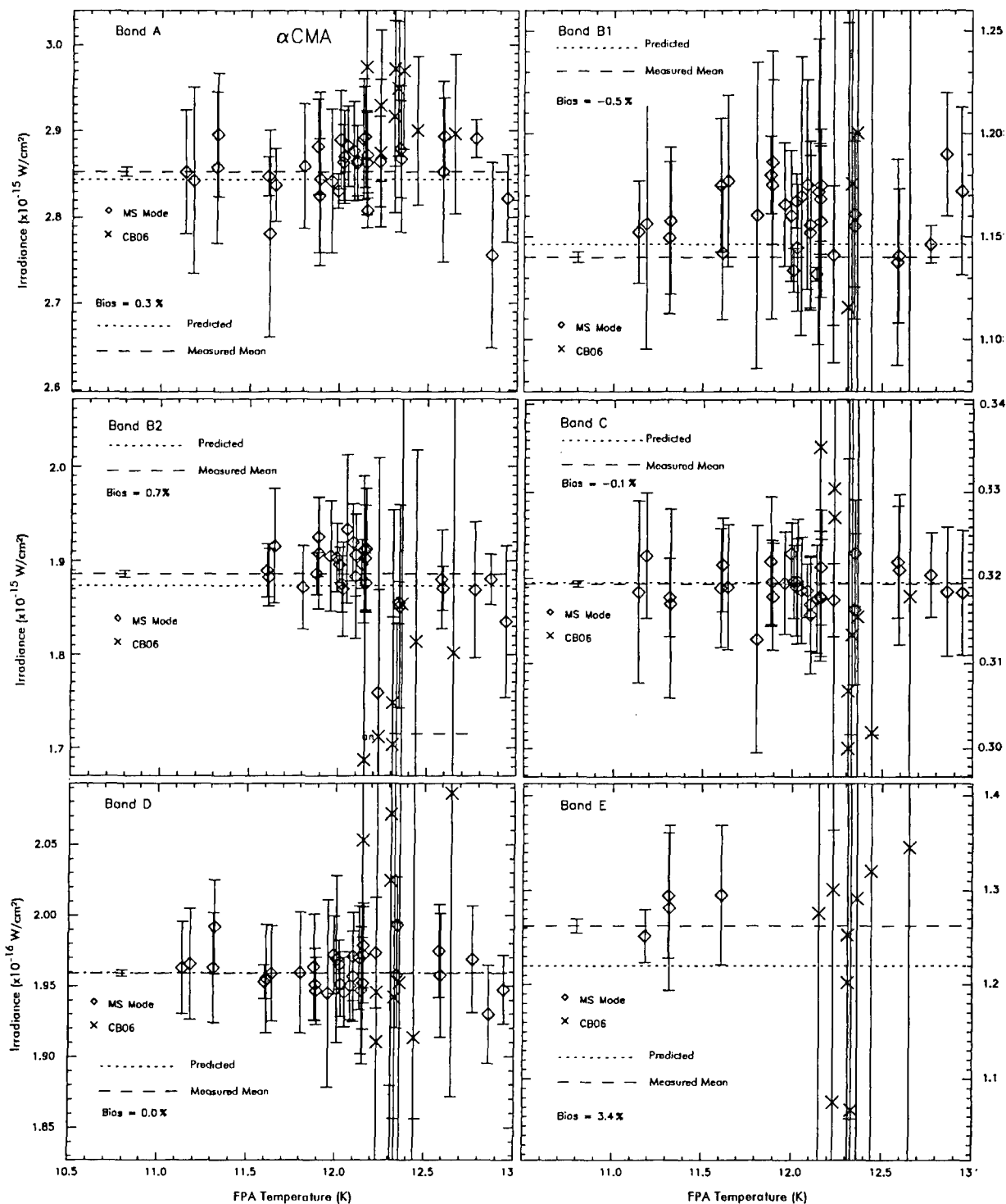


Figure 17: DCE mirror-scan means for α CMA after correcting for temperature dependent responsivity plotted with the standard deviations about the means as error bars. The dashed line gives the measured mission mean and the CWW predicted irradiance value is the dotted line. Diamonds are the mirror-scan (MS) observations and the crosses are the CB06 values.

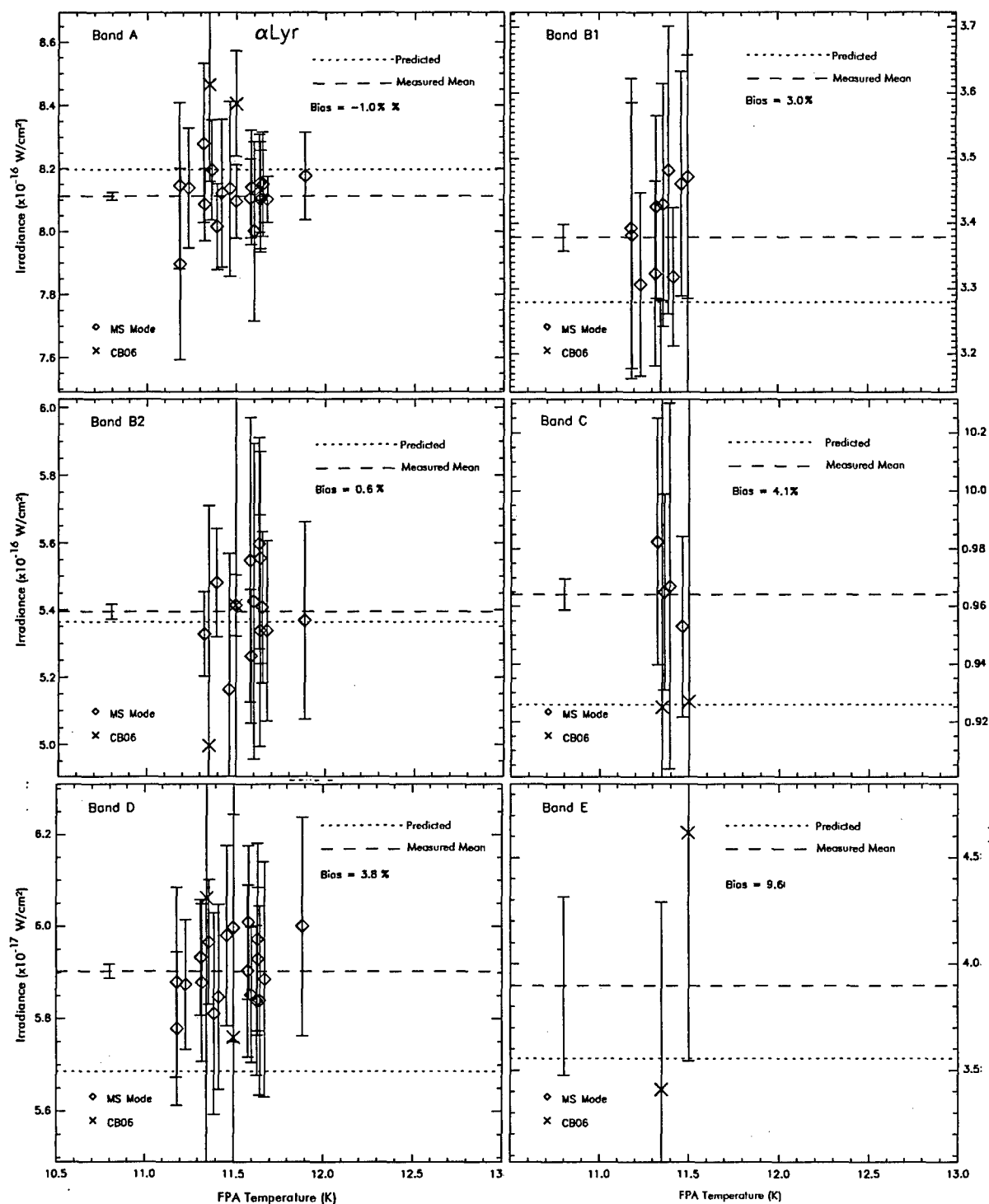


Figure 18: DCE mirror-scan means for α Lyr after correcting for temperature dependent responsivity. Dotted lines are the predicted irradiances and the dashed lines are the measured DCE mean values.

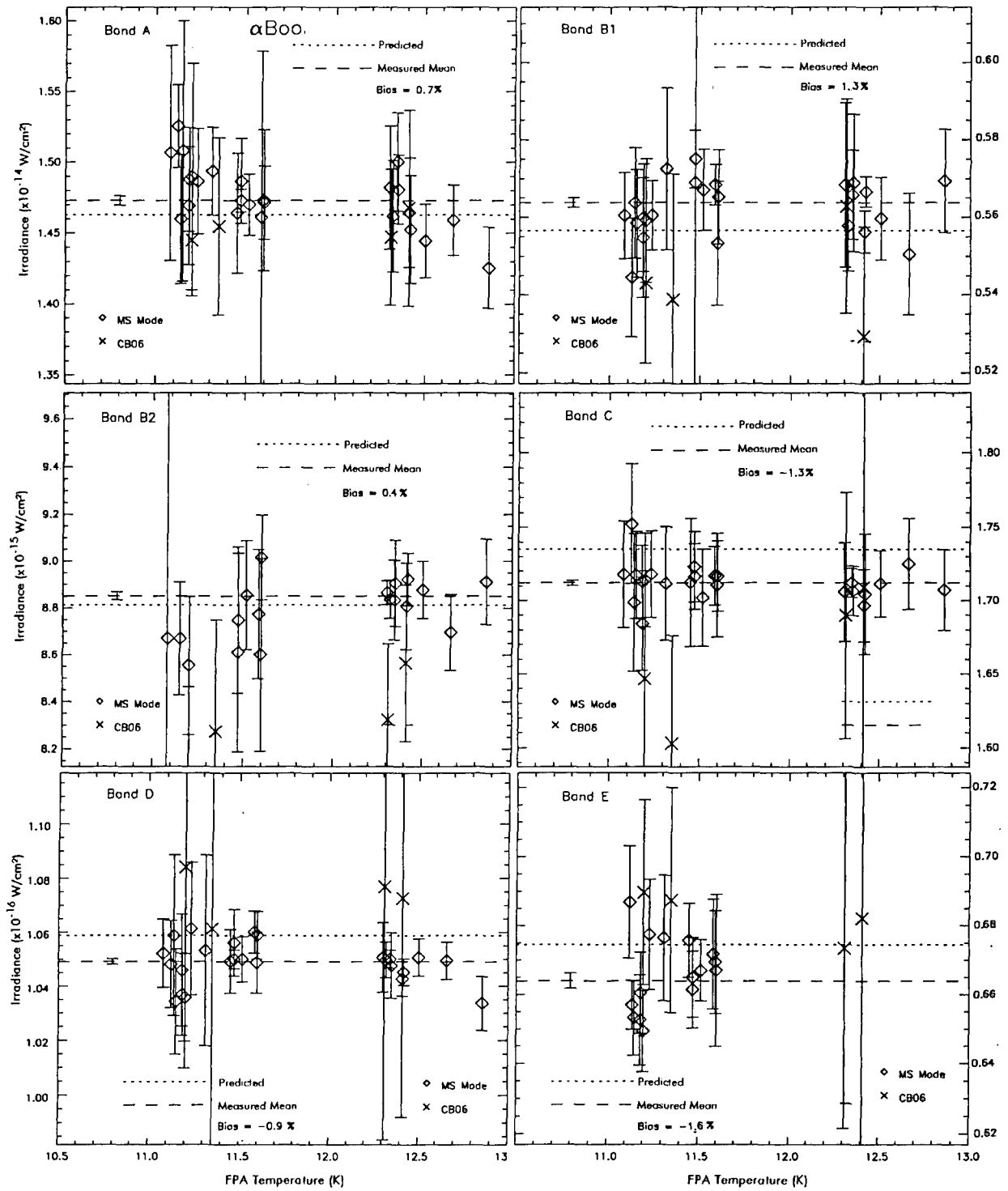


Figure 19: DCE mirror-scan means for α Boo after correcting for temperature dependent responsivity.

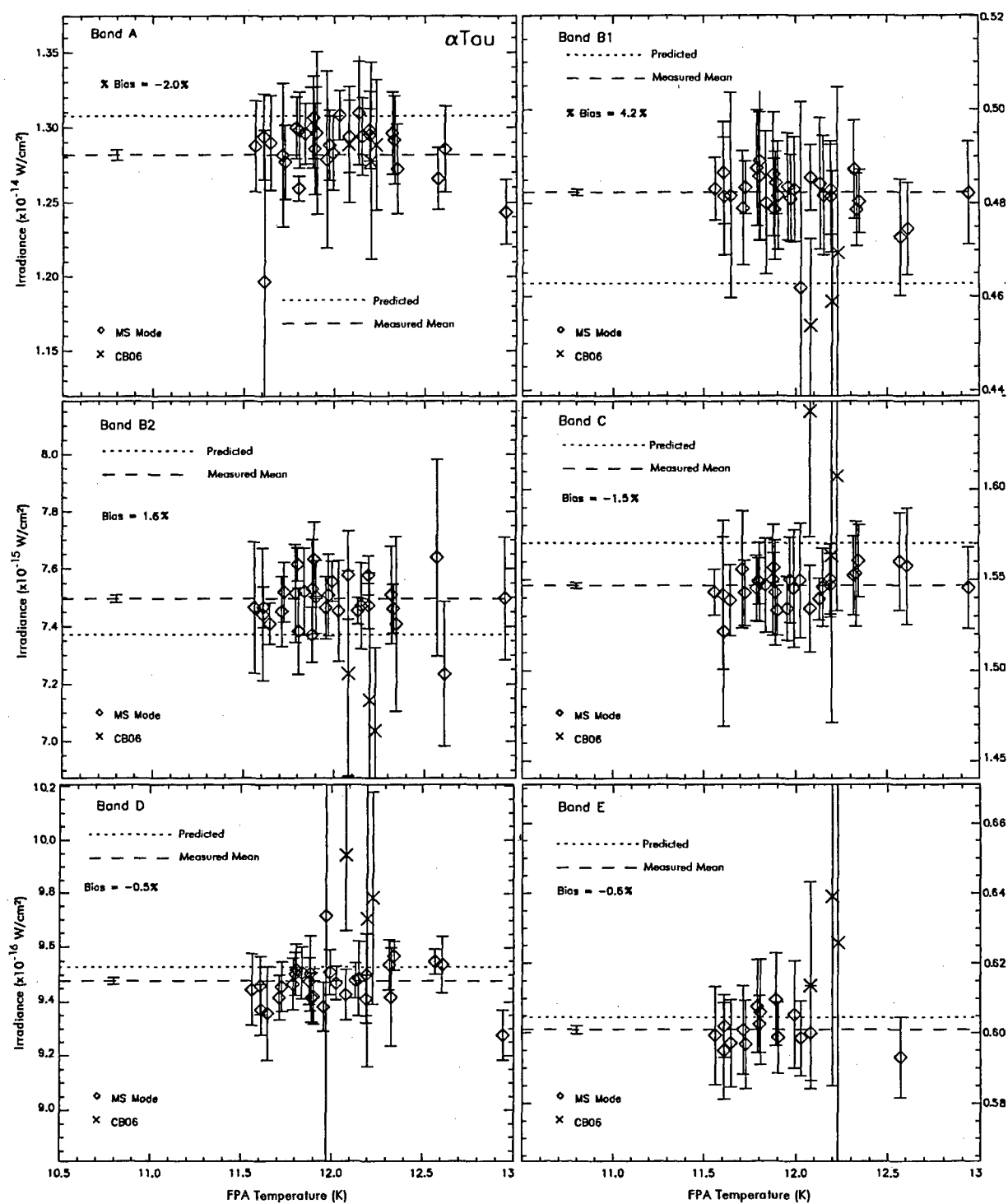


Figure 20: DCE mirror-scan means for α Tau after correcting for temperature dependent responsivity.

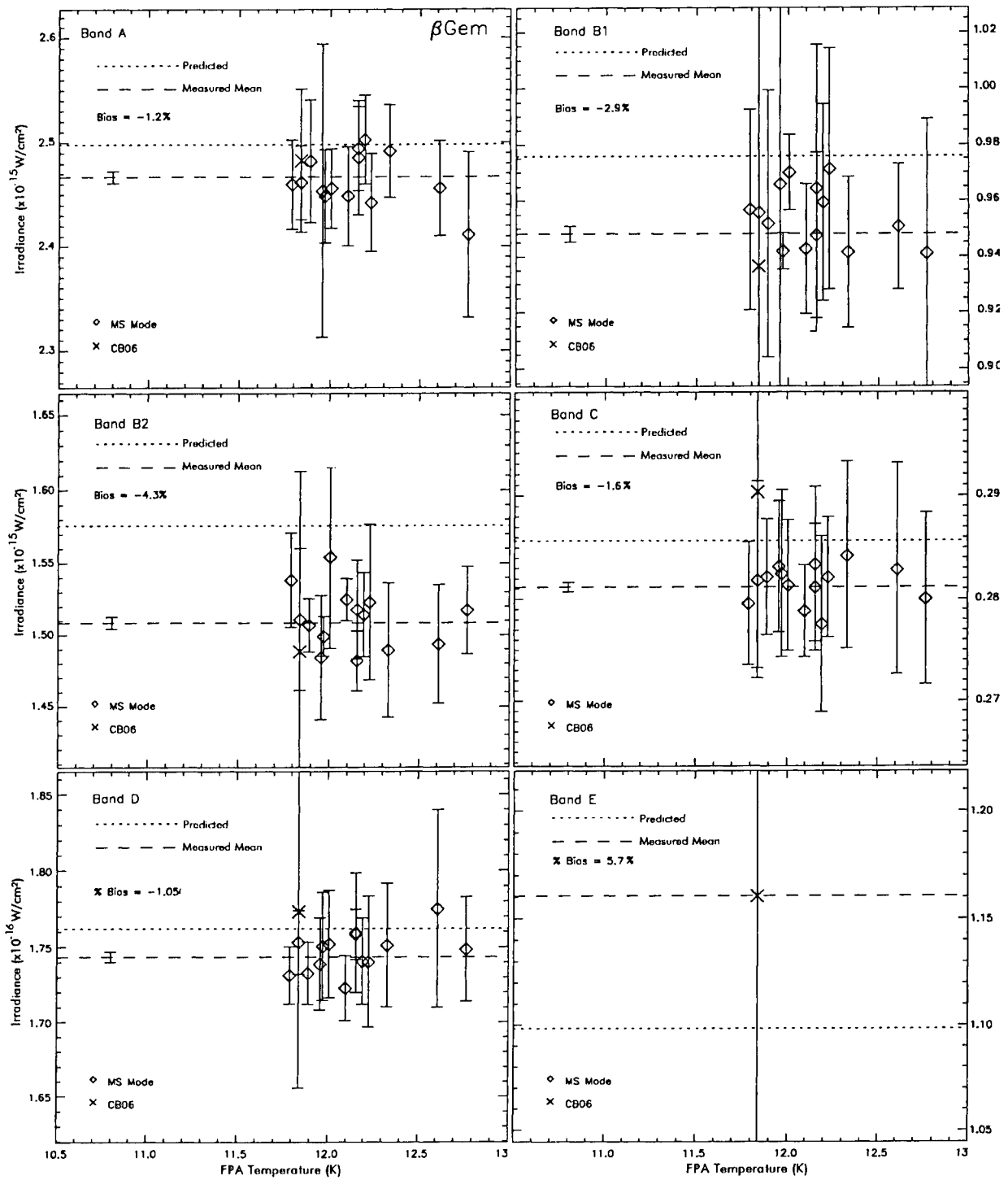


Figure 21: DCE mirror-scan means for β Gem after correcting for temperature dependent responsivity.

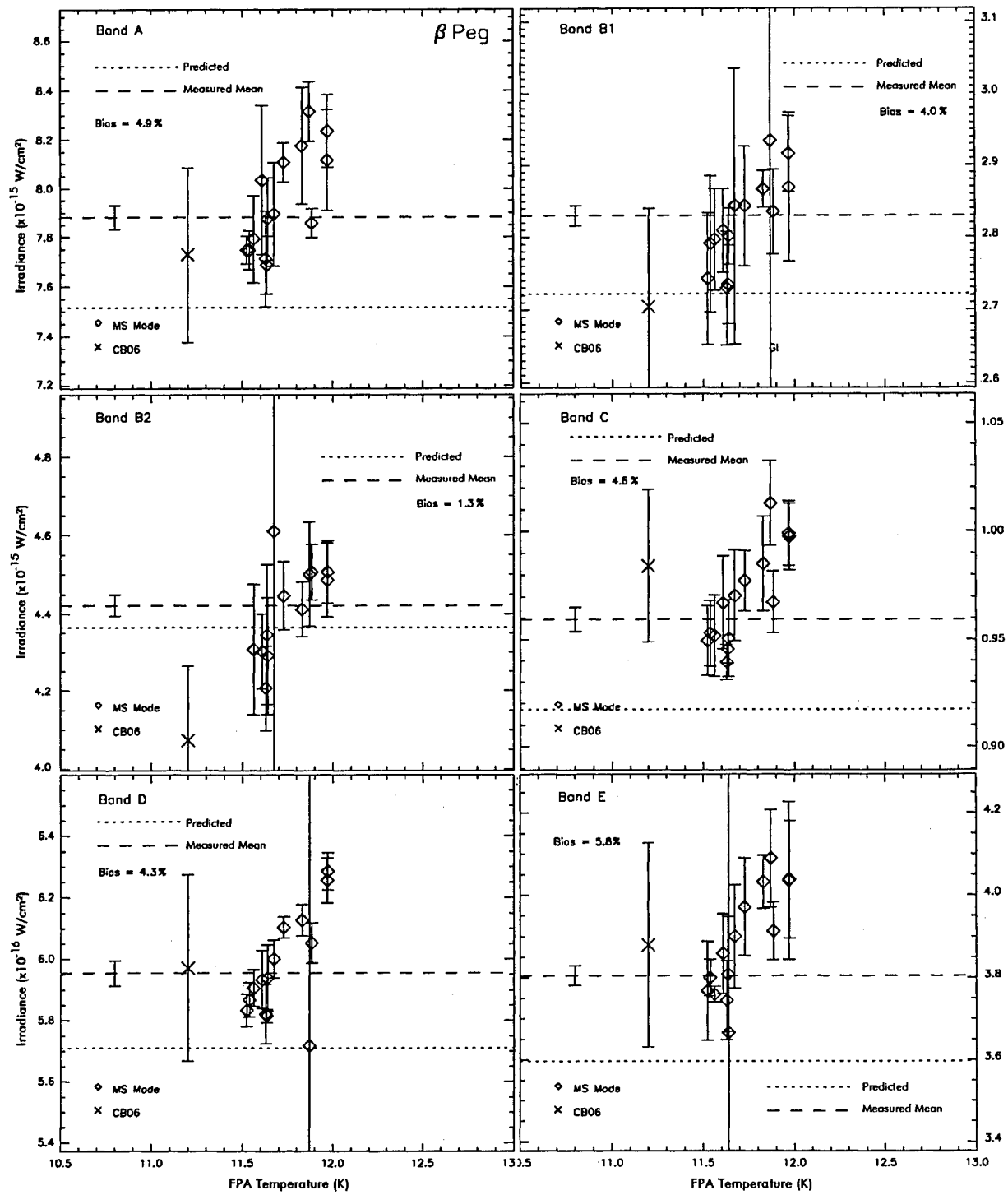


Figure 22: DCE mirror-scan means for β Peg after correcting for temperature dependent responsivity.

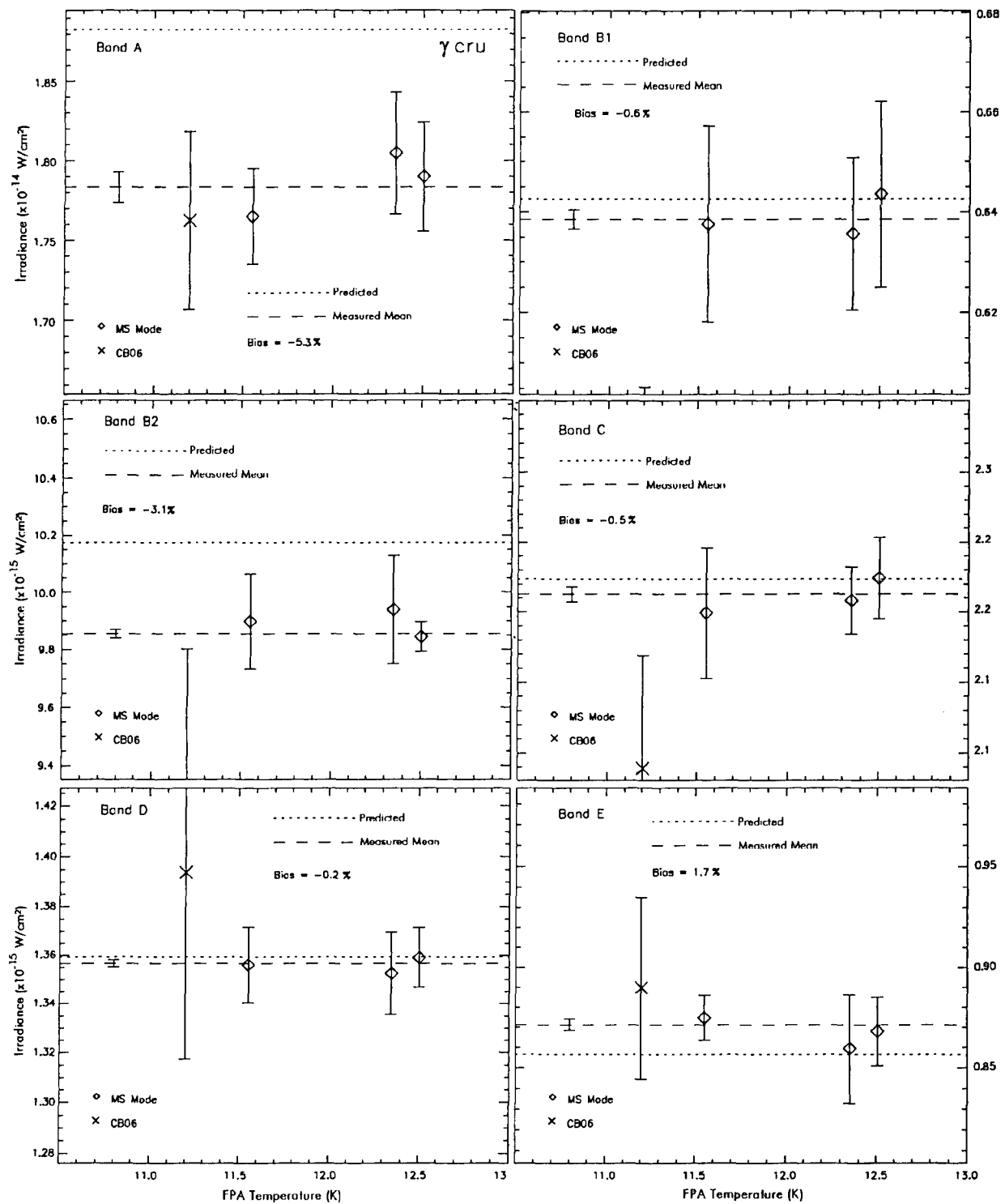


Figure 23: DCE mirror-scan means for γ Cru after correcting for temperature dependent responsivity.

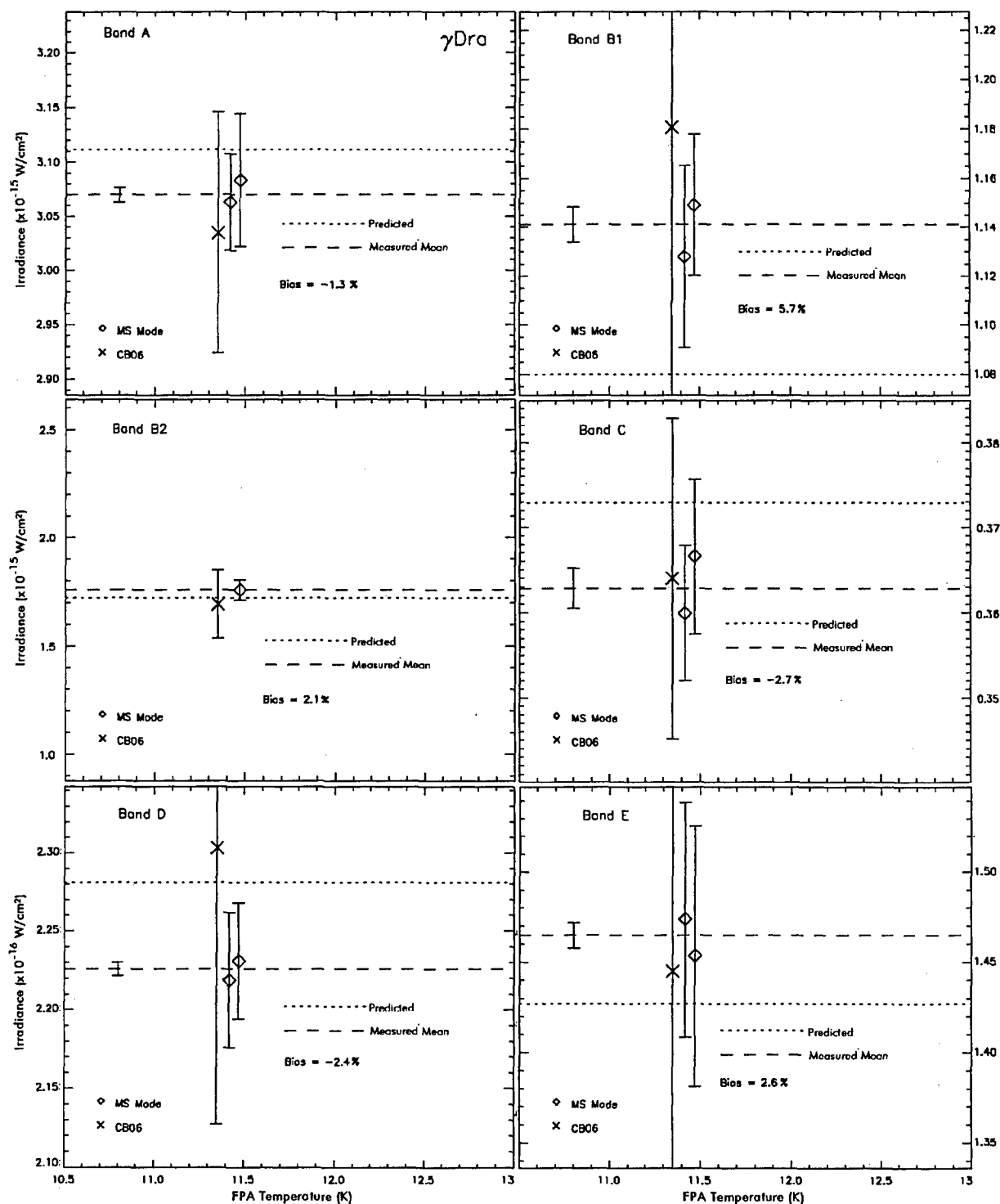


Figure 24: DCE mirror-scan means for γ Dra after correcting for temperature dependent responsivity.

Table 5: Mirror-Scan Weighted Mission Average Fluxes

Star	A flux	B ₁ flux	B ₂ flux	C flux	D flux	E flux
α Boo	1.473×10^{-14} $\pm 0.2\%$	5.638×10^{-15} $\pm 0.2\%$	8.852×10^{-15} $\pm 0.2\%$	1.712×10^{-15} $\pm 0.1\%$	1.049×10^{-15} $\pm 0.1\%$	6.639×10^{-16} $\pm 0.3\%$
α Tau	1.282×10^{-14} $\pm 0.2\%$	4.824×10^{-15} $\pm 0.2\%$	7.496×10^{-15} $\pm 0.2\%$	1.547×10^{-15} $\pm 0.1\%$	9.479×10^{-16} $\pm 0.1\%$	6.010×10^{-16} $\pm 0.2\%$
α Lyr	8.112×10^{-16} $\pm 0.2\%$	3.378×10^{-16} $\pm 0.6\%$	5.395×10^{-16} $\pm 0.4\%$	9.642×10^{-17} $\pm 0.6\%$	5.903×10^{-17} $\pm 0.2\%$	3.897×10^{-17} $\pm 10.7\%$
β Gem	2.467×10^{-15} $\pm 0.2\%$	9.480×10^{-16} $\pm 0.3\%$	1.509×10^{-15} $\pm 0.3\%$	2.812×10^{-16} $\pm 0.2\%$	1.743×10^{-16} $\pm 0.2\%$	1.160×10^{-16} *
γ Dra	3.070×10^{-15} $\pm 0.2\%$	1.141×10^{-15} $\pm 0.6\%$	1.759×10^{-15} *	3.628×10^{-16} $\pm 0.6\%$	2.226×10^{-16} $\pm 0.2\%$	1.465×10^{-16} $\pm 0.5\%$
γ Cru	1.783×10^{-14} $\pm 0.5\%$	6.385×10^{-15} $\pm 0.3\%$	9.855×10^{-15} $\pm 0.2\%$	2.213×10^{-15} $\pm 0.2\%$	1.357×10^{-15} $\pm 0.1\%$	8.713×10^{-16} $\pm 0.3\%$
α CMa	2.853×10^{-15} $\pm 0.2\%$	1.140×10^{-15} $\pm 0.2\%$	1.886×10^{-15} $\pm 0.2\%$	3.193×10^{-16} $\pm 0.1\%$	1.959×10^{-16} $\pm 0.1\%$	1.262×10^{-16} $\pm 0.6\%$

* single DCE mean results in an indeterminate uncertainty. Band E values for α Lyr and β Gem influenced by the flux overestimation bias.

Table 6: CB06 Mission Averaged Fluxes

Star	Band A	Band B ₁	Band B ₂	Band C	Band D	Band E
α Boo	1.458×10^{-14} $\pm 0.8\%$	5.633×10^{-15} $\pm 1.2\%$	8.732×10^{-15} $\pm 1.1\%$	1.710×10^{-15} $\pm 0.8\%$	1.045×10^{-15} $\pm 0.9\%$	6.777×10^{-16} $\pm 1.4\%$
α Tau	1.284×10^{-14} $\pm 0.9\%$	4.694×10^{-15} $\pm 1.3\%$	7.384×10^{-15} $\pm 1.4\%$	1.562×10^{-15} $\pm 0.8\%$	9.600×10^{-16} $\pm 0.8\%$	6.249×10^{-16} $\pm 1.6\%$
α Lyr	8.483×10^{-16} $\pm 1.4\%$	3.274×10^{-16} $\pm 1.8\%$	5.335×10^{-16} $\pm 1.6\%$	-----	5.785×10^{-17} $\pm 2.0\%$	4.268×10^{-17} $\pm 3.0\%$
β Gem	2.446×10^{-15} $\pm 1.2\%$	9.807×10^{-16} $\pm 1.6\%$	1.491×10^{-15} $\pm 2.2\%$	2.901×10^{-16} $\pm 2.8\%$	1.763×10^{-16} $\pm 1.5\%$	1.224×10^{-16} $\pm 3.0\%$
γ Dra	3.049×10^{-15} $\pm 1.4\%$	1.112×10^{-15} $\pm 1.8\%$	1.718×10^{-15} $\pm 2.7\%$	3.790×10^{-16} $\pm 1.2\%$	2.244×10^{-16} $\pm 1.8\%$	1.478×10^{-16} $\pm 2.8\%$
γ Cru	1.782×10^{-14} $\pm 1.2\%$	6.245×10^{-15} $\pm 1.4\%$	1.002×10^{-14} $\pm 2.4\%$	2.215×10^{-15} $\pm 1.3\%$	1.351×10^{-15} $\pm 1.4\%$	8.706×10^{-16} $\pm 2.5\%$
α CMa	2.853×10^{-15} $\pm 0.6\%$	1.135×10^{-15} $\pm 1.1\%$	1.879×10^{-15} $\pm 0.9\%$	3.140×10^{-16} $\pm 0.7\%$	1.946×10^{-16} $\pm 0.5\%$	1.248×10^{-16} $\pm 1.2\%$

Values are in-band irradiances (W cm^{-2})

The responsivity corrections are not usually as dramatic as shown in Figure 16 as may be seen by comparing the standard deviations in the histograms plotted in Figure 25 for the α Boo measurements before and after correcting the responsivity. The histograms are of the measurements before averaging the data on consecutive scans. The mission averaged mean fluxes derived from the peak in the Gaussian curve fitted to the histogram of the temperature corrected observations are tabulated in Table 7.

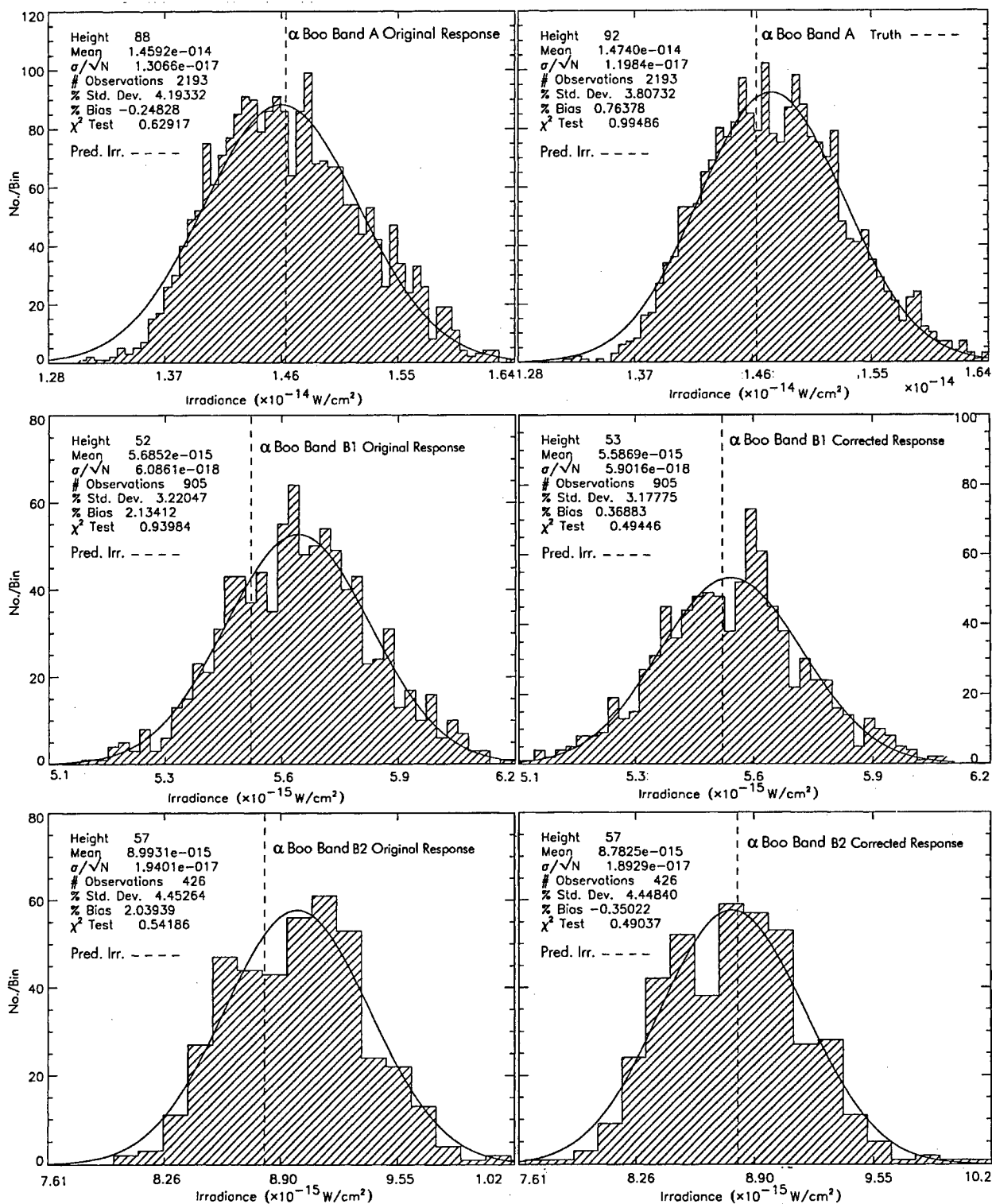


Figure 25: Histograms of the mirror scanned measurements on α Boo. The plots at the left are before the response corrections as a function of focal plane temperature have been applied; those on the right are after. Bands A, B₁ and B₂ are shown.

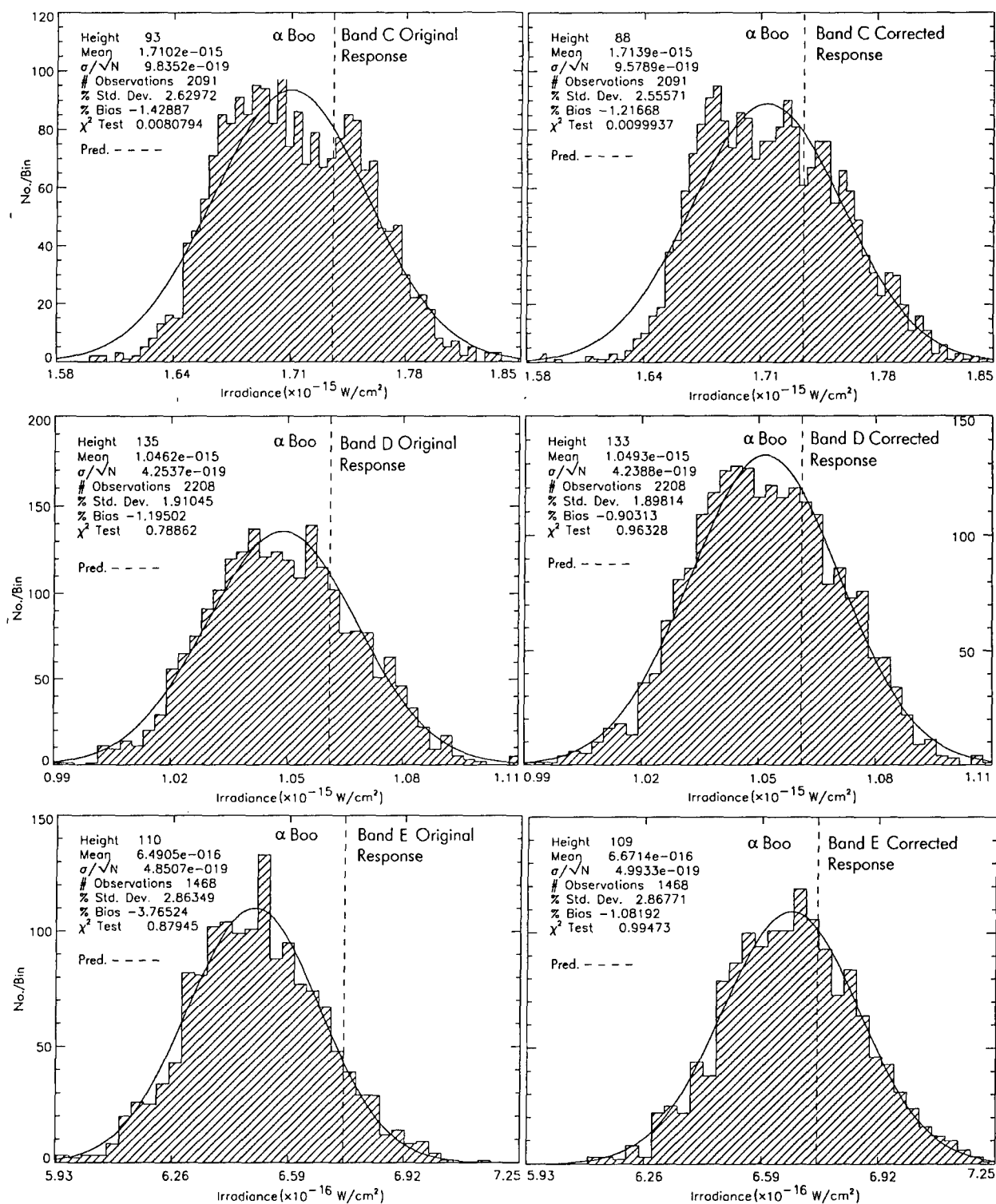


Figure 25 (continued): The histograms of the α Boo mirror scanned measurements in Bands C, D and E before (left) and after (right) the response corrections.

Table 7: Global Histogram Averages

Star	Band A	Band B ₁	Band B ₂	Band C	Band D	Band E
α Boo	1.474×10^{-14} $\pm 0.08\%$	5.587×10^{-15} $\pm 0.11\%$	8.783×10^{-15} $\pm 0.22\%$	1.714×10^{-15} $\pm 0.06\%$	1.049×10^{-15} $\pm 0.04\%$	6.671×10^{-16} $\pm 0.07\%$
α Tau	1.286×10^{-14} $\pm 0.07\%$	4.827×10^{-15} $\pm 0.12\%$	7.482×10^{-15} $\pm 0.16\%$	1.548×10^{-15} $\pm 0.05\%$	9.457×10^{-16} $\pm 0.04\%$	5.988×10^{-16} $\pm 0.09\%$
α Lyr	8.110×10^{-16} $\pm 0.08\%$	3.368×10^{-16} $\pm 0.33\%$	5.386×10^{-16} $\pm 0.41\%$	9.700×10^{-17} $\pm 0.35\%$	5.910×10^{-17} $\pm 0.11\%$	-----
β Gem	2.412×10^{-15} $\pm 0.10\%$	9.487×10^{-16} $\pm 0.28\%$	1.504×10^{-15} $\pm 0.26\%$	2.816×10^{-16} $\pm 0.10\%$	1.743×10^{-16} $\pm 0.08\%$	-----
γ Dra	3.082×10^{-15} $\pm 0.21\%$	1.133×10^{-15} $\pm 0.45\%$	1.732×10^{-15} $\pm 0.76\%$	3.633×10^{-16} $\pm 0.20\%$	2.225×10^{-16} $\pm 0.17\%$	1.454×10^{-16} $\pm 0.50\%$
γ Cru	1.782×10^{-14} $\pm 0.23\%$	6.356×10^{-15} $\pm 0.47\%$	9.899×10^{-15} $\pm 0.39\%$	2.209×10^{-15} $\pm 0.18\%$	1.355×10^{-15} $\pm 0.13\%$	8.707×10^{-16} $\pm 0.18\%$
α CMa	2.861×10^{-15} $\pm 0.06\%$	1.156×10^{-15} $\pm 0.15\%$	1.882×10^{-15} $\pm 0.17\%$	3.196×10^{-16} $\pm 0.06\%$	1.961×10^{-16} $\pm 0.05\%$	1.282×10^{-16} $\pm 0.43\%$

Values are in-band irradiances (W cm^{-2})

Values are without averaging adjacent scans.

No meaningful Band E values for α Lyr and β Gem due to the flux overestimation bias

4.1 Global Mean Fluxes

Separate tables of the DCATT (mirror-scanned) and CB (mirror-fixed) stellar magnitudes were created relative to α CMa, with associated uncertainties, from the mission averaged fluxes in Tables 5 and 6, respectively. For convenience, we adopted an infrared magnitude for Sirius of -1.36 in all the MSX Bands, which is equivalent to assuming that the α CMa irradiance is 3.5 times that from the zero magnitude standard spectral energy distribution. The offset between the CB and DCATT stellar fluxes was obtained by minimizing the average differences between stars in the two magnitude tables. Since the DCATT photometry is well defined, the CB06 values were scaled to the mirror-scan results to normalize the effective beam size of the CB06 point response function fitted photometry. Specifically, the weighted average of the differences between corresponding entries for the same stars in the two tables is taken where the weights are the root sum square of the standard deviations of the mission results for the stars in the two Tables. The CB06 values were scaled by the resulting offset and a weighted average is taken of the two values for a given star. The averaged magnitudes in a given band are then adjusted to force α CMa to have a magnitude of -1.36 . Essentially, the logarithmic average is taken of the two data sets and all the results adjusted to α CMa. The weighted averages of the mirror-scanned DCEs and the mirror-fixed DCEs were combined into a single set of global mean fluxes, which are listed in Table 8.

A reduced χ^2 analysis checked the consistency in estimating the errors in this procedure. The differences between the scaled CB06 and DC magnitudes for a given star were squared and then the sum over the seven CWW stars was taken and the result was divided by the sum of the squares of the uncertainties associated with the two magnitudes. The square root of the result divided by the number of stars in the calculation should be equal to one if the discrepancies were equal to the estimated error for each pair of stars. Table 9 lists the calculated values in each

band. The average for all bands was 0.8 but the formal uncertainties in Bands A, B₂, and E are a factor of about two too large while those in Bands B₁ and C were apparently a bit too small. Thus, it may be concluded that the formal errors are accurate to within 50 percent.

Table 8: Global DCATT + CB Calibration of the CWW Stars

Star	Band A	Band B ₁	Band B ₂	Band C	Band D	Band E
α Boo	1.465×10^{-14} $\pm 0.4\%$	5.598×10^{-15} $\pm 0.7\%$	8.731×10^{-15} $\pm 0.6\%$	1.719×10^{-15} $\pm 0.3\%$	1.049×10^{-15} $\pm 0.2\%$	6.635×10^{-16} $\pm 0.8\%$
α Tau	1.281×10^{-14} $\pm 0.4\%$	4.764×10^{-15} $\pm 0.7\%$	7.417×10^{-15} $\pm 0.6\%$	1.555×10^{-15} $\pm 0.3\%$	9.474×10^{-16} $\pm 0.2\%$	6.023×10^{-16} $\pm 0.8\%$
α Lyr	8.109×10^{-16} $\pm 0.5\%$	3.333×10^{-16} $\pm 1.1\%$	5.339×10^{-16} $\pm 0.9\%$	9.703×10^{-17} $\pm 0.7\%$	5.901×10^{-17} $\pm 0.6\%$	4.167×10^{-17} $\pm 5\%$
β Gem	2.447×10^{-15} $\pm 0.4\%$	9.550×10^{-16} $\pm 0.8\%$	1.495×10^{-15} $\pm 0.7\%$	2.830×10^{-16} $\pm 0.5\%$	1.746×10^{-16} $\pm 0.3\%$	1.195×10^{-16} $\pm 2.7\%$
γ Dra	3.053×10^{-15} $\pm 0.8\%$	1.123×10^{-15} $\pm 1.1\%$	1.734×10^{-15} $\pm 1.4\%$	3.703×10^{-16} $\pm 0.7\%$	2.229×10^{-16} $\pm 0.5\%$	1.462×10^{-16} $\pm 2.2\%$
γ Cru	1.779×10^{-14} $\pm 0.7\%$	6.310×10^{-15} $\pm 0.9\%$	9.823×10^{-15} $\pm 0.9\%$	2.221×10^{-15} $\pm 0.5\%$	1.356×10^{-15} $\pm 0.4\%$	8.610×10^{-16} $\pm 1.2\%$
β And	5.271×10^{-15} $\pm 1.6\%$	1.833×10^{-15} $\pm 1.5\%$	2.997×10^{-15} $\pm 1.8\%$	6.482×10^{-16} $\pm 1.2\%$	3.964×10^{-16} $\pm 1.2\%$	2.429×10^{-16} $\pm 2.8\%$

Table 9: Reduced χ^2 Goodness of Match between DCATT and CB Scaled Mission Means

A	B ₁	B ₂	C	D	E
0.43	1.2	0.54	1.5	1.1	0.57

4.2 Measurement Precision

The improvement in precision that correcting for the response variation and then averaging successive scans has on the three most frequently measured stars is shown in Table 10. The standard deviations of the mirror-scanned measurements for these stars derived from their global histograms are listed. As expected, averaging two measurements made on every other pair of consecutive scans produces the largest change. If the distribution of measurements were random or Gaussian, as is indicated by Figure 25, the averaging would reduce the standard deviation by a factor of $\sqrt{2}$ or ~ 1.4 . A somewhat larger reduction is found for most of the standard deviations, as may be seen by comparing the response corrected values with the last row for each star in which the $\sqrt{2}$ factor has been multiplied back in. The ~ 10 percent larger than expected decrease is attributed to the reduction in the amplitude of the sawtooth pattern by the smoothing. The response correction has a small effect on the standard deviations, as may be inferred from Figures 9 through 14. However, the response correction significantly reduces the deviation between the measured and predicted mean irradiances.

Table 10: Standard Deviations from Histograms of the Original Data, the Data After Averaging Successive Measurements And After Correcting For The Response

Star	Corr.	Band A	Band B ₁	Band B ₂	Band C	Band D	Band E
α Boo	Orig.	4.2	3.2	4.6	2.6	1.9	2.9
	R vs. T	3.8	3.2	4.5	2.6	1.9	2.9
	Scan ave.	2.9	2.4	2.3	1.7	1.2	2.4
	$\times\sqrt{2}$	3.6	3.4	3.3	2.7	1.7	3.4
α Tau	Orig.	3.3	3.0	4.0	2.5	1.9	3.2
	R vs. T	3.3	3.0	4.0	2.5	1.9	2.9
	Scan ave.	2.3	2.25	1.9	1.4	1.1	2.1
	$\times\sqrt{2}$	3.2	3.1	2.8	2.2	1.6	3.0
α CMA	Orig.	3.3	4.6	4.6	3.2	2.7	---
	R vs. T	3.3	4.6	4.5	3.1	2.6	---
	Scan ave.	2.2	3.4	2.5	2.2	1.8	---
	$\times\sqrt{2}$	3.1	4.8	3.5	3.1	2.5	---

The uncertainty in the knowledge of the mission mean derived from the histograms is the standard deviation divided by the square root of the number of measurements. These are the uncertainties listed in Table 7. The uncertainties in the mean are about the same if successive scans are averaged, and the mean irradiances from the histograms with and without scan averaging are within the uncertainties of the mean listed in the Table.

The mission weighted average irradiances derived from the mean irradiance of M individual DCEs is given by:

$$\bar{F} = \frac{\sum_{i=1}^M f_i w_i}{\sum_{i=1}^M w_i}; \quad w_i = N_i / \sigma_i^2 \quad (5)$$

where f_i is the mean flux with the σ_i^2 variance calculated from the N independent observations made during the i^{th} DCE.

A star with M DCE mean fluxes has an uncertainty in the global mean given by:

$$\zeta_{\bar{F}} = \sqrt{\frac{\sum_{i=1}^M (f_i - \bar{F})^2 w_i}{M \sum_{i=1}^M w_i}}. \quad (6)$$

Table 5 lists the uncertainties derived thus for the mirror-scanned mission means while Table 6 provides the corresponding values for the mirror-fixed measurements.

Just as adding consecutive scans reduces the standard deviations by $\sim\sqrt{2}$ between the second and third rows of Table 10, the uncertainties in the mirror-scanned DCE means are reduced by a factor ~ 9 and by ~ 4.4 ($\sqrt{20}$) for the mirror-fixed means compared to the dispersions in the individual DCE measurements. The uncertainty in the global mean should have a standard deviation approximately equal to the square root of the quantity of the average variance of the individual means divided the number of DCE means. As may be seen by comparing the standard deviations in Tables 5 and 6 with those in Table 8, the formal solution using Equation (6) consistently returns larger values. This implies that an additional unknown source of measurement error influences the DCE means. Assuming that this error is random, the uncertainty in the knowledge of the mission means derived from Equation (5) could be accounted for by replacing σ_i^2 in Equations (5) and (6) with $\sigma_i^2 + (0.01f_i)^2$.

The sensitivity of the mean to the method used to process the data is expressed as the root mean square (rms) scatter of the mean fluxes derived from trimmed averages, weighted averages with and without the 1 percent contribution, and means from histogram fits about the global mean. The results are listed in Table 11 and were added in quadrature with the uncertainties in the global averages in Table 8.

Table 11: Precision in Results from Different Processing Procedures

Band:	A	B ₁	B ₂	C	D	E
σ	0.2%	0.8%	0.6%	0.3%	0.1%	0.8%

4.3 Results for the Primary and Secondary Standard Stars

Table 12 contains the ratios of the measured global mean fluxes from Table 8 with respect to Sirius divided by the predicted values from Table 3. The averages in the last row in the table exclude the values for α CMa, to which the fluxes were normalized, the γ Cru ratios and the Band C, D and E fluxes for α Lyr. Two uncertainties are given: the rms of the fluxes in the average in the first line with a backslash, then the second entry does the division to derive the uncertainty in the average value.

Table 12: Measured Divided by the Predicted Fluxes

Star	A	B ₁	B ₂	C	D	E
α Boo	1.0015	1.0057	0.9907	0.9908	0.9907	0.9838
α Tau	0.9795	1.0294	1.0060	0.9903	0.9942	0.9962
α Lyr	0.9893	1.0164	0.9954	1.0479	1.0378	1.172
β Gem	0.9800	0.9786	0.9487	0.9907	0.9909	1.088
γ Dra	0.9812	1.0398	1.0069	0.9931	0.9772	1.0245
γ Cru	0.9738	1.012	1.001	0.9987	0.9976	1.005
α CMa	1 by def	1	1	1	1	1
Ave.*	0.986	1.014	0.990	0.9912	988	1.023
σ/\sqrt{N}	$\pm 0.008/2.24$ ± 0.004	$\pm 0.021/2.24$ ± 0.009	$\pm 0.021/2.24$ ± 0.010	$\pm 0.001/2.0$ ± 0.0005	$\pm 0.007/2.0$ ± 0.003	$\pm 0.04/2.0$ ± 0.020

* Averages exclude α CMa and γ Cru values; α Lyr is excluded from Band C, D & E averages.

The γ Cru values were not included because the Cohen et al. values were not independent of the MSX measurements. Cohen (private communication) renormalized the γ Cru spectrum in Paper VI with MSX photometry from the CB06 analysis in Paper XII. Also, no response corrections were applied to the γ Cru photometry in Paper VI, which not only affects the overall scaling but also the dispersion in the measurements, as shown in Figure 16. We adopted the best fitting of the two γ Cru spectra Cohen (private communication) provided to us. However, since γ Cru is the brightest of the calibration stars we do include it in the qualitative comparisons.

The biases for each star derived are plotted in Figure 26. The percent biases that are plotted are obtained by subtracting one from the flux ratios in Table 12 and multiplying the result by 100. The solid error bars are the appropriate values from Table 8; the dotted error bars are those assigned by Cohen for the MSX in-band uncertainty in the predicted absolute spectral irradiances for the stars. The dashed line is the percent deviation of the MSX Band C and D averaged fluxes from the Cohen et al. predictions. Band C and D fluxes should be measures of the continuum for these stars and they have the smallest uncertainties in Table 8. Since the biases are generally within the errors that Cohen et al. assign to their absolute spectra, it may be said that the MSX observations validate the Cohen et al. calibration spectra relative to α CMa.

As may be seen from Table 12, the average in the ratio of measured and predicted fluxes for the MSX calibration stars is ~ 1 percent low, a 3σ result. The Band A ratio for α Lyr is also about 1 percent low. Since the infrared flux of α CMa in Paper I is derived from α Lyr, the average ratio for all the stars and that for α Lyr in Band A can all be brought into agreement by simply increasing the flux for Sirius by 1 percent, which is within the 1.46 percent bias error assigned to the absolute scale of the Sirius spectrum in Paper I.

The MSX $[X] - [D]$ magnitude differences for the stars are plotted as a function of spectral type in Figure 27. In this plot, K0 is designated as 0 on the spectral type scale, K5 as 5, M0 as 6 and the latest spectral type, M3.4, is 9.4. Band D was chosen as the fiducial band because it is a measure of the continuum and it has high quality measurements on these stars. The MSX measurements are plotted as pluses with the measurement uncertainties and the predicted values are plotted as diamonds, the dashed lines are the least squares linear fits through the MSX values while the dotted lines are the magnitude differences predicted by the Engelke function using the effective temperatures given in Table 1. The systematic deviation of the measured $[A] - [D]$ and $[B_{1,2}] - [D]$ colors from the predicted continuum as a function of spectral type is due primarily to the molecular absorptions in the stellar atmosphere. In Band A, the SiO fundamental absorption band and the $6.3\ \mu\text{m}$ water vapor band are present in all the cooler stars. The difference in bias between B_1 and B_2 in Table 12 averages to 2.25 percent with an rms uncertainty in the mean of 0.8 percent. Band B_2 has a larger spectral bandpass and covers more of the CO absorption band in cool stars, which may qualitatively explain the difference. Cohen et al. assigned large ~ 10 percent uncertainties to these bands because accurate spectral observations were lacking due to the fact that the Earth's atmosphere is opaque at these wavelengths. The stellar CO absorption profile is at its steepest across these bands and the integrated flux is sensitive to spectral shifts. The MSX global mean fluxes are more tightly correlated in the B bands than the Cohen et al. predictions, which indicates the higher precision of the MSX means. Generally, the MSX and predicted values agree to within the measurement and Cohen et al. errors.



58

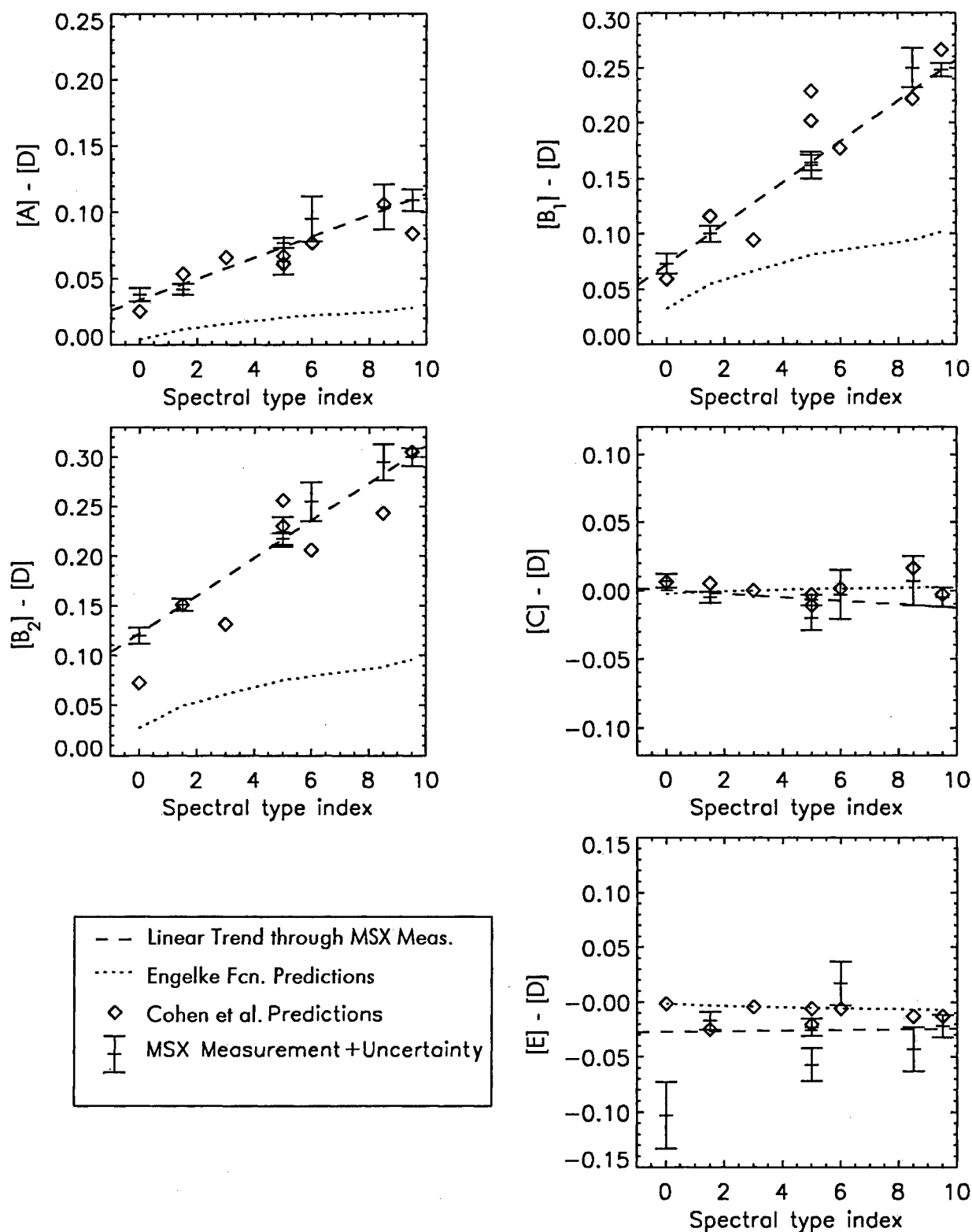


Figure 27: Correlation between MSX magnitude differences with respect to Band D and spectral type. Diamonds are the predicted values; pluses with error bars are MSX measurements. Dashed line is a linear fit through the MSX data, dotted lines are the continuum predictions of the Engelke function.

4.3.1 Variability

Variability is a critical issue as the brightness of standard calibration stars is usually taken to be constant. Of the standard stars measured by MSX, only β Peg was found to change in infrared brightness during the mission. Figure 28 plots the β Peg DCE mean irradiances as a function of time. A clear time dependent correlated variation of ~ 8 percent is evident across all MSX bands from the Figure. (The single mirror-fixed set of values in Figure 22 hints at a pre-minimum observation whose flux is anti-correlated.)

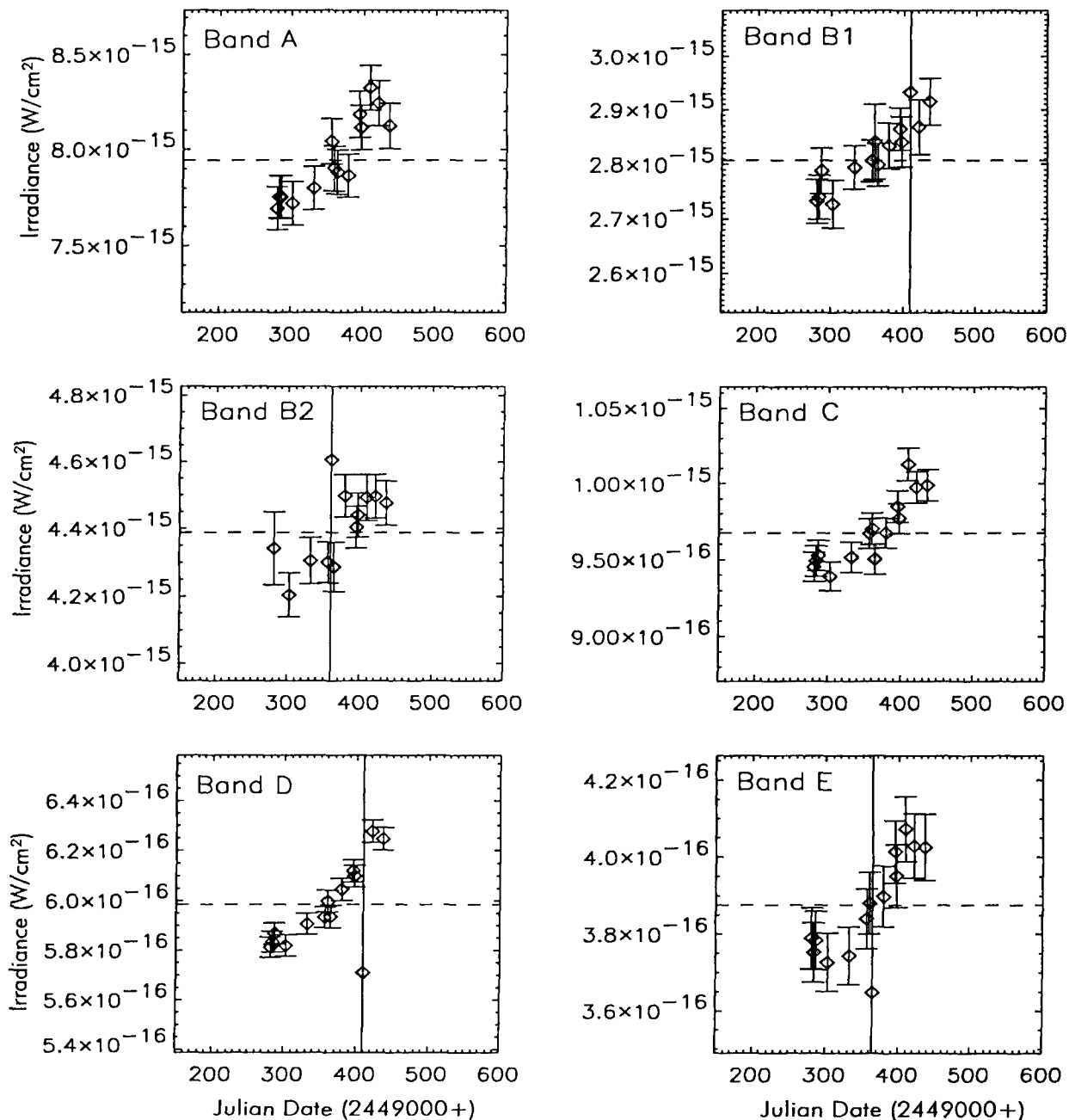


Figure 28: Time variation of the β Peg DCE mean in-band irradiances. The Julian date of observation is the time axis.

Beta Peg is listed as an optical variable in the SIMBAD database. Smith (2003) and Smith, Price and Baker (2004) extracted DIRBE/COBE near- to mid-infrared photometry of the brightest 12 μm sources out of the Galactic plane, including that for β Peg. Figure 29 is a plot of her DIRBE β Peg photometry, which shows a 3 percent flux variation during the 10 month COBE mission, a period comparable to the cryogenic lifetime of SPIRIT III. Smith, Price and Baker (2004) determined amplitudes of 2 – 4 percent in the formal solution for the variability for this star and found that this was statistically significant as all four near-infrared DIRBE bands varied at the 2σ level; analysis of the mid-infrared DIRBE measurements is not conclusive for variability being at the 1σ level. Cohen (private communication) noted that N band photometry by John Africano at the Air Force Maui Optical Site did show an episodic 0.1 magnitude brightening for β Peg during the 1990s.

Smith (2003) also extracted DIRBE infrared photometry for the other stars in Table 3 and found no statistically significant variations in the DIRBE photometry during the COBE mission. This finding is especially important for γ Cru, which is of a later spectral type than β Peg; Smith's formal solution for the variability of γ Cru is smaller than the standard deviation of the solution.

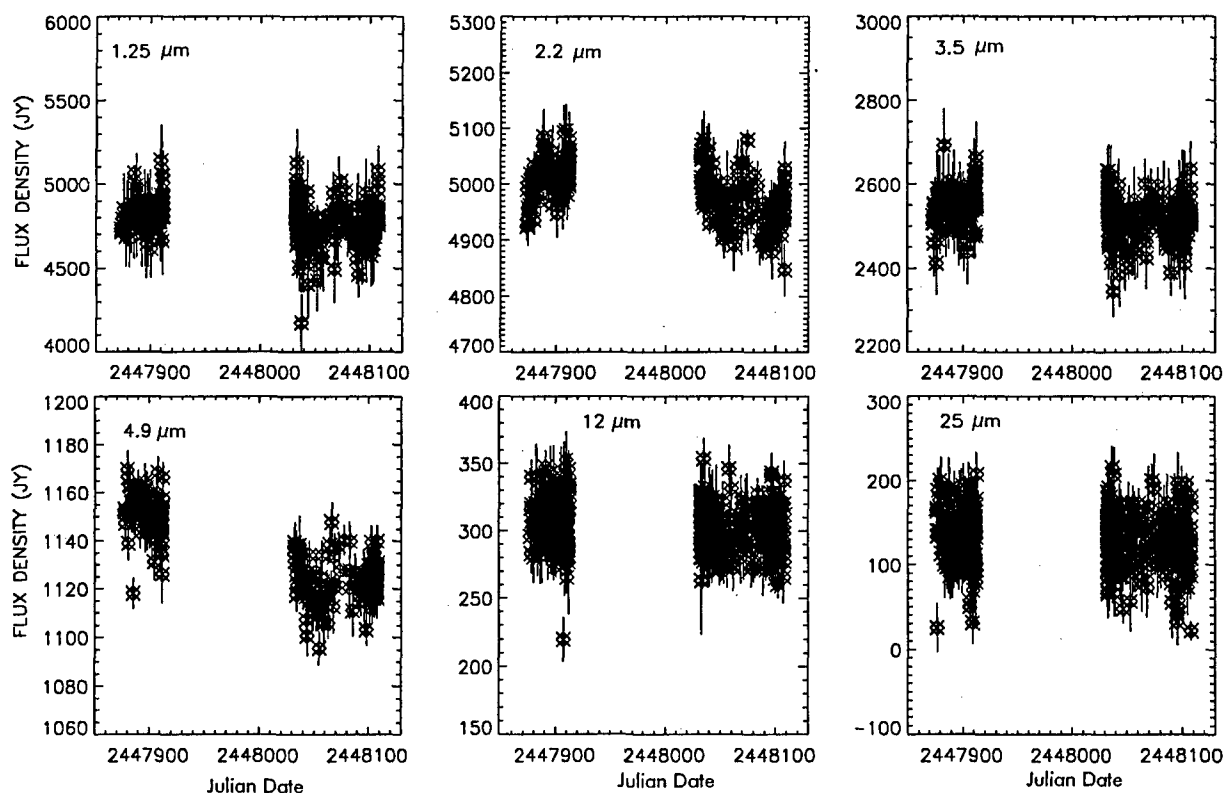


Figure 29: COBE/DIRBE 1.25 – 25 μm photometry of β Peg plotted as a function of Julian day over 10 months in 1993. Wavelength increases from 1.25 μm in the upper left to 25 μm in the lower right.

4.3.2 Flux Excess

The Bands C and D fluxes measured for α Lyr deviate at the $6 - 7 \sigma$ level from those predicted by Cohen et al. The Band C excess may be influenced by an uncompensated flux bias overestimate as all the mirror-scan observations above a focal plane temperatures of 11.6K in this band failed the 0.90 times the number of measurement opportunities test. However, Band D measurements had no such problems. The only valid Band E measurements were from the CB06 observations. Plausibly, excess emission from Vega's debris ring may contribute to the continuum flux at these shorter wavelengths. Heinrichsen, Walker and Klaas (1998) combined ISOPHOT 25 to 200 μ m photometry on Vega with IRAS and submillimeter observations to model the flux excess from the dust ring as a 73K blackbody modified by a $\lambda^{-1.1}$ emissivity. They measured a 25 μ m flux excess that was ~ 50 percent greater the Kurucz model continuum adopted for Vega in Paper I. The 17 percent Band E measured excess in Table 12 is entirely consistent with this model. The Heinrichsen et al. model predicts a Band D flux excess from the dust ring of only 1 – 2 percent compared to the observed excess of 4 percent. However, the 4 percent excess in this band is consistent with the 100K blackbody fit through the Heinrichsen et al. data in their Figure 2. Liu et al. (2004) could detect no mid-infrared (8 – 13.5 μ m) emission from a circumstellar ring above 2 percent of that from the star. However, this finding is compatible with the Band C and D measurements. The shorter wavelength MSX measurements on α Lyr are entirely consistent with the spectral irradiances in Paper I.

Kiss and Ábrahám (2001) tentatively proposed a mid- to far-infrared excess for Sirius based on photometer measurements in the ISO archives. The MSX observations do not show any excess from Sirius out to 21 μ m.

4.4 Assessment of the Calibration Network Stars with Spectral Templates

A principal objective of the CB06 experiment was to validate the use of template spectra for the tertiary standard stars in the network described in Section 2.3. Cohen et al. (2001) measured 33 stars with template spectra in the calibration network (Cohen et al., 1999) on the CB06 experiment, which was a statistically significant sampling of 7.5 percent of the stars in the Version 2 network.

Cohen et al. (2001) apparently used only the β Gem (K0), α Boo (K1.5), α Hya (K3), α Tau (K5) and β And (M0) composites in their comparison. Therefore, we matched the stars with spectral templates observed on the CB06 experiment that were closest to the spectral composite. Table 13 compares the scale factors that we derive between the secondary standard and the template star listed in the fourth column with values from Papers X (second column) and XII (third column). The uncertainties in the least significant figures are in parentheses and are typically dominated by good quality photometry in one MSX band, usually Band A. Thus, the global fit of the template is likely not to be to the same accuracy as the fit in the one band. The last column is the limb-darkened angular diameter derived for the star given the measured flux and an Engelke function with the temperature given in the header row. The derived angular diameters depend on the assumed effective temperatures. Engelke (1992) used a linear empirical relation between T_{eff} and spectral type that is different from the one which Cohen et al. derived using the Infrared Flux Method of Blackwell and colleagues (see, for example, Blackwell et al., 1990).

Table 13: Results for Stars with Spectral Templates

K5 stars: Factors that scale the α Tau composite (T= 3898K)				
Star	Network Scale Factor (Paper X)	CB06 Scale Factor (Paper XII)	Present CB06 Scale Factor	Engelke Fcn – θ
SAO 195639	$8.54(18) \times 10^{-3}$	$7.92(25) \times 10^{-3}$	$8.39(18) \times 10^{-3}$	1.95 mas
31 Ori	$3.06(8) \times 10^{-2}$	$3.19(3) \times 10^{-2}$	$3.01(4) \times 10^{-2}$	3.70 mas
SAO 248381	$1.03(6) \times 10^{-2}$	$9.72(14) \times 10^{-3}$	$9.99(14) \times 10^{-3}$	2.13 mas
G8 and K0 star: Factors that scale the β Gem composite (T= 4866K)				
δ Lep (G8)	$1.08(2) \times 10^{-1}$	$1.05(1) \times 10^{-1}$	$1.08(1) \times 10^{-1}$	2.65 mas
γ^2 Vol (K0)	$9.73(42) \times 10^{-2}$	$9.74(17) \times 10^{-2}$	$9.75(13) \times 10^{-2}$	2.52 mas
K1, K1.5 and K2 stars: Factors that scale the α Boo composite (T= 4362K)				
β Vol (K1)	$1.98(9) \times 10^{-2}$	$1.94(2) \times 10^{-2}$	$1.98(3) \times 10^{-2}$	2.97 mas
γ Pic (K1)	$9.31(44) \times 10^{-3}$	$9.35(9) \times 10^{-3}$	$9.15(13) \times 10^{-3}$	2.02 mas
42 Dra (K1.5)	$9.54(20) \times 10^{-3}$	$9.75(10) \times 10^{-3}$	$9.94(15) \times 10^{-3}$	2.11 mas
56 Ori (K1.5)	$1.41(4) \times 10^{-2}$	$1.31(3) \times 10^{-2}$	$1.29(2) \times 10^{-2}$	2.40 mas
π^6 Ori (K2)	$1.73(4) \times 10^{-2}$	$1.72(1) \times 10^{-2}$	$1.77(3) \times 10^{-2}$	2.81 mas
24 Com (K2)	$6.38(23) \times 10^{-3}$	$6.39(8) \times 10^{-3}$	$6.47(9) \times 10^{-3}$	1.70 mas
β Col (K2)	$3.70(4) \times 10^{-2}$	$3.70(4) \times 10^{-2}$	$3.65(7) \times 10^{-2}$	4.04 mas
α Ari (K2)	$1.11(1) \times 10^{-1}$	$1.12(1) \times 10^{-1}$	$1.15(1) \times 10^{-1}$	7.16 mas
K2.5 & K3: Factors that scale the α Hya composite (Band D magnitude = -1.358) (T= 4141)				
SAO 249451	$4.51(20) \times 10^{-2}$	$4.20(7) \times 10^{-2}$	$4.33(6) \times 10^{-2}$	1.93 mas
τ^2 Ari	$4.03(10) \times 10^{-2}$	$4.10(12) \times 10^{-2}$	$4.09(8) \times 10^{-2}$	1.87 mas
45 Eri	$5.43(17) \times 10^{-2}$	$5.82(11) \times 10^{-2}$	$5.57(8) \times 10^{-2}$	2.19 mas
SAO 783	$4.85(23) \times 10^{-2}$	$5.02(5) \times 10^{-2}$	$4.89(7) \times 10^{-2}$	2.05 mas
ι Aur	$6.42(17) \times 10^{-1}$	$6.49(7) \times 10^{-1}$	$6.47(10) \times 10^{-1}$	7.46 mas
SAO 250019	$4.56(23) \times 10^{-2}$	$4.49(6) \times 10^{-2}$	$4.46(7) \times 10^{-2}$	1.96 mas
SAO 223297	$5.69(7) \times 10^{-2}$	$5.80(6) \times 10^{-2}$	$5.80(9) \times 10^{-2}$	2.23 mas
6 Dra	$7.58(18) \times 10^{-2}$	$7.46(15) \times 10^{-2}$	$7.50(10) \times 10^{-2}$	2.54 mas
M0 stars: Factor that scales the β And Composite (T= 3839)				
IRC+50004	$3.68(11) \times 10^{-2}$	$3.79(4) \times 10^{-2}$	$3.82(6) \times 10^{-2}$	2.68 mas

Numbers in parentheses are the uncertainties in the least significant digits of the scale factor (see text)

Cohen et al. (2001) found between 0 and 8 percent differences between the measured and predicted in-band fluxes with an rms of 3 percent and an average bias of 2 percent. We repeated this analysis using PRF fitted photometry on 23 of the 33 stars measured on the CB06 experiment for which we could obtain reliable results from the individual scans. The measurements had essentially the same scatter (2.8 percent) but with a smaller range of deviations. However, our measured values agreed on the average with the predicted values (ratio

= 0.999). Note that only Band A fluxes had good quality measurements for most of the stars whereas Cohen et al. (2001) included measurements from other bands for many more stars.

4.5 Bright Stars

Some sensors require very bright infrared sources for calibration. While planets and asteroids may fulfill the requirement at longer wavelengths, stellar references such as α Ori are needed in the near- to mid-infrared. ISO Short Wavelength Spectrometer (SWS) spectra of some of the brightest stars in the infrared taken from Sloan et al. (2003) are plotted in Figure 30. As may be seen, γ Cru, which is the brightest star in Table 1, is one to two hundred times fainter in the mid-infrared than the other stars shown but is only about a factor of three fainter in the near-infrared. Most of the brightest infrared stars have time dependent fluxes that have to be either modeled or photometrically tracked in order for these sources be useful for infrared calibration to a reasonable level of accuracy.

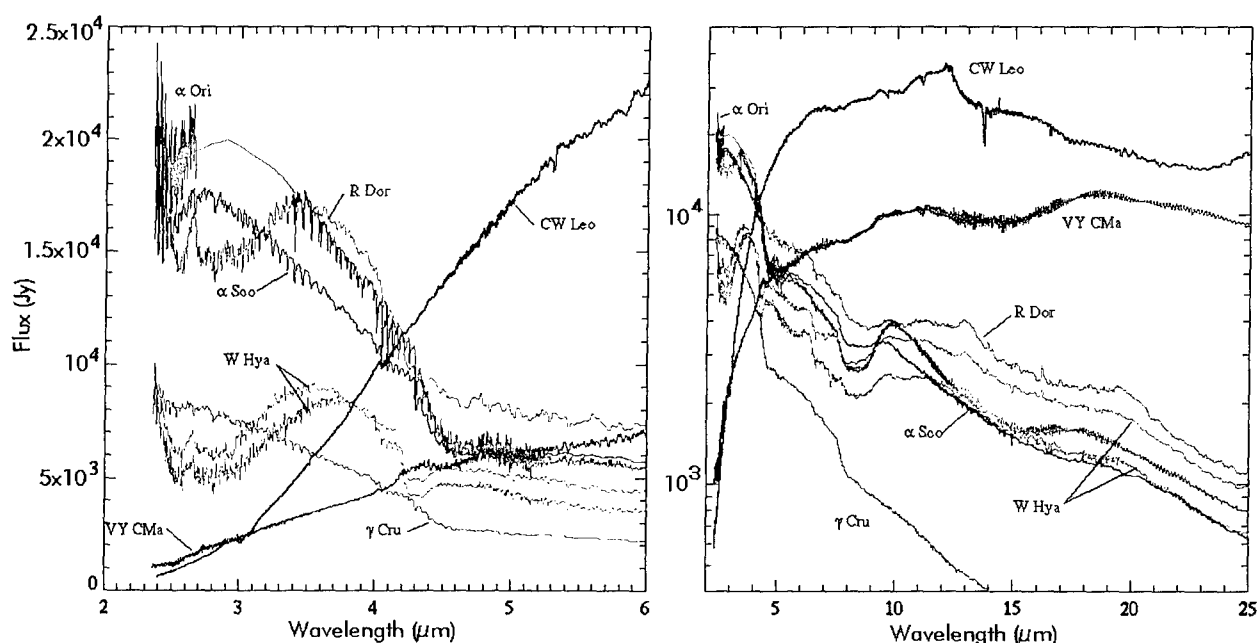


Figure 30: The brightest infrared stars. The two available SWS spectra of W Hya show that this star varies in brightness and that it does not do so uniformly with wavelength.

Walker et al. (2004) assembled a list of infrared sources brighter than zero magnitude between 2 and 12 μ m and assigned 2 – 35 μ m spectral templates to them to create an atlas of bright infrared stellar spectra (IR Bright Star Atlas – Atlas, hereafter). Approximately 1900 objects were initially selected based their having a mid-infrared magnitude > 0 as listed in the IRAS, MSX (Egan et al., 1999, 2003) and Two Micron Sky Survey (TMSS – Neugebauer and Leighton, 1969) catalogs. The number was reduced to 1835 stars in Version 2 of the Atlas by requiring that a source have a good quality spectrum or spectral template that fit the available photometry. The Atlas contains the 16 stars in Table 1 as well as 64 of the stars in the calibration network with spectral templates. Also, Walker et al. (2004) recommend a ‘preferred list’ of an additional 45 bright stars for use as calibrators. These stars exhibited little or no

infrared variability in their literature search. Their spectra are derived from templates but the photometry used to scale the spectra is not as precise as for the stars in the calibration network.

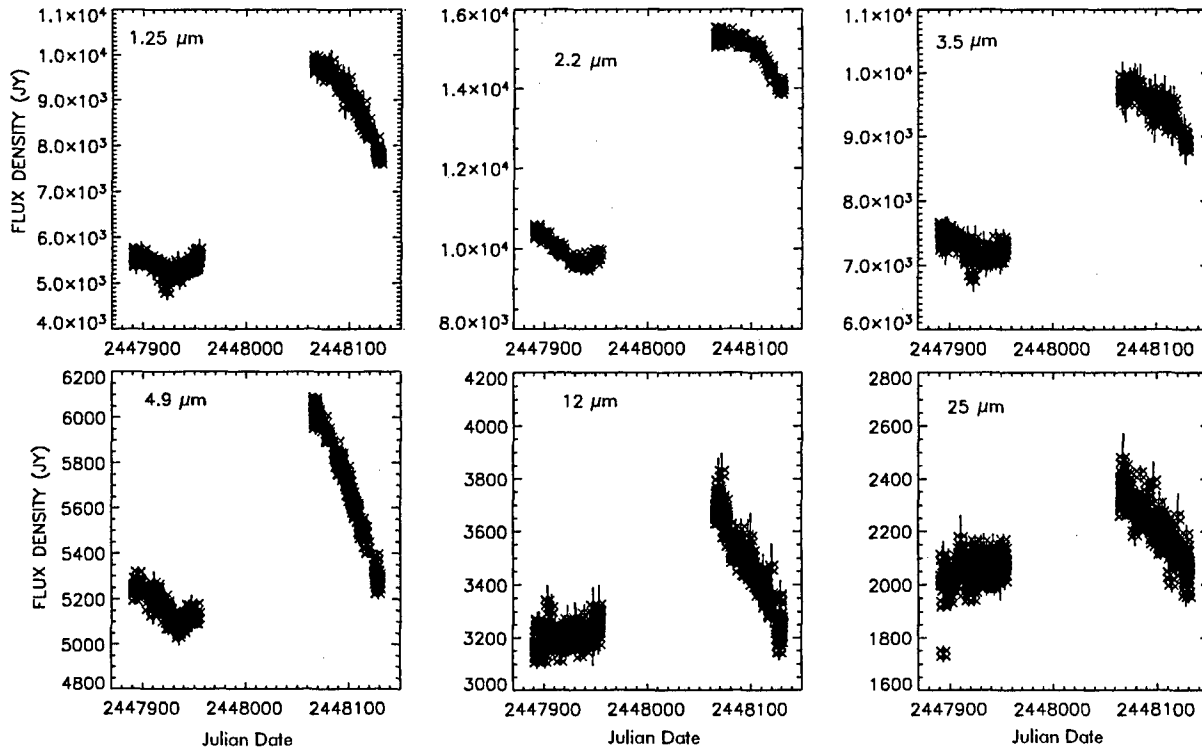


Figure 31: Infrared variability of W Hya during the 10 month COBE DIRBE mission (Smith, private communication). 1.23, 2.2, 3.5, 4.9, 12, and 25 μm fluxes are shown left to right, top to bottom, plotted against the Julian date. The amplitude and phase depend on the wavelength.

Almost all of the remaining 1711 Atlas sources are variable and most of these are Asymptotic Giant Branch stars. Figure 31 shows the 10 month light curve of the moderate amplitude variable W Hya. Version 2 of the Atlas includes the known infrared variability in the error terms. Although the variability is the dominant uncertainty in the absolute flux of an Atlas source, Price and Walker (1976) and Price (1978) have shown that averaging the system response derived from many well-measured variable stars can produce a good calibration.

The MSX mirror-scan calibration experiments also obtained two to eight observations of the infrared bright stars listed in Table 14. Among the stars in the table are α Her, α Ori and α Sco, which have been used as calibration standards or calibration transfers in the early days of infrared astronomy (Aumann, Gillespie and Low, 1969; Becklin et al, 1973; Blackwell et al., 1983, for example). The IRAS processing team used CW Leo (also known as TMSS +10216) to measure the response of the detectors at very low gains.

Table 14: Bright IR Stars Measured on the DC Calibration Experiments

Star	Band A	Band B ₁	Band B ₂	Band C	Band D	Band E	No. Obs
α Her	2.852×10^{-14} $\pm 6.4\%$	9.18×10^{-15} $\pm 1.1\%$	1.392×10^{-15} $\pm 1.2\%$	3.964×10^{-15} $\pm 0.7\%$	2.475×10^{-15} $\pm 0.9\%$	1.806×10^{-15} $\pm 1.7\%$	4
α Ori	7.567×10^{-14} $\pm 0.7\%$	1.886×10^{-14} $\pm 1.0\%$	2.817×10^{-14} $\pm 1.1\%$	1.408×10^{-14} $\pm 0.7\%$	8.332×10^{-15} $\pm 0.5\%$	7.896×10^{-15} $\pm 1.2\%$	3
α Sco	5.087×10^{-14} $\pm 0.9\%$	1.404×10^{-14} $\pm 1.0\%$	2.134×10^{-14} $\pm 1.1\%$	7.097×10^{-15} $\pm 0.7\%$	4.275×10^{-15} $\pm 0.5\%$	3.345×10^{-15} $\pm 1.0\%$	4
μ Cep	1.834×10^{-14} $\pm 0.5\%$	2.592×10^{-15} $\pm 0.9\%$	3.950×10^{-15} $\pm 0.8\%$	4.267×10^{-15} $\pm 0.5\%$	2.556×10^{-15} $\pm 0.4\%$	3.267×10^{-15} $\pm 0.9\%$	8
α Cet	2.868×10^{-14} $\pm 3.0\%$	5.134×10^{-15} $\pm 1.7\%$	8.038×10^{-15} $\pm 5.2\%$	5.953×10^{-15} $\pm 5.1\%$	3.846×10^{-15} $\pm 2.6\%$	4.772×10^{-15} $\pm 4.6\%$	2
NML Cyg	5.572×10^{-14} $\pm 1.7\%$	3.014×10^{-15} $\pm 2.1\%$	5.187×10^{-15} $\pm 2.1\%$	1.852×10^{-14} $\pm 0.8\%$	1.529×10^{-14} $\pm 1.2\%$	1.953×10^{-14} $\pm 1.5\%$	2
IK Tau	2.126×10^{-14} $\pm 1.4\%$	----	2.109×10^{-15} $\pm 2.1\%$	6.462×10^{-15} $\pm 2.3\%$	4.425×10^{-15} $\pm 0.9\%$	6.206×10^{-15} $\pm 1.2\%$	2
CW Leo	1.933×10^{-13} $\pm 0.9\%$	6.829×10^{-15} $\pm 1.6\%$	1.254×10^{-14} $\pm 5.2\%$	8.141×10^{-14} $\pm 0.9\%$	5.320×10^{-14} $\pm 1.0\%$	5.172×10^{-14} $\pm 1.2\%$	2

While the formal precision cited in Table 14 is rather high for some of the stars, it is emphasized that all the stars in the Table are variable. The two MSX NML Cyg observations differed by 10 percent as did the measurements of Mira (α Cet). Mu Cep was the only star observed a sufficient number of times to show a clear variability trend when plotted as a function of time as shown in Figure 32. MSX observed the infrared flux from this star to vary by ~ 7 percent during the mission with the near-infrared B Bands changing in the opposite sense as the mid-infrared bands. CW Leo and IK Tau were fainter by 2.5 and 2 times, respectively, than the mean fluxes listed by Walker et al. (2004). Smith (2003) found that all the stars in Table 14 were measured to be variable with a high degree of confidence. Thus, none of the stars are suitable as standards unless a simultaneous measurement tied to a primary or secondary standard is made. MSX does provide precise measurements for the epoch at which they were obtained.

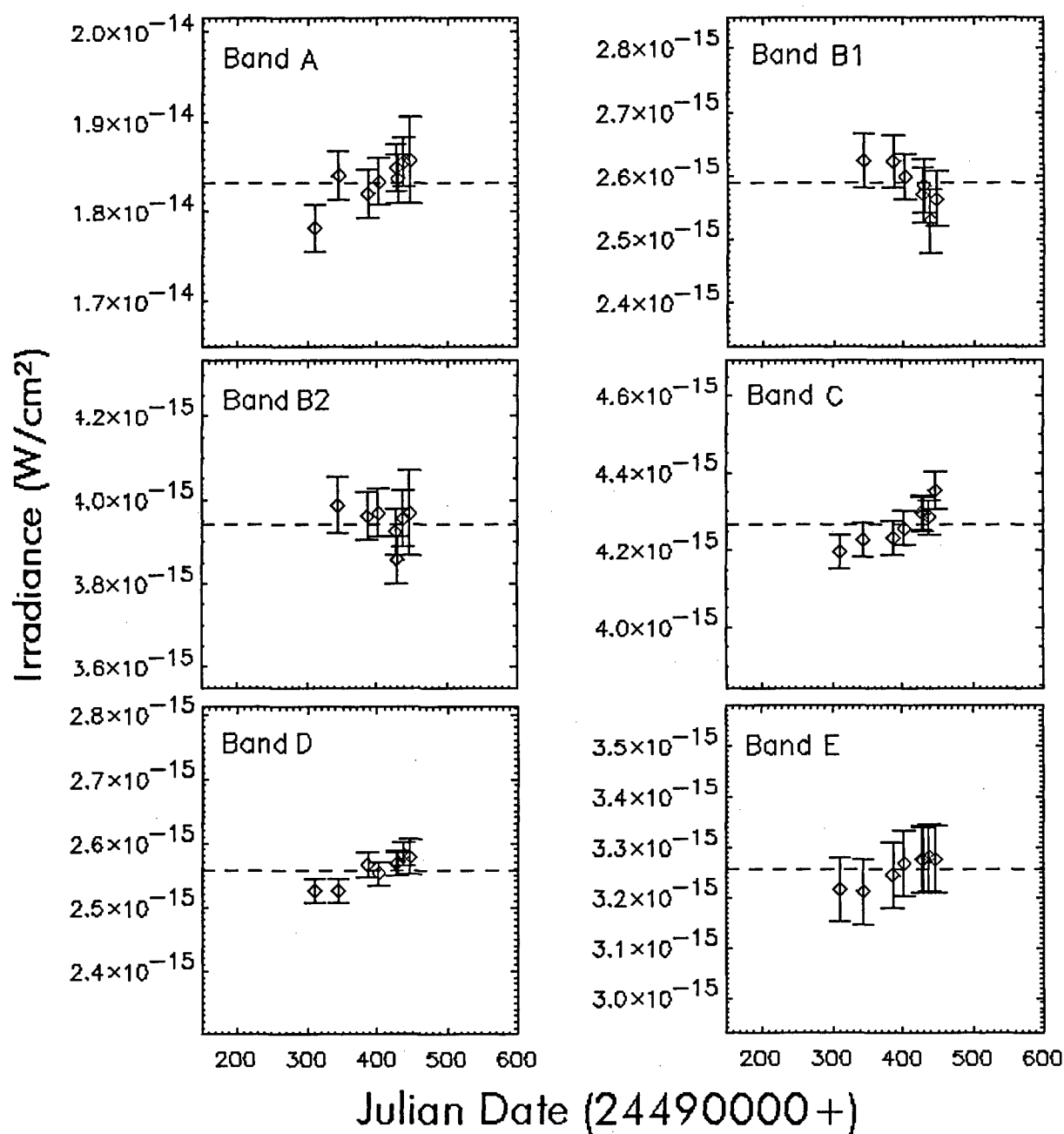


Figure 32: MSX photometry in W cm^{-2} of μ Cep as a function of Julian date (minus 2449000).

5 Reference Spheres

The infrared flux from an emissive reference sphere is determined by the physical properties of the sphere, the range with respect to the MSX spacecraft and the thermal balance between incident radiant energy absorbed by the sphere and the energy radiated away. The governing equation for the thermal balance that expresses the temperature of the sphere, T , as a function of time, t , is:

$$V\rho C_p(T) \frac{dT}{dt} = Area \left[(1-A)F_{Sun} \left(\frac{1}{4} + af_{Earth} \right) + \epsilon_{sphere} \epsilon_{Earth} F_{Earth} - \epsilon_{sphere} \sigma T^4 \right] \quad (7)$$

- V and $Area$ are the volume and area of the sphere, respectively
- ρ is the density of aluminum = 2.7 g cm^{-3}
- C_p is the specific heat of the sphere, which is calculated from Debye theory
- F_{Sun} is the solar flux per unit area at the distance of the sphere from the Sun
- A is the Bond albedo of the sphere
- af_{Earth} is the solar flux reflected from the Sunlit Earth
- $\epsilon_{Earth} F_{Earth}$ is the upwelling Earth radiation incident on the sphere
- ϵ_{sphere} is the average infrared emissivity of the sphere
- σ is the Boltzman constant

Equation (7) may be rewritten in terms of the equilibrium temperature, T_{eq} , which would be the instantaneous temperature of the sphere if it had no thermal mass:

$$\frac{V\rho C_p(T)}{\sigma Area \epsilon_{sphere}} \frac{dT}{dt} = \left[\frac{(1-A)}{\sigma \epsilon_{sphere}} F_{Sun} \left(\frac{1}{4} + af_{Earth} \right) + \frac{\epsilon_{Earth}}{\sigma} F_{Earth} - T^4 \right] = T_{eq}^4 - T^4. \quad (8)$$

Equation (8) has an analytical solution (Kintner and Sohn, 1993a, for example) if the thermal mass and equilibrium temperature are taken as constant, a reasonable first order assumption:

$$\ln \left[\frac{T_{eq} + T}{T_{eq} - T} \right] + 2 \tan^{-1} \left(\frac{T}{T_{eq}} \right) - \ln \left[\frac{T_{eq} + T_0}{T_{eq} - T_0} \right] - 2 \tan^{-1} \left(\frac{T_0}{T_{eq}} \right) + c = \frac{t}{\tau}. \quad (9)$$

The boundary condition is that the sphere temperature at the time of ejection, T_0 , has to equal the measured value. The initial temperatures, T_0 , range from a high of 259.5K for sphere 1 to 258.3K for sphere 5; c is a constant of integration. The characteristic thermal time constant, τ in Equation (9), is given by:

$$\tau = \frac{V\rho C_p(\bar{T})}{4\sigma Area \epsilon_{sphere} T_{eq}^3} \sim 1850 \text{ sec}. \quad (10)$$

A Runge-Kutta integration is used to solve Equation (8) in 50-second time steps. Compared to the time constant, the 50-second time intervals are quite adequate; MSX observed the sphere

approximately eight times within the 50-second time increment. The result at the time of an observation is interpolated between bracketing solutions.

Kintner and Sohn (1993b) solved Equation (8) using nominal or idealized parameters to explore the characteristics of the solution, especially the sensitivity of the solution to uncertainties in the input parameters. Chalupa, Cobb and Murdock (1991a, b) described a similar graybody thermal analysis of a sphere deployed from another satellite. This experiment was not flown but the present analysis is based, in part, on the model formalism developed by these authors. Kintner and Sohn (1993a), Chalupa, Cobb and Murdock (1991a), and Chalupa and Hamilton (1993) provide a more complete and detailed exploration of the sensitivity of the model to uncertainties in the input parameters. Kintner and Sohn (1993a) also provide an approximation for the trajectory of the sphere.

5.1 Physical Characteristics of the Emissive Reference Spheres

The reference spheres are made of 6061-T6 aluminum and were specified to be 1 cm in radius with a ± 0.01 cm tolerance. The density of the sphere was that of aluminum, 2.7 g cm^{-3} . The temperature dependent specific heat was calculated using Debye theory (Kittel, 1985, for example), that is $C_p = \gamma T + A(T)T^3$ where γ and $A(T)$ reproduce the thermal capacities of aluminum at the various temperatures listed in the Handbook of Chemistry and Physics (1958). Marquardt, Le and Rodebaugh (2000), from NIST, fitted the published values of specific heat of 6061-T6 aluminum between 4 and 300K with an eighth order polynomial in the logarithm of the temperature with a cited error of 5 percent. The NIST values are ~ 4.4 percent higher than the Debye calculations in the 260 – 300K range of interest. We split the difference and scaled the Debye values by 1.02, adopting an uncertainty of 2 percent. This uncertainty is larger than the < 1.5 percent deviation over the temperature range observed for the spheres from the mean C_p of 890 J/kg-K at a median 270K temperature applicable to the ERS experiments.

The emissive reference spheres are coated with Martin Black. Wilson (1992) describes the ground-based measurements that characterized the thermal and emissive properties of the reference spheres. Directional spectral reflectivity measurements on witness samples of Martin Black were performed (Surface Optics Corporation Technical Report, 1993) and integrated emissivity measurements were carried out on a witness sample at the Low Background Infrared (LBIR) facility of the National Institute for Standards and Technology (NIST Report, 1993); <http://physics.nist.gov/TechAct.Archive/TechAct.93/844h.html> Figure 7 shows the measurement configuration. The witness samples and test sphere were fabricated of the same aluminum as the spheres and coated with Martin Black at the same time as the spheres. These spectral reflectivity measurements are in substantial agreement with the published measurements of Pompea et al. (1984) taken at lower spectral resolution. Martin Black has a very low reflectivity throughout the visible region of the spectrum, less than 1 percent, with comparable values in the mid-infrared between 6 μm and 40 μm . However, the reflectivity is significantly larger ($\times 10 - 20$) between 1 and 6 μm and at wavelengths longer than 50 μm . The reflectivity is also a strong function of scattering angle, increasing as the secant squared as the scattering angle is increased from 0° to 80° .

Kintner and Sohn (1993a) described how the sphere's mean infrared emissivity and the absorption efficiency with respect to solar flux for the spheres were calculated (Kintner presented the results at the 21 July 1993 MSX PI team meeting). The wavelength and angular

dependences of the reflectivity of Martin Black were weighted by the solar spectrum and the result integrated over wavelength and a hemisphere to derive the Bond albedo for the sphere and its complement, the absorptivity ($1 - \text{Bond albedo}$). Kintner, in his 1993 presentation, derived a Bond albedo of $A = 0.069$ and the corresponding absorptivity of 0.931 , which we adopt. A similar calculation was done to derive the mean infrared thermal emissivity using a 300K blackbody spectral weighting function to represent the thermal emission from the Earth and sphere. Kintner presented a value of 0.97 in his July 1993 briefing. On the other hand, NIST measured the mean infrared emissivity of the Martin Black coated witness sample integrated over all angles and wavelengths to be 0.954 . We average the two results and adopt a value of $\epsilon_{\text{sphere}} = 0.962$.

Using a mean infrared emissivity in the energy balance equation accounts for the spectral properties of the sphere outside the $6.0 - 26.5 \mu\text{m}$ wavelength range of the MSX bands. However, the wavelength dependence must be included in calculating the irradiances from the sphere in the MSX spectral bands. The reflectivity and emissivity of Martin Black integrated over a hemisphere are shown in Figure 33 as a function of wavelength. The \times 's are the results of the numerical integration of the Surface Optics Corporation (SOC) measurements taken every micrometer as a function of angle. The angular dependence of the SOC reflection measurements is well represented by a secant squared function out to a reflection angle of 80° . This is consistent with the bi-directional reflectance measurements that Bartell et al. (1982) obtained at $10.6 \mu\text{m}$. The solid line is an approximation that fits two linear functions in wavelength to the SOC measurements as a function of wavelength and integrates over the hemisphere using the secant squared angular dependence. The numerical integration was used in the modeling.

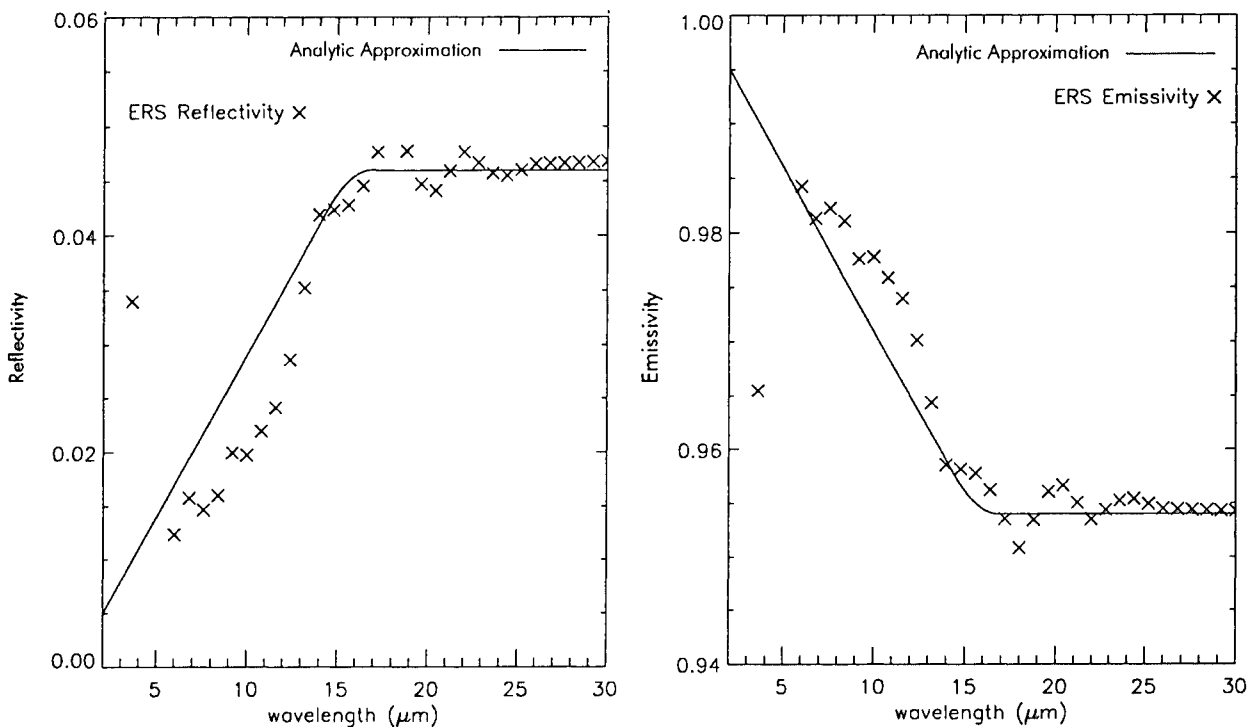


Figure 33: The infrared reflectivity (left) and emissivity (right) of the Martin Black coated sphere as a function of wavelength integrated over a hemisphere.

Since the solar flux gives low weights to the contributions from wavelength and incident angle regimes that are poorly determined for Martin Black, the uncertainty in the solar absorptivity is ~ 1 percent. The uncertainty in the infrared emissivity of the sphere is estimated to be the 1 percent difference between the mean value we adopt and the values obtained by Kintner and NIST. The quantity $V/Area$ in the coefficient of the thermal mass ($V\rho C_p$) divided by ($Area \sigma \epsilon_{sphere}$) on the left hand side of Equation (8) is proportional to the radius, which has an uncertainty of 1 percent. The specific heat has an uncertainty of about 2 – 2.5 percent and the estimated uncertainty in ϵ_{sphere} is about 1 percent. Thus, the root sum square of these uncertainties implies that the uncertainty in the knowledge of the coefficient is ~ 3 percent.

5.2 Thermal Input from the Sun

A solar constant of 1367.28 W m^{-2} is adopted based on the mean value derived by Schatten and Orosz (1990) and Tobiska (2002), for which they show a mean variation of <0.1 percent. The solar constant is scaled by the inverse square of the heliocentric distance of the sphere, in AU, at the time of the experiment. The factor of one-fourth in Equations (7) and (8) arises because the amount of solar radiation intercepted by the sphere is equal to its cross sectional area whereas the Equations are normalized to the surface area; in other words the Bond albedo of the sphere is the reflectivity divided by four.

The Sunlight reflected from the Earth has specular and diffuse components that are given by:

$$af_{Earth} = (0.2 + 0.65 \sin^6 \phi) \left(0.2 \frac{R_E^2 \cos \alpha}{(2d + R_E \cos \alpha)(2d \cos \alpha + R_E)} + 0.8 \sum_{daE} \frac{\cos \alpha \cos \beta}{d^2} \right) daE. \quad (11)$$

The first term on the right side of the equation is the latitude (ϕ) dependent albedo of the Earth. This expression is an approximation to the curve in Figure 1 of Appel (2003). This curve is based on data taken by various Earth resource satellites that may be found on the web, which indicate that the local values of the Earth's albedo are 0.2 – 0.25 in the tropics and increase slowly through the mid-latitudes, reaching values of 0.8 – 0.85 at the poles.

The second term is the geometric expression for the reflected sunlight. We assumed that 20 percent of the contribution is specular and 80 percent is diffuse. We adopted the Chalupa, Cobb and Murdock (1991b) analytic expression for the specular reflected component in the first term inside the parentheses, which they derived by assuming dispersion of incident parallel solar rays from a spherical Earth of radius R_E . To derive the diffuse component, the contributions are summed from the approximately 500 surface elements into which the portion of the Earth visible to the sphere is divided. In the summation, the distance from the sphere to the surface area element, daE , on the Earth is given by d , and α and β are the angles between the local vertical of the surface area element and the direction to the Sun and sphere, respectively. The summation is restricted to surface elements with $\alpha \leq 90^\circ$ as is the specular reflection angle.

The uncertainty in the direct solar flux absorbed by the sphere is essentially the uncertainty in absorptivity, which is ~ 1 percent. The estimated uncertainty in the reflected component is dominated by the imprecise knowledge of the Earth's geometric albedo. MSX and the sphere are in a dawn – dusk orbit and much less than half the Earth visible to the sphere is sunlit during the

experiments. Sunlight reflected by the Earth constitutes less than ~ 1 percent of the total thermal input to the sphere for ERS3 through ERS5. It is larger, ~ 10 percent, at the beginning of the ERS1 and ERS2 experiments but the contribution decreases to insignificant values by the middle of these experiments. Thus, sizable uncertainties in evaluating this component, even of the order of the 20 – 50 percent used by Kintner and Sohn (1993a, b) and Chalupa et al. (1991a, b, 1993) in their analyses, produce only small changes in the total thermal input to the sphere.

5.3 Upwelling Radiation from the Earth

The upwelling Earth radiation incident on the sphere is derived from the narrow band infrared measurements from the Advanced Very High Resolution Radiometer (AVHRR) on the polar orbiting NOAA/POES satellite. NOAA creates thermal maps of the Earth every three hours and the maps closest to the start time of each of the ERS experiments were used. The maximum time difference between a thermal map and an ERS measurement was two hours. The AVHRR $11.5\ \mu\text{m}$ map used for ERS1 is shown in Figure 34 on which the ground track of the sphere is overlain. Bright areas are cool and the darker areas are at warmer temperatures. The black strips near the poles are missing data, values for which are interpolated from surrounding measurements.

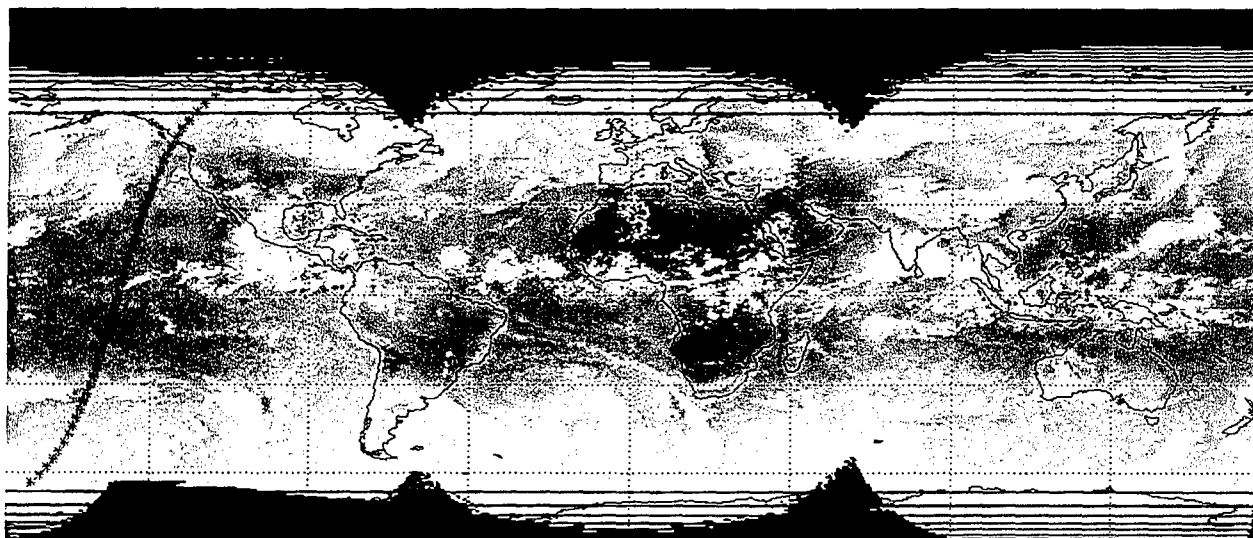


Figure 34: The ground track of the ERS1 is overlain on the AVHRR $11.5\ \mu\text{m}$ map used to calculate the upwelling thermal radiation from the Earth for this experiment. This is the 238^d hour 15 map for 25 August 1996; the experiment was executed between 1334 and 1413 hours on 25 August 1996.

The thermal radiation from the Earth is calculated every 50 seconds from the time the spheres were ejected to $t + 2450$ seconds. The latitude, longitude and altitude of the sphere are derived at each of these times from the orbit calculated for the sphere. These parameters are used to determine the circular sector of the Earth underneath the sphere. A polar coordinate system with the nadir of the sphere as the pole is adopted and the AVHRR $11.5\ \mu\text{m}$ map centered on the nadir latitude and longitude is projected into those coordinates. A 300×325 grid is

overlaid on the portion of the Earth visible from the sphere, the AVHRR data are binned onto this grid and "over the horizon" values are eliminated. The 11.5 μm AVHRR radiance within each grid element is weighted by the cosine of the angle between the vertical of the area element and the direction of the sphere multiplied by the area of the element and divided by the square of its distance. This is summed to derive the total 11.5 μm flux onto the sphere.

The integrated flux is converted into a blackbody brightness temperature. A blackbody spectral energy distribution is calculated using the brightness temperature multiplied by 1.05 and the result is adopted as the source function for the Earth. The upwelling radiation from this source function is modified by the atmospheric transmission calculated with the MODTRAN transmission code (Berk et al., 1989) to create a representative spectral energy distribution from the Earth at a single time index. Increasing the 11.5 μm brightness temperature by 1.05 compensates for the ~80 percent transmission that MODTRAN predicts for upwelling Earth radiation at 11.5 μm . Figure 35, from Hamilton, Howard and Murdock (1997), depicts the procedure. The derived spectrum is strongly influence by absorptions from atmospheric ozone, CO_2 and, to a lesser degree, water vapor.

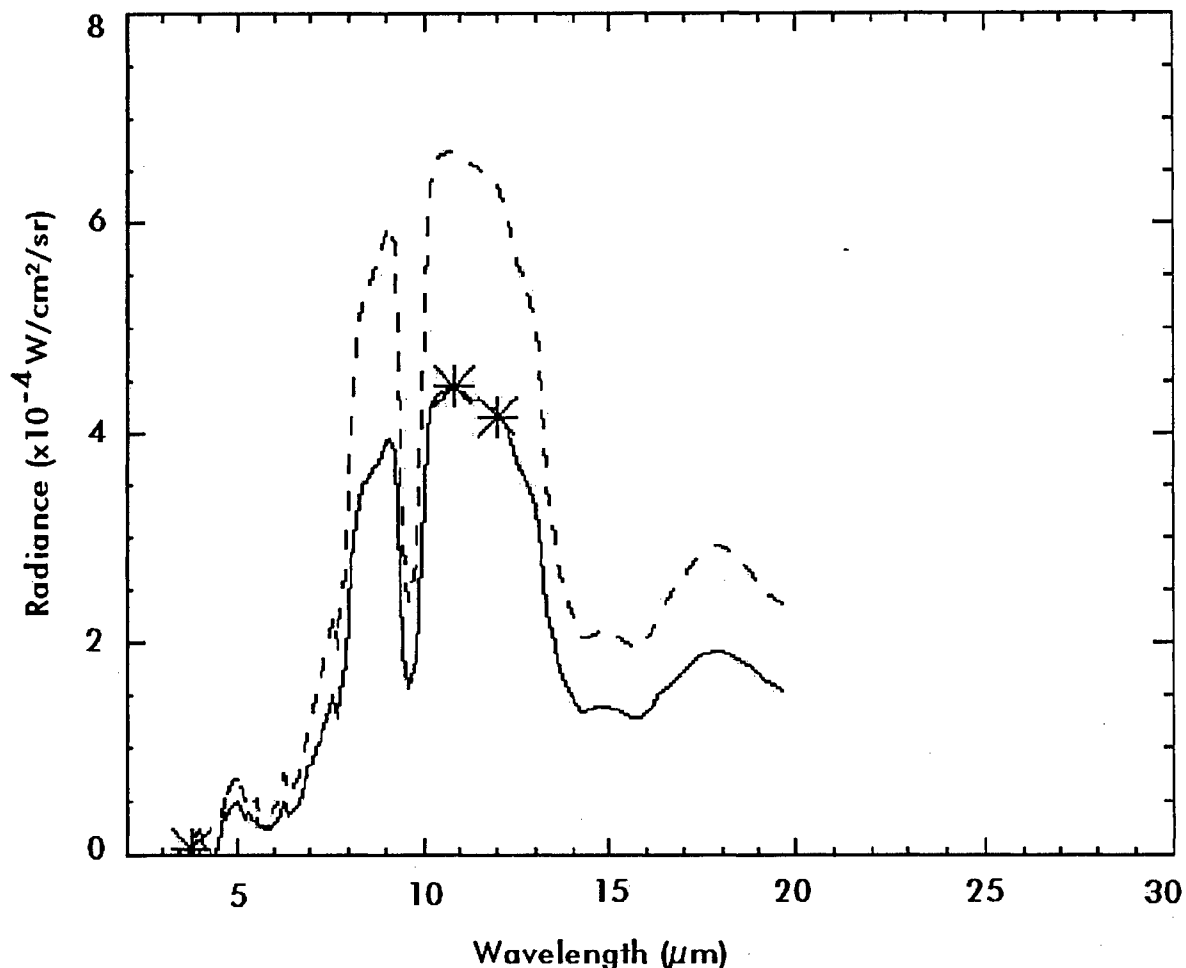


Figure 35: The spectral radiance from the Earth predicted by MODTRAN (dashed line) is scaled by narrow band measurements from AVHRR (asterisks) obtained near or during the ERS DCE to produce the upwelling spectral radiance from the Earth during the sphere measurements.

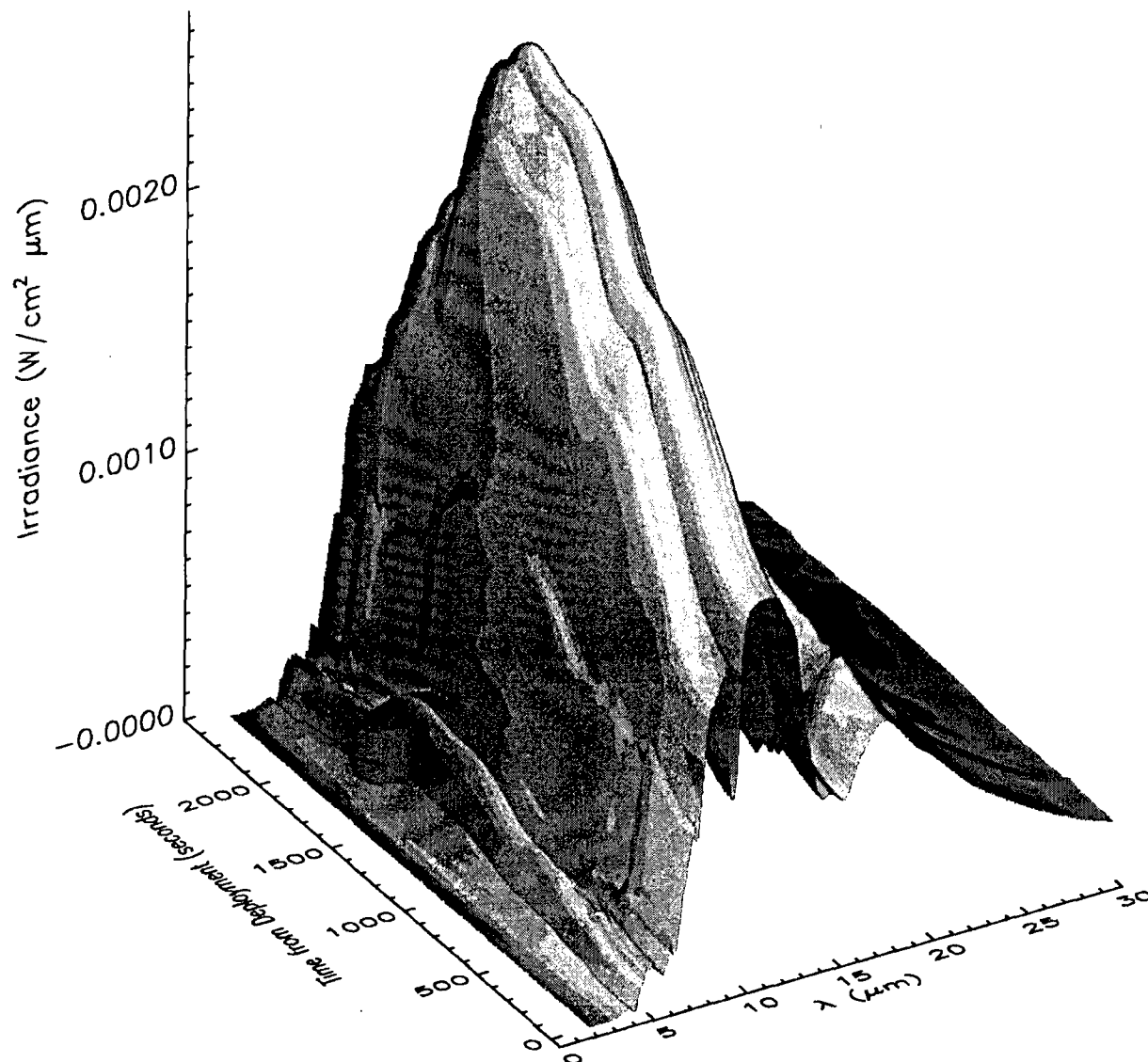


Figure 36: The time evolution of the predicted infrared spectral radiance from the Earth incident on ERS1. Wavelength (μm) is along the x-axis, time, in seconds, along the y-axis and radiance along the z-axis.

The time evolution of the spectrum of upwelling radiation during the DCE is shown in Figure 36. The spectrum at the time of observations is interpolated between the spectra from the bracketing 50-second steps. As may be seen, the thermal flux from the cold polar regions is about half that from the tropics. The subtle variations in the overall flux level in the plot show the influence of cool clouds in the AVHRR data.

The thermal input to ERS1 and ERS5 and the resulting temperature profiles calculated with the model are shown in Figure 37. The flux intercepted by the sphere from the various components is plotted on the left and the resulting temperature is plotted on the right with the ERS1 results shown in the top plots. This sphere is in eclipse from ~ 1550 to 2450 seconds, which causes the temperature of the sphere to drop in the absence of the thermal input from the Sun. The other four spheres remain Sunlit throughout the entire mission and the ERS5 profiles

are typical of these four experiments. The rather long time constant for the spheres to equilibrate, which is approximated by Equation (10), is a characteristic of the thermal profiles.

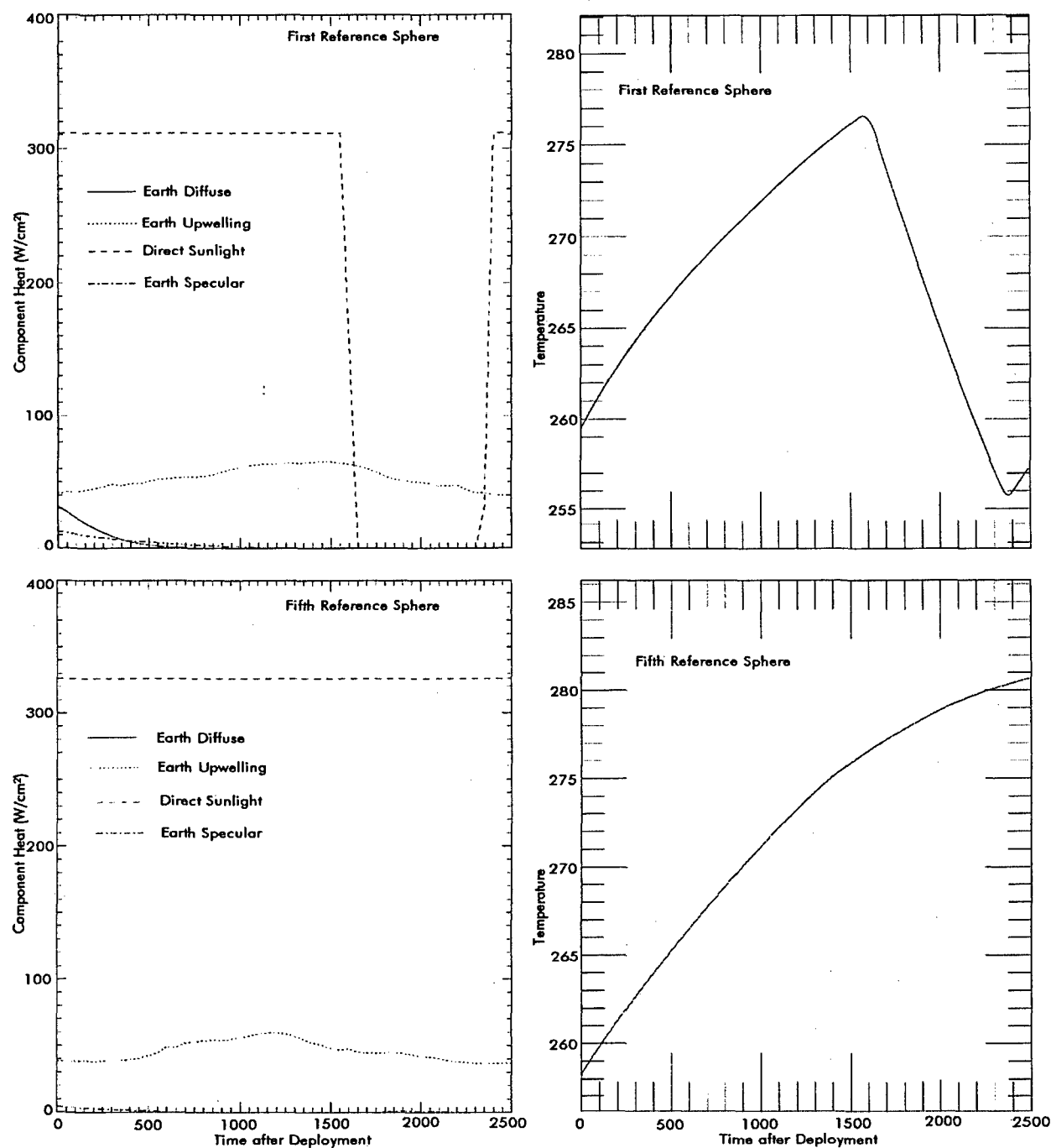


Figure 37: A comparison of the model results for ERS1 (top plots) and ERS5 (bottom plots). The thermal inputs are plotted as a function of time in the plots at the left and the resulting sphere temperatures are plotted on the right. The various thermal inputs are labeled in the left hand plots. Entry and exit from eclipse are apparent in the ERS1 plots.

The influence of the Earth's orbit on the model may be seen in these two figures. The direct solar flux intercepted by the ERS5 experiment, conducted on 22 February 1997, is somewhat higher than that for ERS1, which was executed on 25 August 1996, because the Earth was closer to the Sun during the ERS5 experiment. As previously noted, the profile of Sunlight reflected from the Earth for ERS1 is similar to that for ERS2, while the ERS5 profiles are representative of ERS3 and ERS4; in all cases the thermal input from this component is small or negligible.

Direct sunlight dominates over the other sources of the thermal input to the sphere with this component contributing over 80 percent of the total flux; only 15 – 17 percent comes from the Earth while the sphere is sunlit. According to the model, the total flux absorbed by the sphere varies by ~8 percent during the ERS2 – ERS5 experiments, which means that T_{eq} is constant to within 1 percent and Equation (9) is a very good first order solution to the thermal balance equation.

5.4 Measurement Geometry/Orbit of the Sphere

A spring loaded ejection mechanism deployed the spheres at a nominal velocity of 14.2 m/sec in the MSX orbital plane at an angle of 15° above the spacecraft velocity vector. The sphere was retained by a three-point capture system and a thermistor in one of the contacts of the capture system measured the temperature of the sphere up to the moment of release. Photodetectors with beams placed in tandem at the end of the ejection tube measured the ejection velocity to an accuracy of ±1 percent. The spheres were kept in an optically clean environment under dry nitrogen from the time they were fabricated until MSX was flown. The optically hygienic environment was maintained on the spacecraft until each sphere was ejected.

Ejection velocities between 14.03 and 14.86 m/sec were measured during the ground acceptance test for the six-ejector mechanism flown on MSX. (The gold-coated reflective sixth reference sphere failed to deploy.) The 14.525 m/sec average of these measurements had a 0.34 m/sec standard deviation. Ejection velocities were measured on-orbit for four of the five spheres; the ERS4 measurement failed. These velocities were consistently ~0.4 m/sec (±0.06 m/sec) less than their acceptance test values. Whatever caused the ejection velocities to change between the acceptance tests and the on-orbit experiments, the change was essentially the same for all the spheres. It may have been that the energy stored in the springs decreased by 5.5 percent due to environmental changes between the ground test and in-flight; the ejector mechanisms were 35K colder on the spacecraft than on the ground and operated in a vacuum. We infer that the relative ejection velocities of the spheres are known to better than 1 percent.

The MSX spacecraft was tracked with positional accuracy of <15 m during the reference sphere experiments (Abbot, Gaposchkin and von Braun, 1997). So, range errors were dominated by the uncertainties in the ejection velocity and deployment angles. The MSX satellite was programmed to center the sphere in the SPIRIT III mirror-scan field-of-regard, assuming that the spheres were ejected at 14.5 m/sec with azimuth and elevation angles of 0° and 15°, respectively. The MSX Space Based Visible sensor (SBV) was able to briefly track ERS3 but only could indicate that ERS3 was within 5 percent of its nominal trajectory; SBV did not track the other spheres because they were too faint.

ERS4 was measured to have an anomalous azimuthal deployment angle of about ~2°, as determined from the in-scan position of the spheres in the field-of-regard as a function of time.

Mavrofrides et al. (2002) have shown that such a small azimuthal error has very little effect on the range to the sphere but that an error in the elevation deployment angle has more significant consequences: a 10 percent error in the elevation angle produces a 1.2 percent deviation in range. According to Baca et al. (2002) only ERS2 was deployed at a sufficiently anomalous elevation angle to carry it out of the field of regard until $t + 1200$ seconds; the sphere was detected for the next 200 seconds. ERS2 re-entered the field of regard at $t + \sim 1650$ seconds and remained therein until the end of the DCE at $t + \sim 2000$ seconds. Unfortunately, the SPIRIT III angles-only measurements poorly constrain the ejection velocity and deployment angle uncertainties.

5.5 Estimated Uncertainty in the Model Predictions

The modeled MSX in-band irradiance is sensitive to the error in determining the sphere's temperature. It is directly proportional to the errors in the infrared emissivity and in the projected area of the sphere and is inversely proportional to the square of the range error. Chalupa, Cobb and Murdock (1991b), Chalupa and Hamilton (1993) and, independently, Kintner and Sohn (1993a, b) performed sensitivity analyses of the irradiance with respect to each of the thermal and geometric components of the model. They used analytic approximations for the various thermal inputs and physical parameters in Equations (7) and (8) and adopted rather conservative uncertainties for each component to demonstrate that the irradiances could be predicted to within the program goals of 10 percent absolute in-band irradiance accuracy, 3 percent band-to-band accuracy and 3 percent in precision. Since we use model parameters that are within the uncertainties of the values adopted in the sensitivity analyses, the absolute accuracy of our results should be at least as good as 10 percent.

However, the accuracy of our modeling is demonstrably better than 10 percent. The largest uncertainties in the sensitivity analyses were in the sunlight reflected by the Earth and the thermal flux from the Earth. In our model, the thermal radiation from the Earth is known to better than the ~ 10 percent accuracies adopted in the sensitivity analyses. Also, the uncertainties in the more poorly known reflected sunlight are mitigated by the fact that this component contributes very little to the thermal balance. Furthermore, from Figure 37 we see that > 80 percent of the thermal input onto the sphere outside of eclipse is direct sunlight. Thus, the uncertainty in T_{eq}^4 in Equation (8) is dominated by the estimated 1 percent uncertainties in the absorptivity of the sphere and in the mean infrared emissivity. Combining a generous estimate of a 5 percent uncertainty in flux from the Earth with the uncertainties in the other thermal inputs, the calculated equilibrium temperature of the sphere has an estimated uncertainty of about 1K, which is commensurate with the uncertainty in the initial temperature. The uncertainty in the coefficient on the left hand side of Equation (8) is about 2.5 percent as estimated from the root sum square of the 1 percent in the radius of the sphere, 1 percent in the emissivity and 2 percent in heat capacity. The uncertainty in this coefficient has a relatively small effect on the error analysis and we, therefore, estimate that the model calculates the temperature of the sphere to an accuracy of about 1K, which is less than half the ~ 2 K uncertainty is obtained by Kintner and Sohn (1993a, b). At 270K, a temperature error of 1K translates into a flux variation of 2.3 percent in Band A, 1.7 percent in Band C, 1.4 percent in Band D and 1.1 percent in Band E.

The geometric uncertainty is the root sum square of the estimated 2 percent uncertainty in the cross-sectional area of the sphere, the 1 percent in emissivity and 3 percent uncertainty in the square of the range. The relative ejection velocities are well known since their on-orbit

measured values differ from those measured during the ground-based testing by a constant amount to good accuracy, $\Delta v = 0.4 \pm 0.06$ m/sec. The uncertainty in the ejection velocity is estimated to be ~ 1.5 percent or half the difference between the ground and on-orbit measurements. The total uncertainty in the model predictions for the Band A irradiance from the thermal and geometric components is, therefore, approximately 4 percent.

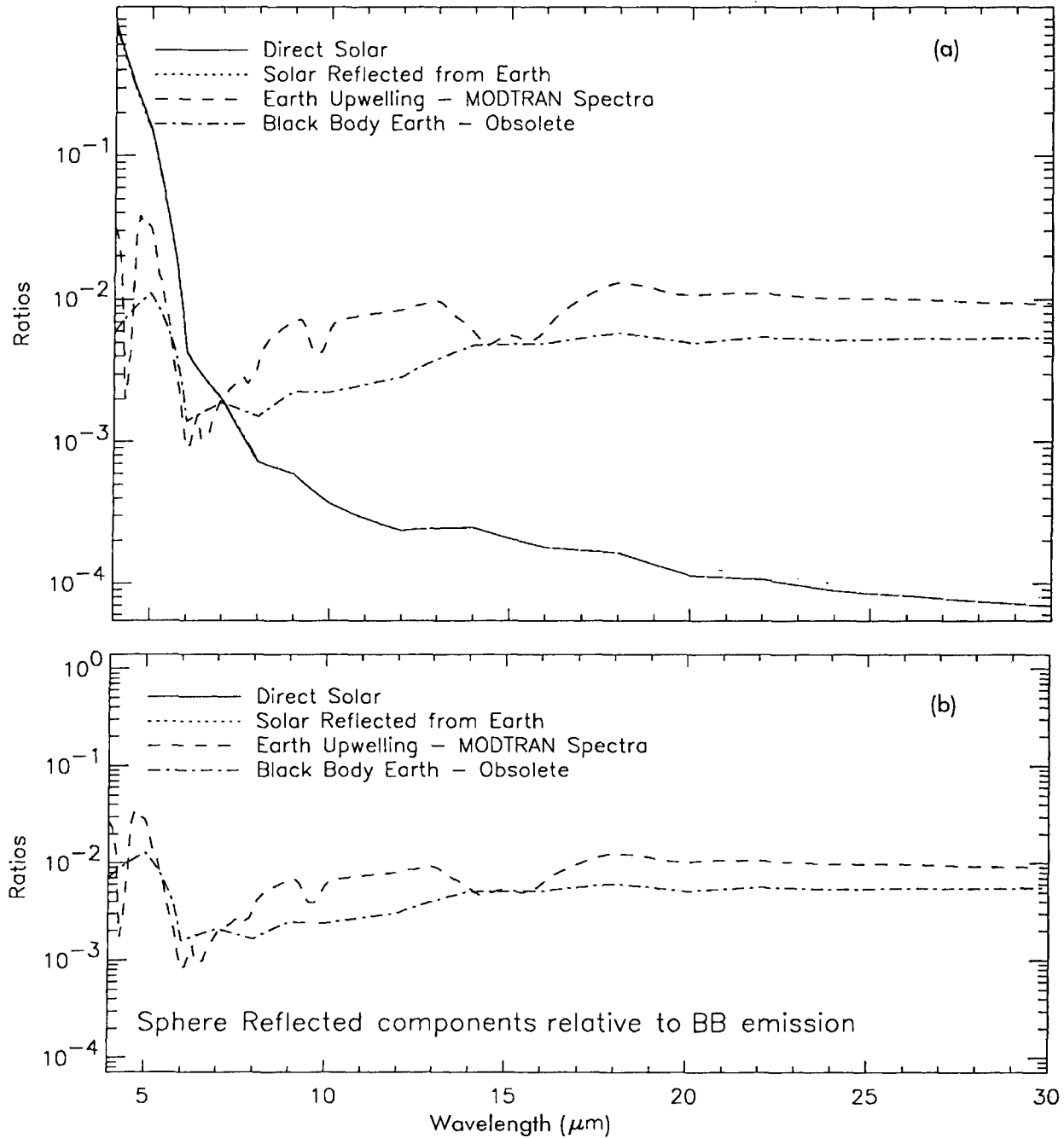


Figure 38: The reflected spectral flux relative to the total of the first emissive reference sphere just before entering eclipse (a) and just after (b). The blackbody approximation for the Earth's spectrum was used in the sensitivity analyses of Chalupa et al. and is included as a comparison with the more detailed spectral signature from the transmission through the Earth's atmosphere.

5.6 Calibration Against the Emissive Reference Spheres

The in-band radiance is calculated at the time of each observation by integrating over wavelength the product of the wavelength dependent emissivity, the normalized spectral response of the MSX bands, and the spectral energy distribution from the blackbody at the temperature of the sphere predicted by the model. This is converted to flux by multiplying by the solid angle subtended by the sphere at the distance derived from the sphere's trajectory. To this is added the direct Sunlight, the Sunlight reflected by the Earth and the upwelling Earth radiation that is reflected by the sphere at the time of observation. The calculated spectral radiances from the Earth, such as those shown in Figure 36, are used in the calculation. The phase function for the reflected components was derived by assuming a secant reflection angle for reflected light. This angular dependence is not quite as steep as that measured in the laboratory but was used to avoid singularities. It results in a simple analytic phase function that is equal to the illuminated fraction of the sphere as seen by the sensor. An example of the reflected contribution for the first sphere is shown in Figure 38 just before and after the sphere entered eclipse. The mid-infrared reflected component from the Earth is usually 10 times larger than that from sunlight reflected by the Earth and constitutes a percent or less of the total in-band flux.

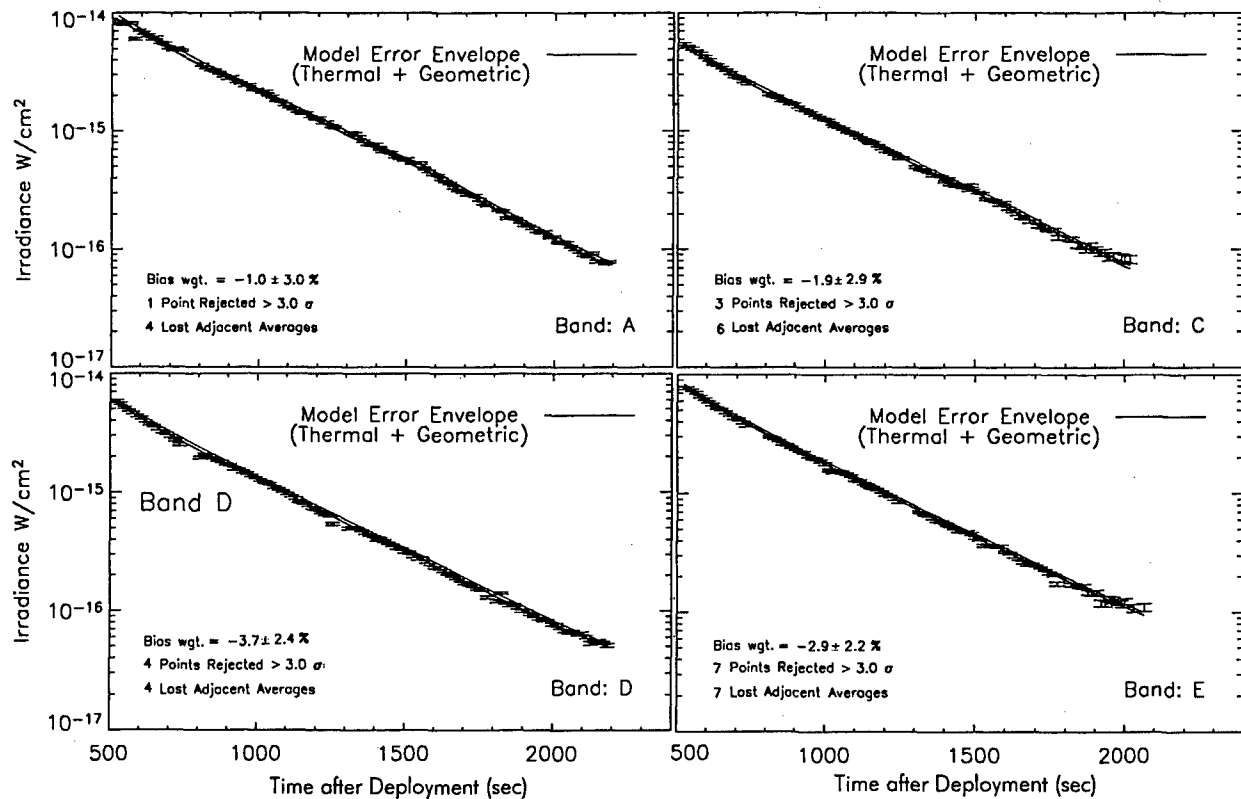


Figure 39: The in-band irradiances plotted as a function of time for ERS1. The error bars on the measurements generally fall within the modeling uncertainty. The dynamic range of the measurements for this experiment is about 100 in all the MSX mid-infrared bands.

The ERS1 measurements in each of the four MSX mid-infrared spectral bands are shown in Figure 39, while those for ERS5 are shown in Figure 40. The measurements are plotted with their associated error bars and the continuous lines are the estimated uncertainty bounds to the model predictions. However, the details are hard to see in these plots because of the large dynamic range. As with the stellar observations, successive back and forth measurements were averaged. A single observation was given half weight and the number of times this happens is noted as "lost averages" in the Figures. Since the analysis of the stellar calibration experiments clearly demonstrated that the measurement uncertainty was more accurately reflected by the rms of the individual fluxes about the mean rather than that inferred from the signal-to-noise ratio, we developed an empirical noise model based on the stellar observations:

Uncertainty in the Band A Irradiance: $Irr \cdot (0.031^2 + 1/SNR^2)^{1/2}$

Uncertainty in the Band C Irradiance: $(0.025^2 + 1/SNR^2)^{1/2}$

Uncertainty in the Band D Irradiance: $(0.019^2 + 1/SNR^2)^{1/2}$

Uncertainty in the Band E Irradiance: $(0.029^2 + 1/SNR^2)^{1/2}$

where the SNR term is a function of temperature. These expressions are used to ascribe an uncertainty to a single sphere measurement. This model was applied to calculate the measurement error bars plotted in the Figures.

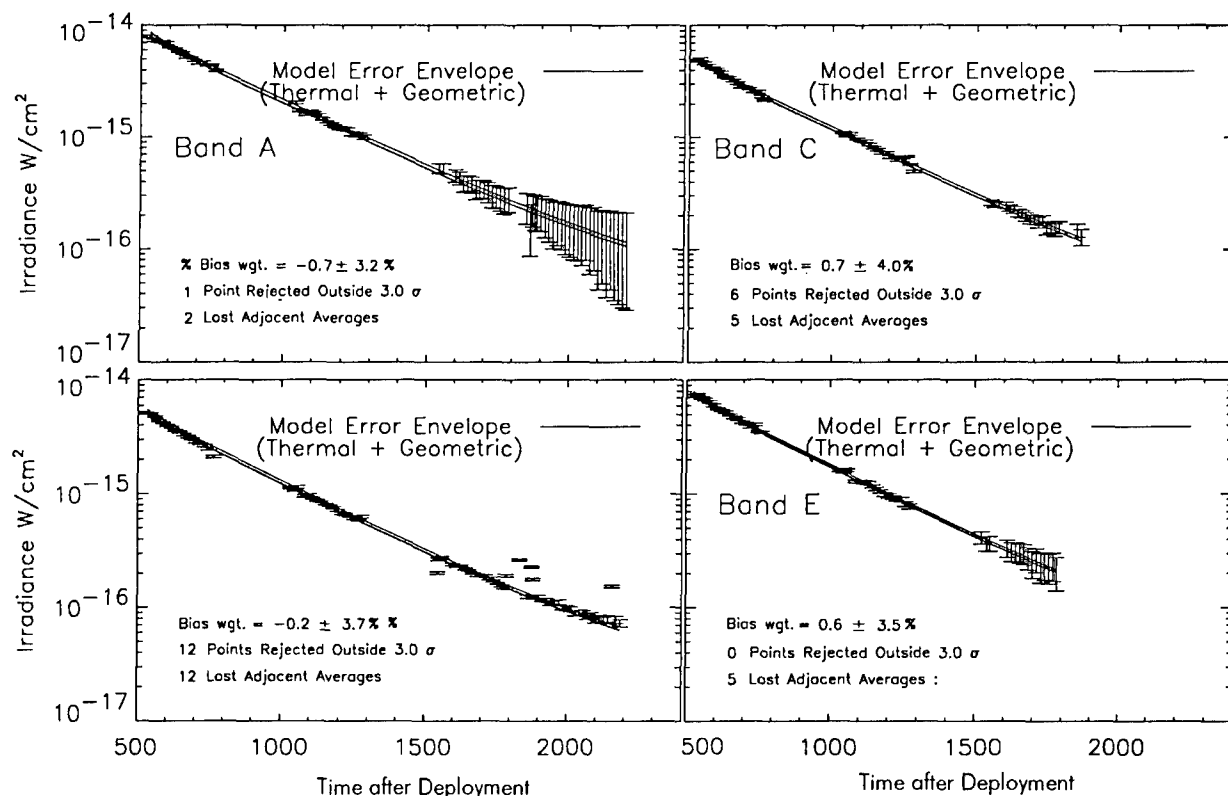


Figure 40: Measured irradiances are plotted as a function of time for the ERS5 experiment. These observations were obtained late in the mission, one month before the cryogen ran out, and our estimate for the increased noise caused by the higher focal plane temperatures at this time is evident.

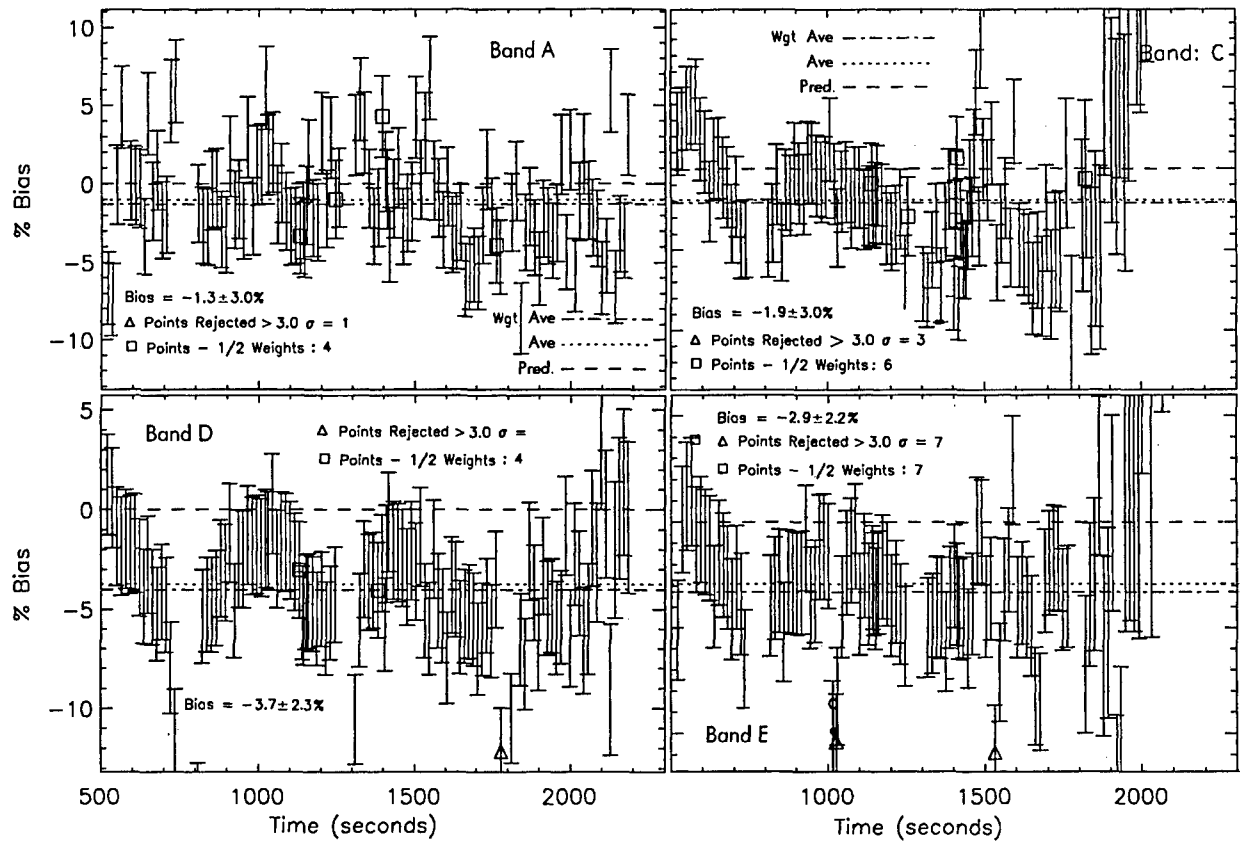


Figure 41: The ERS1 measurement biases. This experiment was executed on 25 August 1996.

The ERS2 – 4 experiments have far fewer measurements and since the large dynamic range makes it difficult to visually compare the observations with the model predictions we do not provide similar figures for these DCEs. The comparison is more clearly seen by plotting the percent biases (measurements divided by model predictions minus 1.0, the quantity multiplied by 100) as a function of time. The biases are plotted for the five reference spheres in Figures 41 through 45.

The dashed horizontal lines at zero in Figures 41 – 45 are the model predictions, the dotted lines are the percent biases of the straight average of the measurements and the dot – dashed lines are the weighted average of the biases. The data are trimmed to reject points greater than 3σ from the mean. The flux overestimation at low signal-to-noise due to the source selection process is apparent at the end of the experiments. We did not attempt to use the signal-to-noise value to adjust the data for this bias, such as describe by Tedesco (1993), because of the uncertain statistical significance of the signal-to-noise in the two-tiered measurement extraction criterion. Instead, applying the inverse variance weighting of these values as well as the 3σ rejection criterion markedly reduced their contribution to the weighted mean.

A 500-second cyclic variation for ERS1, most clearly seen in Band D in Figure 41 with an 8% peak-to-peak amplitude, is unexplained. Perhaps the emissivity varies over the surface of the sphere, which may have been caused by handling or the capture system. However, it would be difficult to account for the size of the effect with such an explanation. None of the other spheres were sampled with sufficient density to unambiguously show such a variation.

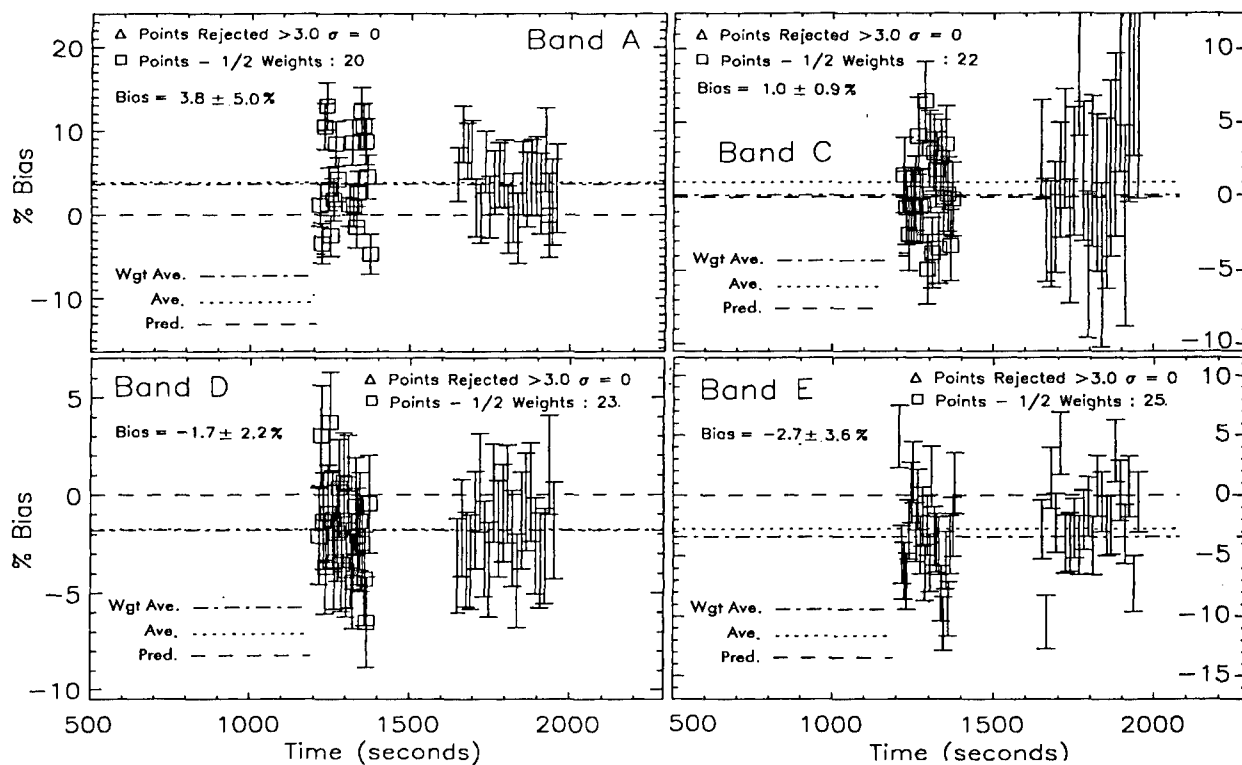


Figure 42: The ERS2 measurement biases. The experiment was executed on 14 Sep 1996.

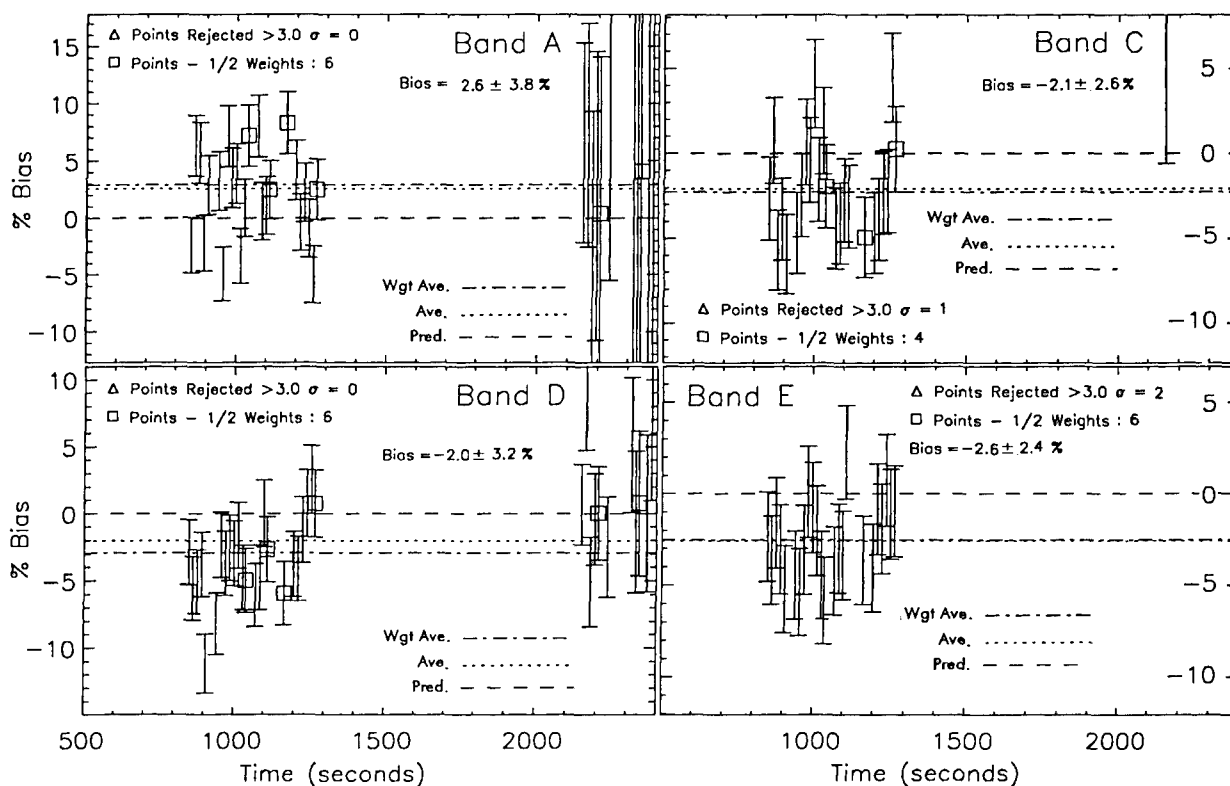


Figure 43: The ERS3 measurement biases. The experiment was executed on 22 November 1996.

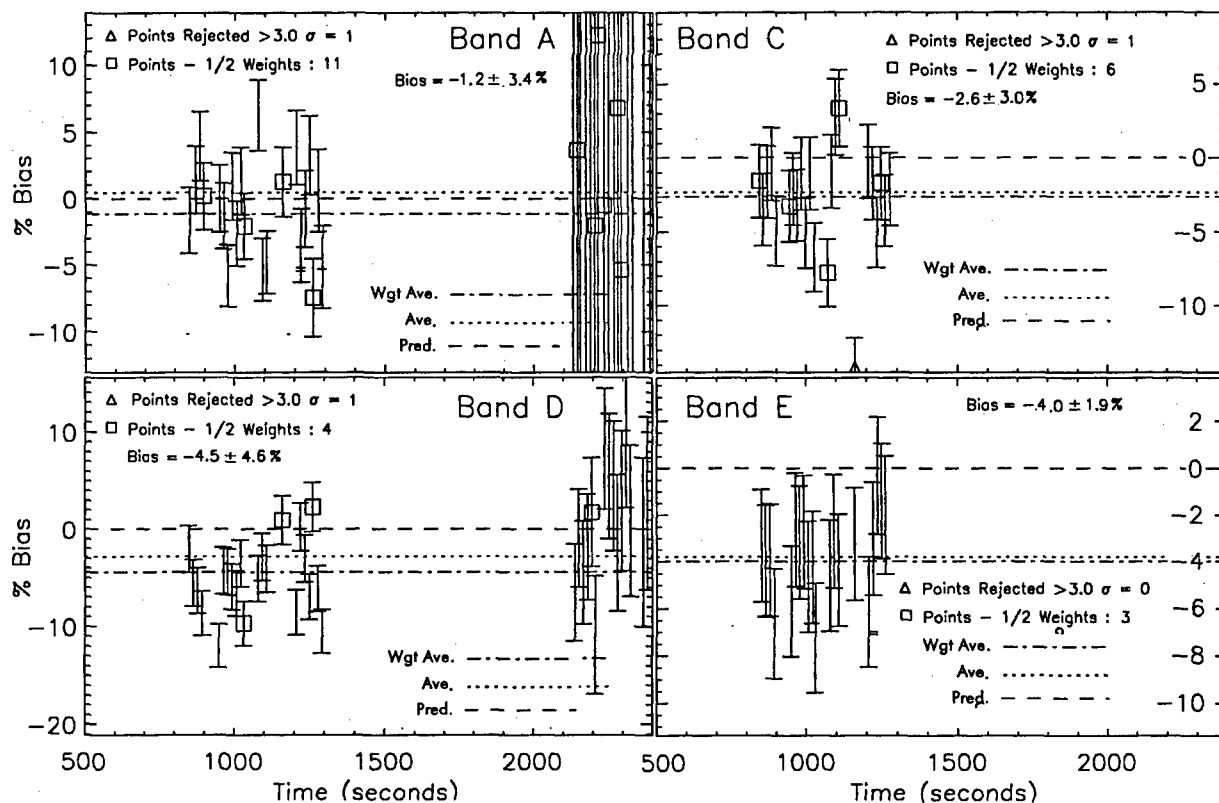


Figure 44: The ERS4 measurement biases. The experiment was executed 19 December 1996.

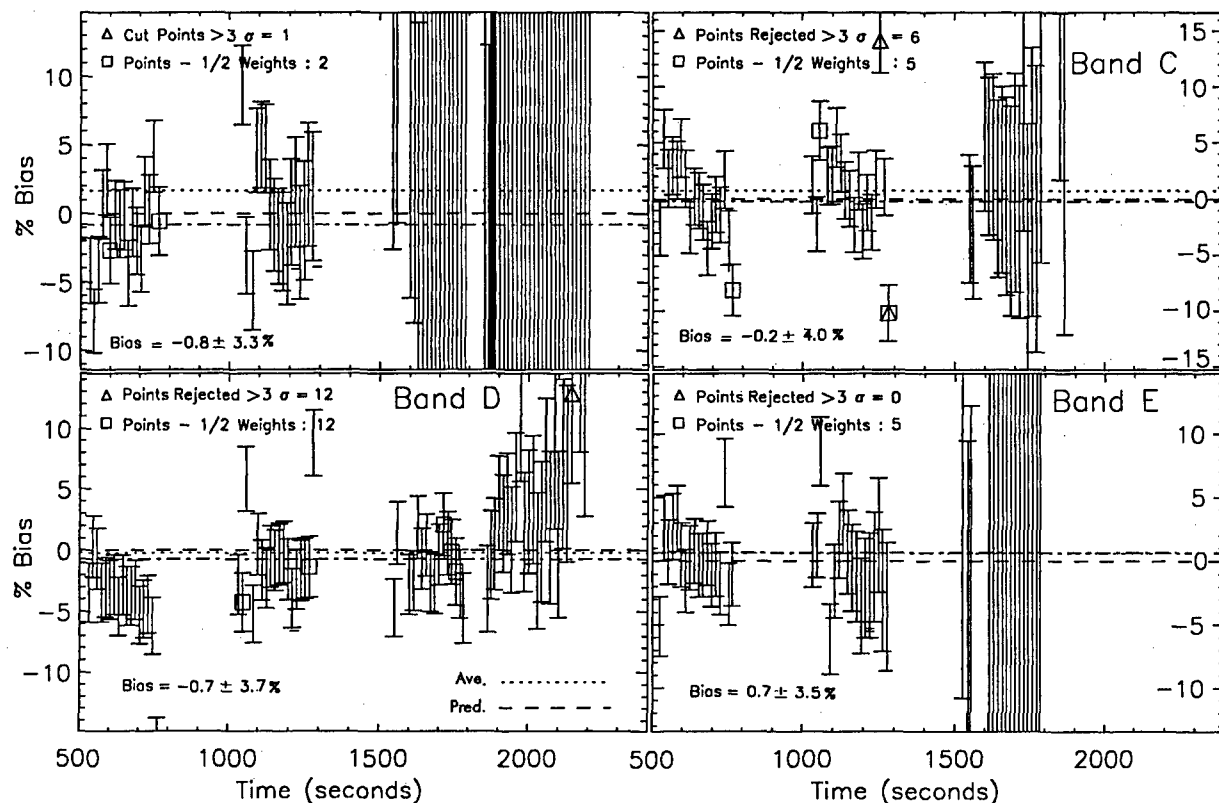


Figure 45: The ERS5 measurement biases. The experiment was executed on 20 February 1997.

The weighted average biases for all five spheres in the four mid-infrared spectral bands are listed in Table 15 and graphically depicted in Figure 46. The variances used in the weighted DCE means are the variances about the bias from the individual means added in quadrature with the Bands A, C, D and E model uncertainties of 4, 3.5, 3.5, and 3.0 percent, respectively. The straight weighted mean is calculated using Equation (5) with these weights and the uncertainty in the means is derived from Equation (6). We also calculated the experiment means using weights that factored the number of measurements made on the experiment into the uncertainties in the measurements and the model. This gives more weight to the more complete and better-defined dataset from ERS1. These means are listed in the last row of the Table. The smaller uncertainties about these means reflect the fact that the number of measurements, N , for ERS1 is much larger than that for the other spheres.

The agreement in the biases derived for the five ERS experiments is quite good, well within the standard deviations. Also, the differences between the two sets of weighted mission means are within 1σ of the formal solution. There is a trend for the mission-averaged biases to become more negative as the wavelength increases. The bias decreases by about 2.5 percent from Band A to Bands D and E and, among the individual experiments, the trend is most pronounced for ERS2. The most direct explanation for the trend is that either the variation in infrared emissivity with wavelength is more pronounced than what we used or that the calibration in each band needs to be changed.

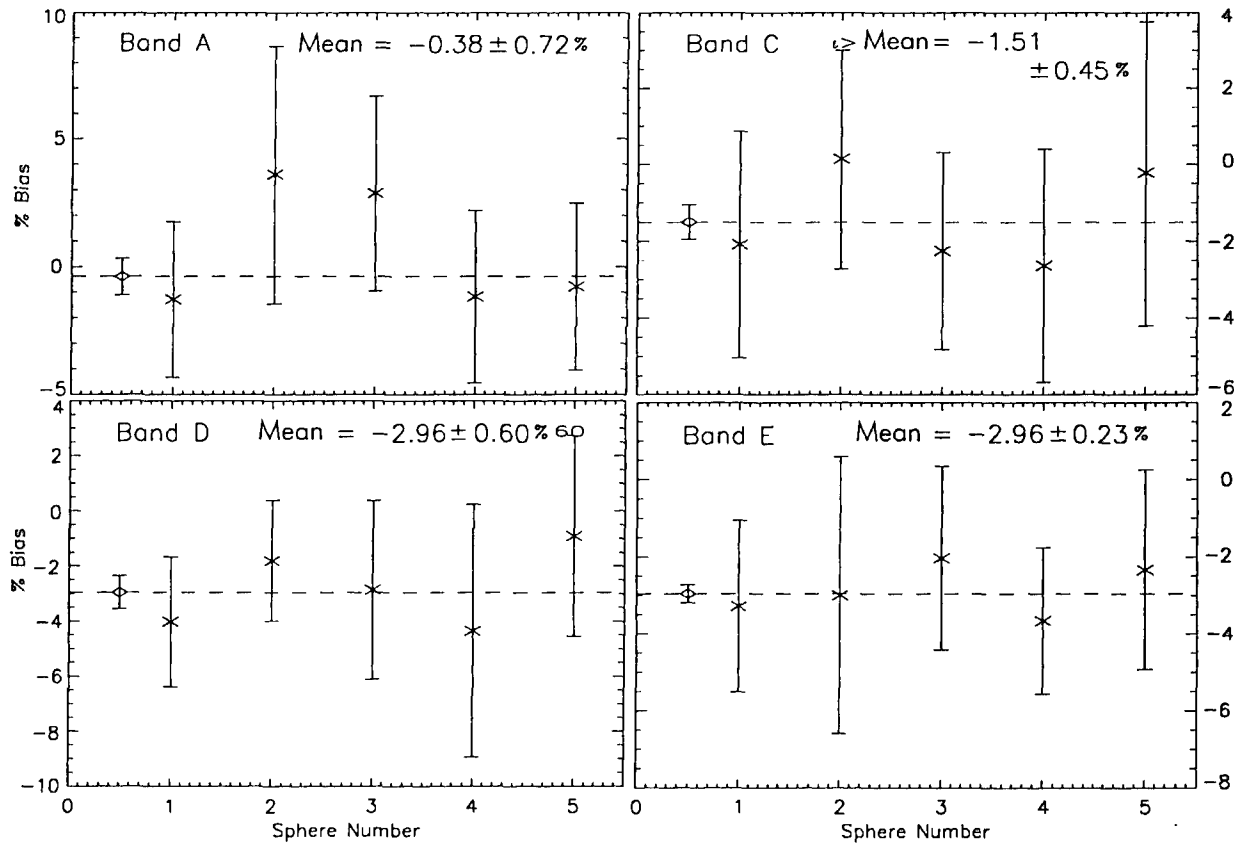


Figure 46: The weighted mean biases and standard deviations for the individual ERS experiments and the weighted average for all five DCEs (dotted lines and diamonds).

Table 15: Percent Biases and Associated Errors for the ERS Experiments

Experiment Bias & error (%)	Band A Mean σ	Band C Mean σ	Band D Mean σ	Band E Mean σ
ERS 1	-1.3 \pm 3.0	-2.1 \pm 2.9	-4.4 \pm 2.4	-3.7 \pm 2.2
ERS 2	3.6 \pm 5.1	0.1 \pm 2.9	-1.8 \pm 2.2	-3.4 \pm 3.6
ERS 3	2.9 \pm 3.8	-2.3 \pm 2.6	-2.9 \pm 3.2	-2.5 \pm 2.4
ERS 4	-1.2 \pm 3.4	-2.6 \pm 3.0	-4.5 \pm 4.6	-4.0 \pm 1.9
ERS 5	-0.8 \pm 3.3	-0.2 \pm 4.0	-0.7 \pm 3.7	0.7 \pm 3.5
Wgt. Mean	0.35 \pm 2.0	-1.5 \pm 1.1	-2.7 \pm 1.3	-2.8 \pm 1.5
Wgt \times N Mean	-0.4 \pm 0.7	-1.5 \pm 0.4	-2.9 \pm 0.6	-2.8 \pm 0.7

The scatter in the averaged means may be reduced by adjusting the model parameters under the constraint that the modeled fluxes in the MSX bands are correlated by the requirement that the sphere has a single temperature at the time of measurements. The question is: are the changes needed to minimize the deviations within the uncertainties assigned to the parameters?

The measurement biases may be decomposed into three categories of modeling error, those arising from: 1) a scaling factor for each band, designated S_X , due to errors in the wavelength dependent emissivity and/or the calibration of the responsivity, 2) geometric factors due to errors in the radius and/or range of the sphere, and 3) errors in the model's thermal balance that are manifested as an error in the temperature, T , of the sphere. The scaling factors depend on the emissive properties and/or response of the sensor, so reasonably they should be the same for all five spheres. To very good first order, the geometric factors due to percentage error in the size of the sphere, the ejection angle and/or ejection velocity, are constant within a given DCE and are the same in all the mid-infrared bands. On the other hand, an error in the temperature of the sphere produces errors that are different for each of the MSX mid-infrared bands. Thus, dividing the flux in one band by that observed in another eliminates the common geometric uncertainty, if the <1 percent contribution of the reflected component from the Earth and Sun is ignored. The result is an estimate of the color temperature of the sphere coupled with the scaling factor.

Adopting the median 270K temperature of the spheres during the experiments, a change in flux is related to a change in the model parameters by:

$$\begin{aligned}
 \Delta A / A &= 6.2 \Delta T / T + \Delta S_A / S_A - 2 \Delta R / R \\
 \Delta C / C &= 4.6 \Delta T / T + \Delta S_C / S_C - 2 \Delta R / R \\
 \Delta D / D &= 3.6 \Delta T / T + \Delta S_D / S_D - 2 \Delta R / R \\
 \Delta E / E &= 2.6 \Delta T / T + \Delta S_E / S_E - 2 \Delta R / R
 \end{aligned} \tag{12}$$

The temperatures of the spheres during the experiments are 270 ± 11 K and the coefficients to the temperature change in Equation (12) differ little over that range.

The band ratios are related to changes in the model by the relations:

$$\begin{aligned}
 \Delta[A/E]/[A/E] &= 3.3\Delta T/T + \Delta S_A/S_A - \Delta S_E/S_E \\
 \Delta[A/C]/[A/C] &= 1.6\Delta T/T + \Delta S_A/S_A - \Delta S_C/S_C \\
 \Delta[A/D]/[A/D] &= 2.4\Delta T/T + \Delta S_A/S_A - \Delta S_D/S_D \\
 \Delta[D/E]/[D/E] &= 0.9\Delta T/T + \Delta S_D/S_D - \Delta S_E/S_E \\
 \Delta[C/E]/[C/E] &= 0.8\Delta T/T + \Delta S_C/S_C - \Delta S_E/S_E
 \end{aligned} \tag{13}$$

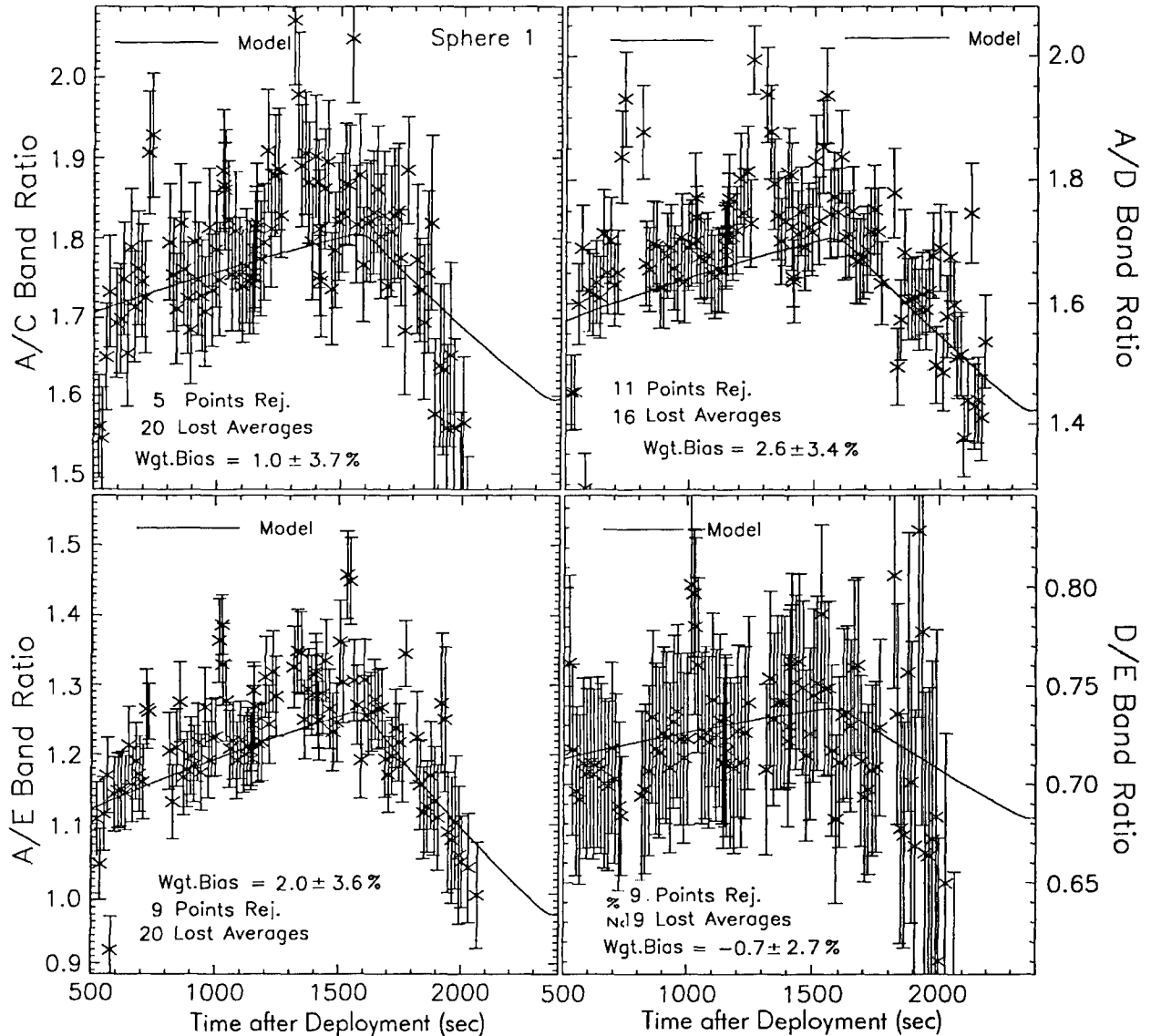


Figure 47: Measured ERS1 color ratios with error bars compared to predictions (solid line).

The measured band ratios for ERS1 through ERS5 are compared to the predicted values in Figures 47 through 51. Plots are provided for the three ratios involving Bands A, D and E, as these bands were purposely co-aligned in the sensor to produce simultaneous measurements, which facilitates the analysis in the observed ratios. Bands C and D are too close in wavelength

to produce a statistically significant ratio and C/E ratios are consistently noisy. The measured band ratios for ERS1 are plotted in Figure 47 along with associated error bars and the model predictions, which are given by the solid lines. The turnover in the ratios at $t + 1500$ seconds marks the entry of the sphere into eclipse, at which time the sphere temperature has reached a maximum temperature of 277K. The sphere then cools to a minimum of 259K by the end of the ERS1 experiment at $t + 2400$ seconds. Since the other four spheres remain in sunlight during the entire experiment (see Figure 37) their temperatures rise to maxima of 280 to 282.5K.

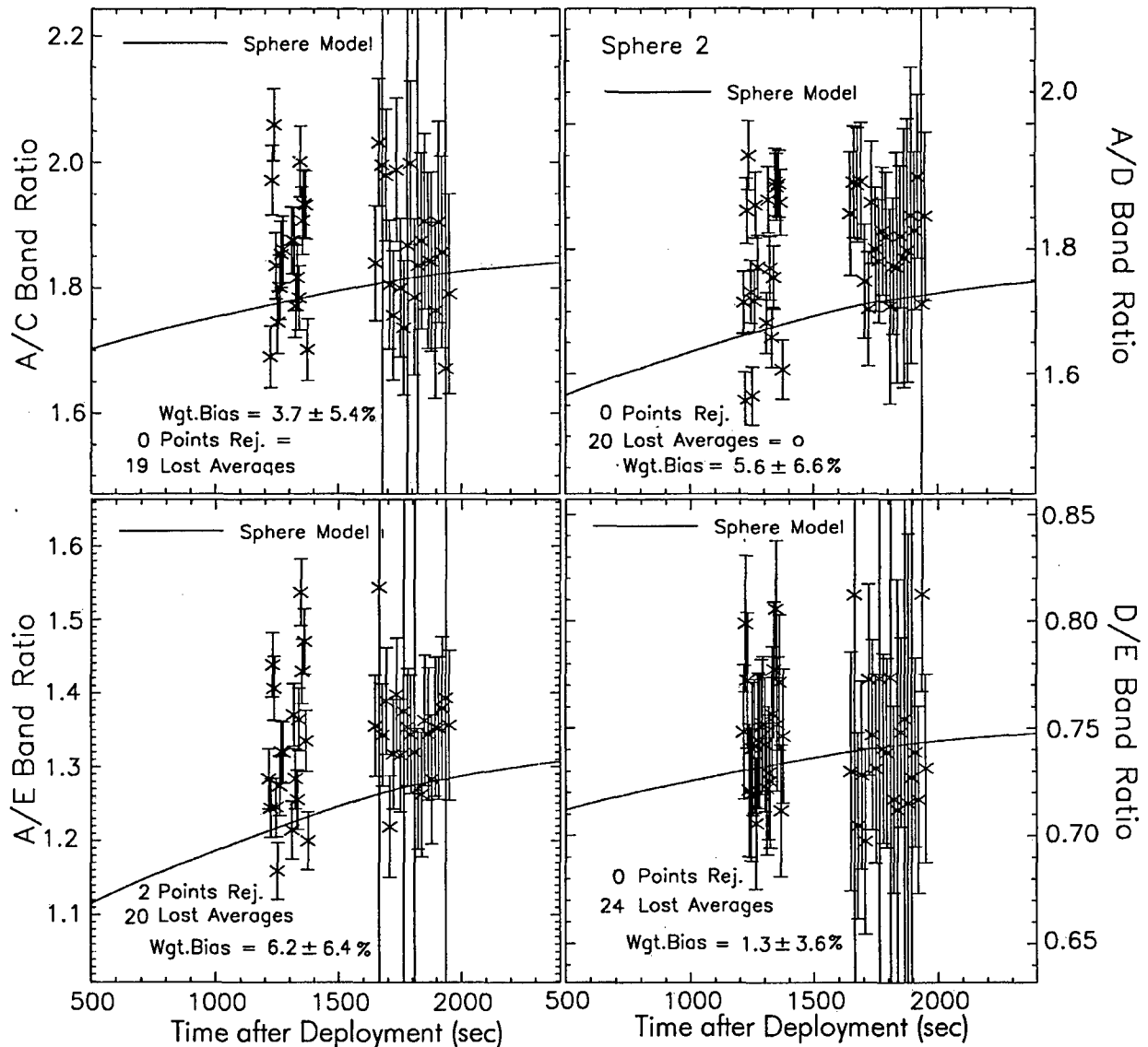


Figure 48: Color ratios measured for the second sphere compared to model predictions.

While not strictly correct, we can uncouple the various components by assuming that the temperature error of the sphere is constant during the DCE. Since the geometric factors cancel in the band ratios and the scale factors are the same for all spheres, we assume that the band ratios averaged over the five experiments are functions only of the scaling factors and that the

deviations from the mean for a given DCE reflect the temperature error. Having defined the temperature corrections for each DCE, the scale factors and geometric corrections are adjusted to match the observed fluxes in each band on each DCE. The scale factors (biases) for the five DCEs in the resulting correlated solution given in Table 16 agree to within 0.4 percent.

Table 16: Correction Factors for Model Components from Band Correlated Solution

Scale Factor Bias		Experiment	Geometric Factor	Temp. Corr.
Band A	0.0	ERS1	$0.2 \pm 0.2\%$	$-0.5 \pm 0.3\text{K}$
Band C	-1.2	ERS2	$-2.5 \pm 0.2\%$	$3.8 \pm 1.1\text{K}$
Band D	-2.9	ERS3	$-1.1 \pm 1.5\%$	$1.6 \pm 4.0\text{K}$
Band E	-2.5	ERS4	$-1.1 \pm 0.1\%$	$0.3 \pm 0.3\text{K}$
		ERS5	$2.9 \pm 0.1\%$	$-1.9\text{K} \pm 0.8\text{K}$

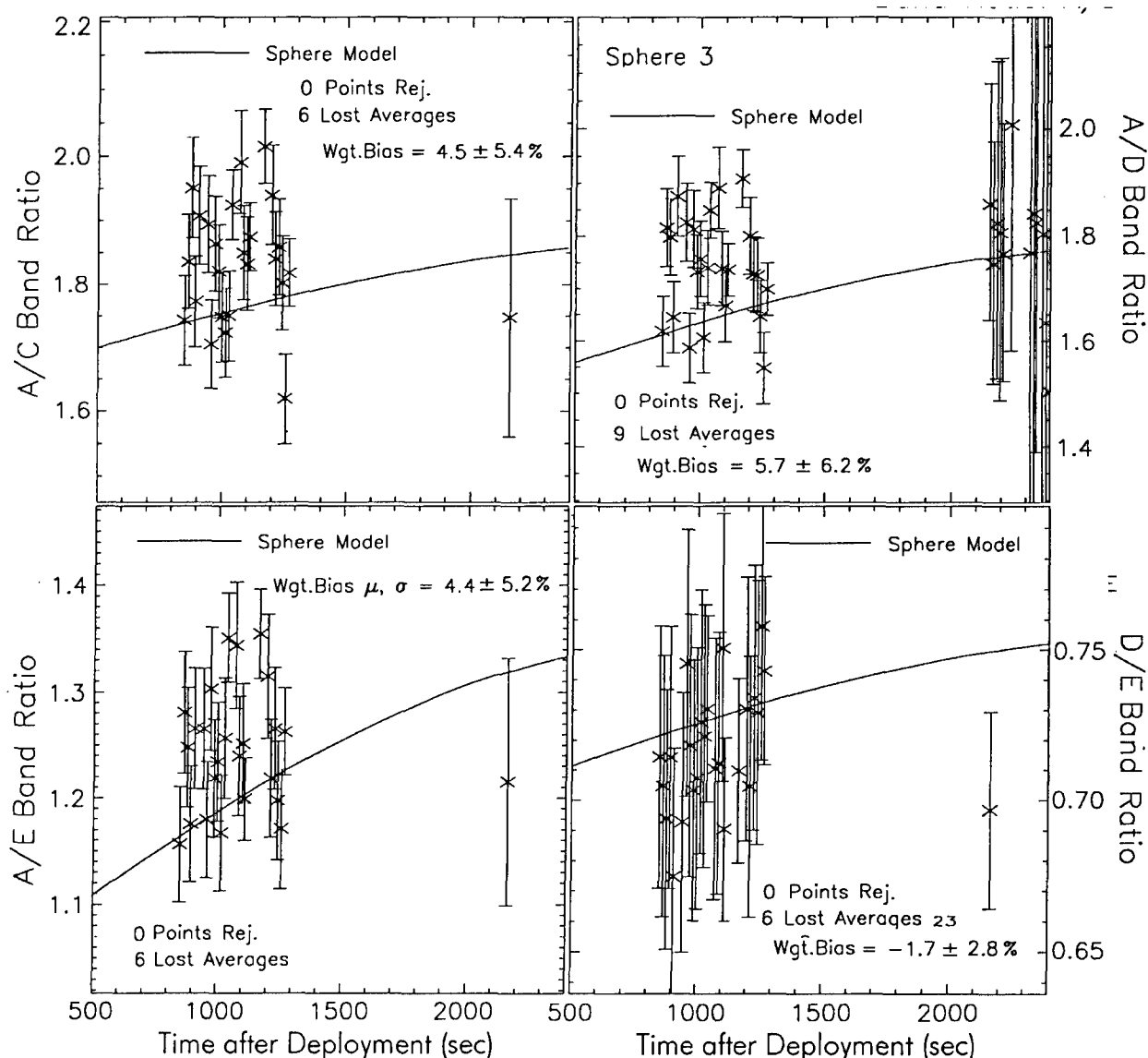


Figure 49: Color ratios measured for the third sphere compared to model predictions.

As expected, the scale factor biases are within the formal errors of the straight weighted means listed in Table 15, as they are not independent of that solution. While there is insufficient information to determine whether the error in the spheres' infrared emissivity or responsivity corrections contribute most to the scale factor biases, the wavelength dependency does mimic that of the infrared emissivity. NIST measured a mean infrared emissivity that was 1.6 percent lower than the value derived using the wavelength dependent emissivity in the model. As may be seen from Figure 33, there is about a 2 percent difference between the averaged emissivity in Band A compared to that in Band E, which is the size of the discrepancy. The geometric factors are within 1σ of the uncertainties in the manufacturing tolerances on the size of the spheres combined with those in the range. The temperature adjustments are within 2σ of the 1K uncertainty in the thermal modeling, except for ERS2, for which a 4σ deviation was found.

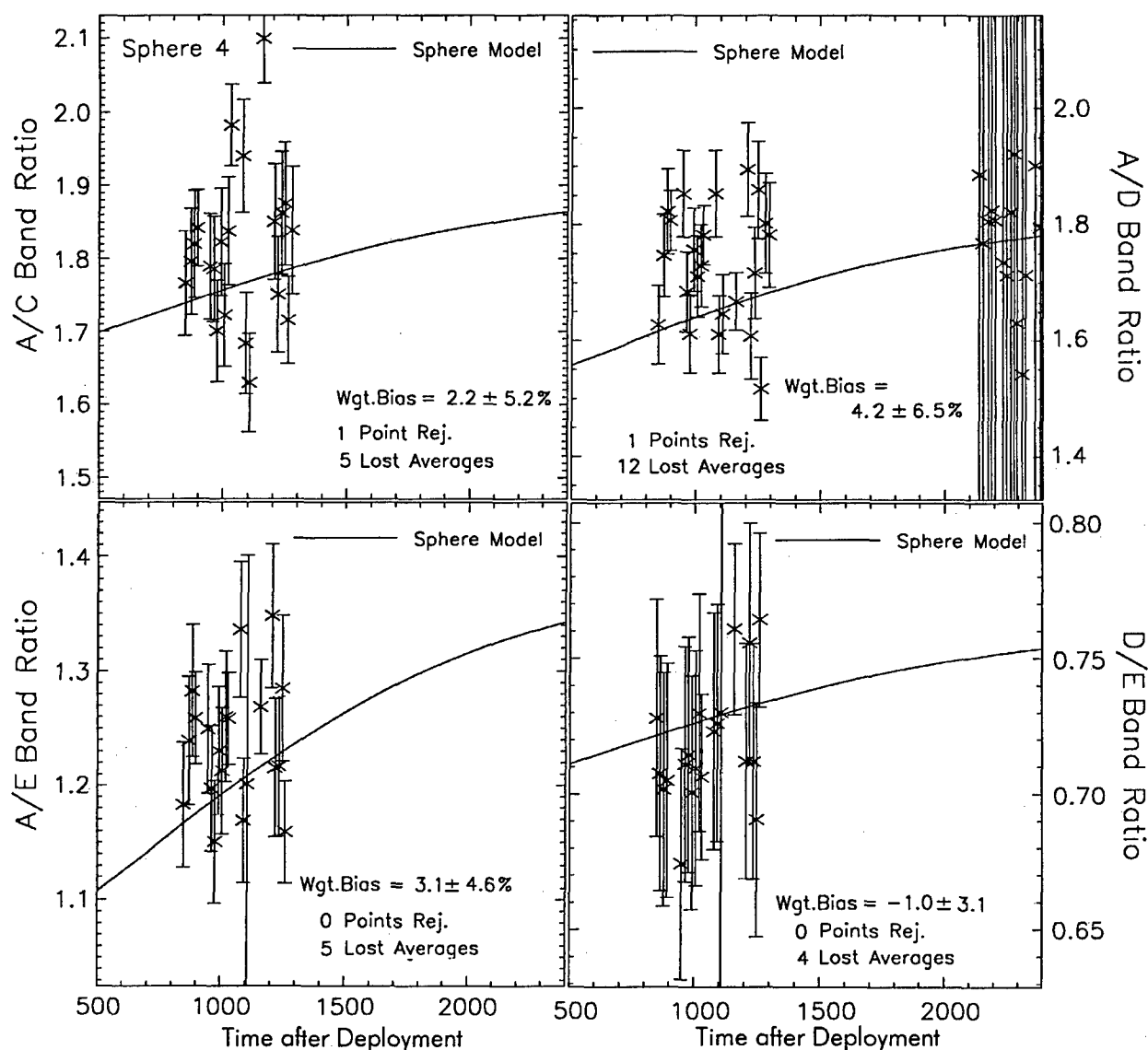


Figure 50: Color ratios measured for the fourth sphere compared to model predictions.

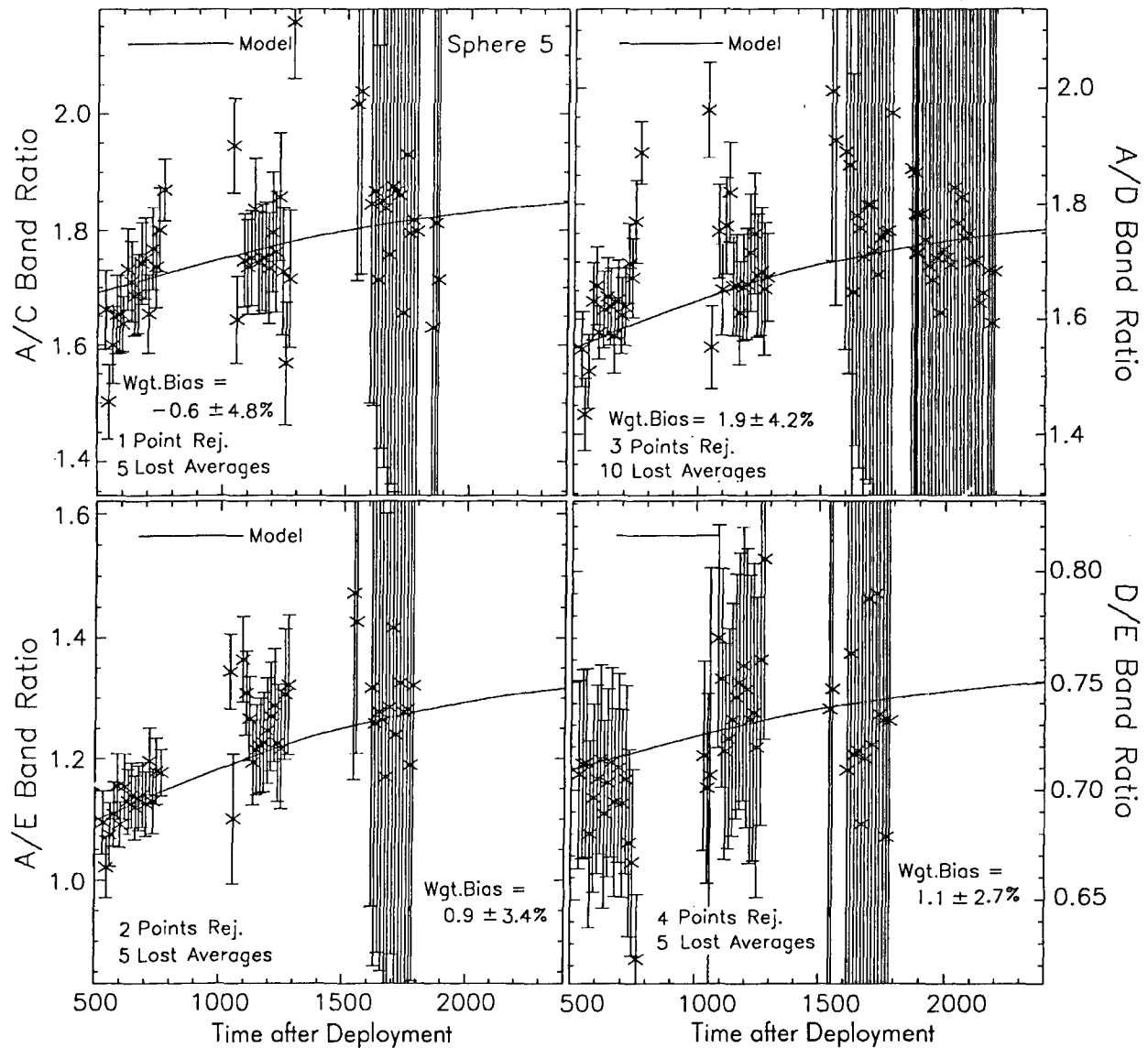


Figure 51: Color ratios measured for the fifth sphere compared to model predictions.

The wavelength dependent trend in the mission averaged scale factors mimics a temperature adjustment of about 2.5K. However, attributing the measured biases to temperature errors produces an improbably large value of $\Delta T \sim +6.3\text{K}$ for ERS2. A 4 percent change in the flux intercepted by the sphere is needed to change the temperature by 1 percent or $\sim 2.7\text{K}$. Since more than 80 percent of the absorbed flux for the sunlit sphere comes from the Sun and the uncertainties in the contribution from this component are small (root sum square of the 1 percent uncertainties from the absorptivity and infrared emissivity) a very large error is required in the contribution from the upwelling Earth radiation, of the order of 60 percent, to adjust the temperature by 6.3K. The smaller 3.8K adjustment for ERS2 from the mean solution in Table 16 is also difficult to reconcile. Baca et al. (2002) did note that that ERS2 was anomalous in that it was deployed at an angle that put the sphere outside the field of regard until 1200 seconds after the sphere was ejected. It exited the field of regard 200 seconds later and was seen again at $t +$

~1650 seconds. However, this is a geometric factor that would have little effect on the color ratios for this sphere.

In any event, the <2K adjustment for the other spheres can be accounted for by reasonable variations in the modeling parameters and inputs as well as the uncertainties in the formal solutions that led to the values in the Table. Thus, the absolute fluxes and the band ratios may be brought into detailed agreement by changing the model parameters within reasonable limits for four of the five reference sphere experiments.

The reference sphere experiments also observed stellar standard stars. The ratio of the DC22 DCE mean irradiances of these stars with the global means in Table 8 are listed in Table 17. The uncertainties listed are in the knowledge of the mean, that is, the standard deviations of the measurements divided by the square of the number of measurements, and do not include the additional 1 percent assigned to the DCE means. As may be seen, there are no systematic differences if the additional 1 percent uncertainty in the means is included. Statistically, these means may be assumed to belong to the global population of means. Thus, the biases derived for the spheres may be compared to the global mean fluxes measured for the stars.

Table 17: The Ratio of the Stellar Fluxes Measured on the DC22s to the Mission Mean Fluxes

Observation	Band A bias	Band C bias	Band D bias	Band E bias
β Peg DC2203	1.02 ± 0.02	1.005 ± 0.02	0.92 ± 0.015	1.04 ± 0.03
DC2204	0.98 ± 0.02	0.98 ± 0.02	0.995 ± 0.015	1.01 ± 0.03
α Boo DC2201	1.006 ± 0.004	1.001 ± 0.004	1.006 ± 0.003	0.995 ± 0.008
α CMa DC2202	0.978 ± 0.003	1.006 ± 0.003	0.998 ± 0.003	1.057 ± 0.012
DC2205	1.003 ± 0.003	1.007 ± 0.003	1.009 ± 0.003	-----
α Lyr DC2201	0.998 ± 0.004	1.042 ± 0.011	1.014 ± 0.006	-----
DC2202	0.999 ± 0.004	1.025 ± 0.011	0.998 ± 0.006	-----
α Tau DC2202	1.011 ± 0.004	0.990 ± 0.004	0.997 ± 0.003	0.984 ± 0.008
DC2205	0.989 ± 0.004	1.001 ± 0.004	1.007 ± 0.003	1.005 ± 0.008
γ Cru DC2201	0.995 ± 0.008	0.989 ± 0.007	0.999 ± 0.006	1.002 ± 0.012

6 Absolute Calibration of the Standard Stars

Before drawing conclusions about the absolute stellar flux calibration from the MSX reference sphere measurements, account must be taken of any bias introduced into the stellar analysis. The stellar analyses normalized the global mean irradiances for α CMa to the absolute values of Cohen et al. in Paper I. The mirror-scan DCE mission means for α CMa did not exactly equal the Cohen et al. predictions because the data for four other calibration stars were included in the derivation of the response correction as a function of focal plane temperature. Scaling the DCATT + CB averaged mean irradiances such that the results for α CMa were equal to the Cohen et al. irradiances was another bias to the α CMa mirror-scan mission means. Since the measured reference sphere irradiances only applied the temperature dependent responsivity correction derived from the DCATT global means, any bias in the DCATT α CMa global means has to be applied to the reference sphere results in order to have the spheres calibration compatible with the global stellar solution. Table 18 lists these DCATT α CMa biases.

Table 18: Mirror-Scan Corrections For α CMa And Uncertainties*

Band A	Band B ₁	Band B ₂	Band C	Band D	Band E
1.004 ± 0.003	1.011 ± 0.007	1.008 ± 0.006	0.998 ± 0.003	1.001 ± 0.002	1.007 ± 0.030

* Uncertainties in the formal solution are listed and do not include the 1.46 percent bias Cohen et al. ascribe to their α CMa absolute spectral irradiances in Paper I.

In Paper I, Cohen et al. derived their zero magnitude irradiances by extrapolating the Hayes (1985) recommended absolute calibration of α Lyr at $0.5556 \mu\text{m}$ into the infrared using a spectral energy distribution of the $T_{\text{eff}} = 9400\text{K}$ Kurucz model. The MSX calibration, however, was normalized to the absolute spectrum of α CMa. The response of the MSX mid-infrared bands has been precisely (<0.5 percent rms) tied to the Cohen et al. absolute irradiances for α CMa in Table 18. To reference the MSX calibration to Vega, we divide the measured fluxes on this star in Table 8 by the zero magnitude fluxes, the results of which are listed in Table 12. The high quality MSX α Lyr Band A and B₂ measurements average to about 1 percent lower than the predictions. The global averages for the high quality observations of the secondary standard stars in Table 8 also average to a 1 percent deficit. Thus, the observations are rationalized by adopting the Cohen et al. zero magnitude absolute irradiances based on Vega for the calculations, at least to $12 \mu\text{m}$, which brings the average bias of the secondary standards to zero but at the expense of having to increase the absolute predicted infrared irradiance for Sirius by 1 percent. If this is done, the reference sphere biases are also increased by 1 percent. Such an increase further reduces the bias in the absolute calibration based on the spheres averaged over all MSX bands and all experiments to -1.2 percent. Table 19 lists our best estimates of the biases in the Cohen et al. zero magnitude fluxes for the MSX mid-infrared bands based on the absolute calibration against the reference spheres. We derived these values by adding the sum of one percent and the biases derived in each band from Table 18 to the weighted means in Table 16.

Table 19: Corrected Weighted Mean Biases

Zero Flux Bias	Band A	Band C	Band D	Band E	Mid-IR Ave
Means	$0.4 \pm 0.7\%$	$-0.4 \pm 0.4\%$	$-1.9 \pm 0.4\%$	$-2.5 \pm 0.6\%$	$-1.1 \pm 0.7\%$

Taking the biases in Table 19 at face value implies that the mid-infrared zero magnitude flux proposed in Paper I is correct in Band A but needs to be increased as a function of wavelength up to 2.5 percent in Band E. However, this trend is not only within the uncertainties of the solution but is also within the uncertainties of the knowledge in the wavelength dependent emissivities used in the model. Thus, it may be said that the absolute MSX calibration against the emissive reference spheres confirms the scale of zero magnitude fluxes proposed by Cohen et al. (1992a) to within the 1.1 percent.

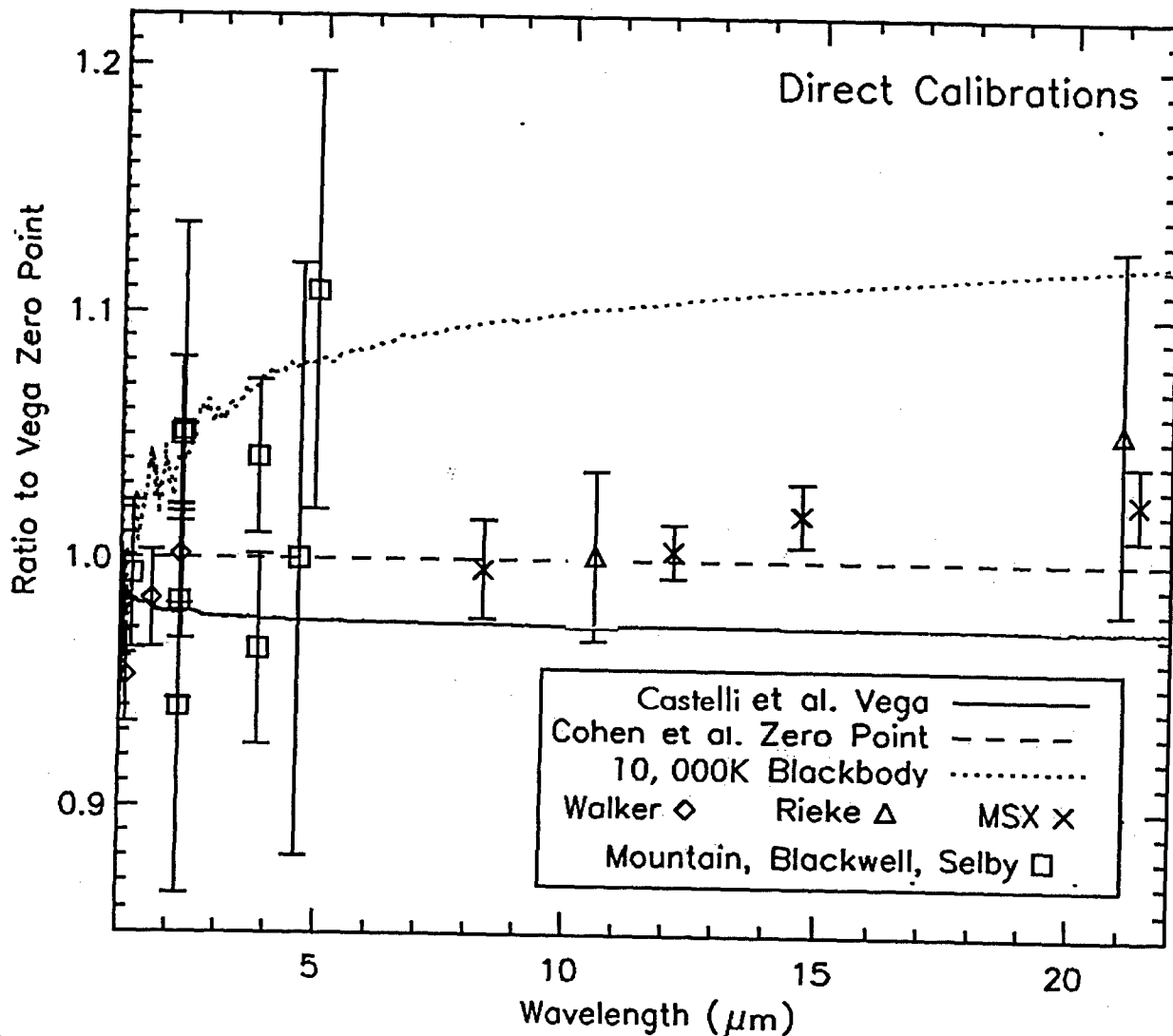


Figure 52: A comparison between various direct absolute infrared calibrations and suggested zero magnitude spectral energy distributions. The data points are labeled as to source. The squares refer to the Imperial College/Oxford University efforts given by Mountain et al. (1985) and references therein, while the dotted line is the 10000K blackbody these researches say is the best fit to their measurements. Walker (1969) performed one of the first direct near-infrared calibrations and Rieke et al. (1985) did the last direct mid-infrared calibration before MSX. Castelli and Kurucz (1994) suggested an 'improved' model spectrum for Vega (solid line) over the one adopted by Cohen et al. (1992) to which the comparisons are normalized (dashed line).

The direct absolute MSX mid-infrared calibration is compared to previous direct calibrations in Figure 52. The calibrations are normalized to the zero magnitude irradiances from Paper I that MSX has confirmed. The uncertainty in the MSX calibration is at least a factor of three times smaller than the best previous direct mid-infrared calibration by Rieke, Lebofsky and Low (1985). Indirect calibrations, which indirectly transfer the absolutely calibrated solar flux to the stellar standards, all tend toward the 10 000K blackbody curve in Figure 52 (Mégessier, 1995, for example). The MSX results also indicate that there is a systematic bias of up to 10 percent in the indirect calibrations.

7 Improvement to the Stellar Standards

The low ($\sim 0.1 \mu\text{m}$) spectral resolution of the Cohen et al. composite spectra smoothes over the spectral detail in the molecular absorptions in the atmospheres of the standard stars, which can introduce errors when calibrating narrow spectral bands or spectral measurements. Sensors that use very narrow spectral bands require photometric standards that have a sufficiently high spectral resolution to accurately reflect the spectral features that are present. The higher formal accuracy of the MSX photometry can be used to reduce these uncertainties, particularly when combined with higher resolution spectra from the ISO spectrometers (Kessler et al., 2003).

7.1 New Calibrated Reference Spectra

We adopt the model spectral energy distributions (SEDs) for Vega and Sirius from Cohen et al. (Sirius is scaled by $\times 1.01$ from Section 6) to preserve the Cohen et al. absolute zero magnitude flux scale even though SWS measurements were available for these two primary standards. The SWS spectra for Vega and Sirius are noisy and plagued by detector non-linearities at wavelengths longer than about $7 \mu\text{m}$.

We have combined the moderate resolution $2.36 - 35 \mu\text{m}$ SWS spectra ($\lambda/\Delta\lambda \sim 400$) (Leech et al., 2003) with the best photometry available on Cohen et al.'s secondary and tertiary standards, referenced to the rescaled absolute infrared spectrum of Sirius, to create absolutely calibrated high resolution spectra for 33 stars, 29 of which are in the Cohen et al. calibration network. (A Cohen et al. tertiary standard is one from Paper X with a template spectrum.) The highest quality photometry was from MSX, DIRBE/COBE and Hammersley et al. (1998); MSX and DIRBE were space-based experiments and, therefore, are free of atmospheric effects. If needed, measurements from the Infrared Astronomical Satellite (IRAS) as well as the photometric resources listed in Appendix A of Walker and Cohen (1998) were also used.

The nine secondary standards with the most accurate absolute infrared fluxes are listed in Table 20. These stars were original Cohen et al. secondary standards from which they spawned the spectral templates for the stars in the calibration network. The 24 secondary standards listed in Table 21 have greater uncertainties. Eighteen of these 24 stars had previously been assigned spectral templates in Paper X. The derived parameters of effective temperature and angular diameter and their associated errors that are listed in the tables are discussed in Section 7.3. References for the photometry and spectroscopy used to create the improved spectra are also listed in the three tables.

The absolute spectral energy distributions for the stars in Table 20 were constructed using the precise photometry from MSX, DIRBE and Hammersley et al. Because the stars are bright, they also have high signal-to-noise SWS spectra over much of the wavelength range. We replaced the template spectrum of β UMi originally created by Walker and Cohen (2003) for use as the representative K4 III template with an absolutely calibrated measured spectrum for this star. MSX obtained precision photometry on β Gem and it is included in Table 20 even though it does not have an SWS spectrum. The SWS $2.36 - 9 \mu\text{m}$ spectra of θ Cen and δ Eri, two stars of similar spectral classification as β Gem, were averaged and adopted as the composite spectrum to which was seamed the $9 - 16 \mu\text{m}$ ISOCAM Circular Variable Filter (CVF - Blommaert et al., 2003) spectrum of δ Dra. The result is in excellent relative agreement with the photometry.

Table 20: Best Secondary Standards

Star	Sp. T.	T_{eff} (K)	θ (mas)	Spectra [to λ] ^a	Photometry ^b
β Gem	K0 III	$4850 \pm 5\%$	$8.03 \pm 3\%$	SEW; SWS θ Cen [9]; CVF δ Dra [16]; A[35]	MSX, DIR, H, S, T, IRAS
α Boo	K1.5 III	$4350 \pm 1.5\%$	$21.06 \pm 1\%$	SEW[2]; HW[2.4]; S[22]; A[35]	MSX, DIR, H, S
β UMi	K4 III	$4150 \pm 4\%$	$10.00 \pm 2\%$	S[17]; A[35]	DIR, IRAS
α Tau	K5 III	$4050 \pm 2\%$	$20.75 \pm 1\%$	SEW[2]; HW [2.4]; S[35]	MSX, DIR, H, S
γ Dra	K5 III	$4030 \pm 2\%$	$10.17 \pm 1\%$	HW [2.4]; S[27]; A[35]	MSX, DIR, H, S
μ UMa	M0 III	$3900 \pm 4\%$	$8.45 \pm 2\%$	HW [2.4]; S[17]; A[35]	DIR, T, S
β And	M0 III	$3900 \pm 4\%$	$13.65 \pm 2\%$	SEW; S[27]; A[35]	MSX, DIR, H, S
α Cet	M2 III	$3750 \pm 4\%$	$12.94 \pm 2\%$	SEW; S[27]; A[35]	DIR, IRAS, S
γ Cru	M4 III	$3626 \pm 2\%$	$26.37 \pm 1\%$	S[35]	MSX, DIR

Note – Spectral types in this and the following tables are from the Heras et al. (2002) and references therein.

^a Spectral segment: SEW = Strecker et al. (1979); HW = Hinkle et al. (1995); WH = Wallace and Hinkle (1996, 1997); S = SWS – Sloan et al. (2003); CVF = ISO/CVF (Engelke et al., 2004); A = *autoshape* (see text). The wavelength (μm) at which that segment ends is given in brackets, [λ]. If available, the SEW data cover 1.2 – 2.36 μm , otherwise the *autoshape* template is used. All the SWS spectra start at 2.36 μm . Adjacent segments start where the previous segment ends.

^b Photometry: MSX = Price et al. (2004); DIRBE = Smith et al. (2004); H = Hammersley et al. (1998); S = Selby et al. (1988); IRAS = IRAS Science Team (1988), T = Tokunaga (1984)

The increased uncertainty for the stars in Table 21 could arise from greater uncertainty in the photometry. For instance, Walker et al. (2004) estimate a 6 – 9 percent uncertainty in the IRAS photometry at 12 and 25 μm , which is about 10 times larger than that for the MSX photometry. Or it could be due to a lower SNR in the SWS spectra which limits the range over which the spectra may be used: this is indicated in the table by the relatively short wavelength at which *autoshape* is substituted for the noisy spectrum. Two of the Cohen et al. secondary standards have been relegated to Table 21: β Peg because it is a low amplitude variable star and α^1 Cen for which we replaced the Cohen et al. (1996a) model spectrum with a calibrated SWS spectrum that has good quality data only to 9 μm . The table also includes δ Dra. Although it was not included in the Cohen et al. calibration network, Cohen did create a calibrated template spectrum for this star for use as an ISO calibration standard. The ISOCAM CVF 9 – 16 μm calibrated spectrum of δ Dra from Engelke, Kraemer and Price (2004) was spliced onto the SWS shorter wavelength spectral segments. The CVF spectrum for this star has a much higher SNR than the SWS data but at much lower spectral resolution. The δ Dra spectrum was an important warm temperature tie point in the analysis of the trends in the continuum and molecular absorption profiles. To anchor the definition of these trends at the cool end, a calibrated spectrum for β Gru, a bright southern M5 III star, was derived even though this star is a low amplitude variable. β Dra is not in the Cohen et al. network but is included because it has both an SWS spectrum and a Strecker, Erickson and Witteborn (1979) near-infrared spectrum, and it provides information on the sparsely populated early G spectral classes in this analysis. Walker et al. (2004) recently noted that δ^2 Lyr has little infrared variability and should provide reasonably “accurate and reliable” calibration; because it has a good quality SWS spectrum, it too is included in Table 21.

Table 21: Additional Secondary Standards

Star	Sp. T.	T_{eff}^a (K)	θ^a (mas)	Spectroscopy ^b	Photometry ^c
α^1 Cen	G2 V	$5870 \pm 4\%$	$8.51 \pm 2\%$	P[2.36]; S[9]; A[35]	B, E, Th
β Dra	G2 II	$5100 \pm 8\%$	$3.35 \pm 5\%$	SEW; S[9]; A[35]	DIR, 2M, IRAS
δ Dra	G9 III	$4950 \pm 8\%$	$3.35 \pm 5\%$	S[10]; CVF[16]; A[35]	H, IRAS
δ Eri	K0 IV	4900	2.48	S[9]; A[35]	B, C, vdB, IRAS
θ Cen	K0 III	$4800 \pm 4\%$	$5.46 \pm 2\%$	S[9]; A[35]	DIR, B, C, vdB, IRAS
α UMa	K0 IIIa	4790	6.68	SEW; S[9]; A[35]	DIR, IRAS, Ken
ξ Dra	K2 III	4570	3.09	S[10]; A[35]	H, S, IRAS
α Ari	K2 III	$4500 \pm 4\%$	$6.89 \pm 2\%$	S[9]; A[35]	MSX, DIR, A, CX
γ And	K3 IIb	$4200 \pm 4\%$	$7.96 \pm 2\%$	SEW; S[10]; A[35]	DIR, A, IRAS
α Tuc	K3 III	$4200 \pm 4\%$	$6.19 \pm 2\%$	S[15]; A[35]	DIR, C, IRAS
λ Gru	K3 III	4200	2.82	S[11]; A[35]	C, IRAS
σ Oph	K3 II	$4100 \pm 8\%$	$3.52 \pm 5\%$	S[10]; A[35]	DIR, H, IRAS
δ Psc	K5 III	4050	3.75	S[12]; A[35]	DIR, S, vdB, IRAS
γ Phe	K4/5 III	3950	6.76	S[10]; A[35]	DIR, IRAS
H Sco	K5/6 III	$3850 \pm 8\%$	$4.90 \pm 5\%$	S[11]; A[35]	DIR, C, IRAS
δ Oph	M1 III	3850	10.23	S[13]; A[35]	DIR, C, IRAS
AE Cet	M1 III	3850	5.19	S[11]; A[35]	DIR, IRAS, F
δ Vir	M3 III	3660	10.71	S[11]; A[35]	DIR, IRAS, Ken
ρ Per	M4 III	3540	15.50	S[19]; A[35]	DIR, A, IRAS
π Aur	M3 III	$3500 \pm 8\%$	$9.05 \pm 5\%$	S[10]; A[35]	DIR, IRAS, Ken
β Peg	M2.5 III	$3490 \pm 8\%$	$17.88 \pm 5\%$	SEW[2.36]; S[35]	MSX, H, S, DIR
β Gru	M5 III	3480	27.80	S[26]; A[35]	DIR, Th, IRAS
GZ (57) Peg	M4 III + A2V	3450	7.82	S[12]; A[35]	DIR, Ker, IRAS
δ^2 Lyr	M4 III	$3300 \pm 8\%$	$11.45 \pm 5\%$	S[27]; A[35]	DIR, IRAS

^a Except where noted, the uncertainty in T_{eff} is ± 6 percent and that on θ is ± 3 percent.

^b Spectral segments are defined in the same manner as for Table 20. P = Pickles (1998)

^c Photometry: A = Alonso et al. (2000); MSX = Price et al. (2004); DIR = Smith et al. (2004); Ker = Kerschbaum & Hron (1994); H = Hammersley et al. (1998); S = Selby et al. (1988); IRAS = IRAS Science Team (1988); vdB=van den Blik, Manfroid & Bouchet (1996); Th = Thomas, Robinson & Hyland (1976); B = Bouchet et al. (1989, 1991); 2M = 2MASS (Skrutskie et al., 2006); C = Carter (1990, 1993); F = Feast, Whitlock & Carter (1990); Ken = Kenyon (1988); E = Engels et al. (1981); CX = Cohen et al. (Paper X)

7.1.1 Rationalizing the SWS Spectroscopy

The ISO SWS obtained over 1250 2.36 to 45 μm spectra on more than 900 objects of which about 50 are most suitable for calibration references: non-variable stars without circumstellar dust emission. The SWS data are available from the ISO Data Archive in the form of 288 individual spectral segments (= 12 detectors \times 12 spectral bands \times 2 scan directions) that were

obtained on a single observation. The archive contains the spectral segments that Sloan et al. (2003) processed: flat-fielding the measurements, removing glitches that typically arise from cosmic ray hits, then smoothing and re-sampling the spectrum onto a standard uniform wavelength grid. The archive also has the single spectrum Sloan et al. obtained by seaming together the average of the spectral segments.

The SWS was originally calibrated against several of the same Cohen stellar standards with composite spectra, such as γ Dra, that are upgraded in the present analysis. A mean relative spectral response for the spectrometer was determined from the SWS observations of a small number of Cohen et al. calibration standards as well as other stars that had model atmosphere spectra. The relative response thus derived was scaled to absolute values with calibrated photometry obtained by the ISO program for that purpose (Hammersley et al., 1998; Hammersley and Jourdain de Muizon, 2003). The SWS team estimated that the relative spectral response has an overall uncertainty of ~ 10 percent but has larger uncertainties of 20 – 30 percent at the longest wavelengths (Leech et al., 2003).

To splice the 12 SWS averaged spectral segments to form a single spectrum, Sloan et al. (2003) assumed that the differences in the overlap regions between segments were either additive or multiplicative. However, noise or the poor responsivity in the overlap regions, as well as incorrect assumptions about the scaling could cause the final spectrum to depart from the correct values at the band edges, occasionally by as much as 10 – 20 percent. Therefore, for a given star, we start with the twelve discrete spectral segments from Sloan et al. (2003). These segments are the average of the "up" and "down" spectra from each of the 12 detectors in the sub-band which improved the signal-to-noise by a factor of about 5 over that from a single scan. The Sloan et al. spectral segments still contain small instrumental artifacts, due to residuals left by the non-linear response correction or imprecise background subtraction, which we identify and remove in the present analysis. Also, the spectra become increasingly noisy at $\lambda > 8 \mu\text{m}$, especially for the fainter stars in Table 21.

The stellar flux decreases by more than four orders of magnitude between 2.36 and 45 μm . Therefore, the SWS spectrum is flattened as an initial step by dividing it by the Engelke (1992) approximate continuum in Equation (1). This normalization scales the entire spectrum to a single well resolved plot and increases the visibility of the small scale local trends and other discrepancies that may be present. Although the errors due to background subtraction, splicing, and uncorrected non-linearities in the detector responses may be as large as 20 percent, they are often smaller and too subtle to recognize without the normalization.

The large scale deviations in the overall shape in the SWS spectra are corrected using the assumed continuum function as a guide. Then the spectra and/or the 12 individual SWS spectral segments are brought into agreement with the accurate infrared photometry by iteratively removing artifacts and making finer scale adjustments in the continuum. Figures 53 and 54 graphically demonstrate the before and after results for α Tau, the first secondary standard for which Cohen et al. created a composite spectrum (Paper II).

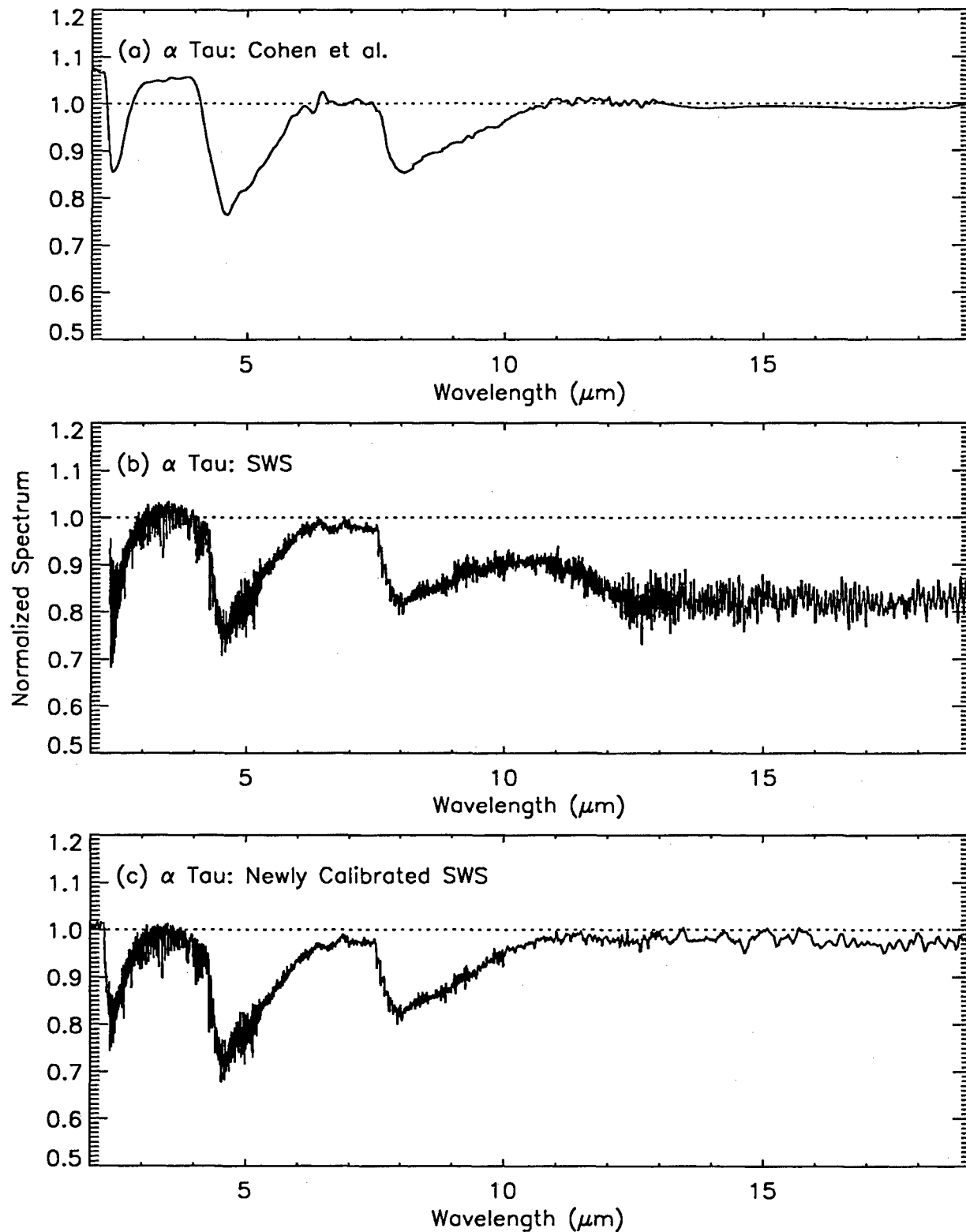


Figure 53: Comparison of the normalized mid-infrared spectra of α Tau. (a) Composite spectrum from Cohen et al. (Paper II). (b) SWS spectrum from Sloan et al. (2003) using the calibration in Version 10.1 of the SWS Pipeline processing. (c) Re-calibrated spectrum from this work. All three spectra are normalized with the Engelke function with $T_{\text{eff}} = 4050\text{K}$ and $\theta = 21.01$ mas.

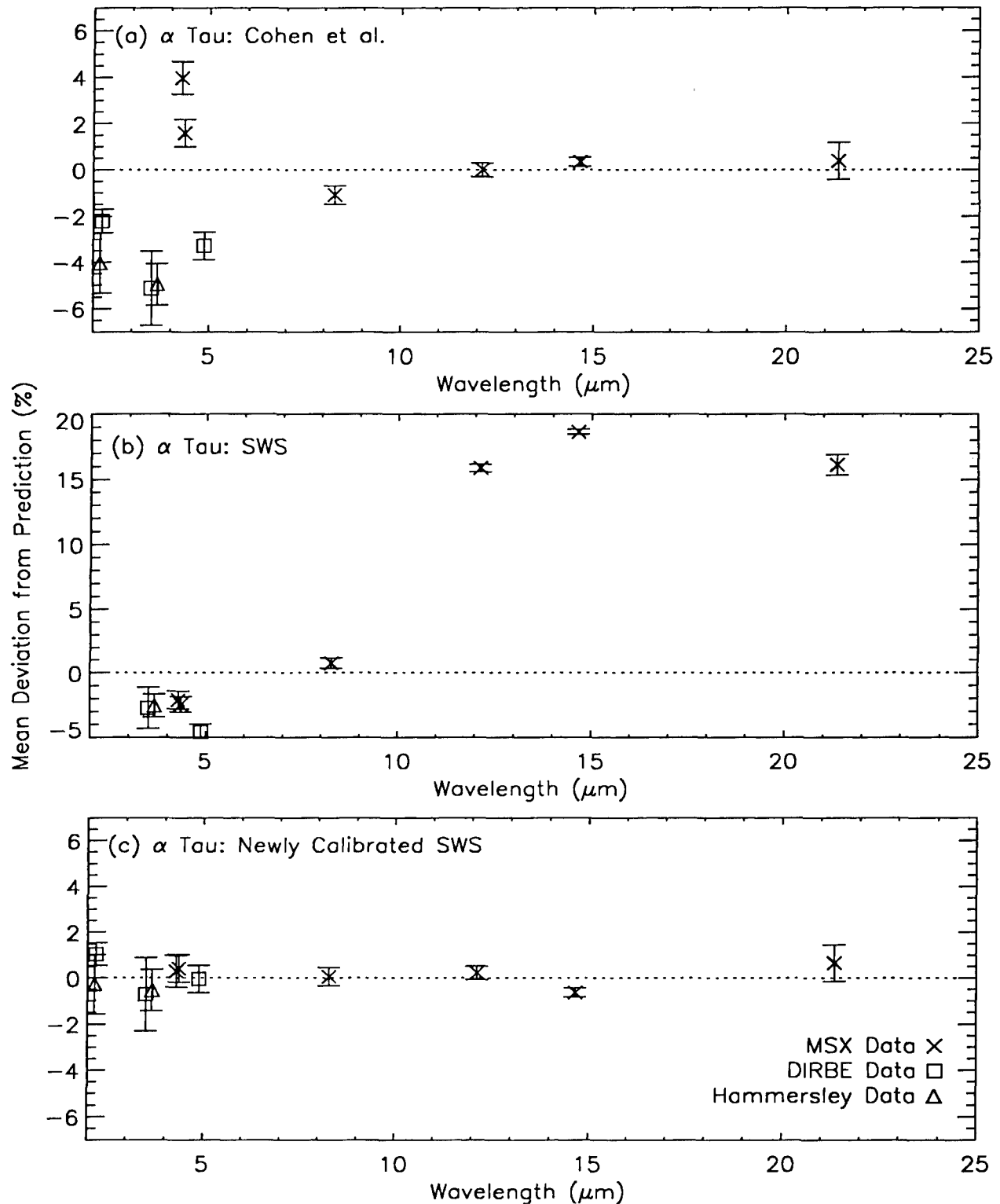


Figure 54: Comparison of the measured photometry on α Tau with that predicted from the spectra shown in Figure 1. (a) The percent difference for the Cohen et al. spectrum shown in Figure 53a; (b) the percent difference of the SWS spectrum shown in Figure 53b; (c) the percent difference for the recalibrated SWS spectrum shown Figure 53c. The crosses are the MSX photometry, the boxes are from DIRBE and the triangles are from Hammersley et al. (1998).

Figure 53a shows the Cohen et al. α Tau composite spectrum after it has been divided by an Engelke function with the effective temperature and angular diameter from Table 20. Figure 53b shows the similarly normalized SWS spectrum from Sloan et al. (2003), and Figure 53c shows our final corrected spectrum. The near-infrared portion of the Cohen et al. spectrum ($\lambda < 4 \mu\text{m}$) is higher than the Engelke reference, a common feature in many of the Cohen et al. spectra. Alternatively, the long wavelength portions of the normalized SWS spectra are often lower than the Engelke reference (20 percent low in the α Tau example).

Figure 54 shows the analogous comparisons between the measured photometry and that calculated from the spectra shown in Figure 53. Significant deviations between the measured and predicted photometry occur for the Cohen et al. composite spectrum (Figure 54a) at wavelengths below $5 \mu\text{m}$. The near-infrared overestimated flux in the Cohen et al. composites and the templates that were generated from them is the likely explanation for most of the discrepancy noted between the photometry from ‘standard’ A and K stars by Reach et al. (2005) in calibrating the Spitzer infrared camera. The photometric comparison using the Sloan et al. spectrum in Figure 54b shows good agreement with the measured photometry in the near-infrared but is almost 20 percent discordant at wavelengths greater than $\sim 10 \mu\text{m}$, which is consistent with the large uncertainty that Leech et al. (2003) assign to the SWS calibration at the longer wavelengths. Finally, Figure 54c shows that the deviations of the measurements from the predictions in our final calibrated spectrum have been reduced by using the photometry to adjust the SWS spectral segments.

Some of the normalized Sloan et al. SWS spectra, such as that of α Tau in Figure 53, show systematic trends with respect to wavelength, which often begin at the transitions between the 12 spectral fragments. Figure 55 shows the adjustment that was necessary for the SWS band 2c segment of α Tau which contains the SiO fundamental band. The solid line is the segment with the initial normalization of Sloan et al. The end of the segment is about 20 percent below where continuity arguments with the continuum approximations suggest it should be. This deficit is the reason why the flux at the longer wavelength spectrum of this star in Figure 53 is systematically low. The ‘droop’ in this spectral segment likely is due to incomplete correction of the non-linear detector response, possibly compounded by over-subtraction of the background. The deviation may be corrected by either (1) adding a constant to the background of 70 Jy or (2) multiplying by weak function of wavelength, $(\lambda / 7.3)^{0.2}$. The offset values or the exponent in the λ^n expression vary with the wavelength range and the star under consideration, but the corrections derived from the two approaches are essentially the same. The exponent, n , is universally small below $\sim 12 \mu\text{m}$; the largest value used for those spectral segments for any of the stars is ~ 0.25 . We chose to use the λ^n form of the correction for the general method of reshaping individual segments for its ease of application and because it can account naturally for problems produced by variations in response. Dotted lines in Figure 55 show the results of applying the corrections to the α Tau spectral segment; the (superimposed) corrections are indistinguishable.

Residual trends and offsets with respect to the normalized continuum are corrected in a piecewise fashion for a given segment or group of consecutive segments. The corrected stellar spectrum was thereby initially made to conform, to within a few percent, to the Engelke function near 4, 7, and $11 \mu\text{m}$, that is, in regions outside of the well-defined absorption bands.

Because the spectral energy distributions for the stars falls steeply with wavelength the SWS spectra become quite noisy at the longest wavelengths, even for the brightest objects. The

spectra beyond $\sim 10 \mu\text{m}$ are smoothed and resampled at a gradually increasing wavelength interval in order to preserve a respectable SNR, albeit at the expense of a somewhat degraded spectral resolution. We chose a wavelength dependent grid spacing with a wavelength interval specified by $(0.0001/\mu\text{m}) \times \lambda^2$, which provides 10000 samples for the final $1 - 35 \mu\text{m}$ spectra. The step size at $2.36 \mu\text{m}$ is equal to 0.02 percent of the wavelength ($\Delta\lambda \sim \lambda/4400$) and the steps are 0.34 percent of the wavelength at $35 \mu\text{m}$ ($\Delta\lambda \sim \lambda/300$). Thus the spectral resolution of the calibrated spectra in Tables 1 and 2 is not uniform across the entire wavelength range to $35 \mu\text{m}$.

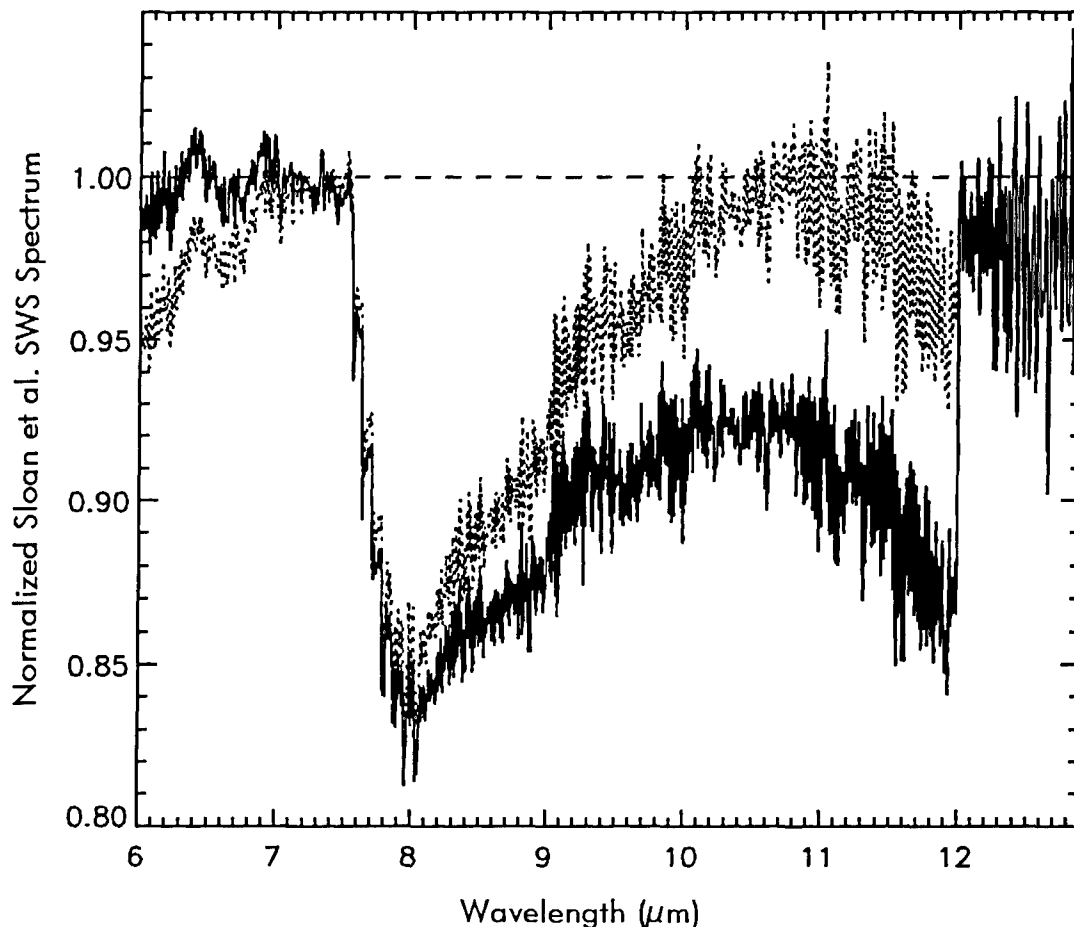


Figure 55: Adjustments to the α Tau SWS spectral segment 2C, which contains the SiO fundamental. The discontinuity at $12 \mu\text{m}$ between SWS bands 2C and 3A is likely due to the non-linear response of the detectors or over-subtraction of the background. Two corrections for the discontinuity are derived by 1) adding a corrective background constant and 2) by multiplying by $\lambda^{0.2}$ normalized so that the correction factor is one at $7.3 \mu\text{m}$. The two corrections overlap as the gray dotted lines and are indistinguishable.

The designation $S[\lambda]$ indicates the spectral range over which SWS data are used in the "Spectroscopy" column of Tables 20 and 21. The SWS spectra begin at $2.36 \mu\text{m}$ and end at the wavelength specified within the brackets. "CVF" denotes that data from the ISOCAM circular variable filter are used for δ Dra and β Gem. When smoothing does not sufficiently reduce the noise, a predicted spectral energy distribution derived with the *autoshape* template procedure is

substituted as indicated by A[35]. Cohen et al. analogously substituted an Engelke function for the noisy or missing longer wavelengths of their spectral composites and templates.

7.1.2 Splicing the Near-IR data to the SWS Spectra

The long wavelength side of the K band and DIRBE band 2 just overlap with the 2.36 μm lower limit to the SWS spectra while the DIRBE band 1 and the Hammersley et al. J and H band photometric data are at wavelengths much less than the SWS short wavelength limit. In order to make use of the near-infrared photometry to adjust the absolute flux levels, the calibrated spectra were extended to the wavelengths shorter than the SWS data by seaming the low spectral resolution ($\lambda/\Delta\lambda \sim 70$) absolute spectra that Strecker et al. (1979) obtained from the NASA Kuiper Airborne Observatory and Lear Jet Observatory between 1.2 and 2.4 μm . The eight stars in Tables 20 and 21 with such spectra are indicated by "SEW" in column 5 (we did not include the Strecker et al. Vega and Sirius spectra as we adopted model spectra for these stars). Prior to splicing, the Strecker et al. spectra are first renormalized to the flux from Sirius from Paper I $\times 1.01$ (Price et al., 2004). Higher resolution 2.02 – 2.41 μm spectra of Wallace and Hinkle (1997) for α Tau, γ Dra and μ UMa were impressed on the Strecker et al. spectra that were appended to the SWS spectra for these three stars, while the same was done for α Boo using the data from Hinkle, Wallace and Livingston (1995). For stars without Strecker et al. data, a pseudo-spectral energy distribution derived from the Strecker et al. spectra and near-infrared photometry was used to extrapolate the SWS spectrum to shorter wavelengths.

7.1.3 Photometric Scaling

While Engelke function was used to assure the continuity of the spectra, the overall spectral shape was defined by iteratively adjusting the rationalized spectral energy distribution of a star to bring it into agreement with high quality photometry on that star. Two resources for accurate photometry have become available since Cohen et al. created the calibration scale and network. The first is the MSX photometry (Price et al., 2004) that provided a much needed longer wavelength lever arm for the absolute flux calibration of the spectra. The second is the photometry in the DIRBE Point Source Catalog (Smith, Price and Baker, 2004). Cohen et al. (1998, Paper IX) confirmed that the DIRBE photometry was entirely consistent with their zero magnitude flux scale and used DIRBE photometry to add tertiary standards to their network. In decreasing order, the preference for photometry to scale the spectra is: MSX, DIRBE, Hammersley et al. (1998), Selby et al. (1988) and, for the secondary standards in Table 21, the photometry used by Cohen et al. (as, for example, given in Appendix A of Walker and Cohen, 1998). Although the DIRBE data set is both exo-atmospheric and extensive, its usefulness for the present analysis varies widely across the sample of stars. Since the DIRBE detectors had large, 42' instantaneous fields of view, the stellar measurements often contain extraneous background emission that degrades the quality of data for the fainter stars. In addition, contributions from nearby stars can only be separated out for measurements in specific scan geometries. Smith et al. (2004) rejected contaminated scans from the photometry, but this frequently produced too few scans at the longer wavelengths to provide for good photometry. For these reasons, we only use the DIRBE near-infrared photometry from bands 1 – 4 ($\lambda < 5 \mu\text{m}$).

The initial absolute spectral energy distribution of a star is weighted by the spectral response of the filters used for the photometric observation and the results are integrated over wavelength

to obtain a predicted absolute flux in each band. These integrated in-band fluxes are divided by the corresponding integrated in-band fluxes of the Sirius model spectrum. The resulting ratios between the star and Sirius in that band are then compared to the ratios actually measured by MSX, DIRBE, Hammersley, etc., such as shown in Figure 54 for α Tau. If there is a significant ($>3\sigma$) discrepancy between the calculated and measured ratios, the stellar spectrum is modified to bring the photometric predictions into better agreement with a given measurement. These discrepancies may be small in absolute terms. For example, the uncertainties in the relative MSX photometry we use are, for the most part, less than 1 percent and, in many cases less than 0.5 percent. The types of adjustments applied are:

- If the trends show a systematic wavelength dependency indicative of an incorrect effective temperature assumed for the continuum of the star, then the effective temperature in the normalization (that is, the Engelke function) is adjusted;
- If the discrepancies show a uniform bias that is independent of wavelength, then the angular size is modified;
- If the discrepancy is limited to a specific range of wavelengths, then the spectral segment(s) in that region is (are) raised or lowered as the photometry indicates. The scale factor that is used to rationalize the overlap between the segments being pieced together has a rather large uncertainty because of the poor responsivity at the edges of the SWS segments and adjacent segments are often rich in stellar lines, particularly at the shorter wavelengths. Since the segments have slightly different resolutions, the best scaling factor to combine the overlap regions is somewhat ambiguous. The λ^n correction applied to a segment may also be changed slightly to include relatively small local corrections if these are within the measurement uncertainty.
- If the star is bright enough to have both a well measured spectrum and good photometry, the departure of the spectrum from the analytic approximation to the continuum is stiffly taken into account. A ‘stiff’ adjustment is one in which the low frequency changes in the slope of the spectral continuum with wavelength $[\Delta(\text{continuum})/\Delta\lambda]$ was the smallest necessary to provide a good fit to the photometry. A modified continuum, discussed in section 7.2, is used for the fainter stars that have less complete photometry.

Since the measured and predicted photometry for each of the stars is expressed relative to Sirius, the absolute calibration of the final spectrum is directly tied to the absolute spectral energy distribution of Sirius. If the detailed Sirius model that we adopt from Paper I (modulo 1.01) were to be revised, then each final spectrum in this analysis could easily be revised as well.

Figure 56 shows the absolute spectra for the twelve stars with the most accurate photometry and/or the most extensive SWS wavelength coverage, which are normalized by an Engelke function with the effective temperatures and angular diameters specified by the box in each panel. The normalization is displayed as the horizontal line at $y = 1$. The spectral types range from G2 to M5 and are arranged in order of decreasing effective temperature or later spectral type. Overlain on each plot is the photometry used to adjust the spectra with respective error bars. The horizontal lines for each photometric value span the wavelength range between the 50 percent intensity response values. The dashed line is the normalized modified continuum approximation discussed in the next section. The dotted line is the *autoshape* template function for the effective temperature assigned to the star. How the *autoshape* template function is created is also discussed in the next section.

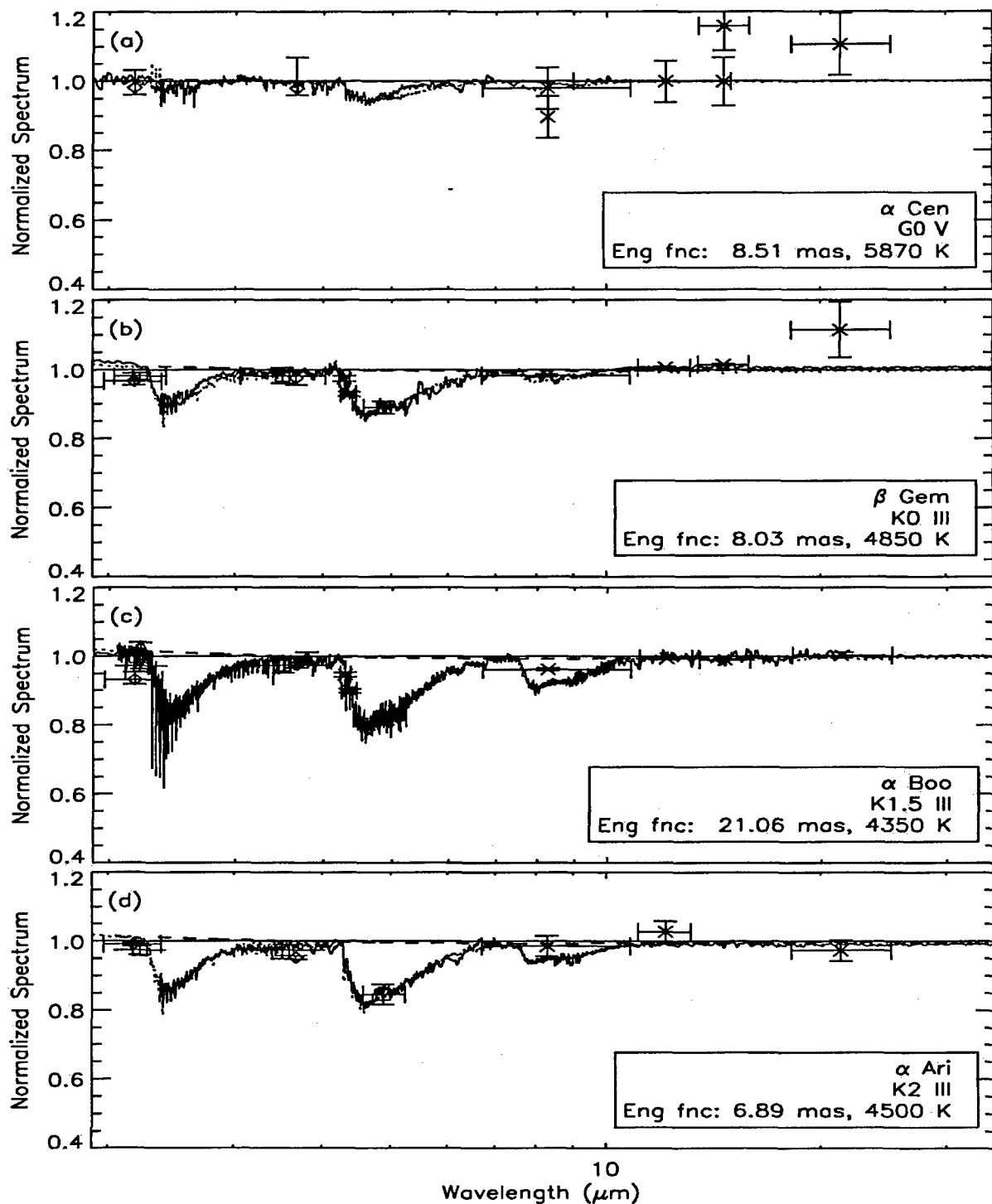


Figure 56: Calibrated SWS spectra (solid line) for 12 standard stars normalized to the Engelke function with the parameters given in the box. The dashed line is the normalized modified continuum given by Equation (14) and the dotted line is the appropriate *autoshape* function. The 1σ photometric uncertainties are denoted by the vertical error bars for each measured value and the horizontal bars indicate the >50 percent response of the spectral band.

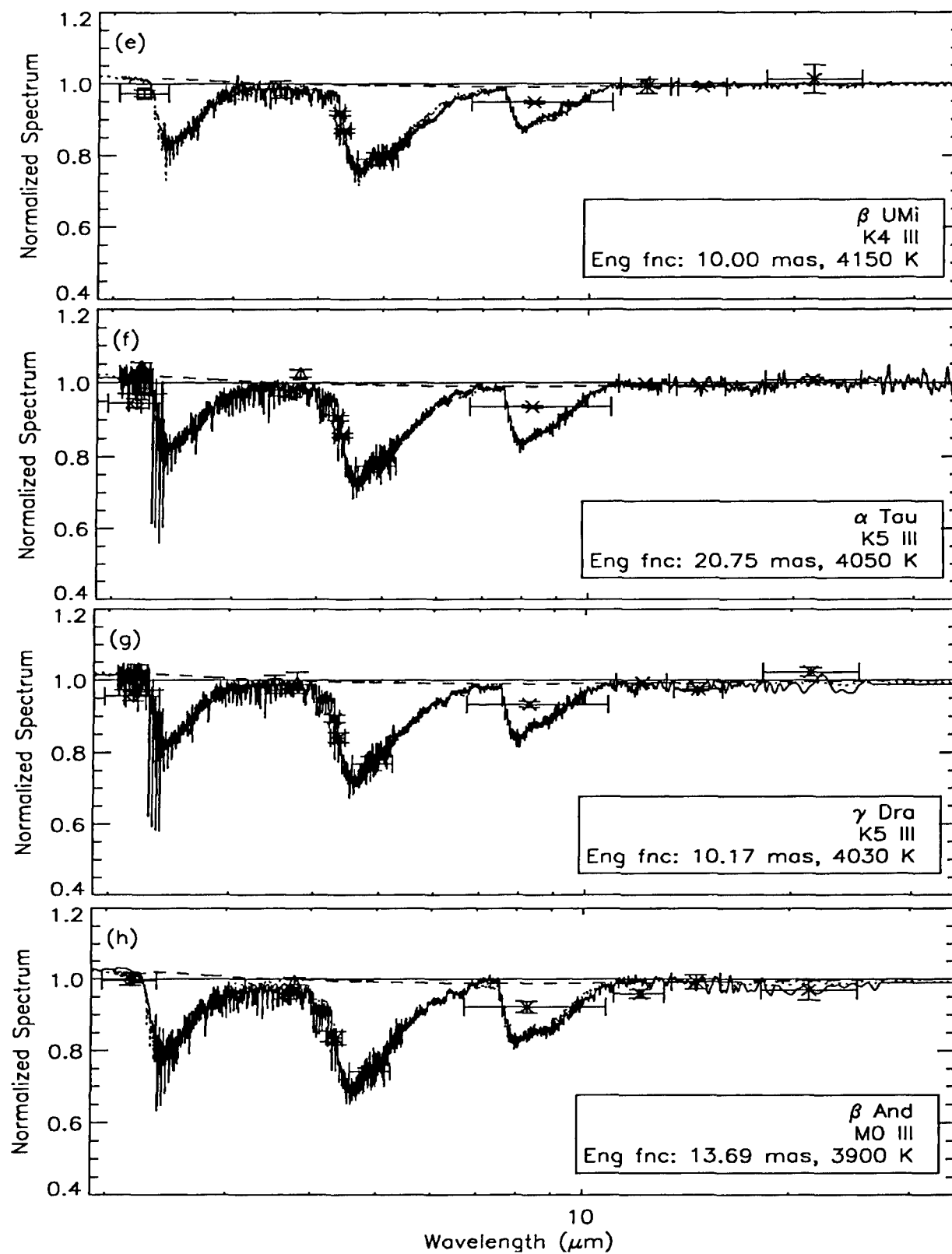


Figure 56 (continued): Normalized spectra for standard stars with intermediate spectral types.

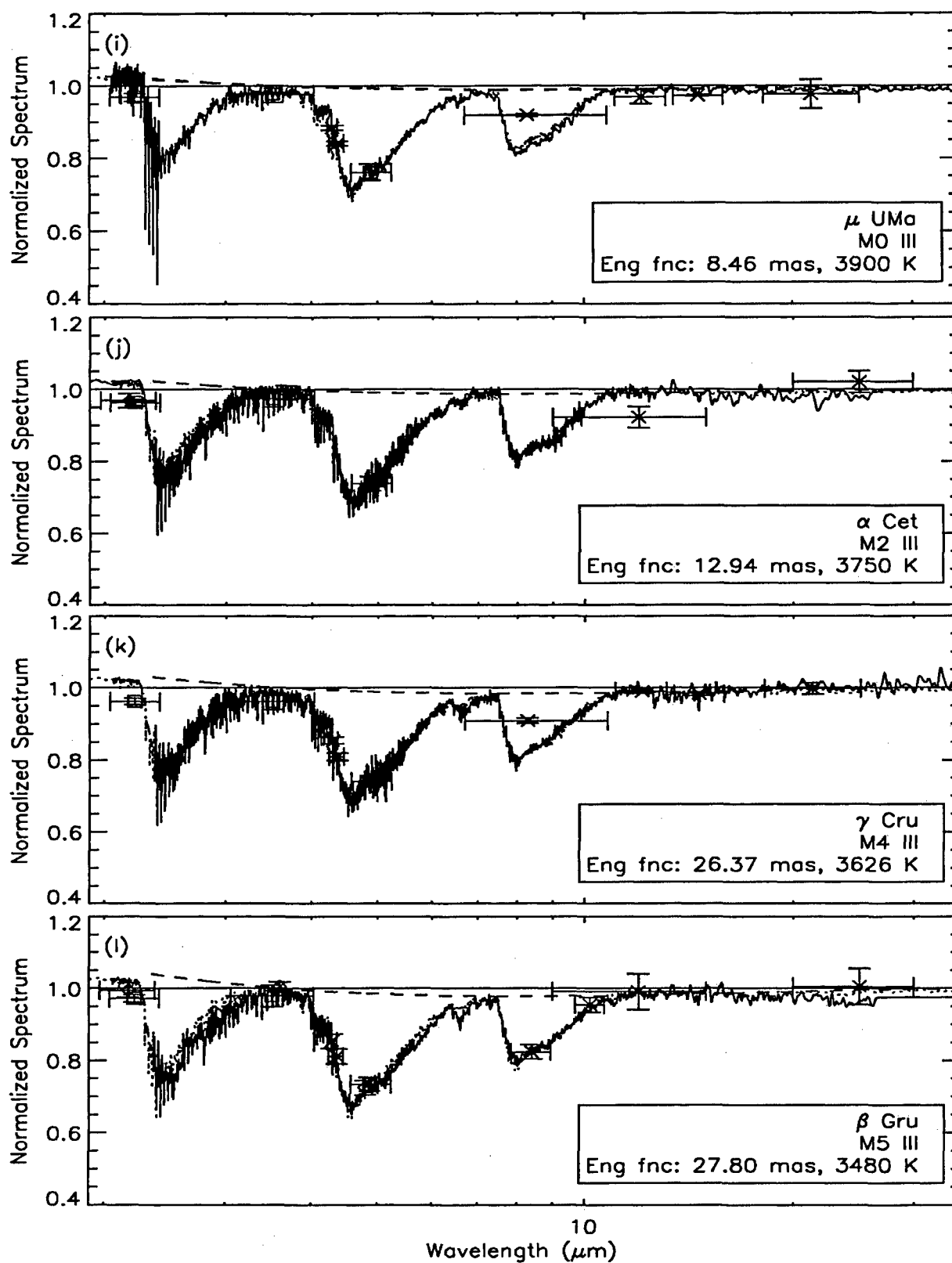


Figure 56 (continued): Normalized spectra of standard stars of cooler temperatures

7.2 The Continuum and Spectral Templates

The continua of the calibrated spectra of the stars in Figure 56 were interactively adjusted to follow the absolute photometry. There are subtle systematic differences between these final calibrated stellar spectra and the corresponding Engelke functions as may be seen by the departure of the spectra from the normalization value at $y=1.0$, the solid horizontal line in the Figure. These discrepancies increase with decreasing temperature. For example, the spectra in later type stars do not rise back to the reference level defined by the Engelke function between the molecular absorption bands, such as at $7\text{ }\mu\text{m}$. On the other hand, the continua increasingly rise above the reference level at the shorter wavelengths as the effective temperature is decreased.

We created an empirical correction to the Engelke function for $\lambda > 2.36\text{ }\mu\text{m}$ from the 12 stars in Figure 56 that is a better approximation to the continua. The shape of the continuum in the modified function is defined by a single input parameter, the effective temperature, T_{eff} . Also, the strength of the major infrared molecular absorption features in the SWS spectra due to CO and SiO were found to be also well correlated functions of the effective temperature. We created a deterministic procedure called *autoshape* based on the correlation of the continua and the molecular features with effective temperature.

Autoshape may be used to create spectral templates for a continuum of effective temperatures, as well as for specific spectral types between G2 and M5. In effect, this approximation uses the correlation of the spectra across the 12 fiducial stars, which means that the results are influenced less by random measurement error or by aberrant features that might be introduced by adopting the spectrum of a single star as the template that represents an entire spectral type. We substituted the appropriate *autoshape* for noisy or missing spectral data for stars in Tables 20 and 21 and used the function to template stars in Table 22; these stars have good photometry but no SWS spectra. We have also derived estimates of temperature and angular diameter based on the absolute spectra energy distribution defined by the function when good stellar photometry is available.

The deviations between the calibrated spectra of the stars in Figure 56 and the respective Engelke function continua arise from a variety of factors, such as additional sources of opacity other than the H^- free-free absorption upon which the Engelke function is based. Atmospheric modeling could, perhaps, provide better estimates for the stellar continua. The detailed models include a more exact treatment of opacity, the variation of temperature with optical depth as well as the gravitational effects that Decin et al. (2004) suggest are necessary to reproduce the detailed Spitzer IRS infrared calibration spectra. Thus, we examined the infrared spectra generated with detailed stellar atmosphere models for the deviations from the Engelke continuum that are similar to those observed in the recalibrated SWS spectra in Figure 56. In particular, Figure 57 shows the normalized difference between the flux from a Kurucz α Boo model atmosphere (<http://kurucz.harvard.edu/stars/ARCTURUS/>) with an effective temperature of 4300K and the corresponding Engelke function (the sharp drop at $\lambda < 1.6\text{ }\mu\text{m}$ is due to the inapplicability of the Engelke function below that wavelength at which the dominant H^- opacity source transitions from free-free to bound-free absorption).

The Engelke function is actually in better agreement with the spectroscopy and photometry on α Boo, particularly in the near infrared, than either the Kurucz α Boo model atmosphere used

in Figure 57 or the earlier models for this star used by Cohen et al. in Paper VII. The 11 other fiducial stars qualitatively show the same deviations, both positive and negative, as seen in Figure 57 but at smaller amplitudes. The dashed lines shown in Figure 56 are the best scaling of the deviation that fit the photometry. These corrections tend to increase with decreasing effective temperature of the star. Thus, the photometry for $\lambda \geq 2 \mu\text{m}$ can be brought into agreement by simply adding a scaled version of the deviations in Figure 57 to Equation (1).

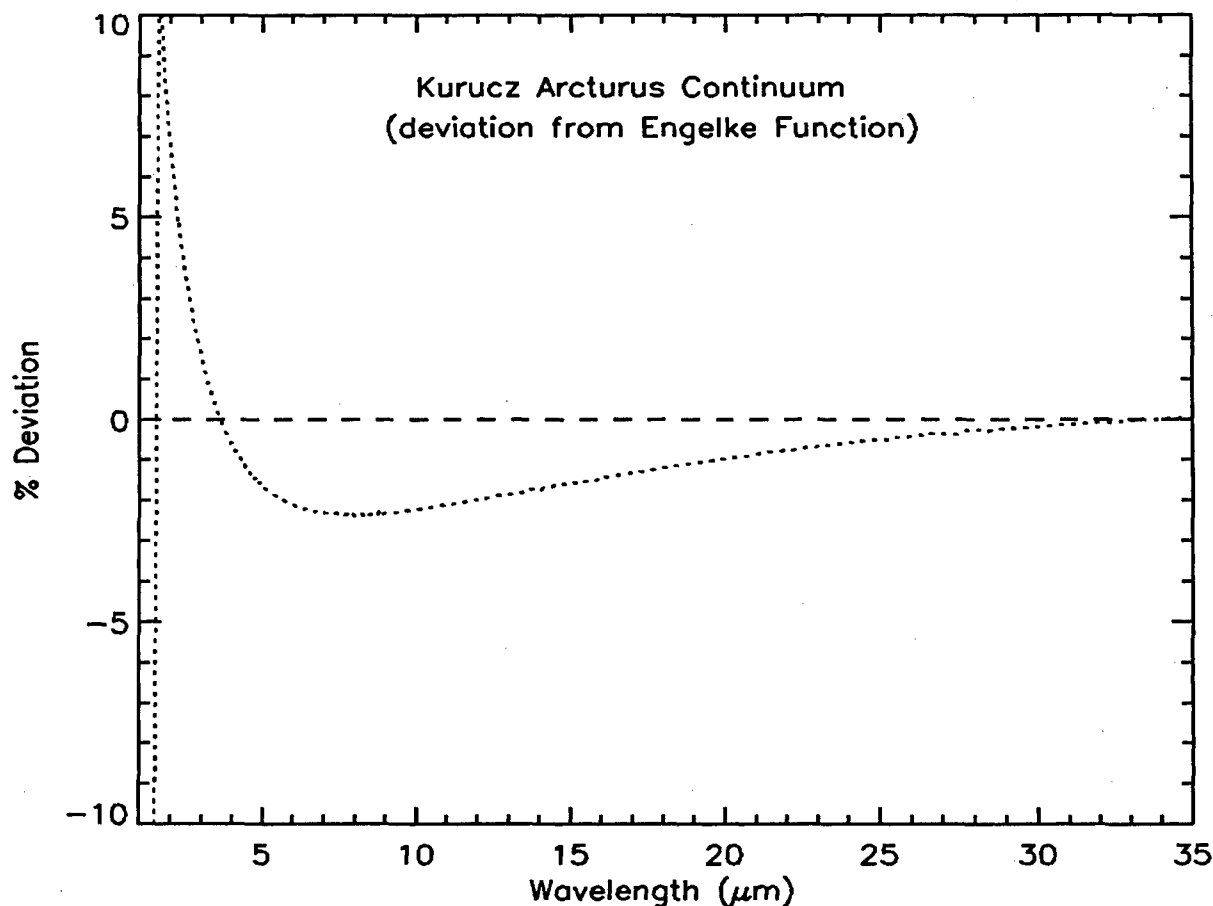


Figure 57: The percent deviation of the spectral flux from a Kurucz model atmosphere for α Boo (dotted line) from the corresponding Engelke function (dashed line). The energy distributions are normalized to the Engelke function.

Figure 58 shows that an inverse linear function of the effective temperature provides a good fit to the scaling factors for the "excess" over the 12 fiducial stars in Figure 56. The dashed line in the figure is a linear least squares fit of $0.00261 \times T_{\text{eff}} - 7.99$. For wavelengths greater than $2.36 \mu\text{m}$, the continuum used in *autoshape* is the Engelke function plus the excess in Figure 57 divided by the scale factor:

$$f(\lambda \geq 2.36\mu\text{m}) = \text{Engelke Fcn}(\lambda, T_{\text{eff}}) \left(1 + \left(\frac{\text{Kurucz}(\lambda, T_{\alpha\text{Boo}}) / \text{Engelke Fcn}(\lambda, T_{\alpha\text{Boo}}) - 1}{0.0026T_{\text{eff}} - 7.99} \right) \right) \quad (14)$$

where $\text{Engelke Fcn}(\lambda, T_{\text{eff}})$ is given in Equation (1) and $\text{Kurucz}(\lambda, T_{\alpha\text{Boo}})$ is the Kurucz model for α Boo at $T_{\alpha\text{Boo}} = 4300\text{K}$. Note that the numerator in the correction factor is the same for all spectra.

The maximum corrections in Figure 56 are small, ~ 3 percent or less for wavelengths greater than $2.5 \mu\text{m}$. The deviations defined by Equation (14) are scaled by about 0.2 for a K0 star, 0.5 at K4, and 1.0 at M4 in Figure 56.

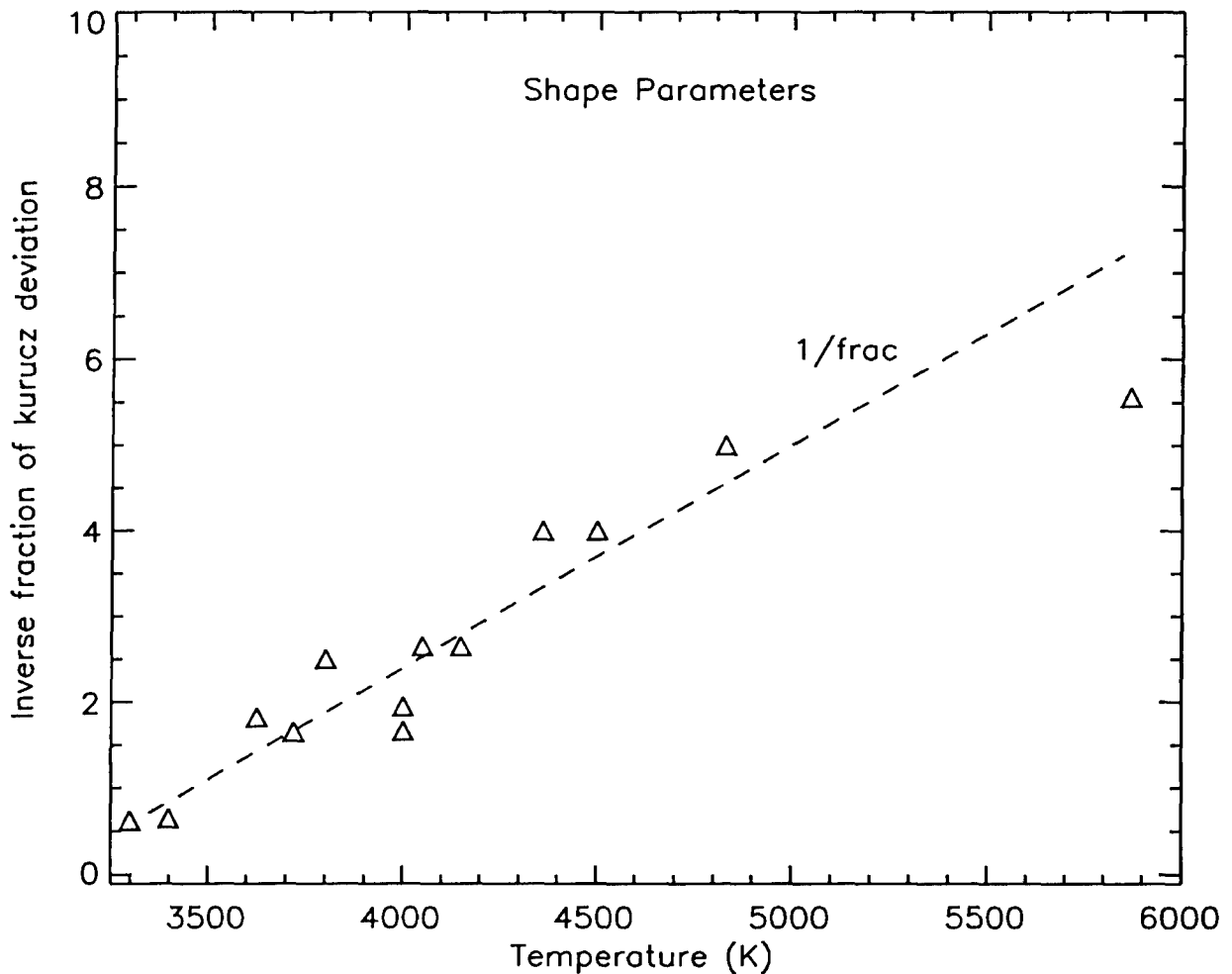


Figure 58: The inverse of the correction factor ($1/\text{frac}$) to Equation (1) versus the effective temperature of the star. The fractional correction is the amount of deviation of the α Boo continuum in Figure 57 needed for the continuum estimates in Figure 56 (the dashed lines in that Figure). The linear fit through the data in this Figure is shown by the dashed line and is equal to $(0.0026 \pm 0.0003)T_{\text{eff}} - 7.99 \pm 1.08$, which is used in Equation 14. The α^1 Cen value is the higher temperature outlier; if not included in the fit, the correction would be $0.0027T_{\text{eff}} - 8.38$.

7.2.1 Molecular Absorption as a Function of Effective Temperature above 2.36 μm

The molecular absorption features in the spectra also correlate with effective temperature and, equivalently, spectral type. Absorption profiles for the CO and SiO fundamental and overtone bands were extracted from the calibrated SWS spectra for the 12 stars in Figure 55 after being normalized by Equation (14). The 12 individual profiles for each of the four molecular bands were then averaged to obtain the mean absorption profiles shown in Figure 59. These mean absorption profiles are then scaled to fit the actual profiles of each star having an absolutely calibrated SWS spectrum in Tables 20 and 21. The scale factors obtained are plotted against the effective temperature of each star in Figure 60.

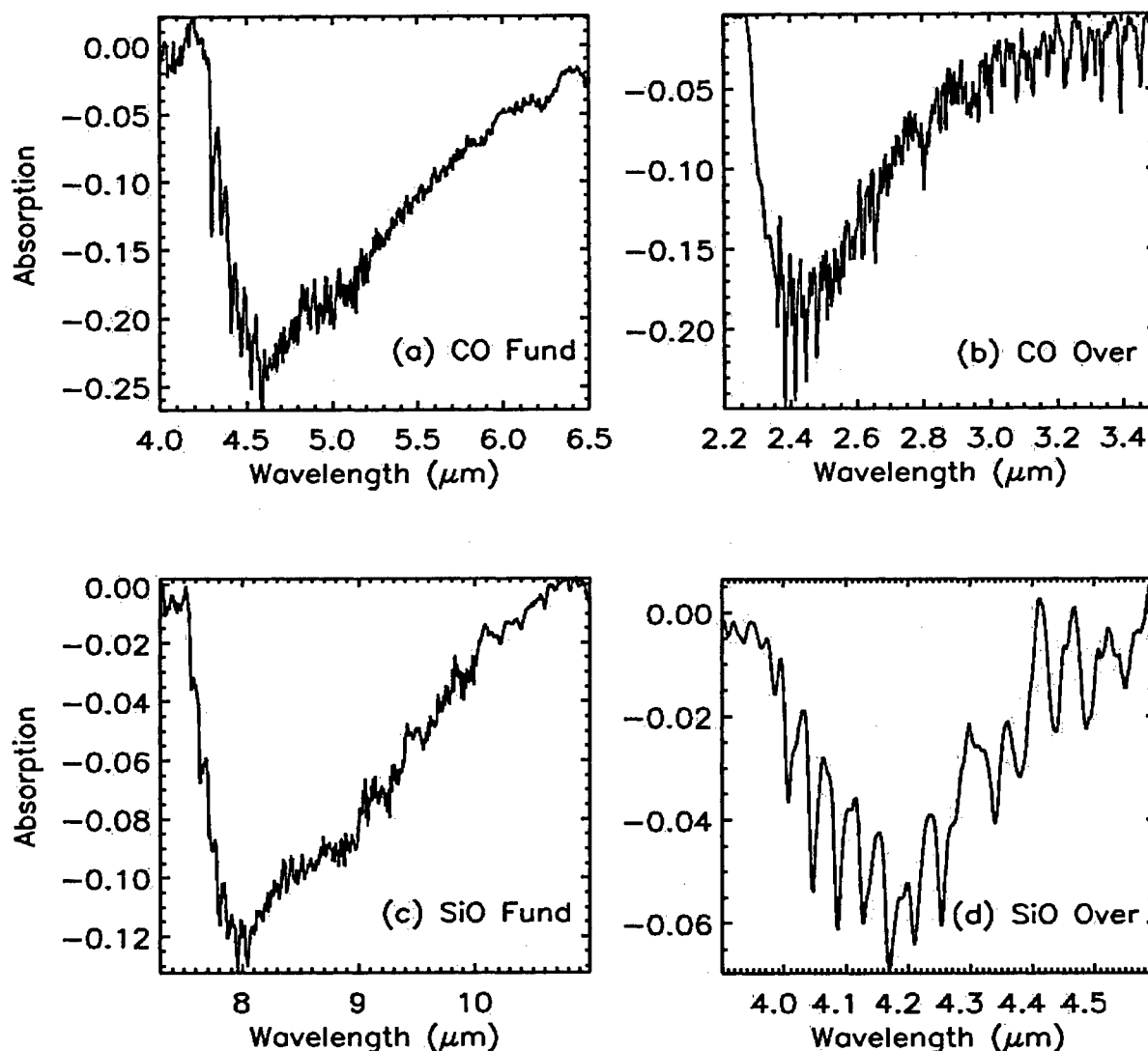


Figure 59: The averaged molecular absorption profiles. (a) The CO fundamental profile averaged over the spectra in Figure 56. A correction has been applied to remove the contribution of SiO overtone at 4.2 μm (see text). (b) The average profile for the CO first overtone. (c) The average SiO fundamental profile. (d) The average SiO overtone profile.

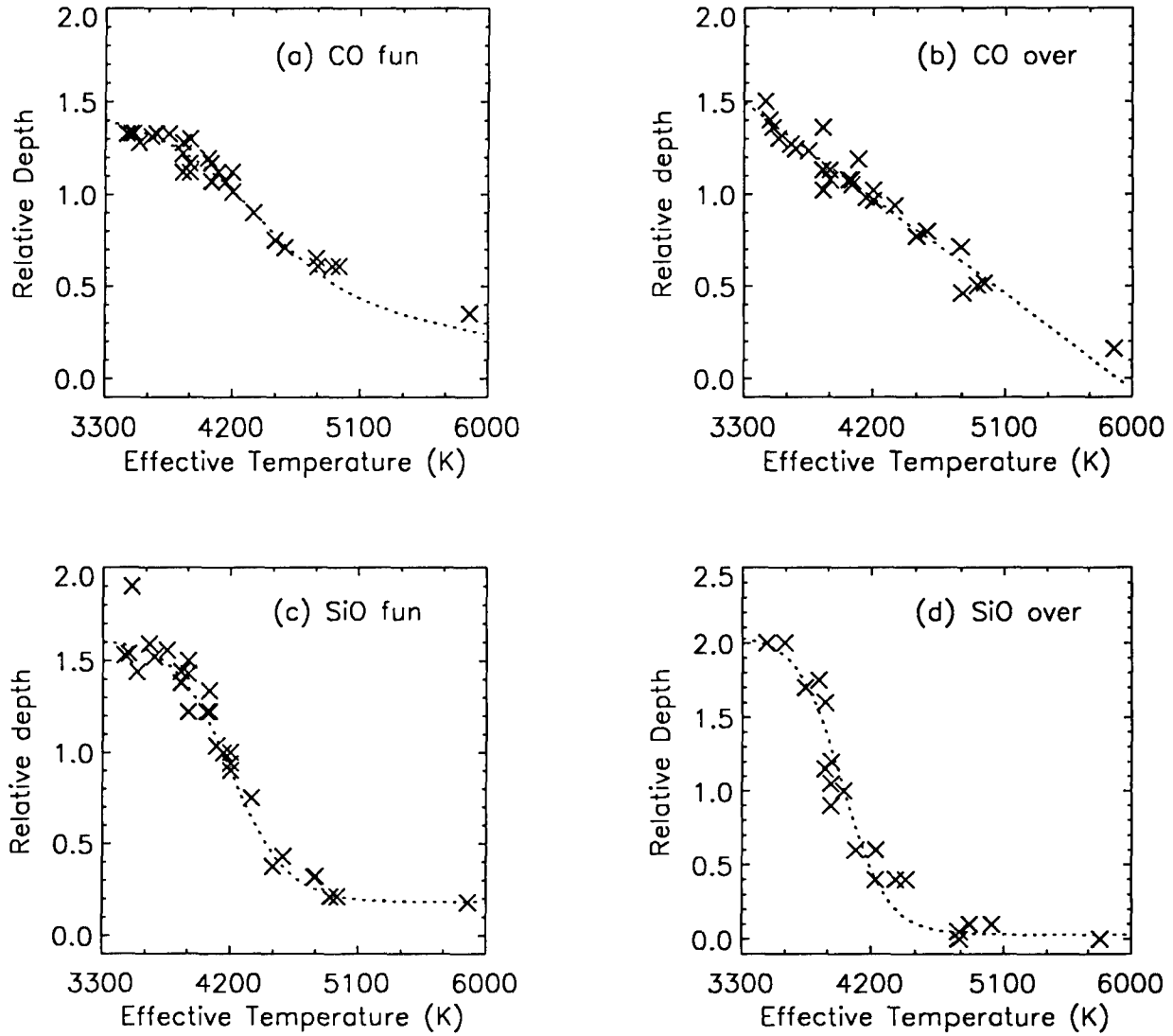


Figure 60: The factors needed to scale the profiles in Figure 59 to fit the spectra of the stars in Tables 20 and 21 plotted as a function of T_{eff} for (a) the CO fundamental, (b) the CO overtone, (c) the SiO fundamental and (d) the SiO overtone bands.

The CO absorption bands and the SiO fundamental were extracted from the normalized spectra in a straightforward fashion. The SiO overtone, however, had to be extricated from the edge of the CO fundamental by taking differences between the averaged spectra of the relatively warm stars in Figures 56a – e and the cooler stars in Figures 56f – l. The higher temperature stars seem to exhibit little SiO overtone absorption and can be scaled relative to the spectra of the cool stars such that the CO fundamental is taken out in the subtraction, thus leaving the SiO overtone.

The relative depth of the CO overtone in Figure 60 shows an approximately linear decrease with increasing effective temperature, while those for the other molecular bands exhibit a more complex behavior. For these bands, little variation is observed in the rather small absorption above a temperature that is specific for each band. The absorption linearly increases with

decreasing temperature below that unique temperature, then the features all saturate at a temperature of about 3800K, which produces an S-shaped curve. The dotted lines in the four panels in Figure 60 are analytic fits to the data. A linear trend with respect to effective temperature was used for the CO first overtone and a hyperbolic tangent function plus a linear tail was fit through the data for the other three bands. Cohen and Davies (1995, Paper V) examined the equivalent width of the SiO fundamental and found a similar trend as ours (see their Figure 10). This S-shaped dependency is also apparent in the equivalent width analysis of the molecular bands by Heras et al. (2002), as may be seen in their Figures 5 and 6. Aringer et al. (1997) provide a theoretical foundation for this behavior of the SiO overtone as a function of effective temperature and gravitational acceleration. Qualitatively, our results are in good agreement with those of others.

The average absorption profiles in Figure 59 are multiplied by the scale factor of the appropriate effective temperature in Figure 60 to fit the measured profile for each star. A quantitative comparison with other analyses may be made by rescaling the y-axes in Figure 60 to indicate either the maximum absorption depth at the band head for each star or the equivalent width of the molecular absorption. The curves in Figure 60 are converted to maximum absorption depths if the ordinates are multiplied by ~ 0.25 for the CO fundamental, by 0.22 for the CO overtone, 0.13 for the SiO fundamental and 0.065 for the SiO overtone.

To obtain equivalent widths, the plots in Figure 60 must be multiplied by the integrated area within each absorption band. For quantitative comparison with Heras et al., the integration has to be limited to the narrow limits that they adopted for each band. However, we made an initial estimate by comparing corresponding points on our Figure 60 with those in Figures 5 and 6 of Heras et al., and obtained integrated areas of $0.08 \mu\text{m}$, $0.011 \mu\text{m}$, $0.13 \mu\text{m}$, and $0.009 \mu\text{m}$ for the CO fundamental, the CO overtone, the SiO fundamental, and the SiO overtone, respectively.

Integrating the CO fundamental between the $4.3 - 4.70 \mu\text{m}$ limits used by Heras et al. produces a $0.08 \mu\text{m}$ equivalent width, which is the value we had estimated visually. A scale factor of $0.289 \mu\text{m}$ converts the y-axis of Figure 60a to equivalent widths for the entire $4 - 6.7 \mu\text{m}$ range spanned by the CO fundamental band, after removing the SiO overtone. The scale factor to integrated area over the $2.38 - 2.45 \mu\text{m}$ range used by Heras et al. for the CO overtone is $0.013 \mu\text{m}$ and the equivalent width of the entire CO overtone band shown in Figure 59b is $0.096 \mu\text{m}$. However, the equivalent width for the entire CO overtone includes the $3.02 - 3.4 \mu\text{m}$ region, which Heras et al. noted is affected by OH absorption. They do not quantitatively analyze OH but comment that it appears in stars as early as K0 and is prominent in the M stars. Integrating over the Heras et al. $7.6 - 9.0 \mu\text{m}$ limits to the SiO fundamental, we derive a factor of $0.137 \mu\text{m}$ to convert Figure 60c to the Heras et al. equivalent width; we obtain an equivalent width of $0.203 \mu\text{m}$ for the entire band. Integrating the SiO overtone over the $4.10 - 4.30 \mu\text{m}$ range adopted by Heras et al. gives $0.0095 \mu\text{m}$; the equivalent width of the entire band is $0.018 \mu\text{m}$. Thus, our results are in excellent quantitative agreement with those of Heras et al.

The agreement is not surprising as we analyzed about two-thirds of the same stars used in the Heras et al. study. However, our spectral rationalization does result in smaller scatter about the trends. Since Heras et al. found the same correlations as we but for a 50% larger sample of stars, the more precise trends that we derive should also apply to the larger data set and, by inference from the random nature of the criteria used to select these stars for SWS observation described by Kraemer et al. (2002), to the general population of giant stars with spectral types G2 and later.

7.2.2 Spectra at $\lambda < 2.36 \mu\text{m}$

A different normalization function is needed for the 1.22-2.5 μm spectral range of the Strecker et al. measurements because of the discontinuity at 1.6 μm apparent in Figure 57. An Engelke function is adopted between 1.6 μm and 2.36 μm . Below 1.6 μm a blackbody with a variable brightness temperature is used for the normalization. The brightness temperature, T_b , of the blackbody increases as a quadratic function of wavelength from the T_{eff} of the star at 1 μm to the warmer value specified by the appropriate Engelke function at 1.6 μm .

The eight Strecker et al. KAO spectra for stars in Tables 20 and 21 are separated into two groups: three ‘warm’ stars (β Dra, α UMa, and β Gem) and five ‘cool’ stars (α Boo, γ And, α Tau, β And, and α Cet). The data are normalized with the angular sizes and temperatures determined from *autoshape* fits to the data at $\lambda > 2.36 \mu\text{m}$. The equivalent temperature of the averaged normalized warm stellar spectrum is 4900K based on the depth of the CO and SiO bands, while the simple average of the individual temperatures of the stars is also about 4900K. Similarly, the averaged cool star spectrum has a temperature of 4040K. We model the near-infrared segment of *autoshape* with a linear interpolation in T_{eff} between the two average spectra divided by their temperature difference:

$$f_{\text{Normed}}(\lambda, T_{\text{eff}}) = \text{hot}(\lambda) + (4900\text{K} - T_{\text{eff}}) * \left(\frac{\text{cool}(\lambda) - \text{hot}(\lambda)}{4900\text{K} - 4040\text{K}} \right) \quad (15)$$

where $\lambda < 2.36 \mu\text{m}$. The spectra predicted by Equation (15) favorably compare with the renormalized Strecker et al. values.

7.2.3 Autoshape and Spectral Templates

The corrections and scaling that were used to create the calibrated spectra for the 12 fiducial stars shown in Figure 56 are strongly constrained by accurate MSX, DIRBE and Hammersley photometry over the entire mid-infrared wavelength range. Except at the longest wavelengths, the spectra for these 12 stars are created from observed data without appeal to model constructs; the Engelke function is used only for trending and continuity in processing the SWS data. It is more difficult to constrain global shape for the fainter stars to which Cohen et al. applied spectral templates, as many of these stars, including those in Table 21, have only a few mid-infrared photometric measurements. Also, the uncertainty in the continuum will be larger for stars that have significant reddening. Fortunately, Walker and Cohen (2003) found a reddening correction was necessary for only two of the stars in Table 2: 0.03 mag for δ Oph and 0.42 mag for π Aur.

We developed an empirical procedure, labeled *autoshape*, from the trends found in the 12 fiducial stars to constrain the scaling of the SWS data for the stars in Table 21 that have only moderate quality photometry from IRAS, for which Walker et al. (2004) estimate a 6 – 9 percent photometric accuracy. *Autoshape* combines the continuum defined by Equation (14) with average absorption profiles for the CO and SiO fundamental and overtone bands shown in Figure 59 scaled by the correlation with effective temperature in Figure 60. Equation (15) extends the spectrum from 2.36 μm down to 1.22 μm . The single input parameter to the *autoshape* algorithm is the effective temperature, T_{eff} . Figure 61 shows examples of normalized spectra produced with *autoshape* at three effective temperatures.

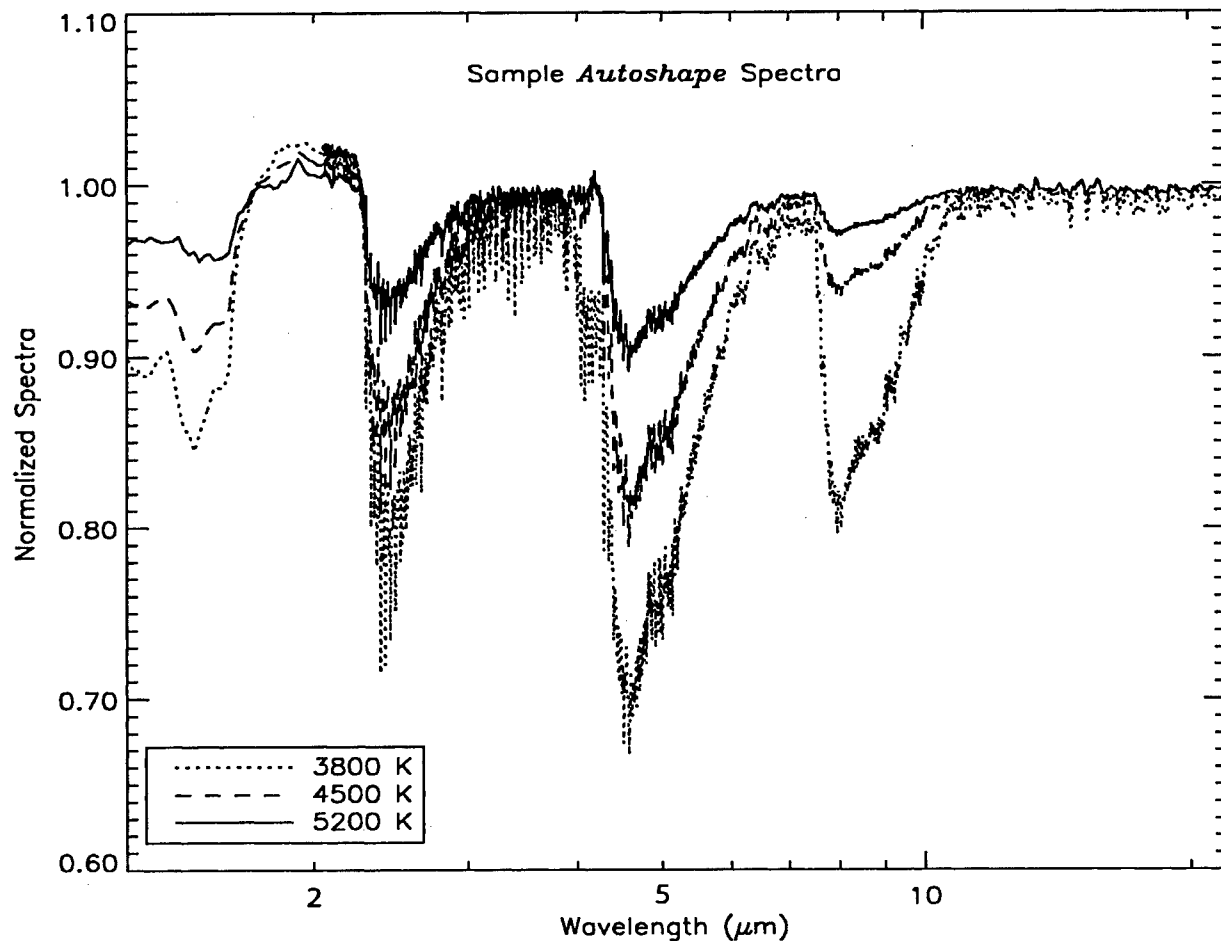


Figure 61: The *autoshape* function at three effective temperatures. The functions are normalized to the appropriate Engelke functions at $\lambda > 1.6$ and by a blackbody with a brightness temperature that varies as a quadratic function in wavelength from the effective temperature at $1.0 \mu\text{m}$ to the temperature of the Engelke function at $1.6 \mu\text{m}$. The strengthening of the CO and SiO fundamental and overtone bands as the temperature is decreased is readily apparent, as is the $\Delta v = 1$ CN red band system between 1.4 and $1.6 \mu\text{m}$ and the CO second overtone at $1.6 \mu\text{m}$; Price (1970b) discussed the temperature dependence of these features. The normalization overestimates the $\lambda < \sim 1.8 \mu\text{m}$ continuum flux, which accounts for the depression in the normalized spectra at the shorter wavelengths.

The *autoshape* spectrum for a given star may be used as a scaffold upon which to overlay the SWS segments. The effective temperature for a star with a small spread in photometry is estimated from the depth of the SWS absorption features through the correlations in Figure 60. The angular size is obtained by multiplying the normalized spectrum of the star by Equation (14) at the temperature thus derived and scaling the result to match the observed fluxes. The *autoshape* template is also substituted for the noisy or unusable SWS spectra at wavelengths longer than $10 \mu\text{m}$ for most of the fainter stars in Table 21. This replacement is analogous to the Cohen et al. substitution of Engelke functions for noisy or missing spectra at wavelengths longer than $13 \mu\text{m}$ (see Figure 62).

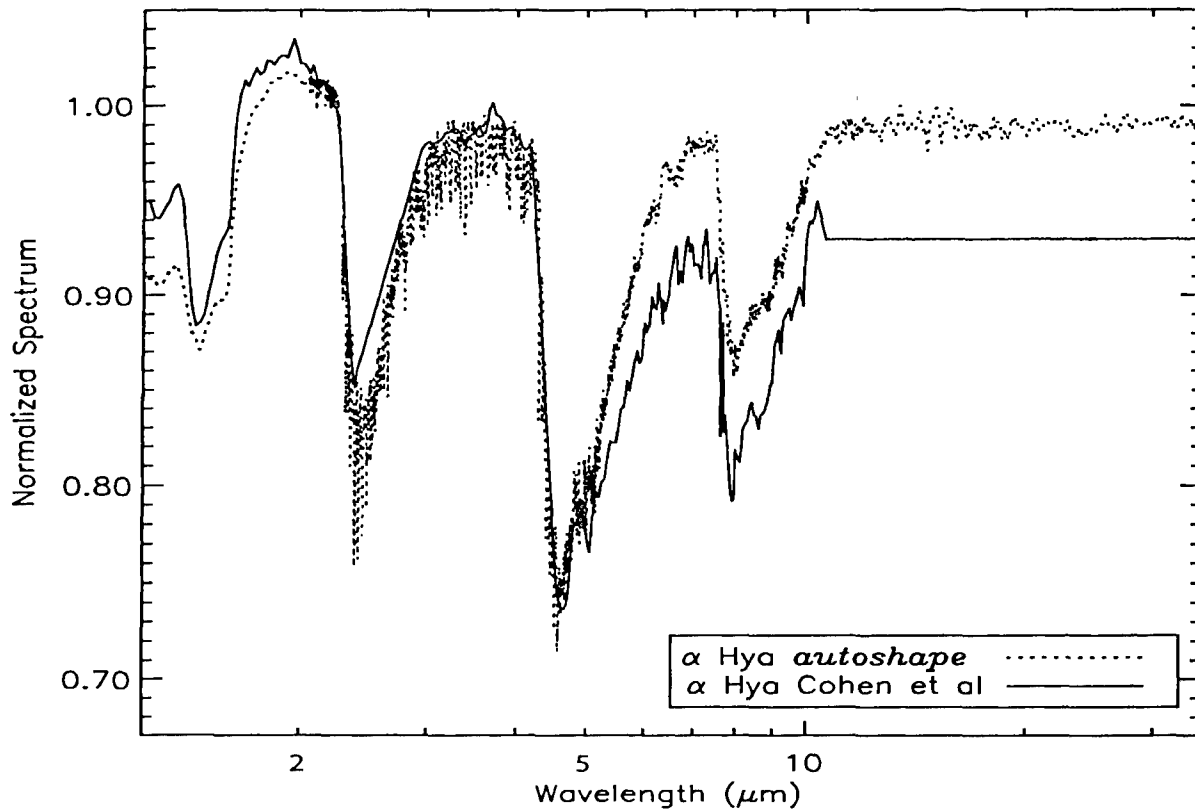


Figure 62: The *autoshape* spectrum for α Hya (dotted line) compared to the Cohen et al. composite spectrum (solid line). Cohen et al. appended an Engelke function at $\lambda > 11 \mu\text{m}$ to the composite spectrum that they created for this star.

Table 22: Templated Standard Stars

Star	Sp. Type	T_{eff} (K)	θ (mas)	Spectra	Photometry
α Aur	G4: III:	5450	10.23	A[35]	DIR, IRAS
α Hya	K3 II – III	4150	9.59	A[35]	DIR, C, B, IRAS
γ Aql	K3 III	4050	7.29	A[35]	DIR, H, S, T
α TrA	K2 II	4000	9.81	A[35]	DIR, C, IRAS
ϵ Car	K3 III + B2V	$3300 \pm 10\%$	$14.59 \pm 10\%$	A[35]	DIR, C, IRAS, 2M

^aThe uncertainty on T_{eff} is ± 7 percent and that on θ is ± 4 percent. Note that the uncertainties in T_{eff} and θ are not independent. The overall absolute flux uncertainty is typically close to that cited for θ .

^bSources of photometry are defined in Tables 20 and 21.

We created spectral templates for α Aur and γ Aql as a test of the *autoshape* routine. Low (1973) performed one of the first direct mid-infrared stellar calibrations against α Aur, as well as α Tau and β And. As shown in Table 22, *autoshape* templates were also created for the three Cohen et al. secondary standards that do not have SWS measurements, α Hya, α TrA and ϵ Cen,

in order to provide improved spectral resolution for all the original Cohen et al. secondary standards. Figure 62 compares the results for α Hya to the Cohen et al. spectral template for this star. The *autoshape* routine may be used to create higher resolution and more accurate templates for other stars in the infrared stellar calibration network (Paper X).

7.3 Derived Parameters

The stellar effective temperature and angular diameter may be derived by fitting *autoshape* to the absolutely calibrated spectrum of the star. These quantities are listed in columns 3 and 4, respectively, in Tables 20 – 22. The uncertainties are estimated by interactively varying the parameters until the fits, such as that shown in Figure 54c, obviously begin to fail. For many of the stars in Table 21, the overall spectral shape is poorly constrained by the photometry. Therefore, the variation in the depth of the CO fundamental band with effective temperature in Figure 60a is used to estimate the temperature. This typically gives uncertainties of ± 3 percent for temperature of $3800\text{K} < T_{\text{eff}} < 5000\text{K}$ with somewhat larger uncertainties above and below these temperature limits. The corresponding uncertainties in angular size, which depend on the uncertainties in both the effective temperature and the absolute flux, are then derived.

7.3.1 Angular Diameters

We compare the derived angular diameters to published values obtained by interferometric means in Table 23 and by indirect means in Table 24. The tables list the number of stars in common, the average of the ratios of the derived to the published angular diameters, and the bias in the ratio. The bias is defined as $(\text{Ratio} - 1) / \sigma_{\text{reduced}}$ where $\sigma_{\text{reduced}} = \sigma_{\text{rms}} / (N)^{1/2}$ and σ_{rms} is the root mean square deviation about the ratio average. The stars of spectral types G and K are listed separately from those with spectral type M as a dichotomy has shown up between the two groups in some of the references.

Table 23: Angular Size Comparison I: Interferometric Values

Reference	G-K Stars			M Stars		
	# of stars	Ratio $\pm \sigma_{\text{rms}}$	Bias ^a	# of stars	Ratio $\pm \sigma_{\text{rms}}$	Bias ^a
Mozurkewich et al. (2003)	10 ^b	0.999 ± 0.018	0.2	9	0.979 ± 0.023	2.7
DiBenedetto & Rabbia (1987)	5	1.023 ± 0.023	2.2	2	0.976 ± 0.031	2.2
Perrin et al. (1998)	2	1.011 ± 0.006	2.6	1	0.981	---
Dyck et al. (1998; UD)	6	1.080 ± 0.070	2.8	5	1.1 ± 0.022	20
DiBenedetto & Rabbia (1987; UD)	4	1.013 ± 0.031	1	2	1.00 ± 0.01	1
Average excluding UD results		1.012 ± 0.011			0.979 ± 0.003	

^aBias = $(\text{Ratio} - 1) / \sigma_{\text{reduced}}$; $\sigma_{\text{reduced}} = \sigma_{\text{rms}} / (N)^{1/2}$; UD = uniform disk

^bLimited to stars with less than 10% DIRBE variability: see Section 7.4.

Table 24: Angular Size Comparison II: Indirect Values

Comparison	G-K Stars			M Stars		
	# of stars	Ratio $\pm \sigma_{\text{rms}}$	Bias	# of stars	Ratio $\pm \sigma_{\text{rms}}$	Bias
Decin et al. (2000)	7	1.006 ± 0.008	2	3	1.033 ± 0.026	2.2
Blackwell et al. (1991)	5	1.020 ± 0.009	5	3	1.030 ± 0.006	9
Alonso et al. (2000)	6	1.010 ± 0.015	1.6	1	1.039 ± 0.026	2.6
Manduca et al. (1981)	5	1.025 ± 0.005	11	2	1.033 ± 0.027	1.7
DiBenedetto (1998)	4	0.999 ± 0.012	0.2	0	---	---
Perrin et al. (1998)	0	---	---	3	1.049 ± 0.025	3.4
Average		1.012 ± 0.011			1.037 ± 0.008	

$$\text{Bias} = (\text{Ratio} - 1) / \sigma_{\text{reduced}}; \quad \sigma_{\text{reduced}} = \sigma_{\text{rms}} / (N)^{1/2}$$

Overall, our sizes average about 1 percent larger than the mean of the values found in the literature. The comparisons with published results on G and K type stars, however, show much less scatter than the comparisons with M stars. Possible explanations for the increased discrepancy in the M star size include: inappropriateness of our fitting function to M stars, limitations in the methods used in the direct measurements perhaps relating to limb-darkening corrections (discussed below), or a lack of constancy among M stars as a group. A large disagreement is also apparent among the published angular diameters for M stars. There is, however, some pattern to the divergence between our results and those obtained in particular studies or with specific methods, such as all M stars from a specific reference are either larger or smaller than ours. Also, there are correlations in the angular diameters obtained by similar methods in the sense that M star interferometric diameters are larger than ours while indirect determinations produce smaller M stars diameters.

7.3.1.1 Interferometric Sizes

The values that we derive for G and K stars are in good agreement with the interferometric diameters from Mozurkewich et al. (2003), Perrin et al. (1998), and Di Benedetto and Rabbia (1987) but average about 2 percent smaller for the M stars, particularly for stars of spectral type M2 and later. The Dyck et al. diameters are ~ 10 percent smaller than our results but their values are given for a uniform disk (UD); the other references in Table 23 apply corrections for limb darkening using model expectations. Di Benedetto and Rabbia (1987) published both uniform disk and limb-darkened diameters. When their uniform disk values are compared to our derived values, the discrepancy between the G & K stars and the M stars is greatly reduced. This suggests that the M star differences in the interferometer measurements may be an artifact of the particular limb-darkening models being applied.

There is empirical support for the application of limb-darkening models to K and G stars but little specific as to their use with M stars. For example, Di Benedetto and Bonneau (1990) found that the visibility function for β And (M0 III) at 1.65 and 2.2 μm was inconsistent with a conventional limb-darkened disk. They proposed that the discrepancies could be explained if the star had a small bright spot. Haniff, Scholz and Tuthill (1995) observed Mira variables and found that Gaussian profiles provided a better approximation to the radial brightness profiles than did uniform disks although, besides being much later types than our sample, these stars also show complicated and asymmetric structure.

Comparing results for individual stars: Quirrenbach et al. (1996) used the MkIII Optical Interferometer to measure the angular diameter of α Boo (K1.5 III) at 5 visual wavelengths. They found that the measured uniform disk diameters quantitatively agreed with wavelength-dependent predictions derived from the limb-darkening coefficients of Manduca (1979). Our derived diameter of 21.1 ± 0.2 mas is in good agreement with their "true limb-darkened diameter" of $21.0 \text{ mas} \pm 0.2 \text{ mas}$. Hutter et al. (1989) also used the Mk III to measure 24 stellar diameters albeit before the calibration and observing techniques were well understood (Mozurkewich et al. 2003). Our agreement is good (within 1σ) for β And (M0 III) and γ Dra (K5 III) although their α Ari (K2 III) is significantly larger than other results including ours, which is consistent with the Mozurkewich et al. (2003) comment that the early Mk III results tended to overestimate the diameters.

Hajian et al. (1998) first confirmed stellar limb darkening for the K giants α Ari and α Cas (K0 III), and subsequently for several additional stars (e.g. Nordgren et al., 1999; Wittkowski et al., 2001), with the Naval Prototype Optical Interferometer. The data confirmed the presence of limb-darkened radial profiles but do not yet allow model-independent determination of empirical limb-darkening profiles. The authors note that the model-dependent limb-darkening corrections are several times larger than the formal uncertainties in the interferometric observations. Our diameter of 6.89 ± 0.14 mas for α Ari is slightly higher than the limb-darkened diameter of 6.80 ± 0.07 mas which they obtained but is well within the uncertainties.

Kervella et al. (2003b) used the INterferometer Commissioning Instrument on the Very Large Telescope (VINCI/VLTI) in the K band to derive a limb-darkened diameter for α^1 Cen (G0 V) of 8.51 ± 0.02 mas, the same value we derive. Kervella et al. (2003a) give 6.01 ± 0.02 mas for Sirius, also at K band. As we noted in section 2.1, this is 1.5σ smaller than the 6.04 mas adopted for Sirius by Cohen et al. in Paper I and 3σ less than the size of 6.07 mas inferred by the revised flux for this star (Price et al., 2004) that we adopt in the present analysis.

Ridgway et al. (1982) made multiple lunar occultation observations on α Tau (K5 III) over a variety of wavelengths to constrain limb darkening and found a corrected angular size of 20.88 ± 0.10 mas, in good agreement with our diameter of 20.75 ± 0.21 mas. More recently, Richichi and Roccatagliata (2005) analyzed a combined set of lunar occultation and long baseline interferometric measurements of α Tau and found an average limb-darkened diameter of 20.58 ± 0.03 mas, again within 1σ of our uncertainty.

The discordance among limb-darkening correction factors is highlighted in studies that observed stars over a range of spectral types. Di Benedetto and Rabbia (1987) observed 11 K and M giants at K band with the I2T interferometer in France. They used the Manduca (1979) limb-darkening models to derive correction factors that ranged from 0.975 for β Gem (K0 III) to 1.036 for β And (M0 III). On the other hand, Perrin et al. (1998) use a correction factor of 1.035 for the K1.5 through M8 stars that they studied; this value is based on the Manduca (1979) models, supplemented by those of Scholz and Takeda (1987) for the coolest stars. Mozurkewich et al. (2003) conducted perhaps the most thorough analysis of limb darkening to date using 85 stars with spectral types from A7 V to M6 III. They examined the variation in measured angular diameters at four visual wavelengths and compare their results with those from other groups at K band. They used correction factors from models by Claret, Diaz-Cordoves and Gimenez (1995) and Diaz-Cordoves, Claret and Gimenez (1995) to derive limb-darkened diameters from their uniform diameter measurements. At 800 nm, the corrections range from about 6 percent at K0 to

almost 10 percent for M4 stars; the 451 nm corrections are about 4 percent larger. The K band corrections grow from about a 1 percent correction for K stars to just over 3 percent for the late M stars. Thus, applying a single correction value to all stars, even at K band, could lead to discrepancies of about 4 percent; the results of Mozurkewich et al. are typical for the midrange of the spectral types.

Besides the limb-darkening issue, other effects could contribute to the disagreement between our derived angular sizes and those from other analyses. In their equivalent width analysis, for instance, Heras et al. (2002) specify wavelength limits for water vapor absorption but derive no values for the corresponding equivalent width over this range. They note that model atmospheres calculated by Decin et al. (2000, 2003a, b, c) indicate that water vapor absorption is broad and depresses the continua of M2 – M4 stars by 2 percent and by 5 percent for stars of M5.

The fact that we do not account for water vapor absorption in developing the *autoshape* routine may contribute to the K – M discrepancies in angular diameters compared to the interferometric determinations. A simplistic view of the situation is that the continuum flux from the lower atmosphere predicted by the Engelke function is more or less uniformly depressed across the infrared by absorption due to water vapor and opacity sources other than H^- . This absorption could be (partially) taken into account by the algorithmic modifications in Equation (14), which depresses the mid-infrared continuum of M stars by 2 – 3 percent. The solid angle of the star in Equation (14) would then increase to compensate for any additional absorption. Thus, a 2 – 5 percent uncompensated absorption would produce a 1 – 2 percent low bias in the derived angular diameters.

7.3.1.2 Indirect Determinations of Angular Diameters

The angular diameters based on the indirect infrared flux model (IRFM; e.g. Blackwell et al. 1991) methods are all systematically smaller than ours (Table 24). Typically, the M star values are 4 percent smaller, while K stars are 1 percent smaller. A primary cause of this discrepancy is the different zero point flux adopted for the flux calibrator used in a particular study. For example, Manduca, Bell and Gustofsen (1981) fit models to the Strecker et al. (1979) 1.2 μm – 5.5 μm spectra for five of the stars in our analysis. They rescaled the Strecker et al. calibration, which was referenced to the Vega model of Schild, Peterson and Oke (1971), to match the Dreiling and Bell (1980) model for Vega. The resulting diameters are uniformly 3 percent lower than ours with negligible scatter about the bias. The lone M star in common, β And, had the same bias as the other stars. This bias is primarily due to the different zero point flux adopted for Vega by Manduca et al., which falls 3 – 4 percent below the Vega flux adopted by Cohen et al. (Paper I) in this wavelength region. Adjusting the Manduca et al. flux reference to the absolute flux scale of Price et al. (2004) reduces the average difference between their diameters and ours to ~ 1.5 percent. Comparing the diameters for the 28 stars from Tables 20 – 22 in common with those derived by Cohen et al., results in a ratio of 1.012 ± 0.026 . The two results are in good agreement given the internal uncertainty estimated by Cohen et al. of 1 percent.

The accuracy of the angular diameters derived by the indirect methods, including the current work, is directly proportional to the accuracy of the adopted absolute flux calibration. The differences in the M star results obtained from some indirect methods may reflect the calibration uncertainty of their photometry for these stars. Alternatively, we may overestimate the mid-

infrared flux for the M stars (although neglecting the water vapor absorption would cause our diameters to change in the wrong direction).

7.3.2 Effective Temperatures

We can also compare the effective temperatures derived from *autoshape* with those in the literature. Table 25 gives the results of such a comparison in which the M stars listed separately from the earlier types. The agreement between the effective temperatures that we derive and those determined by others is generally quite good. Once again, the M stars show a larger disagreement than the earlier spectral types, 3–5 percent for the comparisons with Mozurkewich et al. (2003) and de Jager and Nieuwenhuijzen (1987).

Ramirez and Melendez (2005) recently used the infrared flux method to derive temperatures and angular diameters of giant and dwarf stars. They too found that the direct methods (specifically, that of Mozurkewich et al. 2003) produce lower temperatures for the M stars compared to the infrared flux method results and suggest that the limb-darkening correction for the interferometry may be the source of this discrepancy.

Table 25: Temperature Comparison

Comparison	G-K Stars			M Stars		
	# of stars	Ratio $\pm \sigma_{\text{rms}}$	Bias ^a	# of stars	Ratio $\pm \sigma_{\text{rms}}$	Bias ^a
Heras et al. (2002)	18	1.01 \pm 0.03	1.5	12	1.00 \pm 0.03	0.4
De Jager & Nieuwenhuijzen (1987)	16	1.00 \pm 0.03	0.0	12	1.05 \pm 0.02	8.5
Ridgway et al. (1980)	13	1.00 \pm 0.01	0.0	11	1.00 \pm 0.01	0
Van Belle et al. (1999)	12	1.01 \pm 0.03	1.2	11	1.01 \pm 0.02	1.7
Mozurkewich et al. (2003)	10	1.02 \pm 0.03	2.1	9	1.03 \pm 0.03	3.2
Alonso et al. (2000)	6	1.01 \pm 0.02	1.4	3	1.00 \pm 0.03	0.2
Dyck et al. (1998)	6	0.96 \pm 0.03	3.2	5	0.96 \pm 0.015	5.5
Di Benedetto & Rabbia (1987)	5	1.00 \pm 0.02	0	2	1.04 \pm 0.02	2.6
Blackwell et al. (1991)	5	1.01 \pm 0.014	1.7	3	1.01 \pm 0.01	1.5
Manduca et al. (1981)	5	1.00 \pm 0.01	0.3	2	0.99 \pm 0.03	0.4
Di Benedetto (1998)	4	1.03 \pm 0.02	3.3	0	---	---
Perrin et al. (1998)	2	1.02 \pm 0.01	1.6	1	1.019	---
Average		1.01 \pm 0.016			1.01 \pm 0.02	

^aBias = (Ratio - 1) / (σ_{rms} / \sqrt{N})

De Jager and Nieuwenhuijzen (1987) created an interpolation table using effective temperature and spectral types for 268 stars compiled from the literature. They included tables of temperature versus spectral type for luminosity classes I, III and V, and derived smoothly varying numerical parameters fitted to the discrete classifications. The comparison in Table 24 is between the temperatures predicted for the spectral classes given in Tables 20 and 21 with the temperatures derived herein. The average ratio for K giants is 1.00 \pm 0.03. But, as may be seen in Figure 63, the temperatures for the M giants in Tables 20 and 21 are systematically higher

with respect to the de Jager and Nieuwenhuijzen values. The average ratio to M giants alone is 1.05 ± 0.02 , which corresponds to a difference of about 200 K. The discontinuity in the de Jager and Nieuwenhuijzen data in Figure 63 is due to their inclusion of spectral types K7 and K9 that are not often used (e.g. Ridgway et al., 1980; Dyck et al., 1996) and probably contributes to the temperature discrepancy with our results.

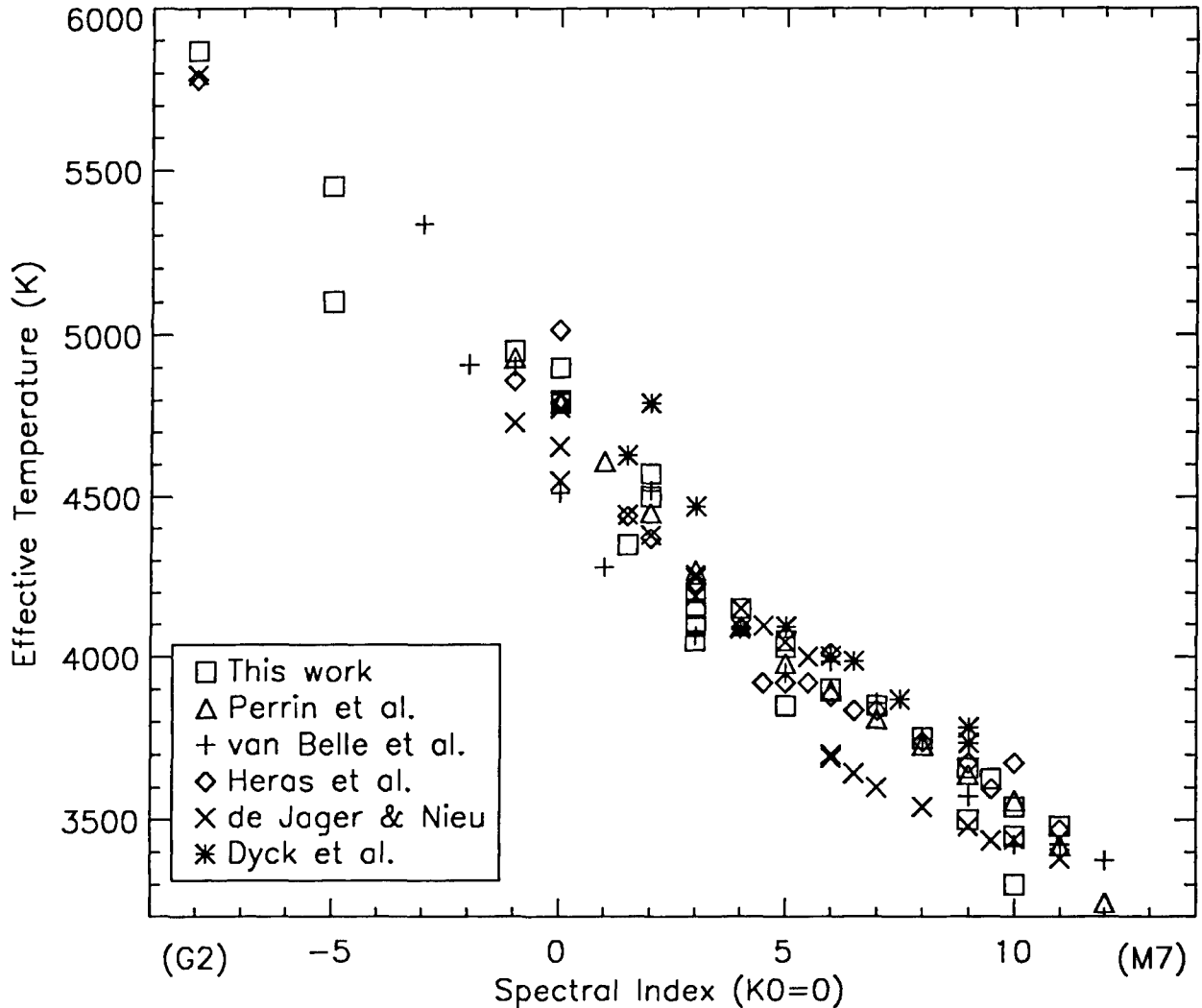


Figure 63: The effective temperatures derived in the present analysis are plotted against spectral index and are compared to those found in the literature. The spectral index ranges from -8 for spectral type G2 to -1 for G9, 0 for K0 to 5 for K5, and 6 for M0 to 12 for M6.

Figure 63 shows the derived temperatures given in Tables 20 and 21 plotted against the spectral type together with previous determined mean effective temperatures from the literature. The scatter in the comparisons is somewhat better for the spectral range G to K than for the M stars but the agreement is consistent for the different spectral types, especially if the discordant de Jager and Nieuwenhuijzen values are excluded. Thus, we conclude that Equation 2 is a good representation of the absolute emergent infrared spectral distribution of late type stars and that its

defining parameter, T_{eff} , is the characteristic temperature of the star. However, water vapor and other sources of infrared opacities may bias the derived angular sizes to values lower than measured. If this is the case, then the M star results obtained from some of the indirect methods may reflect the calibration uncertainty of the photometry for these stars.

7.4 Uncertainties and Caveats

7.4.1 Estimated Uncertainties

Price et al. (2004) derived a formal rms uncertainty of 1.1 percent in the direct calibration of the absolute flux for α CMa, the primary standard star used in this analysis. In addition to this are our uncertainty estimates in seaming the spectral fragments together and in the photometry used to scale the results to absolute fluxes.

In general, we estimate the uncertainty in the local shape to be about 5 percent near 1.2 μm for the *autoshape* extrapolations, 2.5 percent at 2.36 μm , 1 percent between 3 μm up to 12 and perhaps 2 percent at longer wavelengths. These uncertainties were estimated from comparisons of multiple SWS spectra on same star (where available), comparisons of the spectra from different stars of same spectral type, and from the variations in the photometry used in this analysis that were obtained from different sources. Stars with several SWS observations required different trend corrections. The resulting profiles agreed well overall, but there is a 1 – 2 percent local disagreement on the long wavelength side of the SiO bands. Discrepancies between the normalized spectra for two stars of a given spectral type usually are a percent or less and are rarely as large as 2 percent. Variation in the spectral features within a spectral class has also recently been observed in Spitzer IRS calibration data (Sloan et al., in preparation). For stars with Strecker et al. data, we estimate the uncertainty to be ~ 2 percent in the 1.22-2.36 μm range.

We (partially) accounted for water absorption by the manner in which we tied the *autoshape* function to the photometry. However, absorption by the ν_2 bending mode at $\lambda = 6.55 - 6.70 \mu\text{m}$ is apparent on the wings of the CO fundamental for the cooler stars in Figure 56 and there is some ambiguity as to how much the water vapor absorption is present that may lead to the bias in the derived angular diameters for the cool stars. A reasonable flux bias error is 2 – 4 percent, which is about half that needed to rationalize the angular diameters.

Figure 64 shows the root mean square of the deviations between the absolute spectra of α Boo (K1.5 III), α Tau (K5 III), γ Dra (K5 III), β And (M0 III) and γ Cru (M4 III) and their respective *autoshape* spectral energy distributions, normalized to the *autoshape* distributions. The difference between the *autoshape* spectra and the observed, absolutely calibrated spectra is less than 1 percent for most of the wavelength range.

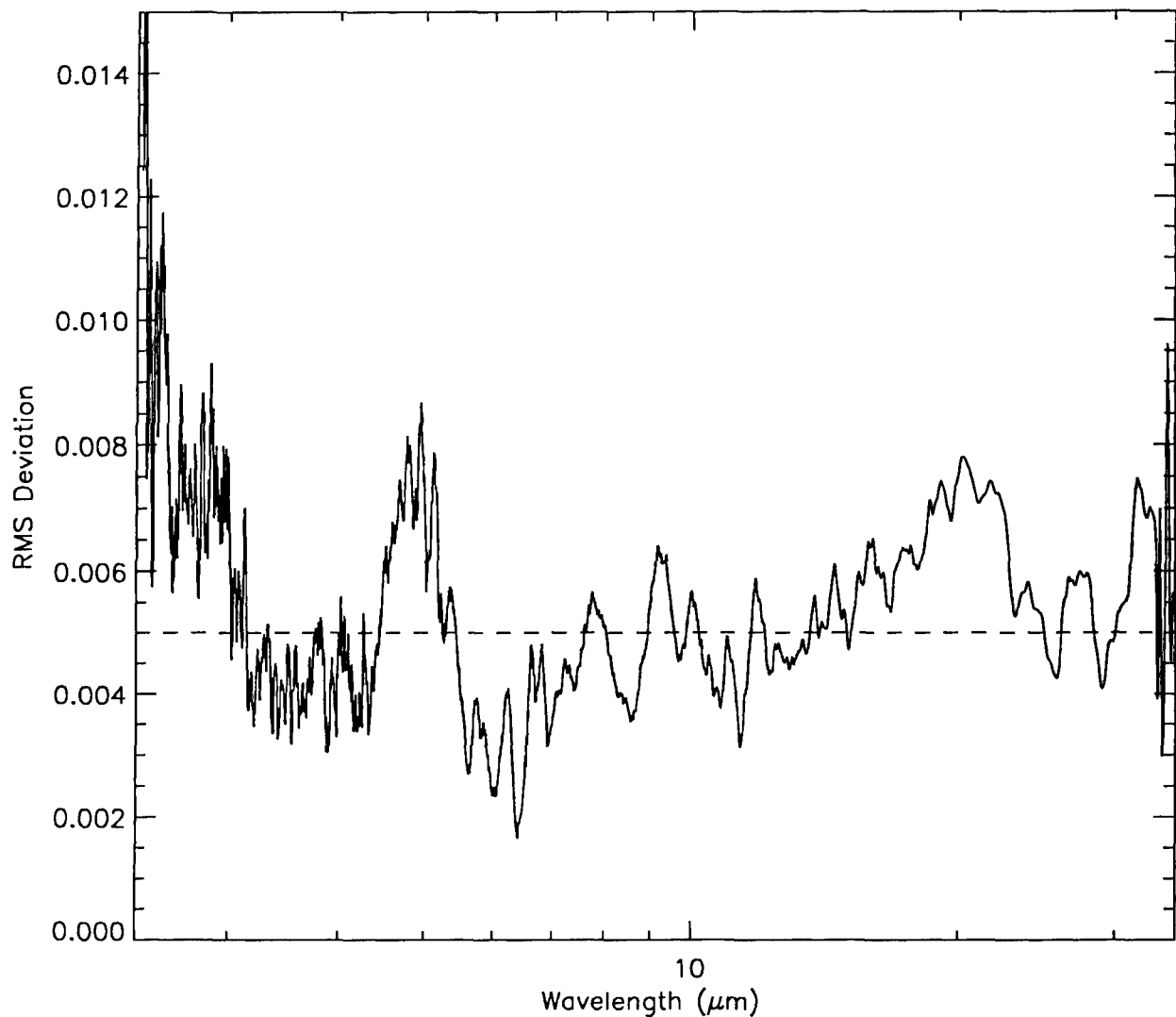


Figure 64: The averaged rms scatter of the deviations of the final calibrated spectra between 2 and 35 μm of α Boo, α Tau, γ Dra, β And and γ Cru after they have been normalized by the respective *autoshape* functions. The rms is calculated after the appropriate *autoshape* functions have been subtracted from the normalized spectra. The rms is less than one percent over most of the wavelength range.

7.4.2 Variability

Several of the stars in this study are known optical variables: γ Dra, β Peg, α Cet, β Gru and GZ Peg for example. Except for γ Dra, which is a K5 III star, the spectral types of these stars are M2 III or later. Thus, they would not have fulfilled one of Cohen et al. original selection criteria that the secondary standard must be of spectral type M2.5 III or earlier to avoid the high probability that the source is variable (Paper X). Cohen et al. relaxed this criterion to M4 III in order to include γ Cru, a calibration source that was brighter than any of those in the original network. The variation in the infrared brightness of a star that is an optical variable or suspected variable is usually much less than that in the visual. Thus, only sources with small amplitude

(suspected) variability in the visual are included in Tables 20 and 21 and the estimated infrared variation should be included in the uncertainty assigned to the calibrated flux.

Table 26: DIRBE Variability

Star	Spectral Type	DIR 1	DIR 2	DIR 3	DIR 4
β Gem	K0 III	$1 \pm 3\%$	$1 \pm 1\%$	$3 \pm 3\%$	$1 \pm 2\%$
α Boo	K1.5 III	$4 \pm 3\%$	$1 \pm 1\%$	$4 \pm 2\%$	$1 \pm 1\%$
β UMi	K4 III	$4 \pm 3\%$	$1 \pm 1\%$	$3 \pm 3\%$	$2 \pm 2\%$
α Tau	K5 III	---	$0 \pm 1\%$	$2 \pm 2\%$	$0 \pm 1\%$
γ Dra	K5 III	$5 \pm 3\%$	$2 \pm 1\%$	$3 \pm 2\%$	$2 \pm 2\%$
μ UMa	M0 III	$3 \pm 3\%$	$1 \pm 1\%$	$3 \pm 3\%$	$3 \pm 3\%$
β And	M0 III	$2 \pm 3\%$	---	---	$1 \pm 1\%$
α Cet	M2 III	$3 \pm 3\%$	$1 \pm 1\%$	$3 \pm 3\%$	$3 \pm 2\%$
γ Cru	M4 III	$4 \pm 3\%$	$0 \pm 1\%$	$3 \pm 2\%$	$2 \pm 1\%$
α Cen	G2 V	$5 \pm 3\%$	---	$1 \pm 6\%$	---
β Dra	G2 II	$5 \pm 4\%$	$4 \pm 3\%$	$9 \pm 7\%$	$10 \pm 10\%$
δ Dra	G9 III	$2 \pm 4\%$	$10 \pm 3\%$	$41 \pm 7\%$	$17 \pm 6\%$
δ Eri	K0 IV	$2 \pm 5\%$	$3 \pm 6\%$	$11 \pm 9\%$	$16 \pm 16\%$
θ Cen	K0 III	---	$1 \pm 2\%$	$7 \pm 5\%$	$6 \pm 5\%$
α UMa	K0 IIIa	$5 \pm 3\%$	$1 \pm 1\%$	$5 \pm 2\%$	$3 \pm 3\%$
ξ Dra	K2 III	$4 \pm 5\%$	$10 \pm 2\%$	$11 \pm 4\%$	$24 \pm 8\%$
α Ari	K2 III	$3 \pm 3\%$	$1 \pm 1\%$	$5 \pm 3\%$	$4 \pm 3\%$
γ And	K3 IIb	$2 \pm 3\%$	$2 \pm 1\%$	$3 \pm 3\%$	$3 \pm 3\%$
α Tuc	K3 III	$3 \pm 3\%$	$2 \pm 2\%$	$3 \pm 4\%$	$4 \pm 4\%$
λ Gru	K3 III	$6 \pm 5\%$	$4 \pm 5\%$	$7 \pm 8\%$	$13 \pm 17\%$
σ Oph	K3 II	$4 \pm 4\%$	$5 \pm 4\%$	$10 \pm 7\%$	$10 \pm 12\%$
δ Psc	K5 III	$8 \pm 4\%$	$6 \pm 3\%$	$7 \pm 5\%$	$14 \pm 10\%$
γ Phe	K4/5 III	$3 \pm 3\%$	---	---	$6 \pm 4\%$
H Sco	K5 III	---	---	$19 \pm 11\%$	$10 \pm 13\%$
δ Oph	M1 III	---	$1 \pm 1\%$	$4 \pm 3\%$	$1\% \pm 2\%$
AE Cet	M1 III	$3 \pm 3\%$	---	---	$3 \pm 5\%$
δ Vir	M3 III	$3 \pm 3\%$	$1 \pm 1\%$	$2 \pm 2\%$	$2 \pm 2\%$
ρ Per	M4 II	---	$1 \pm 1\%$	$5 \pm 2\%$	$4 \pm 2\%$
π Aur	M3 II	---	---	$12 \pm 6\%$	$5 \pm 3\%$
β Peg	M2.5 III	$5 \pm 3\%$	$3 \pm 1\%$	$4 \pm 2\%$	$4 \pm 1\%$
β Gru	M5 III	$6 \pm 3\%$	$2 \pm 1\%$	$4 \pm 2\%$	$2 \pm 1\%$
GZ Peg	M4 III + A2 V	---	$2 \pm 2\%$	$6 \pm 5\%$	---
δ^2 Lyr	M4 III	$2 \pm 2\%$	$2 \pm 1\%$	$4 \pm 3\%$	$3 \pm 2\%$
α Aur	G4: III:	$1 \pm 3\%$	$0 \pm 1\%$	$2 \pm 2\%$	$2 \pm 1\%$
α Hya	K3 II-III	$2 \pm 3\%$	$1 \pm 1\%$	$2 \pm 3\%$	$2 \pm 2\%$
α TrA	K2 II	---	$0 \pm 2\%$	$6 \pm 3\%$	$5 \pm 2\%$
ϵ Car	K3 III	$3 \pm 3\%$	$1 \pm 1\%$	$3 \pm 3\%$	$4 \pm 2\%$
γ Aql	K3 II	$4 \pm 4\%$	$0 \pm 2\%$	$3 \pm 4\%$	$5 \pm 4\%$

MSX measured a systematic 8 percent variation in the infrared irradiance of β Peg during the 10 month mission in 1996/1997. The amplitude and phase of the variation were well correlated across the wavelength range of 4.3 – 21 μm ; the single mirror-fixed measurement is somewhat discordant. Smith et al. (2004) also statistically detected variability in this star during the 10 month DIRBE mission (which did not overlap with the 10 month MSX mission). The β Peg moderate resolution spectrum created under the present work was anchored to the median values of the MSX fluxes. To be conservative, a 4 percent uncertainty should be root sum squared with the ~ 1 percent uncertainty in generating the spectrum and the 1.1 percent uncertainty in the absolute flux calibration and the result used for this star.

None of the other stars in Table 20 that have MSX photometry were measured by MSX or DIRBE to be variable. As part of their processing to create the DIRBE point source catalog, Smith et al. (2004) statistically assessed the variability of the bright infrared stars over the 10 month COBE Mission. Table 26 lists the percent variability in the DIRBE photometry for bands 1 – 4 from this catalog for the stars in Tables 20 – 22 along with the uncertainty in the estimate.

Smith et al. tried to eliminate scans contaminated by extraneous sources in the beam from the analysis used to derive the variability parameters. However, as noted previously for the DIRBE mid-infrared photometry, the statistics for variability are less secure for the fainter stars. Given these difficulties we consider a source to be variable if the DIRBE variability parameter has a significance of 2σ or greater in more than one DIRBE band. Two stars in the list, δ Dra and ξ Dra, have a large variability, greater than 10 percent. Neither star has MSX photometry. However, as noted earlier, δ Dra was used to calibrate the ISO CVF. If the DIRBE results are correct then the CVF calibration uncertainties may be underestimated. Besides β Peg, δ Dra and ξ Dra, four other stars fulfill the 2σ variability in more than one band: α TrA, δ Psc, ρ Per and β Gru. The DIRBE variability of β Gru is somewhat smaller than for β Peg and is well detected because of the high SNR measurements that DIRBE obtained for this star.

7.4.3 Outliers

The derived temperatures for ϵ Car and δ^2 Lyr are anomalously low for their spectral types. ϵ Car (K3 III) is a double star but any contamination from the hotter B2 V should bias the derived temperature high. Interstellar reddening would bias the temperature low as would very thin circumstellar emission, although Cohen et al. use zero reddening in Paper X for ϵ Car. Regardless of the cause of this anomaly, the final calibrated spectrum of ϵ Car fits the infrared photometry to <5 percent. δ^2 Lyr (M4 II) is also cooler than the other M4 stars in our sample (Table 21). It is relatively faint, though, and has correspondingly higher uncertainty in the temperature estimate; thus it is only 1σ below the expected value of $\sim 3500\text{--}3600\text{K}$.

8 Summary and Conclusions

Martin Cohen and his colleagues established a stellar network against which infrared systems could be calibrated under the auspices of the AF Geophysics Laboratory's Stellar Atlas Panel and with partial funding from the Laboratory. The calibration included a recommended zero magnitude flux scale and the absolute spectral energy distributions for primary, secondary and tertiary infrared stellar standards. The Cohen et al. calibration is presented in Section 2 and the zero magnitude flux scale and the absolute spectral fluxes for the primary standards are compared with other calibrations. One issue to emerge from this comparison is that, except for the few other analyses that used the same indirect method as Cohen et al., the majority of the other absolute infrared calibrations systematically diverged from that of Cohen et al. The discrepancies increased with increasing wavelength becoming as large as 10 percent at 10 μm .

Such was the situation as of the mid-1990s when MSX was flown. MSX conducted carefully planned and executed calibration experiments against stellar standards and absolute measurement against emissive reference spheres. Approximately 200 mean stellar fluxes were derived on nine primary and secondary Cohen et al. standard stars from individual data collection events of 20 to 80 individual measurements each. A much smaller data set of DCE means was obtained on very bright variable stars to probe the upper levels of the dynamic range. The formal precision in knowledge of the measured mean fluxes for the five most frequently measured standard stars, α CMa, α Tau, α Boo, α Lyr and β Gem, is less than 1 percent. A sixth standard, β Peg, was found to vary in brightness by eight percent during the 10 month mission. Interestingly, the brightness variation for this star was positively correlated from 4.3 μm to 21 μm , whereas the variation at 4.3 μm for the known infrared variable, μ Cep, was anti-correlated with the MSX mid-infrared bands. Because they had fewer measurements, the flux uncertainties were larger for β And, γ Dra and γ Cru. The MSX Band D and E measurements on α Lyr indicates the presence of excess emission from the low temperature circumstellar dust shell around this star and there is an indication that emission from this dust may have been marginally detected in Band C. Thus, the fundamental standard adopted by Cohen et al. in Paper I, α Lyr, is not a good calibrator at wavelengths greater than 12 μm . We have, therefore, adopted Sirius as the fundamental standard to which all other stars are referenced in our analyses in Sections 3 through 5. Except for α Lyr and β Gem, the MSX relative photometry on the other secondary standard stars was found to be well within the errors that Cohen et al. ascribe to their absolute fluxes if the absolute flux for Sirius in Paper I is increased by 1 percent.

MSX also obtained an absolute mid-infrared calibration against five emissive reference spheres whose absolute in-band fluxes were modeled to an accuracy of 3 – 4 percent. The measurement accuracy in the average of the weighted means for all the MSX mid-infrared bands and all experiments is ~ 1 percent. The absolute calibration using the emissive reference spheres agrees with the Cohen et al. zero magnitude fluxes to within their bias uncertainty of 1.4 percent.

It is noted that MSX was remarkably successful in obtaining an absolute calibration of infrared standard calibration stars against reference spheres, despite the dynamic operating conditions of the SPIRIT III sensor, the secular changes of the response and noise during the mission and the problems that were outlined in Section 3.5. MSX has shown that a more carefully constructed sensor under stable operating conditions can, with appropriately planned and executed calibration experiments, produce more accurate results.

Accurate photometry from space with MSX and COBE/DIRBE and selected high quality ground-based observations were combined with ISO SWS data to create a set of moderate spectral resolution spectra for infrared secondary standards stars. In doing so, we improved the resolution and absolute flux accuracy for 11 of the Cohen et al. secondary standards; Cohen et al. created composite spectra for nine of these stars, adopted a model atmosphere for α^1 Cen and a template spectrum for β UMa. The Strecker et al. (1979) low resolution near-infrared spectra for seven of these stars were seamed onto the SWS spectra after correcting this data set to the Price et al. (2004) flux for Sirius. We adopted the absolute fluxes proposed by Cohen et al. in Paper I for Vega and Sirius ($\times 1.01$) to preserve the zero magnitude fluxes of the Cohen et al. as validated by Price et al. (2004) and because the SWS spectra for these stars become noisy at $\lambda > 7 \mu\text{m}$.

We also created an algorithm that modeled the continuum of the 12 standard stars with the highest quality infrared photometry and the best SWS spectra. This routine, labeled *autosshape*, combines the Engelke function of the appropriate effective temperature with a scaled excess of a Kurucz α Boo atmospheric model spectrum. The excesses with respect to the Engelke function for stars with spectral types between G9 and M5 were well fit by an inverse linear function in effective temperature. The CO and SiO fundamental and overtone band absorption profiles also correlated well with effective temperature, and analytic functions were derived that, when combined with the *autosshape* continuum, produces a representative infrared spectrum for any given spectral type. A pseudo-continuum was created for wavelengths shorter than the $2.36 \mu\text{m}$ lower limit of the SWS based on the Strecker et al. spectra to extend the *autosshape* predictions to $1.2 \mu\text{m}$ for the stars without Strecker et al. near-infrared spectra. The *autosshape* routine was used to generate spectral templates for three of the original Cohen et al. secondary standards that do not have SWS spectra (α Hya, α TrA and ϵ Car). A template for the fourth such secondary standard, β Gem, was created by combining the SWS and CVF spectra of θ Cen, δ Eri and δ Dra, which are of the same spectral class as β Gem, with the *autosshape* template and scaling the results to the high quality MSX, DIRBE and Hammersley et al. (1998) photometry.

Absolute infrared spectra for an additional 21 fainter secondary standards were created by combining their SWS spectra with the *autosshape* spectra over the spectral region in which the SWS data were too noisy to yield useful information and scaled by the best available photometry. All but two of the stars, δ Eri and λ Gru, have high quality DIRBE photometry in at least two DIRBE bands.

The estimated 1σ absolute uncertainties are generally 1 – 2 percent, but may be as high as about 5 percent at $\sim 1 \mu\text{m}$ for spectra that rely on *autosshape*. The minimum uncertainty is dominated by the absolute accuracy in the MSX photometry (Price et al., 2004). Variability in some of the stars in Tables 20 and 21 has been noted by Smith et al. (2004), by more than 10 percent for two of the stars, and the amplitudes of the variability have to be included the flux uncertainty estimates. The uncertainties in the spectra of the fainter secondary standards are higher and reflect the paucity of high quality infrared photometry available for these stars.

The effective temperatures and angular diameters of the stars were derived by the infrared flux method using *autosshape* for the stellar source function. The good agreement between the effective temperatures that we derive and those listed in the literature attests to the fact that *autosshape* provides good approximations to the relative infrared spectral energy distributions, even for cool M giants. However, the opacity sources that become significant for the cool stars, such as water vapor absorption, may bias the derived angular diameters to being too low.

References

- Abbot, R. I., Gaposchkin, E. M., & von Braun, C. (1997), "MSX Precision Ephemeris," *Proc. 1997 Space Control Conf.*, ESC-TR-97-063 Vol. II, 63 – 71.
- Alonso, A., Salaris, M., Arribas, S., Martinez-Roger, C., & Asensio Ramos, A. (2000), "The Effective Temperature Scale of Giant Stars (F0-K5). III. Stellar Radii and the Calibration of Convection," *Astron. Astrophys.*, **355**, 1060 – 1072.
- Ames, H. O., & Burt, D. A. (1992), "Development of the SPIRIT III Sensor," *Proc. SPIE*, **1765**, 10 – 40.
- Ames, H. O., & Burt, D. A. (1994), "Development of the SPIRIT III Sensor," *Proc. SPIE*, **2227**, 74 – 86.
- Appel, P. (2003), "Attitude Estimation from Magnetometer and Earth-Albedo-Corrected Coarse Sun Sensor Measurements," Presentation at 2003 International Academy of Astronautics, Berlin. <http://www.iaanet.org/symp/berlin/IAA-B4-0602.pdf>.
- Aringer, B., Jorgensen, U. G., & Langhoff, S. R. (1997), "SiO Rotation-Vibration Bands in Cool Giants. I. A Grid of Model Spectra for Different Stellar Parameters," *Astron. Astrophys.*, **323**, 202 – 210.
- Arnold, F., & Nelms, F. W. (1976), "AEDC Long Wavelength Test Facility," *Opt. Eng.*, **15**, 549 – 563.
- Arrington, D. C., Bates, R. L., Eisenman, W. L., & Sweet, M. H. (1976), *Properties of Photodetectors (Photodetector Series, 97th Report): Spatial Sensitivity of LWIR Detectors*, NTIS ADA 033 795.
- Arrington, D. C., & Eisenman, W. L. (1977) "LWIR Detector Behavior at Very Low Frequencies," *Proc. SPIE*, **124**, 57 – 68.
- Aumann, H. H., Beichman, C. A., Gillett, F. C., de Jong, T., Houck, J. R., Low, F. J., Neugebauer, G., Walker, R. G., & Wesselius, P. R. (1984), "Discovery of a Shell Around Alpha Lyrae," *Astrophys. J. Lett.*, **278**, L23 – L27.
- Aumann, H. H., Gillespie, Jr., C. M., & Low, F. J. (1969), "The Internal Powers and Effective Temperatures of Jupiter and Saturn," *Astrophys. J.*, **157**, L69 – L72.
- Aversen, J. C., Griffin, R. N., & Pearson, Jr., B. D. (1969) "Determination of Extraterrestrial Solar Spectral Irradiance from a Research Aircraft," *Appl. Opt.*, **8**, 2215 – 2232.
- Baca, M., Elgin, J., Layton, E., Murdock, T. L., Pera, V., Zweil, A. M., Mazuk, S., Russell, R., & Pollack, D. (2002), *SPIRIT III CONVERT 6.0 Certification Report*, Frontier Technology, Inc. Technical Report 6140-02-01-TR.
- Bartell, Jr., F. O., Hubbs, J. E., Notzinger, M. J., & Wolfe, W. L. (1982), "Measurements of Martin Black at $\sim 10\ \mu\text{m}$," *Appl. Opt.*, **21**, 3178 – 3180.
- Becklin, E. E., Hansen, O., Kieffer, H., & Neugebauer, G. (1973), "Stellar Flux Calibration at $10\ \mu$ and $20\ \mu$ using Mariner 6, 7, and 9 Results," *Astron. J.*, **78**, 1063 – 1066.
- Beers, R. (1966), "Decrement of the Solar Continuum in the Far Infrared," *Nature*, **209**, 1226.
- Berk, A., Bernstein, L. W., & Robertson, D. C. (1989), "MODTRAN: A Moderate Resolution Model for LOWTRAN 7," AFGL-TR-89-0122, NTIS ADA 214 337.
- Bersanelli, M., Bouchet, P., & Falomo, R. (1991), "JHKL Photometry on the ESO system: Systematic Effects and Absolute Calibration," *Astron. Astrophys.*, **252**, 854 – 860.
- Bingham, G., Petersen, J., Brown, S., Morse, D., & Bartchi, B. (1995), *CIRRIS 1A Post Flight Calibration. Volume I & II*. NTIS ADA 319 074 & ADA 318 472.

- Blackwell, D. E., Leggett, S. K., Petford, A. D., Mountain, C. M., & Selby, M. J. (1983), "Absolute Calibration of the Infrared Flux from Vega at 1.24, 2.20, 3.76 and 4.6 μm by Comparison with a Standard Furnace," *Mon. Not. R. Astron. Soc.*, **205**, 897 – 905.
- Blackwell, D. E., Lynas-Gray, A. E., & Petford, A. D. (1991), "Effect of Improved H(-) Opacity on the Infrared Flux Method Temperature Scale and Derived Angular Diameters - Use of a Self-Consistent Calibration," *Astron. Astrophys.*, **245**, 567–574.
- Blackwell, D. E., Petford, A. D., Arribas, S., Haddock, D. J., & Selby, M. J. (1990), "Determination of Temperatures and Angular Diameters of 114 F – M Stars Using the Infrared Flux Method (IRFM)," *Astron. Astrophys.*, **232**, 396 – 410.
- Blommaert, J., et al. (2003), *The ISO Handbook CAM – The ISO Camera*, ESA SP – 1262, Vol. II.
- Booth, A. J., Selby, M. J., Blackwell, D. E., Petford, A. D., & Arribas, S. (1989), "Determination of the Absolute flux from Vega at 2.250 μm ," *Astron. Astrophys.*, **218**, 167 – 168.
- Bouchet, P., Schmider, F. X., & Manfroid, J. (1991), "JHKLM Standard Stars in the ESO System," *Astron. Astrophys. Suppl.*, **91**, 409 – 424.
- Bouchet, P., Slezak, E., LeBerte, T., Moneti, A., & Manfroid, J. (1989), "Infrared Photometry and Spectrophotometry of SN 1987A. I - March to October 1987 Observations," *Astron. Astrophys. Suppl.*, **80**, 379 – 397.
- Burdick, S. V., & Morris, D. C. (1997), "SPIRIT III Calibration Stars: In-band Irradiances and Uncertainty," *Opt. Eng.*, **36**, 2971 – 2976.
- Campins, H., Rieke, G. H., & Lebofsky, M. J. (1985), "Absolute Calibration of Photometry at 1 through 5 μm ," *Astron. J.*, **90**, 896 – 899.
- Carbon, D. F., & Gingerich, O. (1969), "The Grid of Model Stellar Atmospheres from 4000° to 10,000°," *Proc. Third Harvard-Smithsonian Conference on Stellar Atmospheres*, MIT Press, 377 – 401.
- Carter, B. S. (1990) "Southern JHKL Standards," *Mon. Not. Roy. Astron. Soc.*, **242**, 1–5.
- Carter, B. S. (1993) "The SAAO JHKL System and Fainter Standards," in *Precision Photometry*, ed. D. Kilkeny, E. Lastovica, & J. W. Menzies (Cape Town: South African Astron. Obs.) 100.
- Castelli, G., & Kurucz, R. L. (1993), "Models for Vega," in *Peculiar Versus Normal Phenomena in A-Type and Related Stars*, ed. M. M. Dworetsky, F. Castelli, & F. Faraggianna, Astron. Soc. Pac. Conf. Series, **44**, 496 – 501.
- Castelli, G., & Kurucz, R. L. (1994), "Model Atmospheres for Vega," *Astron. Astrophys.*, **281**, 817 – 832.
- Chalupa, J., Cobb, W. K., & Murdock, T. L. (1991a), *Thermal History and Error Budget of an Emissive Calibration Sphere for a Space-Based IR Sensor, Part I: Gray-Body Analysis*, General Research Corp. Tech. Rep. 1597-08-91-TR.
- Chalupa, J., Cobb, W. K., & Murdock, T. L. (1991b), "Scattering Contribution to the Error Budget of an Emissive IR Calibration Sphere," *Proc. SPIE*, **1530**, 343 – 351.
- Chalupa, J., & Hamilton, C. L. (1993), *Thermal History and Error Budget of an Emissive Calibration Sphere for a Space-Based IR Sensor, Part II: Spectral Error Analysis*, General Research Corp. Tech. Rep. 1945-03-93-TR.
- Ciardi, D. R., van Belle, G. T., Akeson, R. L., Thompson, R. R., Lada, E. A., & Howell, S. B. (2001), "On the Near-Infrared Size of Vega," *Astron. J.*, **559**, 1147 – 1154.
- Claret, A., Diaz-Cordoves, J. & Gimenez, A. (1995), "Linear and Non-Linear Limb-Darkening Coefficients for the Photometric Bands R I J H K," *Astron. Astrophys. Suppl.*, **114**, 247 –

- Cohen, E. R., & Taylor, B. N. (1994), "The Fundamental Physical Constants," *Physics Today*, **47**, No. 8 (August), 9 – 13.
- Cohen, M. (1998), "Spectral Irradiance Calibration in the Infrared. IX. Calibrated Stellar Spectra Using DIRBE Radiometer," *Astron. J.*, **115**, 2092 – 2096 (Paper IX).
- Cohen, M., & Davies, G. K. (1995), "Spectral Irradiance Calibration in the Infrared. V. The role of UKIRT and the CGS3 spectrometer," *Mon. Not. R. Astron. Soc.*, **276**, 715 – 722 (Paper V).
- Cohen, M., Hammersley, P. L., & Egan, M. P. (2000), "Radiometric Validation of the Midcourse Space Experiment's (MSX) Point Source Catalog and the Properties of Normal Stars," *Astron. J.*, **120**, 3362 – 3370.
- Cohen, M., Megeath, S. T., Hammersley, P. L., Martin-Luis, F., & Stauffer, J. (2003a), "Spectral Irradiance Calibration in the Infrared XIII. "Supertemplates" and On-Orbit Calibrators for the SIRTf Infrared Array Camera," *Astron. J.*, **125**, 2645 – 2663 (Paper XIII).
- Cohen, M., Walker, R. G., Barlow, M. J., & Deacon, J. R. (1992a), "Spectral Irradiance Calibration in the Infrared. I. Ground Based and IRAS Broadband Calibration," *Astron. J.*, **104**, 1650 – 1657 (Paper I).
- Cohen, M., Walker, R. G., Barlow, M. J., Deacon, J. R., Witteborn, F. C., Carbon, D., & Gustafson, G. (1993), "Absolute Spectrally Continuous Stellar Radiance Calibration in the Infrared" in *Astronomical Infrared Spectroscopy: Future Observational Directions*, ed. S. Kwok, Astron. Soc. Pac. Conf. Series, **41**, 55 – 92.
- Cohen, M., Walker, R. G., Carter, B., Hammersley, P., & Kidger, M. (1999), "Spectral Irradiance Calibration in the Infrared. X. A Self-Consistent Radiometric All-Sky Network of Absolutely Calibrated Stellar Spectra," *Astron. J.*, **117**, 1864 – 1889 (Paper X).
- Cohen, M., Walker, R. G., Jayaraman, S., Barker, E., & Price, S. D. (2001), "Spectral Irradiance Calibration in the Infrared. XII. Radiometric Measurements from the Midcourse Space Experiment," *Astron. J.*, **121**, 1180 – 1191 (Paper XII).
- Cohen, M., Walker, R. G., & Witteborn, F. C. (1992), "Spectral Irradiance Calibration in the Infrared. II. α Tau and the Recalibration of the IRAS Low Resolution Spectrometer," *Astron. J.*, **104**, 2030 – 2044 (Paper II).
- Cohen, M., Wheaton, W. A., & Megeath, S. T. (2003b), "Spectral Irradiance Calibration in the Infrared XIV: the Absolute Calibration of 2MASS," *Astron. J.*, **126**, 1090 – 1096 (Paper XIV).
- Cohen, M., Witteborn, F. C., Bregman, J. D., Wooden, D. H., Salama, A., & Metcalfe, L. (1996a), "Spectral Irradiance Calibration in the Infrared. VI. 3 – 35 μ m Spectra of Three Southern Standard Stars," *Astron. J.*, **112**, 241 – 251 (Paper VI).
- Cohen, M., Witteborn, F. C., Carbon, D. F., Augeson, G., Wooden, D., Bregman, J., & Goorvitch, D. (1992b), "Spectral Irradiance Calibration in the Infrared. III. The Influence of CO and SiO," *Astron. J.*, **104**, 2045 – 2062 (Paper III).
- Cohen, M., Witteborn, F. C., Carbon, D. F., Davies, J. K., Wooden, D. H., & Bregman, J. D. (1996b), "Spectral Irradiance Calibration in the Infrared. VII. New Composite Spectra, Comparison with Model Atmospheres, and Far Infrared Extrapolation," *Astron. J.*, **112**, 2274 – 2285 (Paper VII).
- Cohen, M., Witteborn, F. C., Roush, T., Bregman, J., & Wooden, D. (1998), "Spectral Irradiance Calibration in the Infrared. VIII. 5 – 14 Micron Spectroscopy of the Asteroids Ceres, Vesta and Pallas," *Astron. J.*, **115**, 1671 – 1670 (Paper VIII).

- Cohen, M., Witteborn, F. C., Walker, R. G., Bregman, J. D., & Wooden, D. H. (1995), "Spectral Irradiance Calibration in the Infrared. IV. 1.2 – 35 μ m Spectra of Six Standard Stars," *Astron. J.*, **110**, 275 – 289 (Paper IV).
- Colina, L., & Bohlin, R. C. (1997), "Absolute Flux Distributions of Solar Analogs from the UV to the Near-IR," *Astron. J.*, **113**, 1138 – 1144.
- Colina, L., Bohlin, R. C., & Castelli, F. (1996), "The 0.12 – 2.5 Micron Absolute Flux Distribution of the Sun for Comparison with Solar Analog Stars," *Astron. J.*, **112**, 307 – 315.
- Coulais, A., & Abergel, A. (2000), "Transient Correction of the LW – ISOCAM data for Low Contrasted Radiation," *Astron. Astrophys. Suppl.*, **141**, 533 – 544.
- Davis, J., & Tango, W. J. (1986), "New Determination of the Angular Diameter of Sirius," *Nature*, **323**, 234 – 235.
- de Jager, C., & Nieuwenhuizen, H. (1987), "A New Determination of the Statistical Relations Between Stellar Spectral and Luminosity Classes and Stellar Effective Temperature and Luminosity," *Astron. Astrophys.*, **177**, 217 – 227.
- Decin, L., Morris, P. W., Appleton, P. N., Chamandaris, V., Armus, L., & Houck, J. R. (2004), "MARCS: Model Stellar Atmospheres and Their Application to the Photometric Calibration of the Spitzer Space Telescope Infrared Spectrograph (IRS)," *Astrophys. J. Suppl.*, **154**, 408 – 412.
- Decin, L., Vandenbussche, B., Waelkens, C., Eriksson, K., Gustafsson, B., Plez, B., Sauval, A. J., & Hinkle, K. (2003a), "ISO ISO – SWS Calibration and the Accurate Modeling of Cool-Star Atmospheres II. General Results," *Astron. Astrophys.*, **400**, 679 – 694.
- Decin, L., Vandenbussche, B., Waelkens, C., Eriksson, K., Gustafsson, B., Plez, B., & Sauval, A. J. (2003b), "ISO – SWS Calibration and the Accurate Modeling of Cool-Star Atmospheres III. A0 to G2 Stars," *Astron. Astrophys.*, **400**, 709 – 727.
- Decin, L., Vandenbussche, B., Waelkens, C., Decin, G., Eriksson, K., Gustafsson, B., Plez, B., Sauval, A. J., & Hinkle, K. (2003c), "ISO – SWS Calibration and the Accurate Modeling of Cool-Star Atmospheres IV. G9 to M2 Stars," *Astron. Astrophys.*, **400**, 679 – 694.
- Decin, L., Waelkens, C., Eriksson, K., Gustafsson, B., Plez, B., Sauval, A. J., Van Assche, W., & Vandenbussche, B. (2000), "ISO – SWS Calibration and the Accurate Modeling of Cool-Star Atmospheres I. Method," *Astron. Astrophys.*, **364**, 137 – 156.
- Diaz-Cordoves, J., Claret, A., & Gimenez, A. (1995) "Linear and Non-Linear Limb-Darkening Coefficients for LTE Model Atmospheres," *Astron. Astrophys. Suppl.* **110**, 329 – 350.
- Di Benedetto, G. P. (1998), "Towards a Fundamental Calibration of Stellar Parameters of A, F, G, K Dwarfs and Giants," *Astron. Astrophys.*, **339**, 858 – 871.
- Di Benedetto, G. P., & Bonneau, D. (1990), "Evidence from Michelson interferometry for small-scale structure in the source geometry of the M0 giant Beta Andromedae," *Astrophys. J.*, **358**, 617 – 621.
- Di Benedetto, G. P., & Rabbia, Y. (1987), "Accurate Angular Diameters and Effective Temperatures for Eleven Giants Cooler Than K0 By Michelson Interferometry," *Astron. Astrophys.*, **188**, 114 – 124.
- Dreiling, L. A., & Bell, R. A. (1980), "The Chemical Composition, Gravity, and Temperature of VEGA," *Astrophys. J.*, **241**, 736 – 758.
- Dyck, H. M., Benson, J. A., van Belle, G. T., & Ridgway, S. T. (1996), "Radii and Effective Temperatures for K and M Giants and Supergiants," *Astron. J.*, **111**, 1705 – 1712.
- Dyck, H. M., van Belle, G. T., Thompson, R. R. (1998), "Radii and Effective Temperatures for K and M Giants and Supergiants. II.," *Astron. J.*, **116**, 981 – 986.

- Egan, M. P., Price, S. D., Kraemer, K. E., Mizuno, D. R., Carey, S. J., Wright, C. O., Engelke, C. W., Cohen, M., & Gugliotti, G. M., (2003), *The Midcourse space Experiment Point Source Catalog Version 2.3 Explanatory Guide*, AFRL-VS-TR-2003-1589, NTIS ADA 418 993.
- Egan, M. P., Price, S. D., Moshir, M. M., Cohen, M., Tedesco, E., Murdock, T. L., Zweil, A., Burdick, S., Bonito, N., Gugliotti, G. M., & Duszlak, J. (1999), *The Midcourse Space Experiment Point Source Catalog Version 1.2 Explanatory Guide*, AFRL-TR-1999-1522, NTIS ADA 381 933.
- Engelke, C. W. (1992), "Analytic Approximations to the 2 – 60 μm Infrared Continua for Standard Calibration Stars with Application to the Calibration of Spectroscopy and Photometry, and the Determination of Effective Temperature and Angular Size from IR Measurements," *Astron. J.*, **104**, 1248 – 1259.
- Engelke, C. W., Kraemer, K. E., & Price, S. D. (2004), "A Uniform Database of 2.2 - 16.5 Micron Spectra from the ISOCAM-CVF Spectrometer," *Astrophys. J. Suppl.*, **150**, 343 – 365.
- Engelke, C. W., Price, S. D., & Kraemer, K. E. (2006), "Spectral Irradiance Calibration in the Infrared. XVI. Improved Accuracy in the Infrared Spectra of Secondary and Tertiary Standard Calibration Stars," *Astron. J.* (submitted).
- Engels, D., Sherwood, W. A., Wamsteker, W. & Schultz, G. V. (1981), "Infrared Observations of Southern Bright Stars," *Astron. Astrophys. Suppl.*, **45**, 5 – 9.
- Feast, M. W., Whitelock, P. A., & Carter, B. S. (1990), "M Giant Populations and Galactic Structure," *Mon. Not. R. Astron. Soc.*, **247**, 227 – 236.
- Fouqué, P., Chevallier, L., Cohen, M., Galliano, E., Loup, C., Alard, C., de Batz, B., Bertin, E., Borsenberger, J., Cioni, M. R., Copet, E., Dennefeld, M., Derriere, S., Deul, E., Duc, P.-A., Egret, D., Epchtein, N., Forveille, T., Garzón, F., Habing, H.J., Hron, J., Kimeswenger, S., Lacombe, F., Le Bertre, T., Mamon, G. A., Omont, A., Paturel, G., Pau, S., Persi, P., Robin, A. C., Rouan, D., Schultheis, M., Simon, G., Tiphène, D., Vauglin, I., & Wagner, S. J., (2000), "An Absolute Calibration of DENIS (Deep Near-infrared Southern Sky Survey)," *Astron. Astrophys Suppl.*, **141**, 313 – 317.
- Fouks, B. (1993), "Nonstationary Processes in Extrinsic Photoconductors," *Proc. SPIE.*, **1762**, 519 – 530.
- Garlick, D. S., Greenman, M., Larsen, M. R., Sargent, S., & Hanson, J. S. (1996), "Algorithms for Calibration and Point Source Extraction for an LWIR Space-based Sensor," *Proc. SPIE*, **2759**, 182 – 193.
- Glaccum, W. J. (1999), *Far-infrared Spectrophotometry of Oxygen-rich and S-Type Stars*, PhD Thesis, Univ. Chicago.
- Gulliver, A. F., Hill, G., & Adelman, S. J. (1994), "Vega: A Rapidly Rotating Pole-On Star," *Astrophys. J. Lett.*, **429**, L81 – L84.
- Hajian, A. R., Armstrong, J. T., Hummel, C. A., Benson, J. A., Mozurkewich, D., Paulus, T. A., Hutter, D. J., Elias, N. M., II, Johnston, Kenneth J., Rickard, L. J. & White, N. M. (1998), "Direct Confirmation of Stellar Limb Darkening with the Navy Prototype Optical Interferometer," *Astrophys. J.*, **496**, 484 – 489.
- Hall, F. F. (1961), "Measurements of Stellar and Planetary Magnitudes in the Lead Sulphide Spectral Region," *Infrared Information Symp.* **1**, 681 – 688.
- Hall, R. T. (1974), *A Catalog of 10- μm Celestial Objects*, SAMSO-TR-74-212.

- Hamilton, C., Howard, J., & Murdock, T. (1997), 'MSX SPIRIT III Emissive Reference Sphere Analysis,' *presentation in Proc. SDL/USU Seventh Symposium on Infrared Radiometric Sensor Calibration* May 13 – 15 1997*
- Hammersley, P. L., & Jourdain de Muizon, M. (2003), "The Development of Stellar Photometric Standards for ISO," in *The Calibration Legacy of the ISO Mission*, ed. L. Metcalfe, A. Salama, S. B. Peschke, & M. F. K. Kessler, ESA SP-481, 129 – 134.
- Hammersley, P. L., Jourdain de Muizon, M., Kessler, M. F., Bouchet, P., Joseph, R. D., Habing, H. J., Salama, A., & Metcalfe, L. (1998), "Infrared Standards for ISO," *Astron. Astrophys. Suppl.*, **128**, 207 – 219.
- Hanbury-Brown, R., Davis, J., & Allen, L. R. (1974), "The Angular Diameter of 32 Stars," *Mon. Not. R. Astron. Soc.*, **161**, 121 – 136.
- Handbook of Chemistry and Physics*, 39th Ed, (1958), ed. C. D. Hodgman, R. C. Weast, & S. M. Selby (Cleveland: Chem. Rubber Pub. Co.).
- Haniff, C. A., Scholz, M., & Tuthill, P. G. (1995), "New Diameter Measurements of 10 Mira Variables - Implications for Effective Temperatures, Atmospheric Structure and Pulsation Modes," *Mon. Not. R. Astron. Soc.*, **276**, 640 – 650.
- Hayes, D. S. (1985), "Stellar Absolute Fluxes and Energy Distributions from 0.32 to 4.0 microns," in *Calibration of Fundamental Stellar Quantities*, ed. D. S. Hayes, E. Pasenetti, & A. G. Davis Phillip, (Dordrecht: Reidel Pub. Co.), IAU Symp. **111**, 225 – 252.
- Hayes, D. S., Latham, D. W., & Hayes, S. H. (1975), "Measurements of the monochromatic flux from Vega in the near-infrared," *Astrophys. J.*, **197**, 587 – 592.
- Heinrichsen, I., Walker, H. J., & Klaas, U. (1998), "Infrared Mapping of the Dust Disc around Vega," *Mon. Not. R. Astron. Soc.*, **293**, L78 – L82.
- Heras, A. M., Shipman, R. F., Price, S. D., de Graauw, Th., Walker, H. J., Jourdain de Muizon, M., Kessler, M. F., Prusti, T., Decin, L., Vandenbussche, B., & Waters, L. B. F. M. (2002), "Infrared spectral classification of normal stars," *Astron. Astrophys.*, **394**, 539 – 552.
- Hinkle, K., Wallace, L., & Livingston, W. (1995), "Infrared Atlas of the Arcturus Spectrum, 0.9-5.3 microns," *Publ. Astron. Soc. Pacific*, **107**, 1042 – 1046.
- Hutter, D. J., Johnston K. J., Mozurkewich D., Simon, R. S., Colavita, M. M., Pan, X. P., Shao, M., Hines, B. E., Staelin, D. H., Hershey, J. L., Hughes, J. A. & Kaplan, G. H. (1989), "Angular Diameter Measurements of 24 Giant and Supergiant Stars From the Mark III Optical Interferometer," *Astrophys. J.*, **340**, 1103 – 1111.
- IRAS Science Team (1988) *IRAS Catalogs and Atlases, Ver. 2, Explanatory Suppl.* ed. C. A. Beichman, G. Neugebauer, H. J. Habing, P. E. Clegg, & T. J. Chester (NASA Publ. 1190; Washington, DC: NASA).
- Johnston, H. L. (1965), "The absolute calibration of the Arizona photometry," *Comm. of the Lunar and Planetary Lab.*, **3**, 73.
- Kenyon, S. J. (1988), "The Cool Components of Symbiotic Stars. II - Infrared Photometry," *Astron. J.*, **96**, 337 – 345.
- Kessler, M., et al. (2003), *The ISO Handbook ISO – Mission and Satellite Overview*, ESA SP-1262 Vol I.
- Kerschbaum, F., & Hron, J. (1994), "Semiregular Variables of Types Sra and Srb. New JHKLM-Photometry For 200 Stars," *Astron. Astrophys. Suppl.*, **106**, 397 – 411.
- Kervella, P., Thévenin, F., Di Folco, E., & Ségransan, E. (2004), "The Angular Sizes of Dwarf Stars and Subgiants. Surface Brightness Relations Calibrated by Interferometry," *Astron. Astrophys.*, **426**, 297 – 307.

- Kervella, P., Thévenin, G., Morel, P., Bordé, P., & Di Falco, E. (2003a), "The Interferometric Diameter and Internal Structure of Sirius A," *Astron. Astrophys.*, **408**, 681 – 688.
- Kervella, P., Thévenin, F., Ségransan, D., Berthomieu, G., Lopez, B., Morel, P. & Provost, J. (2003b), "The Diameters Of Alpha Centauri A And B. A Comparison of the Asteroseismic and VINCI/VLTI Views," *Astron. Astrophys.*, **404**, 1087 – 1097.
- Kessler, K., et al. (2003), *The ISO Handbook: ISO – Mission and Satellite Overview*, ESA SP-1262, Vol. I.
- Kintner, E. C., & Sohn, R. B. (1993a), "Thermal Modeling of MSX Spacecraft Emissive Reference Spheres for LWIR Sensor Calibration," *Lincoln Lab Project Report SDP-368*, 1993.
- Kintner, E. C., & Sohn, R. B. (1993b), "Emissive Reference Spheres as Absolute Calibration Sources for an Orbiting LWIR Sensor," *Proc SPIE*, **1938**, 153 – 162.
- Kiss, Cs., & Ábrahám, P. (2001), "Zodiacal Light Disk Around Sirius," *Publ. Astron. Dept. Eötvös Univ.*, **11**, 59 – 64.
- Kittel, C. (1985), *Introduction to Solid State Physics* (New York: John Wiley & Sons), 135 – 141.
- Kondratyev, K. Y., Andreev, S. D., Badinov, I. Y., Grishechkin, V. S., & Popova, L. V. (1965), "Atmospheric Optics Investigations on Mt. Elbrus," *Appl. Opt.*, **4**, 1069 – 1076.
- Kraemer, K. E., Sloan, G. C., Price, S. D., & Walker, H. J. (2002), "Classification of 2.4 - 45.2 Micron Spectra from the Infrared Space Observatory Short Wavelength Spectrometer," *Astrophys. J. Suppl.*, **140**, 389 – 406.
- Labs, D., & Neckel, H. (1968), "The Radiation of the Solar Photosphere from 2000 Å to 100 μ," *Zeit. Astrophys.*, **69**, 1 – 79.
- Labs, D., & Neckel, H. (1970), "Transformation of the Absolute Solar Radiation data into the 'International Practical Temperature Scale' of 1968," *Solar Phys.*, **15**, 79 – 87.
- Larsen, M. F., & Sargent, S. D. (1997), "Temperature-dependent Linearity Calibration for the SPIRIT III Radiometer," *Opt. Eng.*, **36**, 2956 – 2962.
- Larsen, M. F., Sargent, S. D., & Tansock, Jr., J. J. (1998), "On-Orbit Goniometric Calibration for the SPIRIT III Radiometer," *Proc. SPIE*, **3373**, 32 – 43.
- Larsen, M. F., Tansock, Jr., J. J., Sorensen, G., Garlick, D. S., & Hansen, J. S. (1996), "Impact of the SPIRIT III Sensor Design on Algorithms for Background Removal, Object Detection and Point Source Extraction," *Proc. SPIE*, **2759**, 194 – 204.
- Larsen, M. F., Thurgood, V. A., & Sargent S. D. (1998), "SPIRIT III Stability and On-Orbit Responsivity Verification," *presentation in Proc. SDL/USU Symposium on Infrared Radiometric Sensor Calibration* Sept 22 – 24 1998*
- Leech, K., et al. (2003), *The ISO Handbook SWS – The Short Wavelength Spectrometer*, ESA SP-1262 Vol.V, ed. K. Leech.
- Leggett, S. K. (1985), "The Flux Distribution of Vega for $10\ \mu\text{m} \leq \lambda \leq 100\ \mu\text{m}$, and the Calibration of IRAS at 12 μm and 25 μm," *Astron. Astrophys.*, **153**, 273 – 277.
- Leggett, S. K., Bartholomew, M., Mountain, C. M., & Selby, M. J. (1986), "Narrow-band 1 – to 5 μm Photometry of A-Type Stars," *Mon. Not. R. Astron. Soc.*, **223**, 443 – 447.
- Liu, W. M., Hinz, P. M., Hoffman, W. F., Brusa, G., Wildi, F., Miller, D., Lloyd-Har, M., Kenworthy, M. A., McGuire, P. C., & Angel, R. P. (2004), "Adaptive Optics Nulling Interferometric Constraints on the Mid-Infrared Exozodiacal Dust Emission Around Vega," *Astrophys. J.*, **610**, L125 – L128.

- Lockwood, G. W., Tüg, H., & White, N. M. (1992), "A New Solar Irradiance Calibration from 3295 Å to 8500 Å Derived from Absolute Spectrophotometry of Vega," *Astrophys. J.*, **390**, 668 – 678.
- Logan, L. L., Balsamo, S. B., & Hunt, G. R. (1973), "Absolute Measurements and Computed Values for Martian Irradiance between 10.5 and 12.5 μm ," *Icarus*, **18**, 451 – 458.
- Logan, L. M., Hunt, G. R., Long, A. L., & Dybwad, J. P. (1974), *Absolute Infrared Radiance Measurements of Venus and Jupiter*, AFCRL-TR-74-0573, Env. Research Papers 494, NTIS ADA 003 662.
- Low, F. J. (1973), *Groundbased Infrared Measurements*, AFCRL-TR-73-0371, AD 0768620.
- Manduca, A. (1979), "Infrared Limb-Darkening Coefficients for Late-Type Giant Model Atmospheres," *Astron. Astrophys. Suppl.*, **36**, 411 – 414.
- Manduca, A., Bell, R. A., Gustafsson, B. (1981), "The Analysis of Infrared Fluxes of Some Late-Type Stars," *Astrophys. J.*, **243**, 883 – 893.
- Marquardt, K. D., Le, J. P., & Rodebaugh, R. (2000), *Cryogenic Material Properties Data Base*, presentation to the 11th Int. Cryocooler Conf., Keystone, CO, 20-22 June 2000
- Matty, J. J., Dawbarn, R., & Menzel, R. (1991), "Test Facilities for calibration and evaluation of LWIR sensors at AEDC," *Proceedings of the 13th Aerospace Testing Seminar*, (A93-36201 14-14), 363 – 69. <http://cryogenics.nist.gov/NewFiles/publications.html>.
- Mavrofrides, M. A., Burdick, S. B., Murdock, T., & Pollack, D. (2002), *The Use of Reference Spheres for the On-Orbit Calibration of Spatial InfraRed Imaging System III*, AFRL-VS-TR-2002-1611. ADA 413 345.
- Mazuk, S., & Lillo, W. (1998), "Applications of Neural Networks to Modeling the Point Response of the Spatial InfraRed Imaging Telescope III (SPIRIT III) Radiometer," presentation in *Proc. SDL/USU Symposium on Infrared Radiometric Sensor Calibration* Logan, UT, Sept 22 – 24 1998
- Mégessier, C. (1995), "Accuracy of the Astrophysical Absolute Flux Calibrations: Visual and Near-Infrared," *Astron. Astrophys.*, **296**, 771 – 778.
- Mill, J. D., O'Neil, R. R., Price, S. D., Romick, G. J., Uy, O. M., Gaposchkin, E. M., Light, G. C., Moore, Jr., W. W., Murdock, T. L., & Stair, Jr., A. T. (1994), "Midcourse Space Experiment: Introduction to the Spacecraft, Instruments, and Scientific Objectives," *J. Spacecraft and Rockets*, **31**, 900 – 907.
- Mountain, C. M., Leggett, S. K., Selby, M. J., Blackwell, D. E., & Petford, A. D. (1985), "Measurement of the Absolute Flux from Vega at 4.92 μm ," *Astron. & Astrophys.*, **151**, 399 – 402.
- Mozurkewich, D., Armstrong, J. T., Hindsley, R. B., Quirenbach, A., Hummel, C. A., Hutter, D. J., Johnston, K. J., Hajian, A. R., Elias II, N. M., Bucher, D. F., & Simon, R. S. (2003), "Angular Diameters of Stars from the Mark III Optical Interferometer," *Astron. J.*, **126**, 2502 – 2520.
- Murcray, F. H., Murcray, D. G., & Williams, W. J. (1964), "The Spectral Radiance of the Sun from 4 μ to 5 μ ," *Appl. Opt.*, **3**, 1373 – 1377.
- Neckel, H. (1996), "On the Wavelength Dependency of Solar Limb Darkening (λ 303 to 1099 nm)," *Solar Phys.*, **167**, 9 – 23.
- Neckel, H., & Labs, D. (1981), "Improved Data of Solar Spectral Irradiance from 0.33 to 1.25 μ ," *Solar Phys.*, **74**, 321 – 249.
- Neugebauer, G., & Leighton, R. B. (1969), *Two-Micron Sky Survey*, NASA-SP3047.

- Nicholson, R. A., Mead, K. D., & Smith, R. W. (1992), "Testing of focal plane arrays at the AEDC," *Proc. SPIE*, **1686**, 2 – 12.
- NIST Report, (1993), *Absolute Broadband LWIR Radiant Flux Measurements of Martin Black Samples of Simulated Reference Spheres for the MSX Program*, NIST Measurement 844/LBIR-7-93, TP-010700-001-F01.00-930909, 9 September 1993.
- Nordgren, T. E., Germain, M. E., Benson, J. A., Mozurkewich, D., Sudol, J. J., Elias II, N. M., Hajian, A. R., White, N. M., Hutter, D. J., Johnston, K. J., Gauss, F. S., Armstrong, J. T., Pauls, T. A., & Rickard, L. J. (1999), "Stellar Angular Diameters of Late-Type Giants and Supergiants Measured with the Navy Prototype Optical Interferometer," *Astron. J.*, **118**, 3032 – 3038.
- Olson, F. M., & Raimond, E. (1986), "IRAS Catalogs and Atlases. Atlas of Low Resolution Spectra," *Astron. Astrophys.*, **65**, 607 – 1065.
- Onaka, T., Ishihara, D., Ootsubo, T., Chan, K.-W., Yamamura, I., Murakami, H., Tanabe, T., Roellig, T. L., & Cohen, M. (2003), "Flight Calibration of the Mid-Infrared Spectrometer (MIRS) on board the IRTS," in *The Calibration Legacy of the ISO Mission*, ed. L. Metcalfe, & M. F. K. Kessler, ESA SP **481**, 119 – 122.
- Perrin, G., Coude Du Foresto, V., Ridgway, S. T., Mariotti, J.-M., Traub, W. A., Carleton, N. P., & Lacasse, M. G. (1998), "Extension of the Effective Temperature Scale of Giants to Types Later Than M6," *Astron. Astrophys.*, **331**, 619 – 626.
- Pickles, A. J. (1998), "A Stellar Spectral Flux Library: 1150-25000 Å," *Publ. Astron. Soc. Pac.*, **110**, 863 – 878.
- Pierce, A. K. (1954), "Relative Solar Energy distribution in the Spectral Region 10,000 – 25,000 Å," *Astrophys. J.*, **119**, 312 – 327.
- Pierce, A. K., Slaughter, D., & Weinberger, D. (1977), "Solar Limb Darkening in the Interval 7404 – 24 018 Å," *Solar Phys.*, **52**, 179 – 189.
- Pompea, S. M., Bergener, D. W., Shepard, D. F., Russak, S., & Wolfe, W. L. (1984), "Reflectance Measurements on an Improved Optical Black for Stray Light Rejection from 0.3 to 500 µm," *Opt. Eng.*, **23**, 149 – 152.
- Price, S. D. (1970a), *Stellar Standards at 10 Microns*, AFCRL-70-0402, NTIS AD 711 364.
- Price, S. D. (1970b), *Quantitative Interpretation of the Infrared Spectra of Late-Type Stars*, PhD Thesis, the Ohio State University.
- Price, S. D. (1978), "Calibration of Infrared Celestial Sensors in Space," *Proc. SPIE*, **132**, 89 – 96.
- Price, S. D. (2004), "Infrared Irradiance Calibration," *Space Science Reviews*, **113**, 409 – 456.
- Price, S. D., Egan, M. P., Carey, S. J., Mizuno, D., & Kuchar, T. A. (2001), "MSX Survey of the Galactic Plane," *Astron. J.* **121**, 2819 – 2842.
- Price, S. D., & Murdock, T. L. (1983), *The Revised AFGL Infrared Sky Survey Catalog*, AFGL-TR-83-0161, ADA 134 007.
- Price, S. D., Murdock, T. L., & Shivanandan, K. (1983), *The Far Infrared Sky Survey Experiment Final Report*, AFGL-TR-83-0055, ADA 131 966.
- Price, S. D., Noah, P. V., Mizuno, D., Walker R. G., & Jayaraman, S. (2003), "Midcourse Space Experiment Mid-Infrared Measurements of the Thermal Emission from the Zodiacal Dust Cloud," *Astron. J.*, **125**, 962 – 983.
- Price, S. D., Paxson, C., Engelke, C., & Murdock, T. L. (2004), "Spectral Irradiance Calibration in the Infrared. XV. Absolute Calibration of Standard Stars by Experiments on the Midcourse Space Experiment," *Astron. J.*, **128**, 889 – 910 (Paper XV).

- Price, S. D., Sloan, G. C., & Kraemer, K. E. (2002), "Artifacts at 4.5 and 8.0 Microns in Short-Wavelength Spectra from the Infrared Space Observatory," *Astrophys. J. Lett.*, **565**, L55 – L58.
- Price S. D., & Walker, R. G. (1976), *The AFGL Four Color Infrared Sky Survey: Catalog of Observations at 4.2, 11.0, 19.8 and 27.4 μm* , AFGL-TR-76-0208, AD A034 448.
- Price, S. D., & Walker, R. G. (1978), *Calibration of the HI STAR sensors*, AFGL-TR-78-0172, ADA 061 020.
- Quirrenbach, A., Mozurkewich, D., Buscher, D. F., Hummel, C. A., & Armstrong, J. T. (1996), "Angular diameter and Limb Darkening of Arcturus," *Astron. Astrophys.*, **312**, 160 – 166.
- Ramirez, I., & Melendez, J. (2005), "The Effective Temperature Scale of FGK Stars. II. T_{eff} :Color:[Fe/H] Calibrations," *Astrophys. J.*, **626**, 446 – 485.
- Reach, W. T., Megeath, S. T., Cohen, M., Hora, J., Carey, S., Surace, J., Willner, S. P., Barmby, P., Wilson, G., Glaccum, W., Lowrance, G., Marengo, M., & Fazio, G. G. (2005), "Absolute Calibration of the Infrared Array Camera on the Spitzer Space Telescope," *Publ. Astron. Soc. Pac.*, **117**, 978 – 990.
- Richichi, A., & Roccatagliate, V. (2005), "Aldebaran's Angular Diameter: How Well Do We Know It?," *Astron. Astrophys.*, **433**, 305 – 312.
- Ridgway, S. T., Jacoby, G. H., Joyce, R. R., Siegel, M. J., & Wells, D. C. (1982), "Angular Diameters by the Lunar Occultation Technique. VI - Limb Darkening of Alpha Tauri," *Astron. J.*, **87**, 1044 – 1050.
- Ridgway, S. T., Joyce, R. R., White, N. M., & Wing, R. F. (1980), "Effective Temperatures of Late-Type Stars - The Field Giants from K0 To M6," *Astrophys. J.*, **235**, 126 – 137.
- Rieke, G. H., Lebofsky, M. J., & Low, F. J. (1985), "An Absolute Photometric system at 10 and 20 μm ," *Astron. J.*, **90**, 900 – 906.
- Saiedy, F., 1960, "Solar Intensity and Limb Darkening Between 8.6 and 13 μ ," *Mon. Not. R. Astron. Soc.*, **121**, 483 – 495.
- Saiedy, F., & Goody, R. M. (1959), "The Solar Emission Intensity at 11 μ ," *Mon. Not. R. Astron. Soc.*, **119**, 213 – 222.
- Sargent, S. D. (1997), "Temperature Dependent Responsivity Correction for the SPIRIT III Radiometer," *Opt. Eng.*, **36**, 2948 – 2955.
- Schatten, K. H., & Orosz, J. (1990), "Solar Constant Secular Changes," *Solar Phys.*, **125**, 179 – 184.
- Schick, S., & Bell, G. (1997), "Performance of the SPIRIT III Cryogenic System," *Proc SPIE*, **3122**, 69 – 77.
- Schild, R., Peterson, D. M., & Oke, J. B. (1971), "Effective Temperatures of B- and A-Type Stars," *Astrophys. J.*, **166**, 95 – 108.
- Scholz, M. & Takeda, Y. (1987), "Model Study Of Wavelength-Dependent Limb-Darkening and Radii of M-Type Giants and Supergiants," *Astron. Astrophys.*, **186**, 200 – 212.
- Schulz, B., Huth, S., Laureijs, R. J., Acosta-Pulido, J. A., Braum, M., Castañada, H. O., Cohen, M., Cornwall, L., Gabriel, C., Hammersley, P., Heinrichsen, I., Klaas, U., Lemke, D., Müller, T., Osip, D., Román-Fernández, P., & Telesco, C. (2002) ISOPHOT – Photometric calibration of Point Sources, *Astron. Astrophys.*, **381**, 1110 – 1130.
- Sclar, N. (1983), "Development Status of Silicon Extrinsic Detectors," *Proc. SPIE*, **443**, 11 – 41.
- Selby, M. J., Blackwell, D. E., Petford, A. D., & Shallis, M. J. (1980), "Measurement of the absolute flux from Vega in the K band (2.2 microns)," *Mon. Not. R. Astron. Soc.*, **119**, 111 – 114.

- Selby, M. J., Hepburn, I., Blackwell, D. E., Booth, A. J., Haddock, D. J., Arribas, S., Leggett, S. K., & Mountain, C. M. (1988), "Narrow Band 1 micron-4 micron Infrared Photometry of 176 Stars," *Astron. Astrophys. Suppl.*, **74**, 127 – 132.
- Selby, M. J., Mountain, C. M., Blackwell, D. E., Petford, A. D., & Leggett, S. K. (1983), "Measurements of the Absolute Monochromatic flux from Vega at λ 2.20 and 3.80 μ m by Comparison with a Furnace," *Mon. Not. R. Astron. Soc.*, **203**, 795 – 800.
- Simpson, W. R. (1995), "AEDC Aerospace Chamber 7V - An Advanced Test Capability for Infrared Surveillance and Seeker Sensors," *Proc. SPIE*, **2470**, 369 – 379.
- Skrutskie, M. F., Cutri, R. M., Stiening, R., Weinberg, M. D., Schneider, S., Carpenter, J. M., Beichman, C., Capps, R., Chester, T., Elias, J., Huchra, J., Liebert, J., Lonsdale, C., Monet, D. G., Price, S., Seitzer, P., Jarrett, T., Kirkpatrick, J. D., Gizis, J. E., Howard, E., Evans, T., Fowler, J., Fullmer, L., Hurt, R., Light, R., Kopan, E. L., Marsh, K. A., McCallon, H. L., Tam, R., Van Dyk, S., & Wheelock, S. (2006), "The Two Micron All Sky Survey (2MASS)," *Astron. J.*, **131**, 1163 – 1183.
- Sloan G. C., & Price, S. D. (1998), "The Infrared Spectral Classification of Oxygen-Rich Dust Shells," *Astrophys. J. Suppl.*, **119**, 141 – 158.
- Sloan, G. C., Kraemer, K. E., Price, S. D., & Shipman, R. F. (2003), "A Uniform Database of 2.4 – 45.4 μ m Spectra from the ISO Short Wavelength Spectrometer," *Astrophys. J. Suppl.*, **147**, 379 – 401.
- Smith, B. J. (2003), "Infrared Colors and Variability of Evolved Stars for COBE DIRBE Data," *Astron. J.*, **126**, 935 – 963.
- Smith, B. J., Price, S. D., & Baker, R. I. (2004), "The COBE-DIRBE Point Source Catalog," *Astrophys. J. Suppl.* **154**, 673 – 704.
- Spickler, P. T., Benner, D. C., & Russell III, J. M. (1996), "Solar Center-to-Limb Infrared Intensity from the Halogen Occultation Experiment," *Solar Phys.*, **165**, 33 – 39.
- Stierwalt, D. L. (1975), "Low Temperature Transmittance of Materials for the Infrared," *Proc. SPIE*, **67**, 53 – 58.
- Stierwalt, D. L., & Eisenman, W. L. (1978), "Problems in using Cold Spectral Filters with LWIR Detectors," *Proc. SPIE*, **132**, 134 – 140.
- Strecker, D. W., Erickson, E. F., & Witteborn, F. C. (1979), "Airborne stellar spectrophotometry from 1.2 to 5.5 microns - Absolute calibration and spectra of stars earlier than M3," *Astrophys. J. Suppl.*, **41**, 501 – 512.
- Su, K. Y. L., Rieke, G. H., Misselt, K. A., Stansberry, J. A., Moro-Martin, A., Stapelfeldt, K. R., Werner, M. W., Twilling, D. E., Bendo, G. H., Gordon, K. D., Hines, D. C., & Wyatt, M. C. (2005), "The Vega Debris Disk: A Surprise from Spitzer," *Astrophys. J.*, **628**, 487 – 500.
- Surface Optics Corporation Technical Report (1993), *Directional Reflectance Measurements on Seven MIT/LL Supplied Sample Materials*, SOC-R761-001-0493, April 1993.
- Tedesco, E. F. (1993), "Asteroid Albedos and Diameters," in *Asteroids, Comets and Meteors 1993*, ed. A. Milai, M. Di Martino, & A. Cellino, IAU Symp., **160**, 55 – 74.
- Thomas, J. A., Hyland, A. R., & Robinson, G. (1973), "Southern Infra-Red Standards and the Absolute Calibration of Infra-Red Photometry," *Mon. Not. R. Astron. Soc.*, **165**, 201 – 211.
- Thomas, J. A., Robinson, G., & Hyland, A. R. (1976), "Intermediate Bandwidth Spectrometry in the 10-Micron Region and Its Interpretation," *Mon. Not. R. Astron. Soc.*, **174**, 711 – 723.
- Thuillier, G., Floyd, L., Woods, N., Cebula, R., Hilsenrath, E., Hersé, M., & Labs, D. (2004), "Solar Irradiance Reference Spectra for Two Solar Active Levels," *Adv. Space Res.*, **34**, 256 – 261.

- Thuillier, G., Hersé, M., Labs, D., Foujols, T., Peetermans, W., Gillotay, D., Simon, P. C., & Mandel, H. (2003), "The Solar Spectral Irradiance from 200 to 2400 nm as Measured by the SOLSPEC Spectrometer from the Atlas and Eureka Missions," *Solar Phys.*, **214**, 1 – 22.
- Thurgood, A., Larsen, M. F., & Sargent, S. D. (1998), "SPIRIT III Ground Calibration Overview," presentation in Proc. *SDL/USU Symposium on Infrared Radiometric Sensor Calibration* Sept 22 – 24 1998, Logan, UT
- Tobiska, W. K. (2002), "Variability in the Solar Constant from Irradiances Shortward of Lyman-Alpha," *Adv. Space. Sci.*, **29**, 1969 – 1974.
- Tokunaga, A. T. (1984), "A reevaluation of the 20-micron magnitude system," *Astron. J.*, **89**, 172 – 175.
- Tüg, H., White, N. M., & Lockwood, G. W. (1977), "Absolute Energy Distributions of Alpha Lyrae and 109 Virginis from 3295 Å to 9040 Å," *Astron. Astrophys.*, **61**, 679 – 684.
- van Belle, G. T., Lane, B. F., Thompson, R. R., Boden, A. F., Colavita, M. M., Dumont, P. J., Mobley, D. W., Palmer, D., Shao, M., Vasisht, G. X., Wallace, J.K., Creech-Eakman, M.J., Koresko, C.D., Kulkarni, S.R., Pan, X.P., & Gubler, J. (1999), "Radii and Effective Temperatures for G, K, and M Giants and Supergiants," *Astron. J.*, **117**, 521 – 533.
- van der Bliek, N. S., Manfroid, J., & Bouchet, P. (1996), "Infrared Aperture Photometry at ESO (1983-1994) and Its Future Use," *Astron. Astrophys. Suppl.*, **119**, 547 – 557.
- Vardya, M. S., de Jong, T., & Willems, F. J. (1986), "IRAS Low-Resolution Spectrograph Observations of Silicate and Molecular SiO Emission in Mira Variables," *Astrophys. J. Lett.*, **304**, L29 – L3.
- Vernazza, J. E., Avrett, E. H., & Loeser, R. (1976), "Structure of the Solar Chromospheres II. The Underlying Photosphere and Temperature-Minimum Region," *Astrophys. J. Suppl.*, **30**, 1 – 60.
- Volk, K., & Cohen, M. (1989), "On the Calibration of the IRAS Low-Resolution Spectra," *Astron. J.*, **98**, 1918 – 1934.
- Von Braun, C., Sharma, J., & Gaposchkin, E. M. (1997), "SBV Metric Accuracy," *Proc. 1997 Space Control Conf.*, ESC-TR-97-063 Vol. II, 49 – 70.
- Wainscoat, R. J., Cohen, M., Volk, K., Walker, H. J., & Schwartz, D. E. (1992), "A model of the 8-25 micron point source infrared sky," *Astrophys. J. Suppl.*, **83**, 111 – 146.
- Walker, R. G. (1969), "Near Infrared Photometry of Late-Type Stars," *Phil. Trans. Roy. Soc. London, Ser. A. Math. Phys. Sci.*, **264**, 209 – 225.
- Walker, R. G., & Cohen, M. (1998), *Infrared Celestial Backgrounds Studies Volume 2: A Radiometric All-sky Network of Absolutely Calibrated Stellar Spectra*, AFRL-VS-TR-98-0104(II), ADA 366 960.
- Walker, R. G., & Cohen, M. (2003), *Irradiance Calibration of Space-Based Infrared Sensors Ann. Report No. 4*, AFRL-TR-2003-1551, ADA 418 543.
- Walker, R. G., Jayaraman, S., Cohen, M., & Barker, E. (2004), *Irradiance Calibration of Space-Based Infrared Sensors Ann. Scientific Report No. 5*, AFRL-VS-HA-TR-2004-1161, ADA 435 636.
- Walker, R. G., & Price, S. D. (1975), *The AFCRL Infrared Sky Survey: Volume I, Catalog of Observations at 4, 11 and 20 Microns*, AFCRL-TR-75-0373, ADA 016 397.
- Wallace, L., & Hinkle, K. (1996), "High-Resolution Spectra of Ordinary Cool Stars in the K Band," *Astrophys. J. Suppl.*, **107**, 312 – 390.
- Wallace, L., & Hinkle, K., (1997), "Medium-Resolution Spectra of Normal Stars in the K Band," *Astrophys. J. Suppl.*, **111**, 445 – 458.

- Wamstecker, W. (1981), "Standard Stars and Calibration for JHKLM Photometry," *Astron. Astrophys.*, **97**, 329 – 333.
- Wilson, C. F. (1992), "Calibration of MSX Reference Spheres," Proc. *SDL/USU Third Symposium on Infrared Radiometric Sensor Calibration* Sept 14 – 17 1992, Logan, UT
- Witteborn, F. C., Cohen, M., Bregman, J. D., Wooden, D. H., Heere, K., & Shirley, E. L. (1999), "Spectral Irradiance Calibration in the Infrared. XI. Comparison of α Bootes and 1 Ceres with a Laboratory Standard," *Astron. J.*, **117**, 2552 – 2560 (Paper XI).
- Wittkowski, M., Hummel, C. A., Johnston, K. J., Mozurkewich, D., Hajian, A. R., & White, N. M. (2001), "Direct Multi-Wavelength Limb-darkening Measurements of Three Late-type Giants with the Navy Prototype Optical Interferometer," *Astron. Astrophys.*, **377**, 981 – 993.
- XONTECH (1988), *Sensors for Surveillance, Acquisition and Discrimination (87-688) Infrared Sensor Calibration Techniques and Standards. Infrared Calibration Handbook*, ADB121813
- Zachor, A. S., & Huppi, E. R. (1981), "Nonlinear Response of Low-Background extrinsic Silicon Detectors. 1: A Phenomenological Model," *Appl. Opt.*, **20**, 1000 – 1004.
- Zachor, A. S., Huppi, E. R., Coleman, I., & Grodsham, D. G. (1982), "Nonlinear response of low-background extrinsic silicon detectors. 2. A revised model," *Appl. Opt.*, **21**, 2027 – 2035.
- *Available from the Space Dynamics Laboratory of the Utah State University

Appendix A Photometric Scaling of the Calibrated Spectra

This appendix contains information on the adjustments that were used to rationalize the spectra and to scale the result to absolute values for each of the stars in Tables 20, 21 and 23. The stars are listed in the order that they appear in the tables. The adjustments, photometric scaling and derived parameters are listed for each star. A plot follows the parameter list that displays the measured photometry against what is predicted from the absolute spectrum.

The ISO SWS spectra we used were the averaged spectral fragments given by Sloan et al. (2003) and the listed adjustments are applied to those fragments. The short wavelength spectra from Strecker, Eickson, and Witteborn (1979) are seamed onto the SWS with the listed adjustments. Additional short spectral fragments from other resources were used for a small number of stars as noted.

For convenience, the photometric magnitude scale for a given photometric reference was adjusted so that $[IR_{\text{Sirius}}] = -1.36$. The DIRBE photometry was taken from Smith, Price and Baker (2004) but 0.045 magnitudes was added to DIRBE Band 1 results to correct for bias for Sirius in the DIRBE data. If a photometric reference had no Sirius measurement, Vega then is used with magnitudes being calculated using the band pass and Cohen et al. model. The MSX photometry is from Price et al. (2004) while the IRAS information was obtained from the Vizier web site (<http://vizier.hia.nrc.ca/viz-bin/VizieR>).

The stellar effective temperature (T_{eff}) and angular diameter (θ) in milli-arcseconds were derived by fitting the *autoshape* function to the photometry. The plots show how well the *autoshape* function using the derived parameters fits the observations.

Star: β Gem
HD62509, HR2990, IRAS07422+2808
K0 III
CWW composite star

Fit Parameters: $T_{\text{eff}} = 4850 \text{ K}$, $\theta = 8.03 \text{ mas}$

Spectral Data: SWS = (Average of normalized δ Eri and θ Cen) \times Engelke function with $T_{\text{eff}} = 4850 \text{ K}$ and $\theta = 8.03 \text{ mas}$
SEW: (1.22 to 2.36 μm)

Photometry (with Sirius defined as -1.36):

DIRBE1: -0.500 (0.030)	lightcurve ampl: 0.01 (0.03)
DIRBE2: -1.081 (0.009)	lightcurve ampl: 0.01 (0.01)
DIRBE3: -1.149 (0.022)	lightcurve ampl: 0.03 (0.03)
DIRBE4: -1.067 (0.020)	lightcurve ampl: 0.01 (0.02)

Hammersley et al. (1998) J: -0.525 (0.009)	Selby et al. (1988) J: -0.545 (0.01)
Hammersley et al. (1998) H: -0.999 (0.009)	
Hammersley et al. (1998) K: -1.088 (0.012)	Selby et al. (1988) K: -1.119 (0.01)
Hammersley et al. (1998) L: -1.151 (0.020)	Selby et al. (1988) L: -1.199 (0.02)

MSX A: -1.197 (0.008)	MSX C: -1.228 (0.004)
MSX B ₁ : -1.162 (0.007)	MSX D: -1.235 (0.003)
MSX B ₂ : -1.115 (0.006)	

Tokunaga (1984) 10.1: -1.24 (0.025)
Tokunaga (1984) 20.1: -1.21 (0.025)

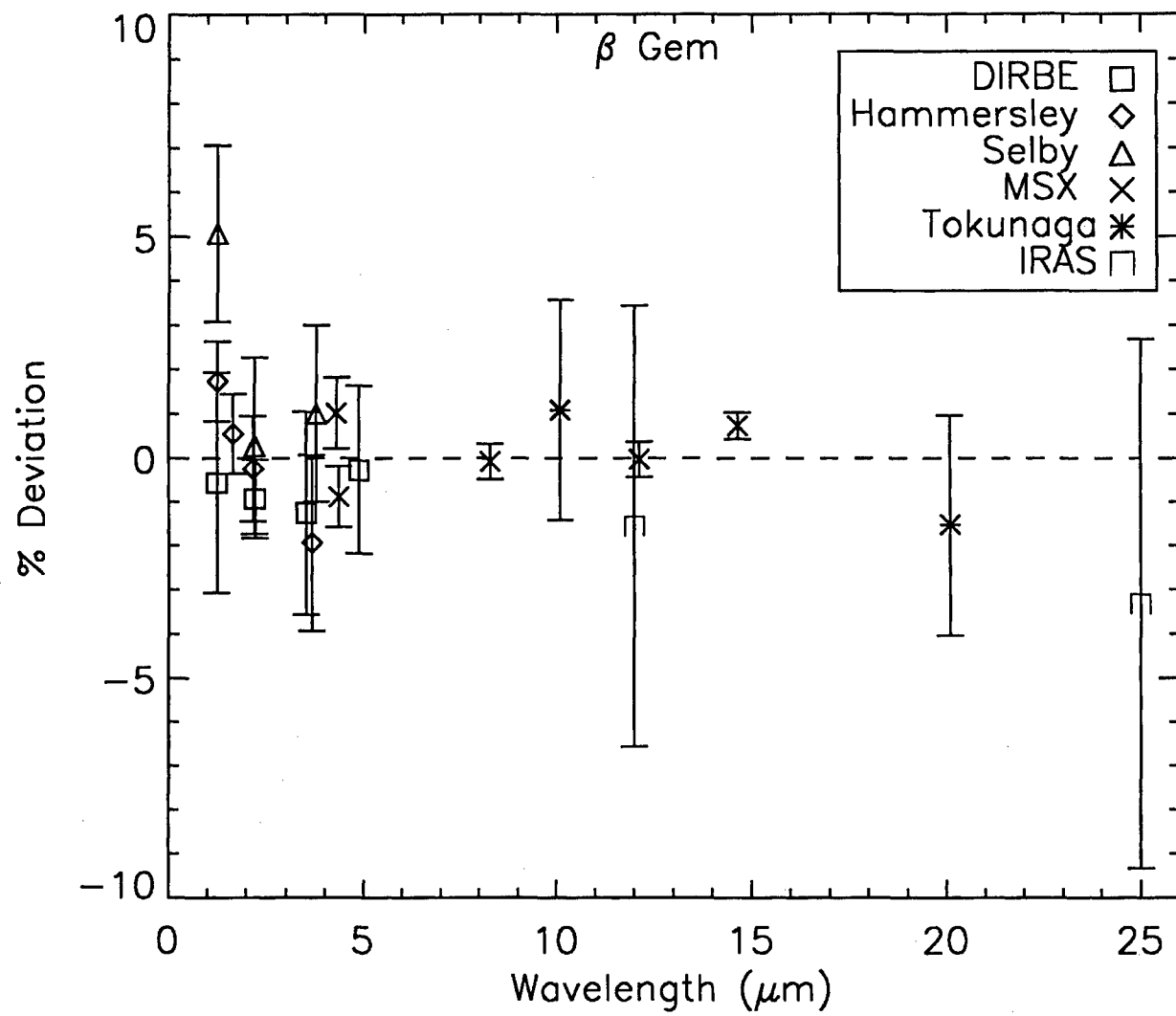
IRAS 12: -1.21 (0.04)
IRAS 25: -1.19 (0.05)

Uncertainty: In shape: 5% near 1 μm , 3% near 2 μm ,
1% from 2.5 μm to 12 μm , 1.5% beyond
In normalization relative to Sirius: 1%
In absolute flux of Sirius: 1.2%

Adjustments:

SWS: see comments for δ Eri and θ Cen

SEW: 1.015 \times



Star: α Boo
 HD124897, HR5340, IRAS14133+1925
 K1.5 III
 CWW composite star

Fit Parameters: $T_{\text{eff}} = 4350 \text{ K}$, $\theta = 21.06 \text{ mas}$

Spectral Data: SWS TDT: 45200101 (2.4 μm to 21 μm)
 Hinkle, Wallace & Livingston (1995) (2.1 μm to 2.4 μm)
 SEW: (1.22 μm to 2.4 μm)

Photometry (with Sirius defined as -1.36):

DIRBE1: -2.221 (0.030)	lightcurve ampl: 0.04 (0.03)
DIRBE2: -2.988 (0.009)	lightcurve ampl: 0.01 (0.01)
DIRBE3: -3.083 (0.022)	lightcurve ampl: 0.04 (0.02)
DIRBE4: -2.934 (0.020)	lightcurve ampl: 0.01 (0.01)

Hammersley et al. (1998) J: -2.198 (0.007)	Selby et al. (1988) J: -2.215 (0.02)
Hammersley et al. (1998) H: -2.853 (0.007)	
Hammersley et al. (1998) K: -2.964 (0.014)	Selby et al. (1988) K: -3.049 (0.02)
Hammersley et al. (1998) L: -3.097 (0.010)	Selby et al. (1988) L: -3.139 (0.02)

MSX A: -3.140 (0.004)	MSX C: -3.187 (0.003)
MSX B ₁ : -3.082 (0.007)	MSX D: -3.182 (0.002)
MSX B ₂ : -3.031 (0.006)	MSX E: -3.199 (0.008)

Uncertainty: In shape: 5% near 1 μm , 3% near 2 μm ,
 1% from 2.5 μm to 12 μm , 1.5% beyond
 In normalization relative to Sirius: 0.15%
 In absolute flux of Sirius: 1.2%

Adjustments:

SWS:

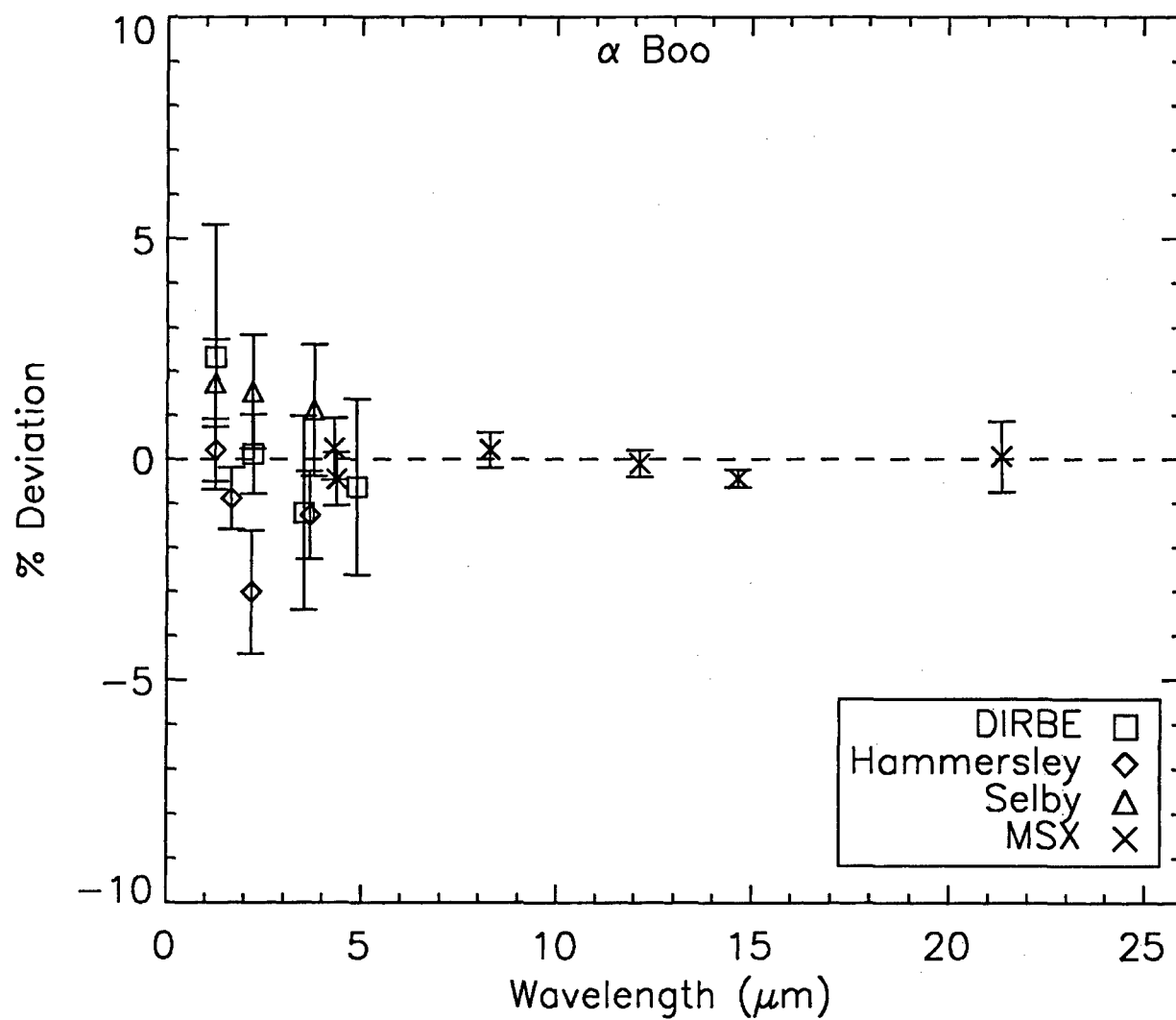
1A	$0.94 \times (\lambda / 2.5)^{0.10}$
1B	$0.95 \times (\lambda / 2.6)^{0.02}$
1D	$0.96 \times (\lambda / 3.0)^{0.13}$
1E	$0.975 \times (\lambda / 3.7)^{0.17}$
2A	$1.06 \times (\lambda / 4.05)^{0.16}$
2B	$1.12 \times (\lambda / 5.35)^{0.15}$
2C	$0.975 \times (\lambda / 7.40)^{0.20};$

$(\lambda/8.5)^{0.15}$ ($8.5 < \lambda < 10.5 \mu\text{m}$);
 $1.03 \times (\lambda/10.4)^{-0.5}$ ($10.5 < \lambda < 11.9 \mu\text{m}$);
 $0.920 \times$ ($\lambda > 11.9 \mu\text{m}$)

3A $1.074 \times (\lambda/12.0)^{0.1}$
 3C $1.06 \times$
 3D $1.04 \times (\lambda/18)^{0.15}$

SEW: $0.98 \times (\lambda/2.0)^{0.05}$

Hinkle et al: $1.005 \times (\lambda/2.2)^{-0.35}$



Star: β UMi
HD 131873, HR 5563, IRAS 14508+7421
K4 III
CWW template star

Fit Parameters: $T_{\text{eff}} = 4150 \text{ K}$, $\theta = 10.00 \text{ mas}$

Spectral Data: SWS TDT: 18205639 (2.36 μm to 16 μm)

Photometry (with Sirius defined as -1.36):

DIRBE1: -0.469 (0.026)	lightcurve ampl: 0.04 (0.03)
DIRBE2: -1.292 (0.010)	lightcurve ampl: 0.01 (0.01)
DIRBE3: -1.410 (0.023)	lightcurve ampl: 0.03 (0.03)
DIRBE4: -1.215 (0.023)	lightcurve ampl: 0.02 (0.02)

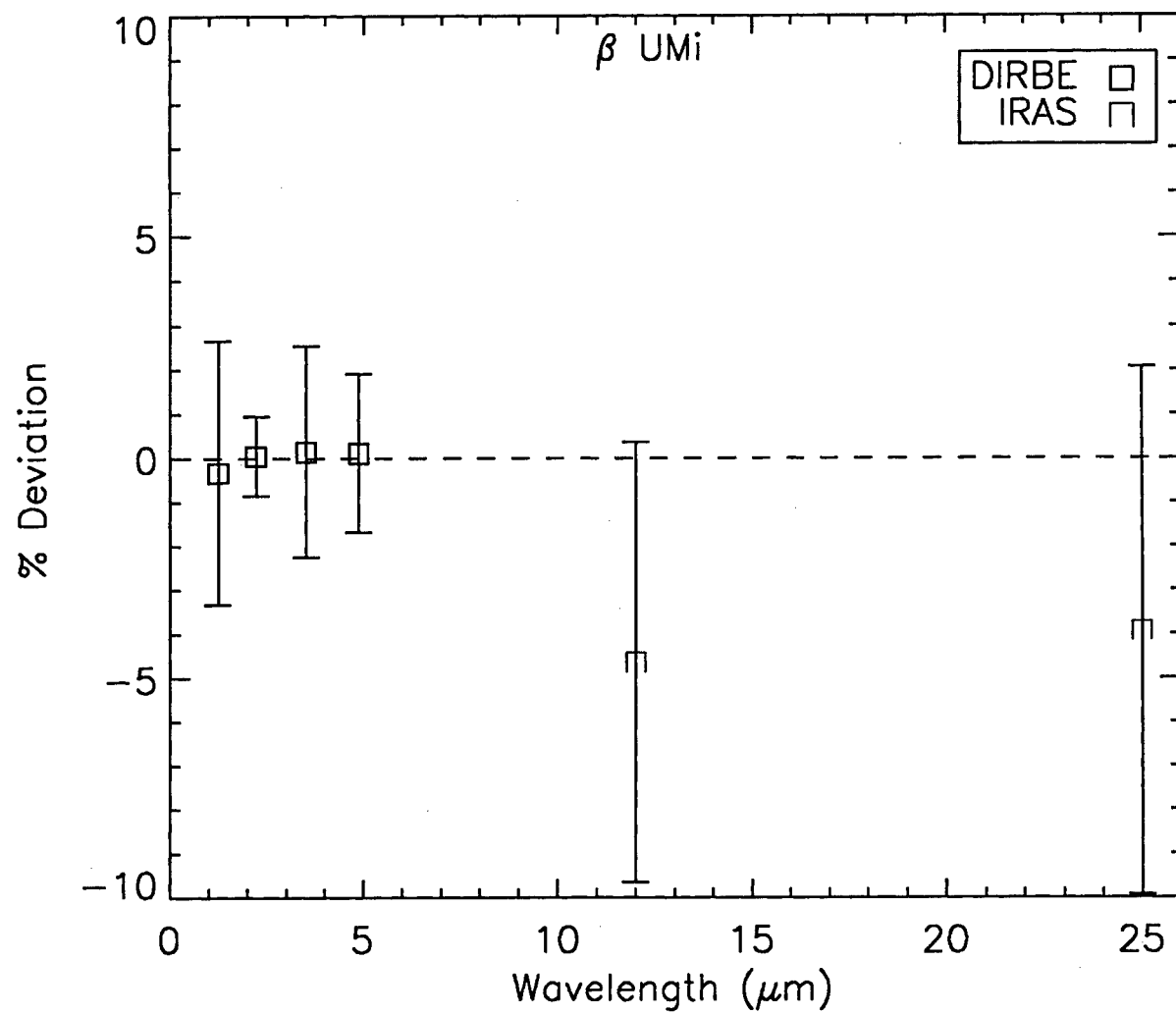
IRAS 12: -1.47 (0.05)

IRAS 25: -1.48 (0.06)

Uncertainty: In shape: 5% near 1 μm , 3% near 2 μm ,
1% from 2.5 μm to 12 μm , 1.5% beyond
In normalization relative to Sirius: 0.5% for average

Adjustments:

SWS:	1A	0.98 \times
	1B	0.98 \times
	1D	0.98 \times
	1E	0.98 \times
	2A	0.932 \times
	2B	$0.91 \times (\lambda/7.0)^{0.04}$
	2C	$0.92 \times (\lambda/7.0)^{0.04}$
	3A	0.89 \times
	3C	0.95 \times



Star: γ Dra
HD164058, HR6705, IRAS1755+5129
K5 III
CWW composite star

Fit Parameters: $T_{\text{eff}} = 4030 \text{ K}$, $\theta = 10.17 \text{ mas}$

Spectral Data: SWS TDT: 37704637 (2.36 μm to 27 μm)
Wallace & Hinkle (1996, 1997) (2.01 μm to 2.36 μm)

Photometry (with Sirius defined as -1.36):

DIRBE1: -0.400 (0.030)	lightcurve ampl: 0.05 (0.03)
DIRBE2: -1.281 (0.013)	lightcurve ampl: 0.02 (0.01)
DIRBE3: -1.410 (0.023)	lightcurve ampl: 0.03 (0.02)
DIRBE4: -1.185 (0.020)	lightcurve ampl: 0.02 (0.02)

Hammersley et al. (1998) J: -0.382 (0.007)	Selby et al. (1988) J -0.396 (0.02)
Hammersley et al. (1998) H: -1.123 (0.007)	
Hammersley et al. (1998) K: -1.281 (0.013)	Selby et al. (1988) K: -1.344 (0.02)
Hammersley et al. (1998) L: -1.416 (0.009)	Selby et al. (1988) L: -1.449 (0.03)

MSX A: -1.437 (0.008)	MSX C: -1.520 (0.007)
MSX B ₁ : -1.338 (0.010)	MSX D: -1.500 (0.006)
MSX B ₂ : -1.276 (0.014)	MSX E: -1.557 (0.050)

Uncertainty: In shape: 5% near 1 μm , 3% near 2 μm ,
1% from 2.5 μm to 12 μm , 1.5% beyond
In normalization relative to Sirius: 0.2% for average
Amplitude of variation possibly as high as 1.5% (1% 1 σ ?)
In absolute flux of Sirius: 1.2%

Adjustments:

SWS:	1A	$0.976\times$
	1B	$0.973\times$
	1D	$0.975\times$
	1E	$0.98\times(\lambda/3.8)^{0.07}$
	2A	$0.933\times$
	2B	$0.98\times(\lambda/6.8)^{0.22}$

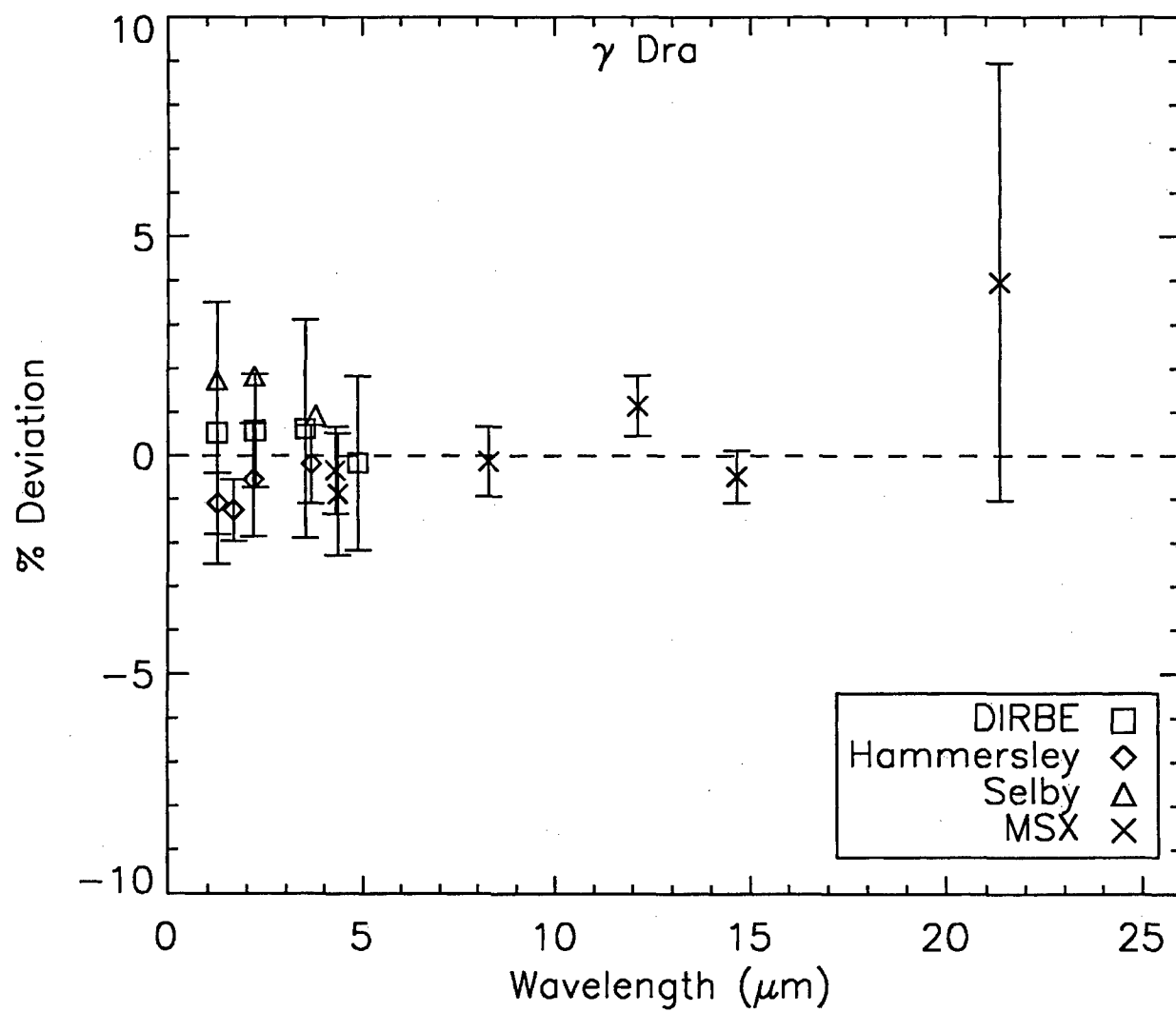
$$2C \quad 0.885 \times (\lambda/7.0)^{0.035}$$

$$3A \quad 0.972 \times$$

$$3C \quad 0.94 \times$$

$$3D \quad 0.89 \times$$

$$\text{SEW:} \quad 0.95 \times (\lambda/2.4)^{-0.2}$$



Star: α Tau
HD29139, HR1457, IRAS04330+1624
K5 III
CWW composite star

Fit Parameters: $T_{\text{eff}} = 4050 \text{ K}$, $\theta = 20.75 \text{ mas}$

Spectral Data: SWS TDT: 63602102 (2.4 μm to 35 μm)
SEW: (1.22 μm to 2.4 μm)
Wallace & Hinkle (1996, 1997) (2.04 μm to 2.4 μm)

Photometry (with Sirius defined as -1.36):

DIRBE1: ---
DIRBE2: -2.834 (0.005) lightcurve ampl: 0.00 (0.01)
DIRBE3: -2.958 (0.016) lightcurve ampl: 0.02 (0.02)
DIRBE4: -2.748 (0.006) lightcurve ampl: 0.00 (0.01)

Hammersley et al. (1998) J: -1.887 (0.016)	Selby et al. (1988) J: -1.932 (0.02)
Hammersley et al. (1998) H: -2.624 (0.007)	
Hammersley et al. (1998) K: -2.826 (0.013)	Selby et al. (1988) K: -2.914 (0.02)
Hammersley et al. (1998) L: -2.960 (0.009)	Selby et al. (1988) L: -3.039 (0.02)

MSX A: -2.994 (0.004)	MSX C: -3.078 (0.003)
MSX B ₁ : -2.907 (0.007)	MSX D: -3.071 (0.002)
MSX B ₂ : -2.854 (0.006)	MSX E: -3.094 (0.008)

Uncertainty: In shape: 5% near 1 μm , 3% near 2 μm ,
1% from 2.5 μm to 12 μm , 1.5% beyond
In normalization relative to Sirius: 0.2%
In absolute flux of Sirius: 1.2%

Adjustments:

SWS:

1A	$0.980\times$
1B	$0.985\times$
1D	$0.976\times(\lambda/3.3)^{-0.05}$
1E	$0.965\times(\lambda/3.3)^{0.05}$
2A	$0.995\times(\lambda/4.1)^{-0.1}$
2B	$1.07\times(\lambda/5.5)^{0.12}$
2C	$0.93\times(\lambda/7.0)^{0.10}$, ($\lambda \leq 9.3 \mu\text{m}$)

$$0.96 \times (\lambda/9.3)^{0.45}, (\lambda > 9.3 \mu\text{m})$$

$$3A \quad 0.88 \times$$

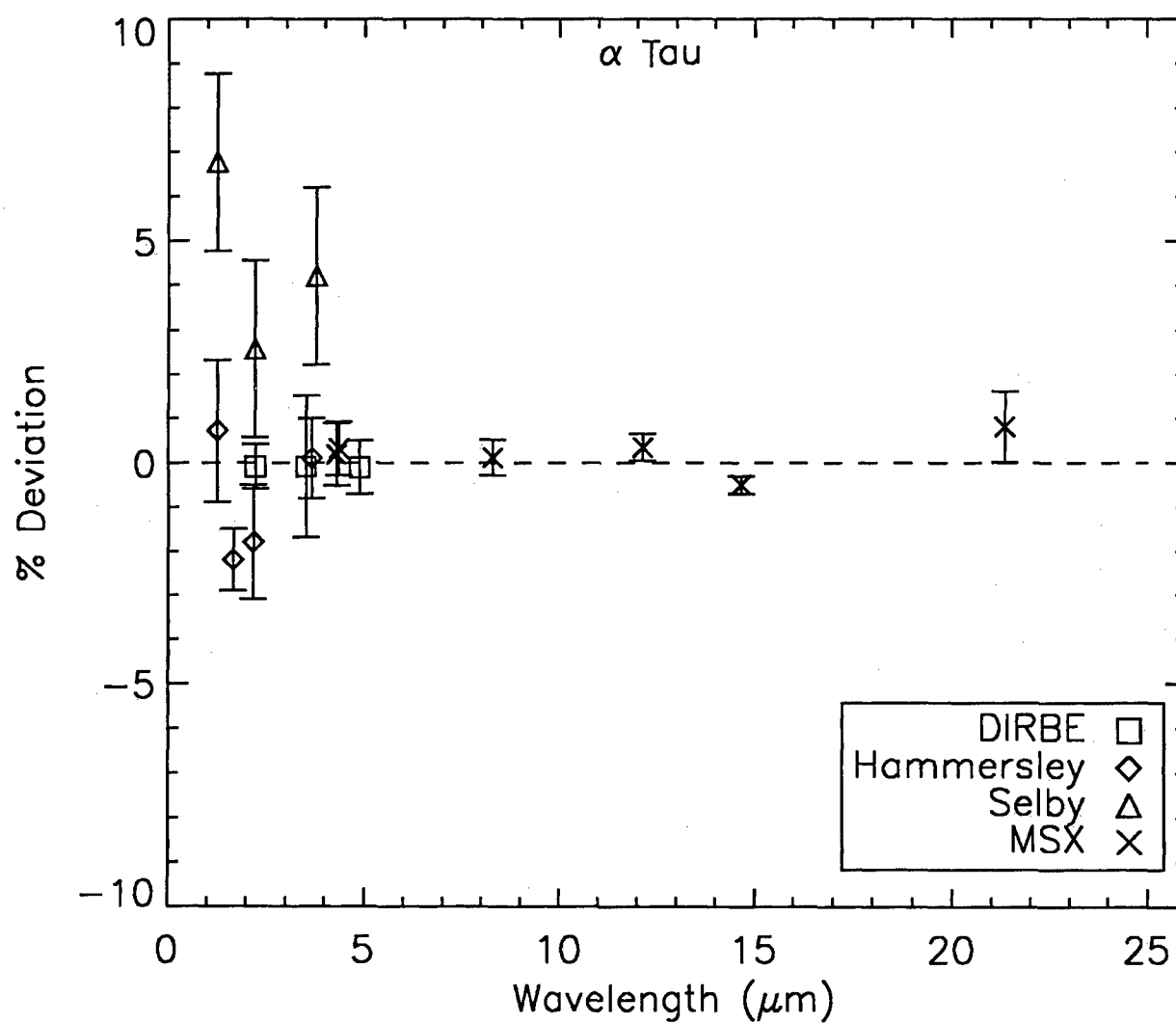
$$3C \quad 0.825 \times$$

$$3D \quad 0.94 \times (\lambda/28)^{-2}$$

$$3E \quad 1.00 \times (\lambda/31)^{-0.7}$$

$$\text{SEW:} \quad 0.993 \times (\lambda/2.2)^{0.05}$$

$$\text{Wallace \& Hinkle:} \quad 1.00 \times (\lambda/2.35)^{-0.3}$$



Star: μ UMa
HD89758, HR4069, IRAS10193+4145
Spectroscopic binary
M0 III
CWW composite star

Fit Parameters: $T_{\text{eff}} = 3900 \text{ K}$, $\theta = 8.45 \text{ mas}$

Spectral Data: SWS TDT: 16000806 (2.4 μm to 9.9 μm)
Wallace & Hinkle (1996, 1997) (2.05 μm to 2.4 μm)

Photometry (with Sirius defined as -1.36):

DIRBE1: 0.126 (0.03)	lightcurve ampl: 0.03 (0.03)
DIRBE2: -0.817 (0.01)	lightcurve ampl: 0.01 (0.01)
DIRBE3: -0.950 (0.02)	lightcurve ampl: 0.03 (0.03)
DIRBE4: -0.730 (0.02)	lightcurve ampl: 0.03 (0.03)

Tokunaga (1984) 10.1: -1.03 (0.025)

Tokunaga (1984) 20.1: -1.08 (0.025)

IRAS 12: -0.98 (0.05)

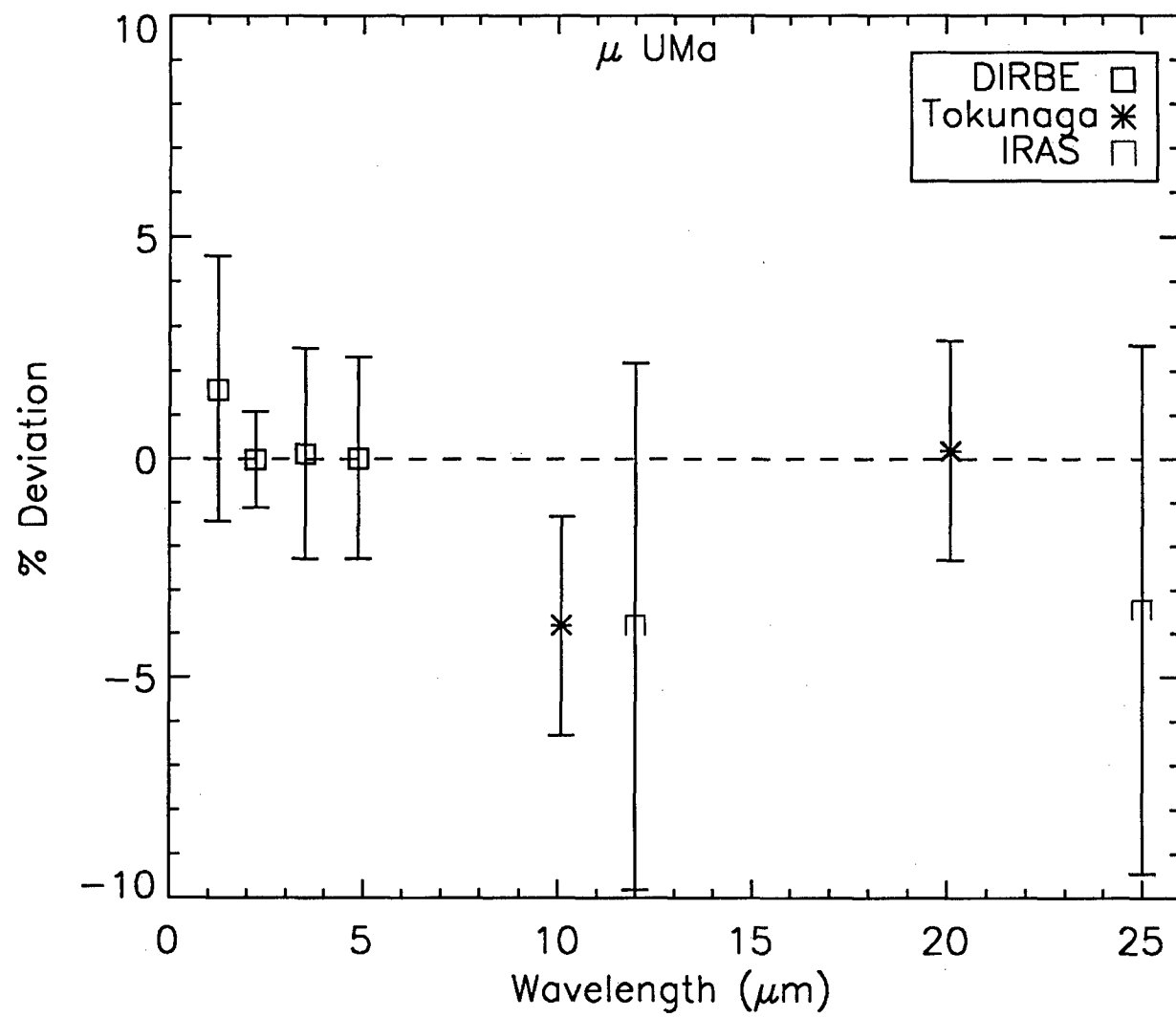
IRAS 25: -1.04 (0.06)

Uncertainty: In shape: 5% near 1 μm , 3% near 2 μm ,
1% from 2.5 μm to 12 μm , 1.5% beyond
In normalization relative to Sirius: 0.5% for average
In absolute flux of Sirius: 1.2%

Adjustments:

SWS:

1A	$0.951 \times$
1B	$0.955 \times (\lambda/3.0)^{0.1}$
1D	$0.96 \times$
1E	$0.965 \times (\lambda/3.9)^{0.1}$
2A	$1.01 \times$
2B	$0.972 \times (\lambda/5.5)^{0.1}$
2C	$1.022 \times (\lambda/7.0)^{-0.07}$
3A	$1.10 \times (\lambda/12.5)^{0.35}$



Star: β And
HD6860, HR337, IRAS01069+3521
K5 III
CWW composite star

Fit Parameters: $T_{\text{eff}} = 3900 \text{ K}$, $\theta = 13.65 \text{ mas}$

Spectral Data: SWS TDT: 79501002 (2.36 μm to 27 μm)
SEW (1.22 μm to 2.36 μm)

Photometry (with Sirius defined as -1.36):

DIRBE1: -0.873 (0.025)	lightcurve ampl: 0.02 (0.03)
DIRBE2: -1.844 (0.015)	lightcurve ampl: 0.01 (0.01)
DIRBE3: -1.978 (0.022)	lightcurve ampl: 0.04 (0.02)
DIRBE4: -1.749 (0.016)	lightcurve ampl: 0.01 (0.01)

Hammersley et al. (1998) J: -0.911 (0.007)	Selby et al. (1988) J: -0.892 (0.02)
Hammersley et al. (1998) H: -1.731 (0.007)	
Hammersley et al. (1998) K: -1.914 (0.013)	Selby et al. (1988) K: -1.904 (0.01)
Hammersley et al. (1998) L: -1.983 (0.009)	Selby et al. (1988) L: -2.049 (0.01)

MSX A: -2.03 (0.016)	MSX C: -2.128 (0.012)
MSX B ₁ : -1.87 (0.015)	MSX D: -2.128 (0.02)
MSX B ₂ : -1.87 (0.018)	MSX E: -2.108 (0.028)

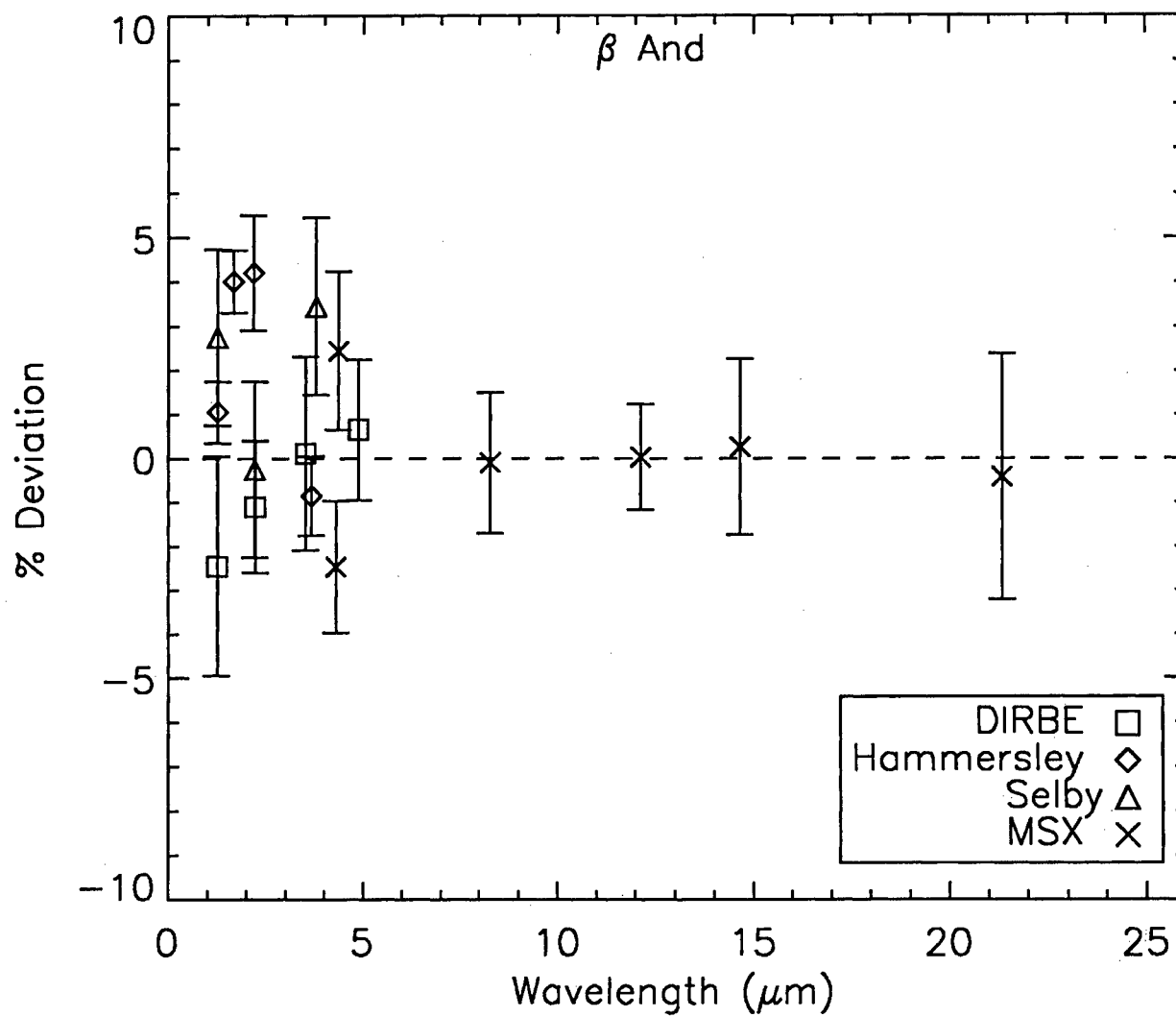
Uncertainty: In shape: 5% near 1 μm , 3% near 2 μm ,
1% from 2.5 μm to 12 μm , 1.5% beyond
In normalization relative to Sirius: 1.0%
In absolute flux of Sirius: 1.2%

Adjustments:

SWS:	1A	0.95×
	1B	0.95×
	1D	0.945×
	1E	1.03×
	2A	1.117×
	2B	$0.90 \times (\lambda/7.5)^{0.107}$
	2C	1.0×

$$\begin{aligned}
 3A & 1.09 \times (\lambda/13.0)^{0.05} \\
 3C & 1.015 \times (\lambda/18.0)^{0.20} \\
 3D & 1.03 \times (\lambda/24.0)^{0.20}
 \end{aligned}$$

SEW: 0.97x



Star: α Cet
HD 18884, HR911, IRAS02596+0353
M2 III
CWW composite star

Fit Parameters: $T_{\text{eff}} = 3750 \text{ K}$, $\theta = 12.94 \text{ mas}$

Spectral Data: SWS TDT: 79702803 (2.36 μm to 27 μm)
SEW (1.22 μm to 2.36 μm)

Photometry (with Sirius defined as -1.36):

DIRBE1: -0.672 (0.020)	lightcurve ampl: 0.03 (0.03)
DIRBE2: -1.667 (0.009)	lightcurve ampl: 0.01 (0.01)
DIRBE3: -1.812 (0.023)	lightcurve ampl: 0.03 (0.03)
DIRBE4: -1.568 (0.020)	lightcurve ampl: 0.03 (0.02)

Selby et al. (1988) J: -0.667 (0.02)
Selby et al. (1988) K: -1.692 (0.02)
Selby et al. (1988) L: -1.845 (0.02)

IRAS 12: -1.93 (0.04)
IRAS 25: -1.99 (0.05)

Uncertainty: In shape: 5% near 1 μm , 3% near 2 μm ,
1% from 2.5 μm to 12 μm , 1.5% beyond
In normalization relative to Sirius: 1.0%
In absolute flux of Sirius: 1.2%

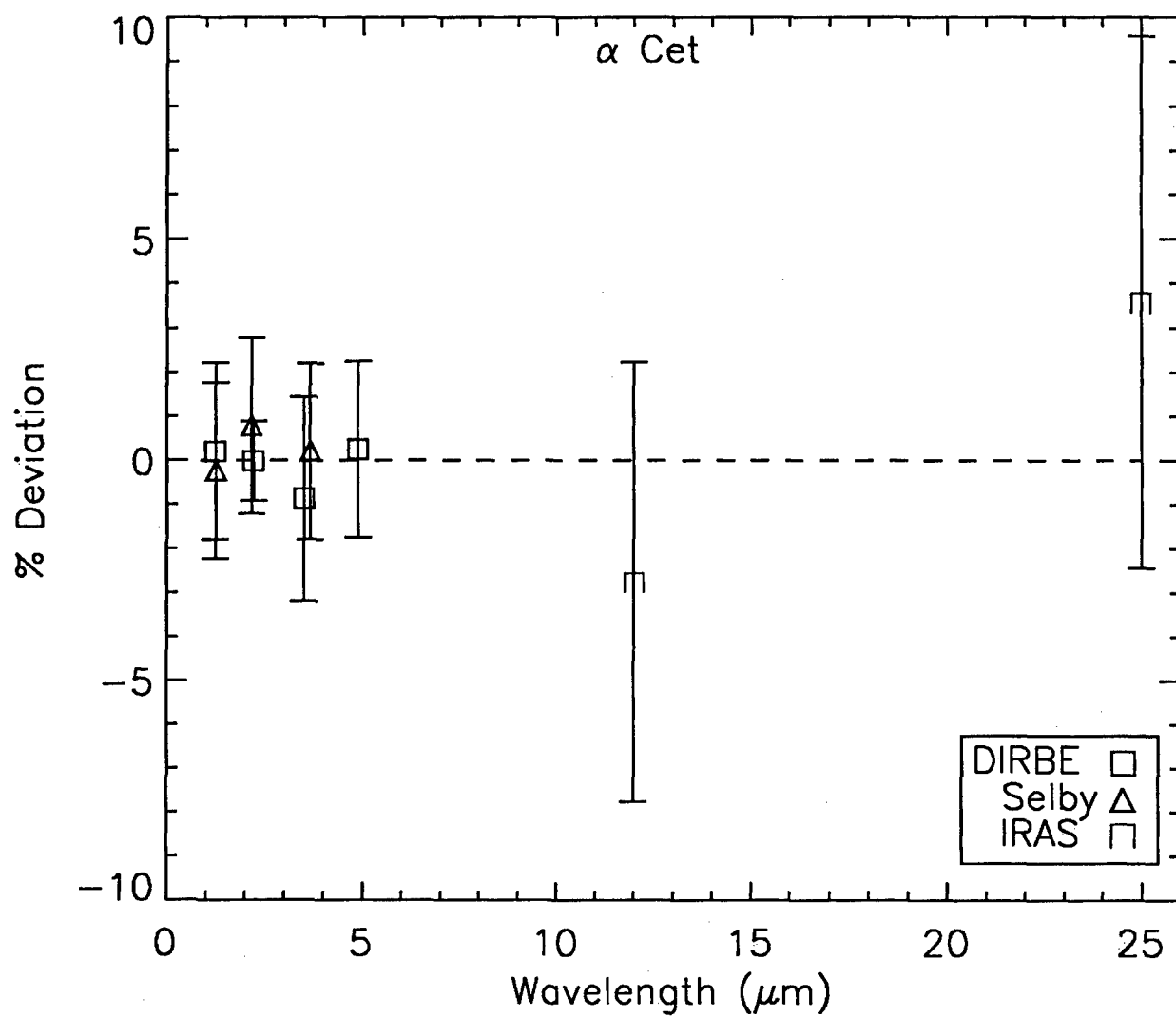
Adjustments:

SWS:

1A	$0.91\times$
1B	$0.91\times(\lambda/2.56)^{0.15}$
1D	$0.96\times(\lambda/3.1)^{0.11}$
1E	$0.97\times(\lambda/3.6)^{0.10}$
2A	$0.97\times$
2B	$1.013\times(\lambda/5.9)^{0.15}$
2C	$0.85\times(\lambda/7.0)^{0.14}$
3A	$0.99\times(\lambda/12.7)^{-0.16}$
3C	$0.97\times$

3D 0.95x

SEW: $0.99 \times (\lambda/2.2)^{0.045}$



Star: γ Cru
 HD108903, HR4763, IRAS12283-5650
 M4 III
 CWW composite star

Fit Parameters: $T_{\text{eff}} = 3626 \text{ K}$, $\theta = 26.37 \text{ mas}$

Spectral Data: SWS TDT: 60900804 (2.36 μm to 12 μm ;
 averaged with TDT 25806177 for $\lambda > 8 \mu\text{m}$)

Photometry (with Sirius defined as -1.36):

DIRBE1: -2.112 (0.026)	lightcurve ampl: 0.04 (0.03)
DIRBE2: -3.151 (0.009)	lightcurve ampl: 0.00 (0.01)
DIRBE3: -3.295 (0.022)	lightcurve ampl: 0.03 (0.02)
DIRBE4: -3.072 (0.016)	lightcurve ampl: 0.02 (0.01)

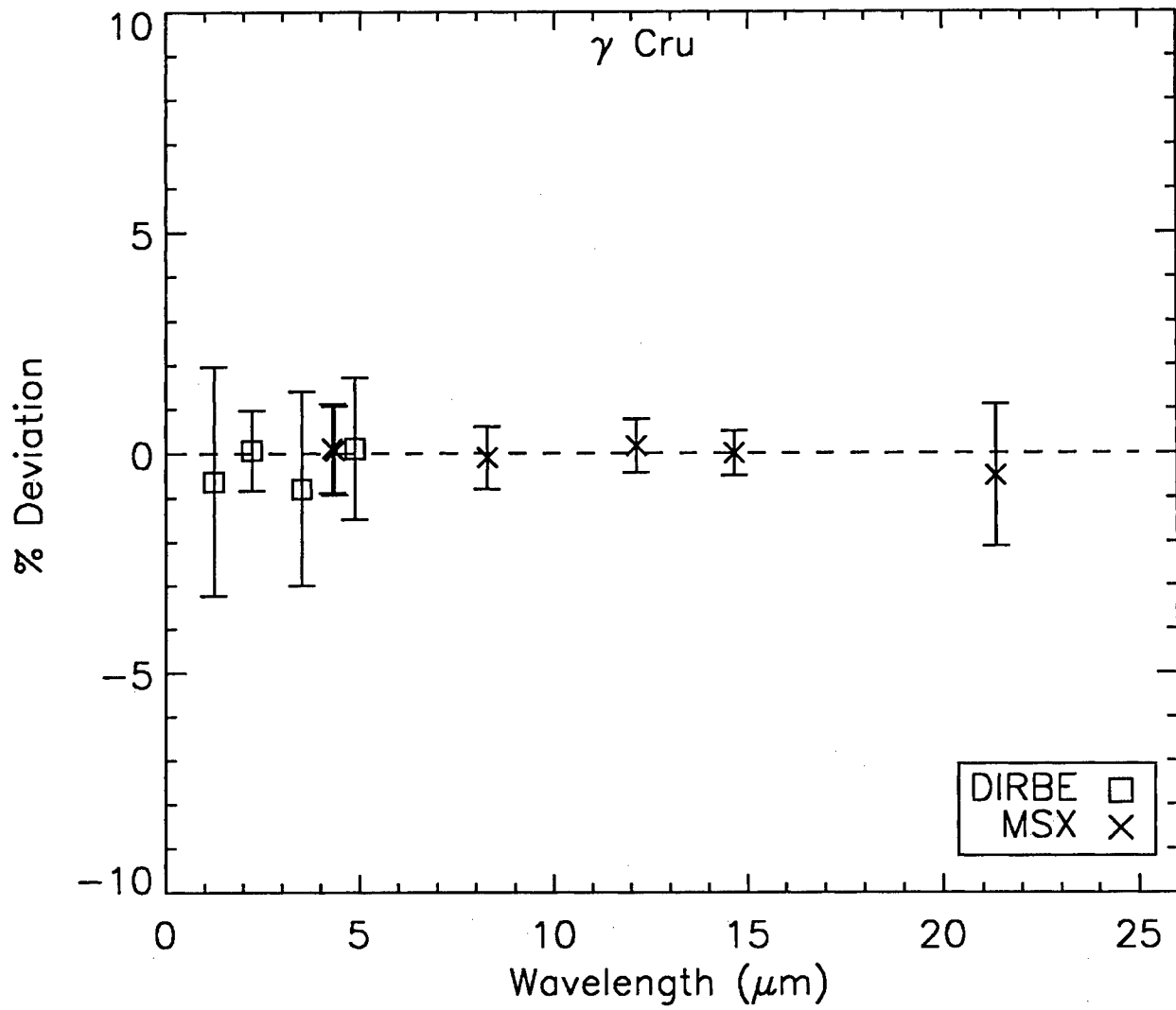
MSX A: -3.351 (0.007)	MSX C: -3.465 (0.006)
MSX B ₁ : -3.212 (0.010)	MSX D: -3.460 (0.005)
MSX B ₂ : -3.159 (0.010)	MSX E: -3.482 (0.016)

Uncertainty: In shape: 5% near 1 μm , 3% near 2 μm ,
 1% from 2.5 μm to 12 μm , 1.5% beyond
 In normalization relative to Sirius: 0.2%
 In absolute flux of Sirius: 1.2%

Adjustments:

SWS:

1A	$1.29\times$
1B	$1.33\times$
1D	$1.07\times(\lambda/3.0)^{-0.17}$
1E	$1.04\times$
2A	$0.80\times(\lambda/4.0)^{0.22}$
2B	$0.82\times(\lambda/5.5)^{0.30}$
2C	$0.739\times(\lambda/7.0)^{0.25}$
3A	$2.2\times(\lambda/14.0)^{-0.25}$ plus TDT 25806177
3C	$1.13\times$



Star: α Cen A
 HD128620 J, HR5563, IRAS14359-6037
 G2 V
 CWW model star

Fit Parameters: $T_{\text{eff}} = 5870 \text{ K}$, $\theta = 8.51 \text{ mas}$

Spectral Data: SWS TDT: 60702006 (2.36 μm to 9 μm)
 Pickles (1.0 μm to 2.36 μm)

Photometry (with Sirius defined as -1.36):

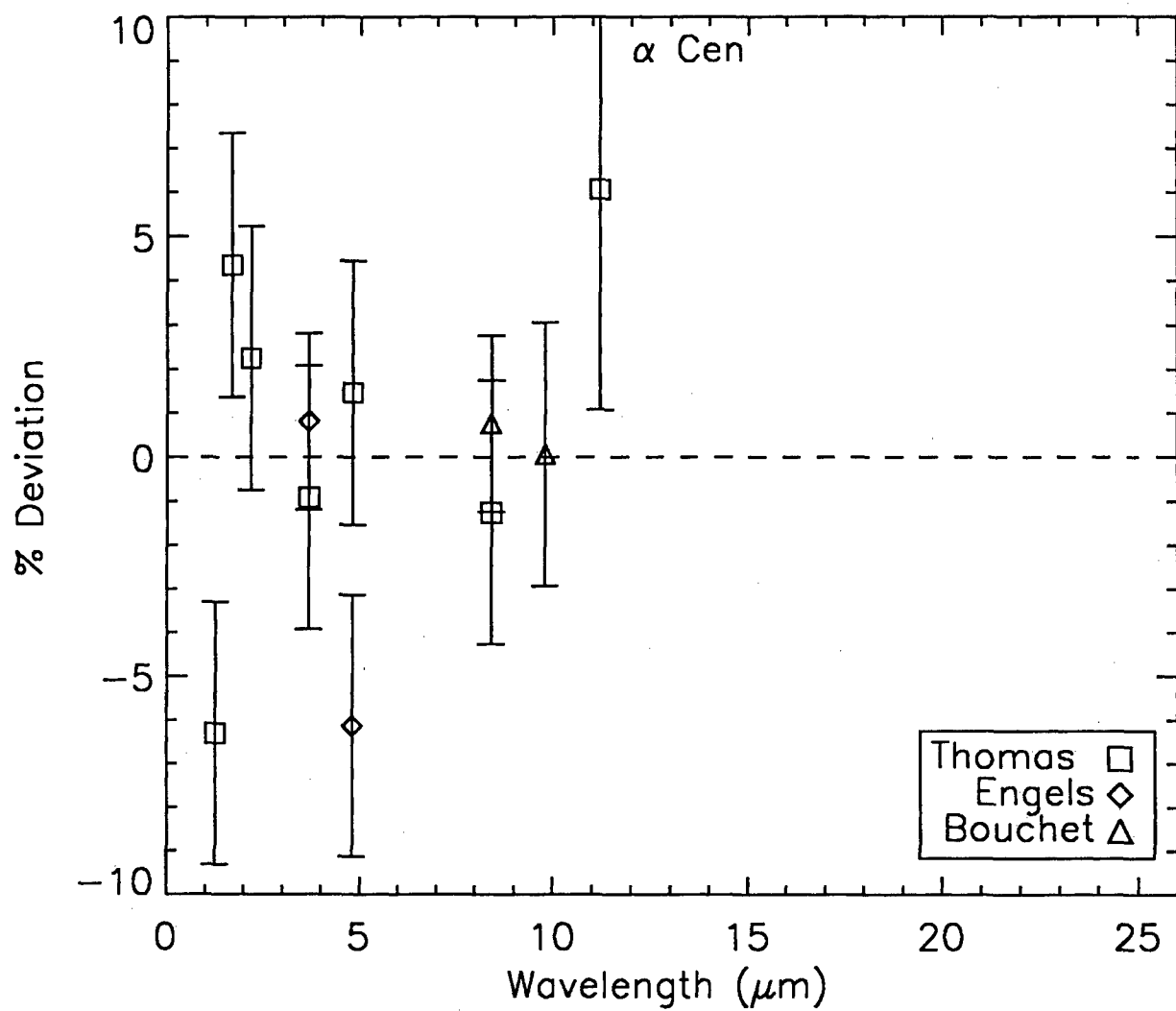
Engels et al. (1981)	L:	-1.550 (0.02)
Engels et al. (1981)	M:	-1.440 (0.03)
Bouchet et al. (1989) N1 (8.4 μm):		-1.557 (0.02)
Bouchet et al. (1989) N2 (9.8 μm):		-1.553 (0.03)
Thomas et al. (1973) J:		-1.062 (0.03)
	H:	-1.488 (0.03)
	K:	-1.523 (0.03)
	L:	-1.531 (0.03)
	M:	-1.524 (0.03)
	8.4:	-1.535 (0.03)
	N:	-1.62 (0.05)
	11.2:	-1.62 (0.05)

Uncertainty: In shape: 5% near 1 μm , 3% near 2 μm ,
 1% from 2.5 μm to 12 μm , 1.5% beyond
 In normalization relative to Sirius: 0.75% for average
 In absolute flux of Sirius: 1.2%
 DIRBE contaminated with alpha Cen B (~50% too bright)

Adjustments:

SWS:	1A	0.961 \times
	1B	0.961 \times
	1D	0.964 \times
	1E	0.960 \times

2A 1.048×
 2B 1.096×
 2C $0.89 \times (\lambda/7.3)^{-0.09}$



Star: β Dra
HD159181, HR6536, IRAS17292+5220
G2 II
NO CWW template or composite

Fit Parameters: $T_{\text{eff}} = 5100 \text{ K}$, $\theta = 3.345 \text{ mas}$

Spectral Data: SWS TDT: 0800163 (2.36 μm to 9.1 μm)
SEW (1.24 μm to 2.36 μm)

Photometry (with Sirius defined as -1.36):

DIRBE1: 1.212 (0.030)	lightcurve ampl: 0.05 (0.04)
DIRBE2: 0.743 (0.010)	lightcurve ampl: 0.04 (0.03)
DIRBE3: 0.667 (0.030)	lightcurve ampl: 0.09 (0.07)
DIRBE4: 0.716 (0.030)	lightcurve ampl: 0.10 (0.10)

2MASS J:	1.383 (0.05)
2MASS H:	0.827 (0.05)
2MASS K:	0.786 (0.05)

IRAS 12:	0.58 (0.05)
IRAS 25:	0.61 (0.06)

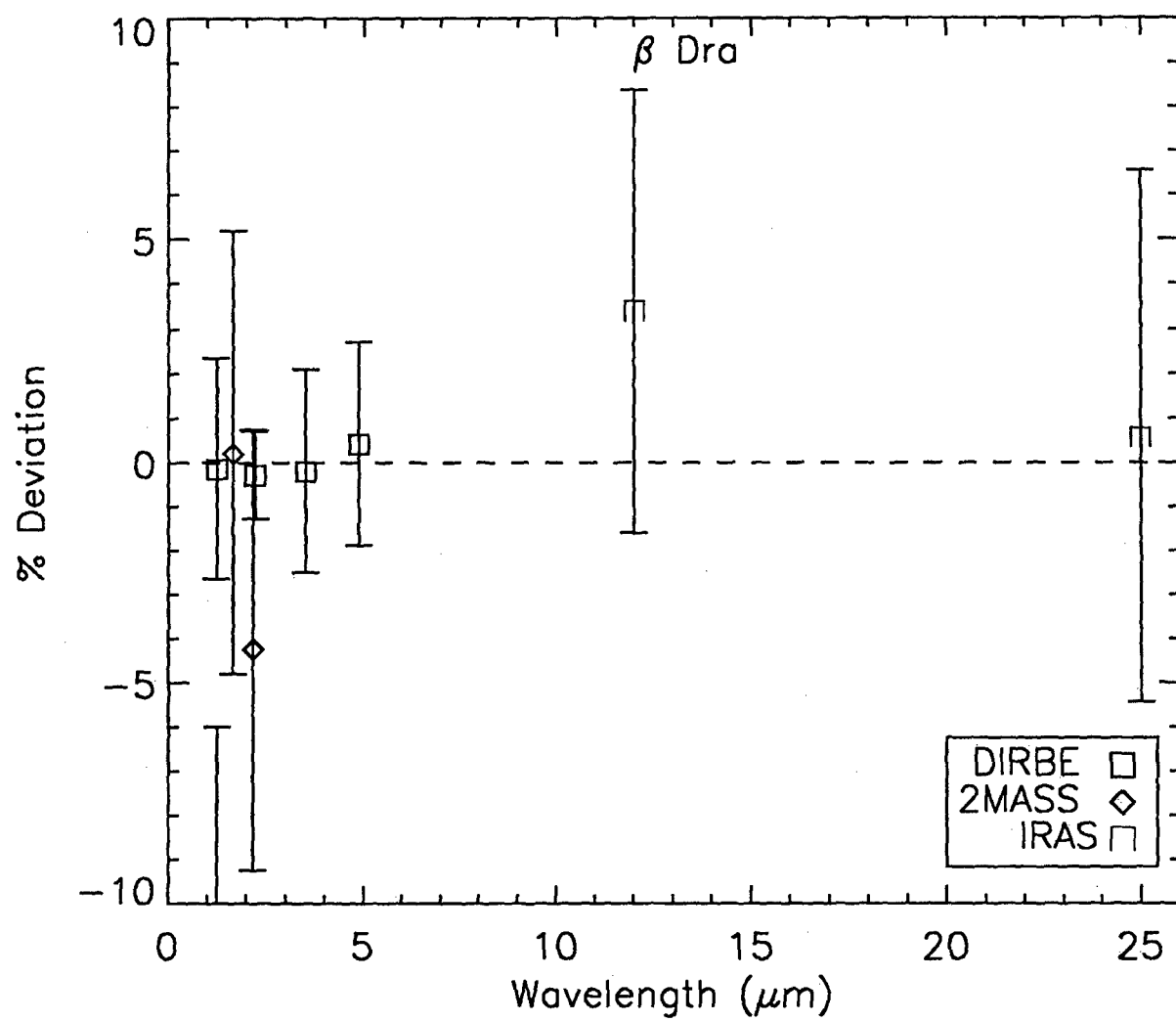
Uncertainty: In shape: 5% near 1 μm , 3% near 2 μm ,
1% from 2.5 μm to 12 μm , 1.5% beyond
In normalization relative to Sirius: 2.0%
In absolute flux of Sirius: 1.2%

Adjustments:

SWS:	1A	0.91 \times
	1B	0.91 \times
	1D	$0.942 \times (\lambda/3.05)^{0.05}$
	1E	0.934 \times

	2A	0.953 \times
	2B	0.953 \times
	2C	$1.049 \times (\lambda/7.0)^{-0.1}$

SEW:	1.01 \times
------	---------------



Star: δ Dra
 HD180711, HR7310, IRAS19125+6734
 G9 III
 Cohen template for ISO

Fit Parameters: $T_{\text{eff}} = 4950 \text{ K}$, $\theta = 3.349 \text{ mas}$

Spectral Data: SWS TDT: 20601232 (2.36 μm to 10 μm)
 ISOCAMCVF TDT 49600802 & 49600803 (10 μm to 15.5 μm)

Photometry (with Sirius defined as -1.36):

 Hammersley et al. (1998) K: 0.768 (0.01)
 Hammersley et al. (1998) L': 0.71 (0.06)

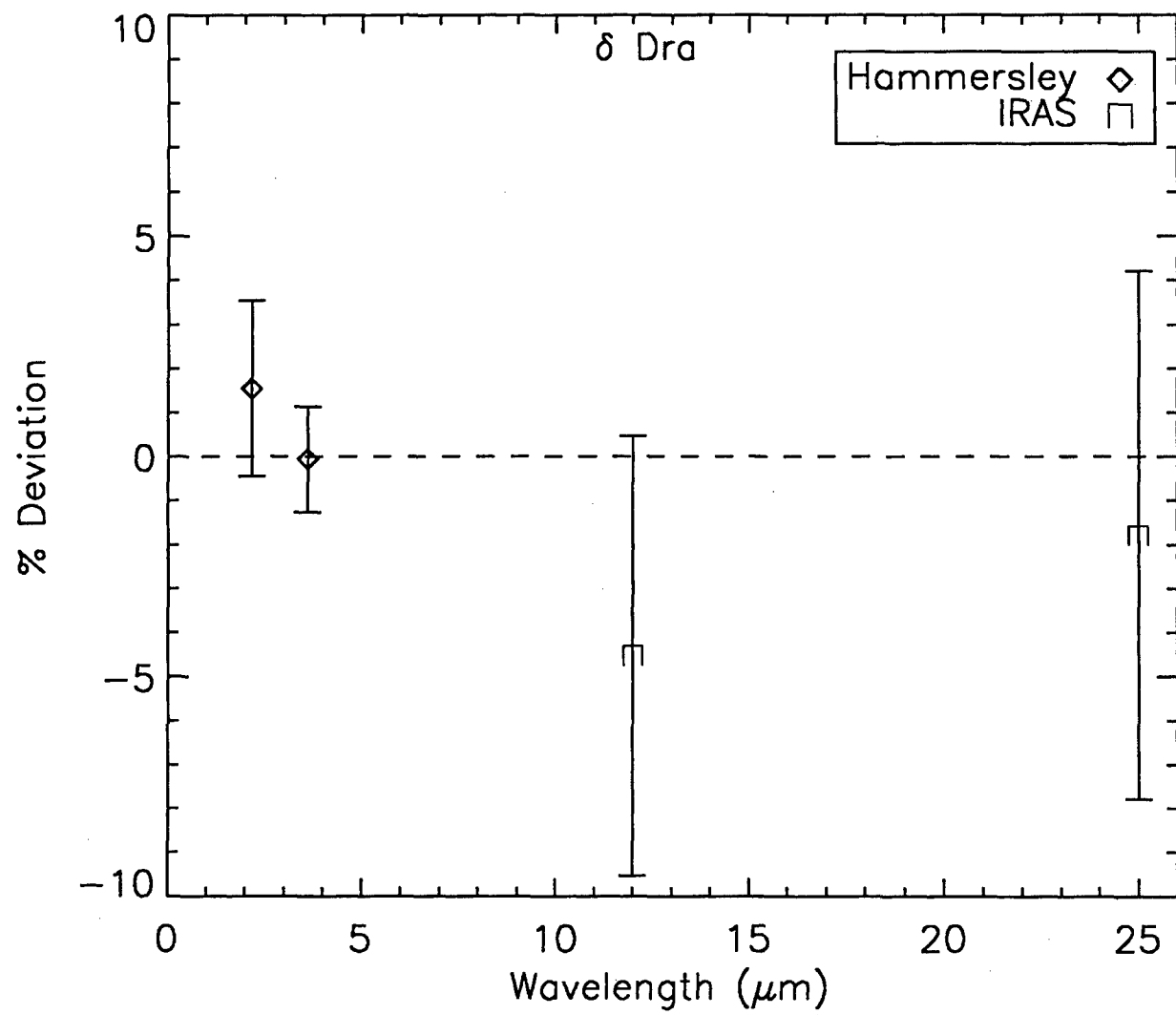
 IRAS 12: 0.71 PSC or 0.70 FSC
 IRAS 25: 0.68 PSC or 0.70 FSC

Uncertainty: In shape: 5% near 1 μm , 3% near 2 μm ,
 1% from 2.5 μm to 12 μm , 1.5% beyond
 In normalization relative to Sirius: 5%
 In absolute flux of Sirius: 1.2%
 Variable?

Adjustments:

SWS: 1A $0.99\times$
 1B $1.008\times(\lambda/3.0)^{0.05}$
 1D $1.05\times(\lambda/3.5)^{0.11}$
 1E $1.05\times$

 2A $1.025\times(\lambda/4.2)^{0.22}$
 2B $1.027\times(\lambda/7.0)^{-0.02}$
 2C $1.12\times(\lambda/7.0)^{-0.08}$



Star: δ Eri
 HD23249, HR1136, IRAS03408-0955
 K0 IV
 CWW template

Fit Parameters: $T_{\text{eff}} = 4900 \text{ K}$, $\theta = 2.476 \text{ mas}$

Spectral Data: SWS TDT: 66301815 (2.36 μm to 8.8 μm)

Photometry (with Sirius defined as -1.36):

Bouchet H (1.65 μm): 1.595 (0.03)
Bouchet K (2.20 μm): 1.478 (0.02)
Bouchet L (3.79 μm): 1.374 (0.02)
Bouchet M (4.73 μm): 1.468 (0.02)

Carter (1993) J: 2.005 (0.03)
Carter (1993) H: 1.512 (0.03)
Carter (1993) K (2.17 μm): 1.427 (0.03)
Carter (1993) L (3.43 μm): 1.412 (0.03)

Narrowband van der Blik et al. (1996) ESO:

H_0 (1.61 μm): 1.550 (0.005)
 K_0 (2.22 μm): 1.434 (0.005)
 L_0 (3.72 μm): 1.365 (0.005)
 N_1 (8.34 μm): 1.30 (0.03)
 N_2 (9.8 μm): 1.30 (0.03)
 N_3 (12.8 μm): 1.32 (0.04)

IRAS 12: 1.35 (0.05)

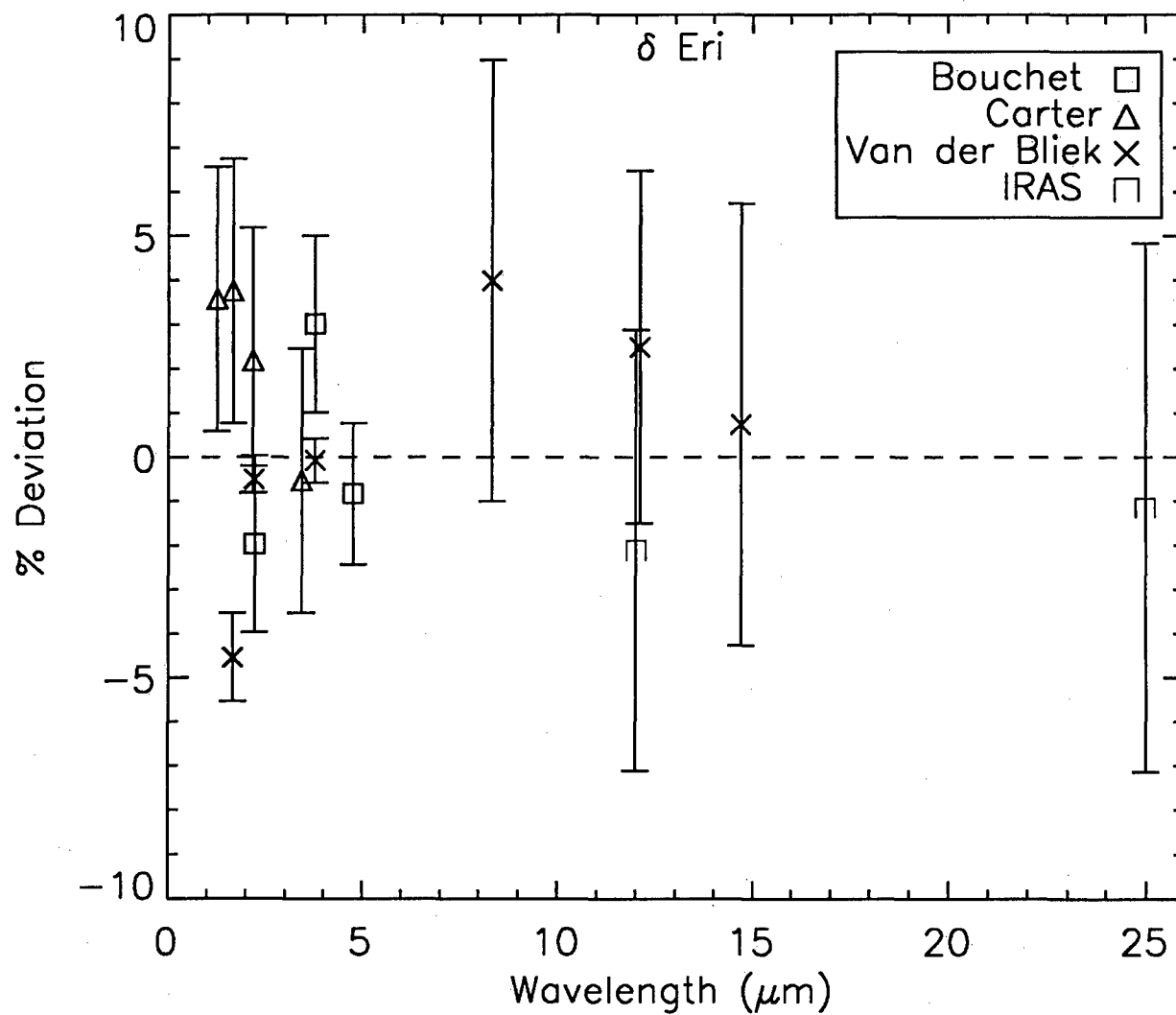
IRAS 25: 1.34 (0.06)

Uncertainty: In shape: 5% near 1 μm , 3% near 2 μm ,
 1% from 2.5 μm to 12 μm , 1.5% beyond
 In normalization relative to Sirius: 2%
 In absolute flux of Sirius: 1.2%

Adjustments:

SWS: 1A $0.895\times$
 1B $0.906\times(\lambda/2.6)^{0.1}$

1C	$0.931 \times (\lambda/3.1)^{0.10}$
1E	$0.931 \times (\lambda/3.05)^{0.07}$
2A	$0.960 \times (\lambda/4.3)^{-0.04}$
2B	$0.931 \times (\lambda/6.1)^{0.20}$
2C	$0.99 \times (\lambda/7.5)^{-0.30}$



Star: θ Cen
 HD 123139, HR 5288, IRAS 14037-3607
 K0 III
 CWW template star

Fit Parameters: $T_{\text{eff}} = 4800 \text{ K}$, $\theta = 5.46 \text{ mas}$

Spectral Data: SWS TDT: 43600940 (2.36 μm to 9.1 μm)

Photometry (with Sirius defined as -1.36):

DIRBE1:	-----	-----
DIRBE2:	-0.231 (0.012)	lightcurve ampl: 0.01 (0.02)
DIRBE3:	-0.307 (0.038)	lightcurve ampl: 0.07 (0.05)
DIRBE4:	-0.201 (0.039)	lightcurve ampl: 0.06 (0.05)

Bouchet et al. (1991)
Bouchet H: -0.180 (0.05)
Bouchet K: -0.299 (0.05)
Bouchet L: -0.363 (0.05)
Bouchet M: -0.195 (0.05)

Carter (1990) J: 0.376 (0.03)
Carter (1990) H: -0.156 (0.03)
Carter (1990) K: -0.253 (0.03)
Carter (1990) L: -0.351 (0.03)

van der Blik et al. (1996):
 K_0 : -0.251 (0.01)
 L_0 : -0.323 (0.001)

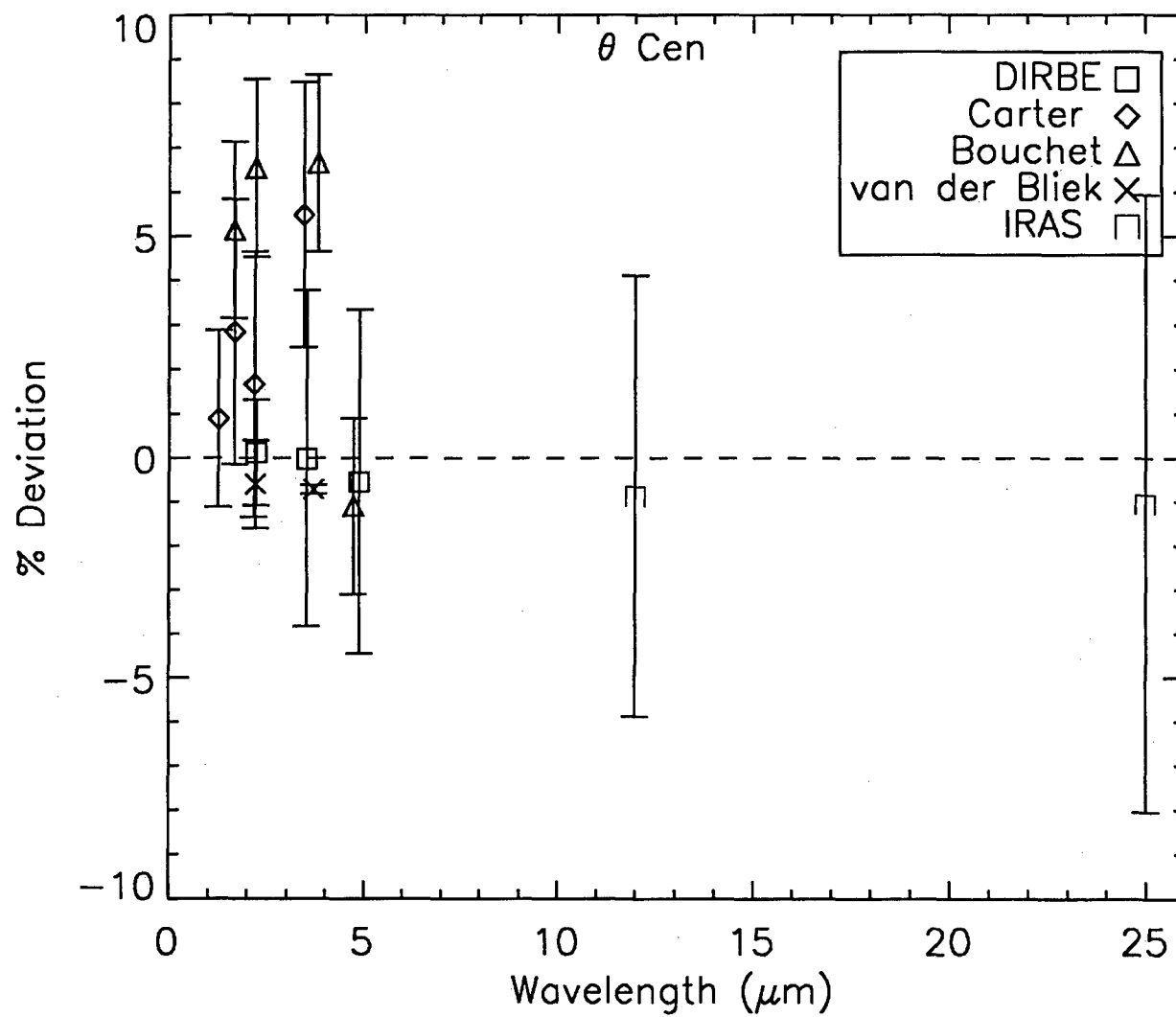
IRAS 12: -0.36 (0.05)
IRAS 25: -0.36 (0.06)

Uncertainty: In shape: 5% near 1 μm , 3% near 2 μm ,
 1% from 2.5 μm to 12 μm , 1.5% beyond
 In normalization relative to Sirius: 2.0%
 In absolute flux of Sirius: 1.2%

Adjustments:

SWS:	1A	0.97×
	1B	0.99×

1C	1.00×
1E	1.00×
2A	$1.04 \times (\lambda/4.2)^{-0.08}$
2B	$0.99 \times (\lambda/5.6)^{0.20}$
2C	$1.14 \times (\lambda/7.0)^{-0.25}$



Star: α UMa
 HD95689, HR4301, IRAS11006+6201
 K0 IIIab
 CWW template star

Fit Parameters: $T_{\text{eff}} = 4790 \text{ K}$, $\theta = 6.684 \text{ mas}$

Spectral Data: SWS TDT: 14300723 (2.36 μm to 8.7 μm)
 SEW: (1.23 μm to 2.36 μm)

Photometry (with Sirius defined as -1.36):

DIRBE1: -0.0089 (0.025)	lightcurve ampl: 0.05 (0.03)
DIRBE2: -0.6600 (0.010)	lightcurve ampl: 0.01 (0.01)
DIRBE3: -0.7497 (0.023)	lightcurve ampl: 0.05 (0.02)
DIRBE4: -0.6301 (0.023)	lightcurve ampl: 0.03 (0.03)

Kenyon (1988) H: -0.581 (0.03)
 Kenyon (1988) K: -0.689 (0.03)

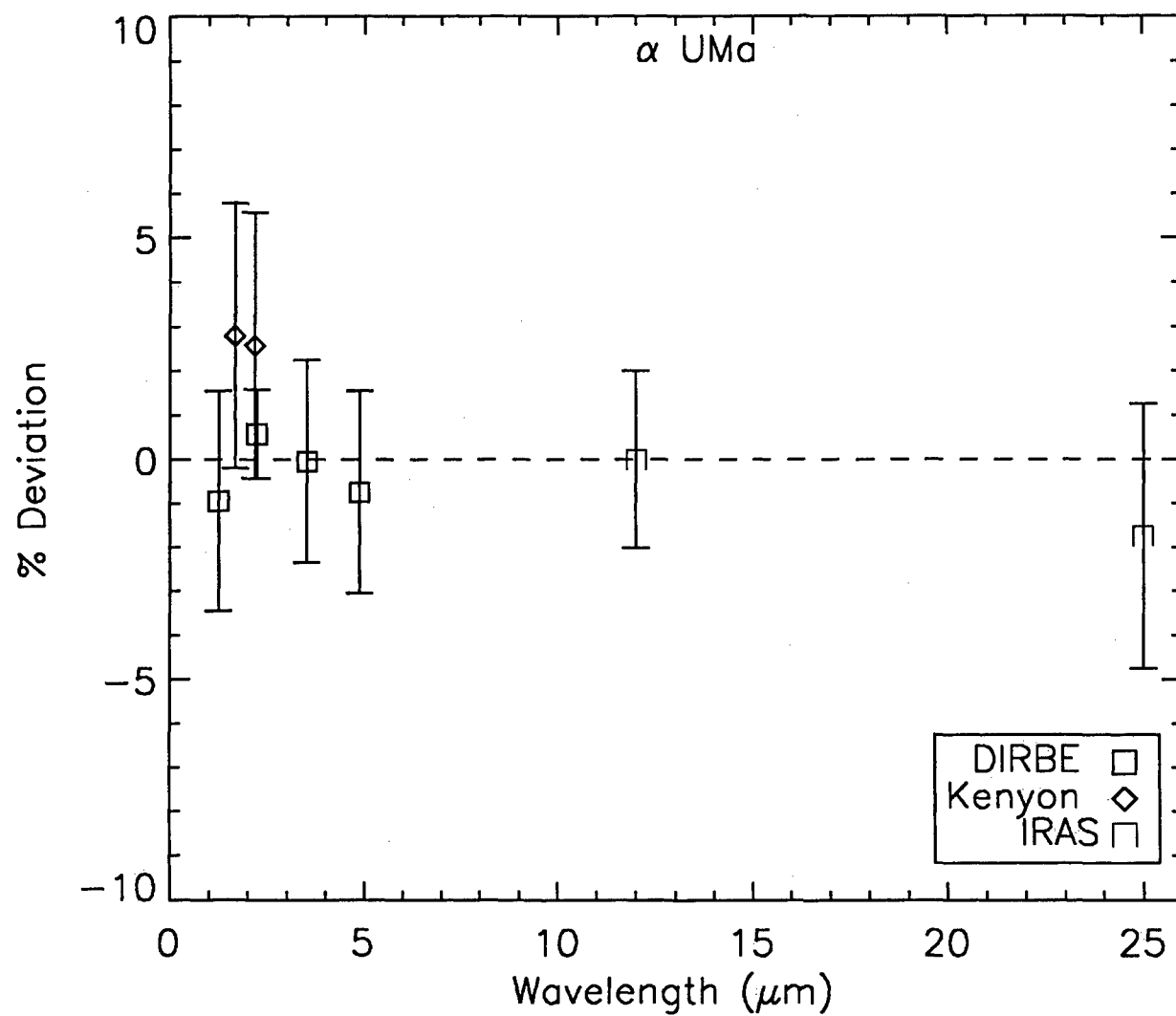
IRAS 12: -0.805 (0.02)
 IRAS 25: -0.784 (0.03)

Uncertainty: In shape: 5% near 1 μm , 3% near 2 μm ,
 1.5% from 2.5 μm to 12 μm , 1.5% beyond
 In normalization relative to Sirius: 0.5%
 In absolute flux of Sirius: 1.2%

Adjustments:

SWS:	1A	$0.978 \times$
	1B	$0.978 \times (\lambda/2.65)^{0.10}$
	1D	$1.035 \times$
	1E	$1.045 \times (\lambda/3.6)^{0.05}$
	2A	$1.00 \times (\lambda/4.1)^{-0.05}$
	2B	$0.93 \times (\lambda/5.4)^{-0.15}$
	2C	$0.978 \times (\lambda/7.0)^{-0.05}$

SEW: $0.99 \times$



Star: ξ Dra
 HD 163588, HR 6688, IRAS 17526+5652
 K2 III
 CWW template

Fit Parameters: $T_{\text{eff}} = 4570 \text{ K}$, $\theta = 3.09 \text{ mas}$

Spectral Data: SWS TDT: 31404910 (2.36 μm to 10. μm)

Photometry (with Sirius defined as -1.36):

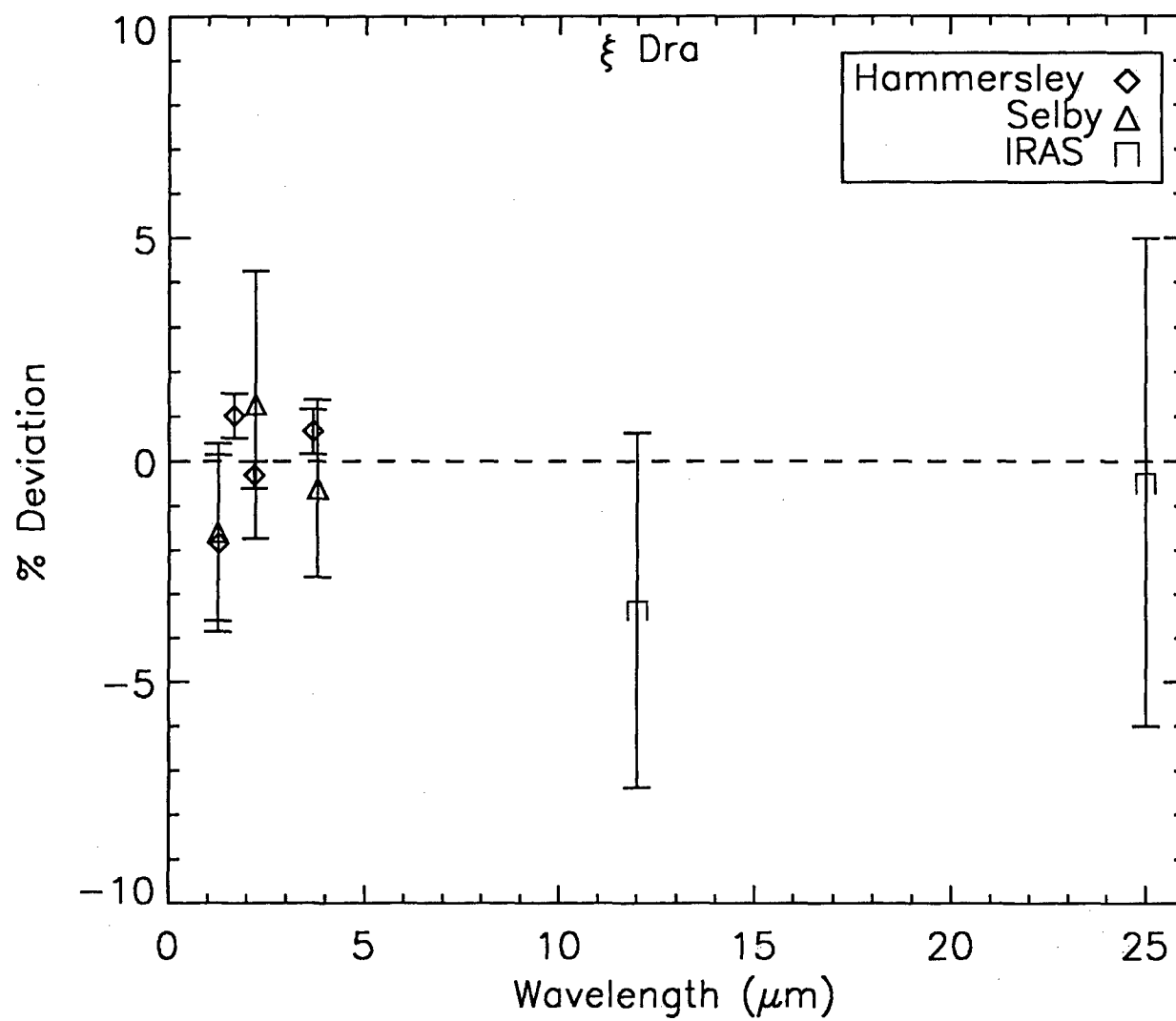
Hammersley et al. (1998) J: 1.789 (0.020)	Selby et al. (1988) J: 1.805 (0.02)
Hammersley et al. (1998) H: 1.197 (0.008)	
Hammersley et al. (1998) K: 1.084 (0.005)	Selby et al. (1988) K: 1.04 (0.03)
Hammersley et al. (1998) L: 0.988 (0.005)	Selby et al. (1988) L: 0.981 (0.02)
IRAS 12: 0.959 (0.05)	
IRAS 25: 0.926 (0.06)	

Uncertainty: In shape: 5% near 1 μm , 3% near 2 μm ,
 1% from 2.5 μm to 12 μm , 1.5% beyond
 In normalization relative to Sirius: 1.5%
 In absolute flux of Sirius: 1.2%

Variability 10-20%
 affected by background in DIRBE aperture, DOUBLE star?
 Hammersley et al. (1998) & Selby et al. (1988) don't show much scatter

Adjustments:

SWS:	1A	$0.940 \times$
	1B	$0.930 \times (\lambda/2.6)^{0.06}$
	1C	$0.97 \times (\lambda/3.3)^{0.28}$
	1E	$0.965 \times (\lambda/3.05)^{0.028}$
	2A	$1.089 \times (\lambda/4.2)^{-0.02}$
	2B	$1.078 \times (\lambda/5.5)^{-0.25}$
	2C	$0.992 \times (\lambda/8.0)^{-0.20}$



Star: α Ari
 HD12929, HR 617, IRAS02043+2313
 K2 III
 CWW template star

Fit Parameters: $T_{\text{eff}} = 4500 \text{ K}$, $\theta = 6.893 \text{ mas}$

Spectral Data: SWS TDT: 45002411 (2.36 μm to 9.2 μm)

Photometry (with Sirius defined as -1.36):

DIRBE1: 0.080 (0.020)	lightcurve ampl: 0.03 (0.03)
DIRBE2: -0.620 (0.009)	lightcurve ampl: 0.01 (0.01)
DIRBE3: -0.705 (0.022)	lightcurve ampl: 0.05 (0.03)
DIRBE4: -0.586 (0.020)	lightcurve ampl: 0.04 (0.03)

Alonso et al. (2000) H: -0.525 (0.03)
Alonso et al. (2000) K: -0.662 (0.03)
Alonso et al. (2000) L: -0.693 (0.03)

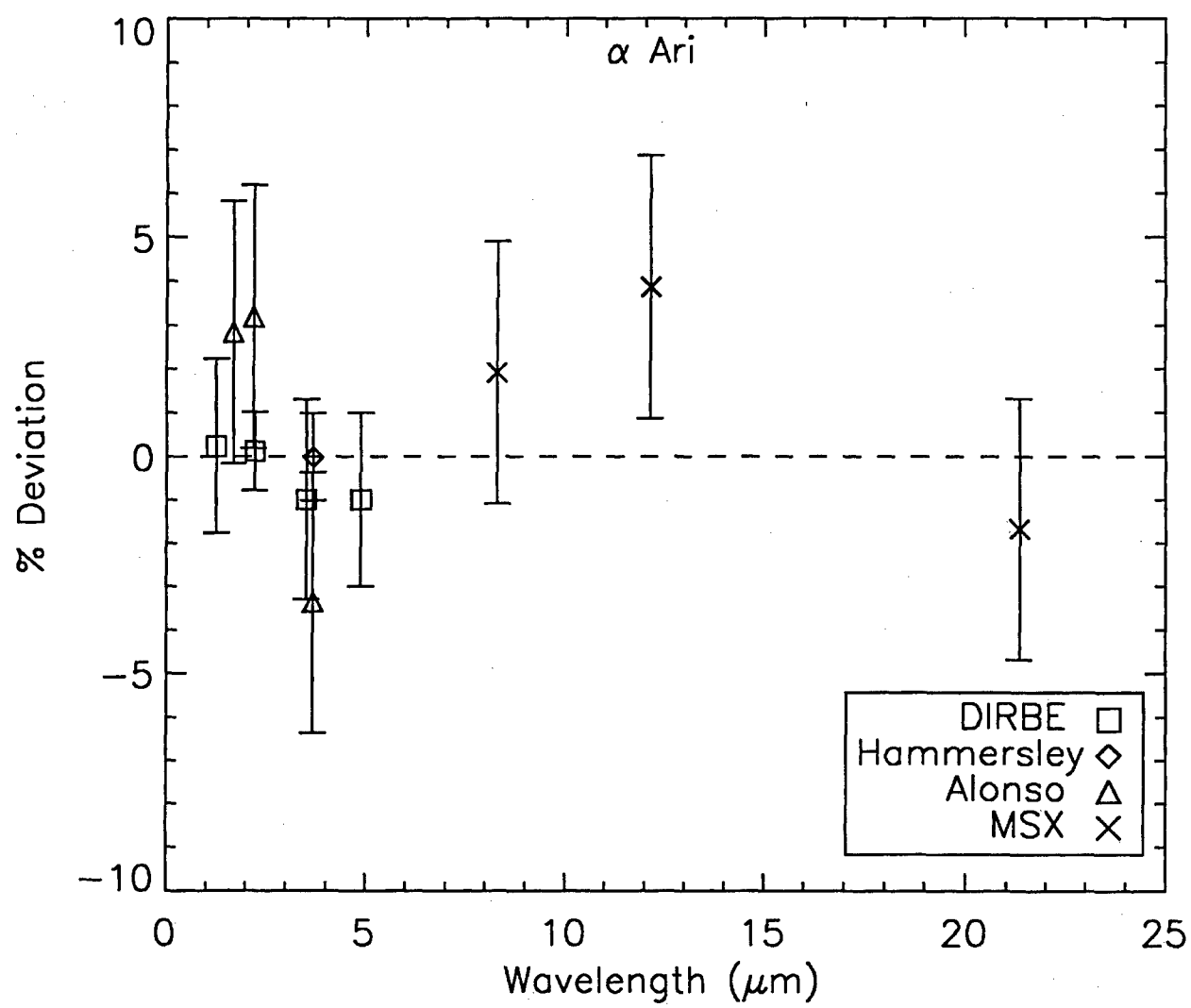
Cohen et al. (Paper X) L: -0.74 (0.01)

MSX A: -0.781 (0.03)
MSX C: -0.836 (0.03)
MSX E: -0.778 (0.03)

Uncertainty: In shape: 5% near 1 μm , 3% near 2 μm ,
 1% from 2.5 μm to 12 μm , 1.5% beyond
 In normalization relative to Sirius: 1.0%
 In absolute flux of Sirius: 1.2%

Adjustments:

SWS:	1A	$0.90\times$
	1B	$0.905\times(\lambda/2.56)^{0.12}$
	1D	$0.943\times(\lambda/3.1)^{0.10}$
	1E	$0.95\times(\lambda/3.6)^{0.10}$
	2A	$1.04\times$
	2B	$1.023\times(\lambda/5.9)^{0.15}$
	2C	$1.11\times(\lambda/7.0)^{-0.045}$



Star: γ And
HD12533, HR603, IRAS 02008+4205
K3 IIb
CWW template

Fit Parameters: $T_{\text{eff}} = 4200 \text{ K}$, $\theta = 7.96 \text{ mas}$

Spectral Data: SWS TDT: 43502924 (2.36 μm to 10 μm)
SEW (1.22 μm to 2.36 μm)

Photometry (with Sirius defined as -1.36):

DIRBE1: -0.031 (0.020)	lightcurve ampl: 0.02 (0.03)
DIRBE2: -0.804 (0.011)	lightcurve ampl: 0.02 (0.01)
DIRBE3: -0.929 (0.022)	lightcurve ampl: 0.03 (0.03)
DIRBE4: -0.722 (0.023)	lightcurve ampl: 0.03 (0.03)

Alonso et al. (2000) H: -0.701 (0.014)

Alonso et al. (2000) K: -0.847 (0.005)

Alonso et al. (2000) L: -0.932 (0.005)

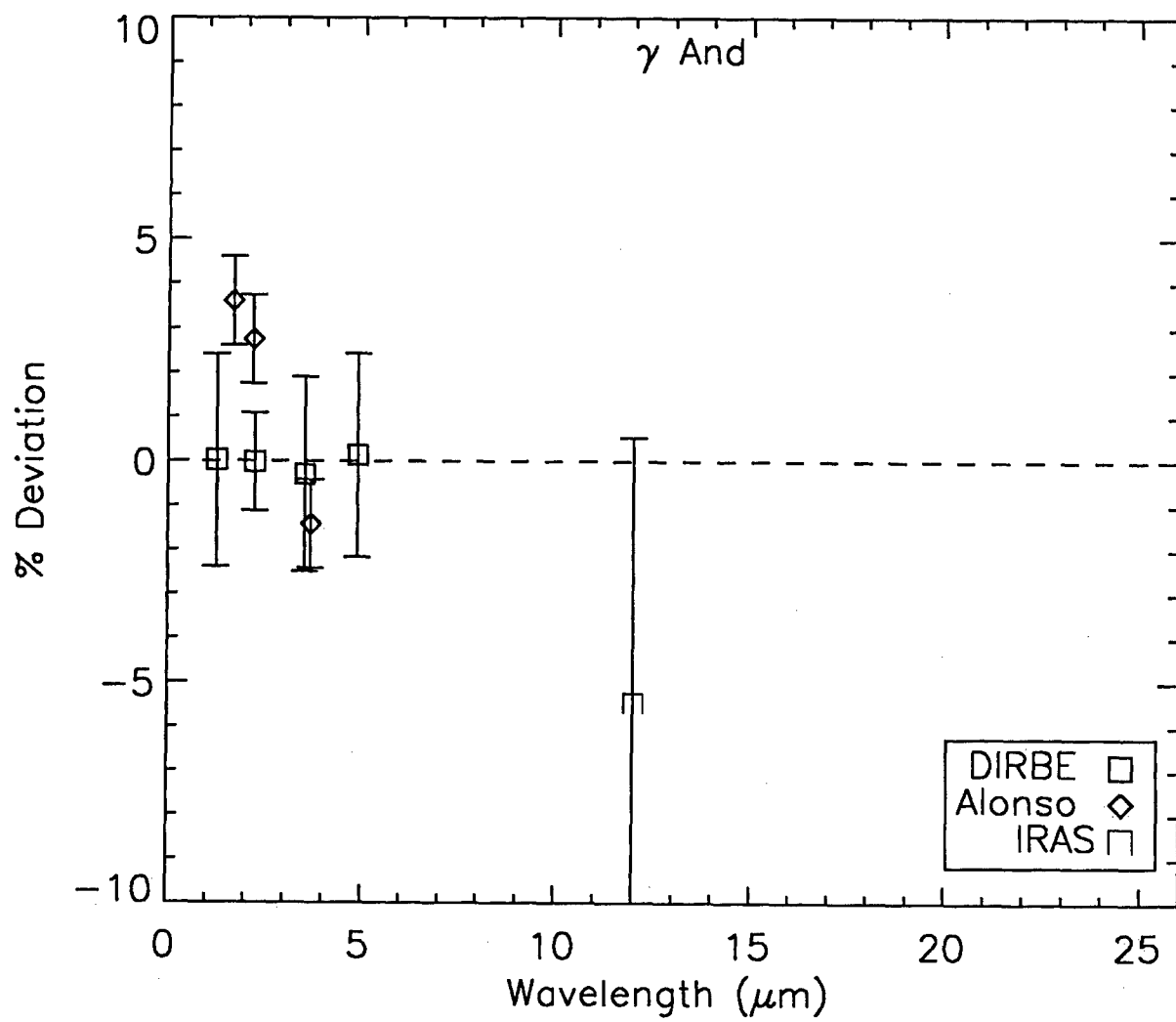
IRAS 12: -0.97 (0.05)

Uncertainty: In shape: 5% near 1 μm , 3% near 2 μm ,
1% from 2.5 μm to 12 μm , 1.5% beyond
In normalization relative to Sirius: 1.0%
In absolute flux of Sirius: 1.2%

Adjustments:

SWS:	1A	$0.957\times$
	1B	$0.96\times(\lambda/2.56)^{0.01}$
	1C	$0.993\times$
	1E	$0.9905\times(\lambda/3.5)^{0.1}$
	2A	$0.9955\times$
	2B	$0.956\times$
	2C	$0.985\times$

SEW: $1.02\times(\lambda/2.2)^{0.09}$



Star: α Tuc
 HD211416, HR8502, IRAS22150-6030
 K3 III
 CWW template star

Fit Parameters: $T_{\text{eff}} = 4200 \text{ K}$, $\theta = 6.19 \text{ mas}$

Spectral Data: SWS TDT: 86602401 (2.36 μm to 15 μm)

Photometry (with Sirius defined as -1.36):

DIRBE1: 0.538 (0.03)	lightcurve ampl: 0.03 (0.03)
DIRBE2: -0.274 (0.014)	lightcurve ampl: 0.02 (0.02)
DIRBE3: -0.389 (0.029)	lightcurve ampl: 0.03 (0.04)
DIRBE4: -0.204 (0.033)	lightcurve ampl: 0.04 (0.04)

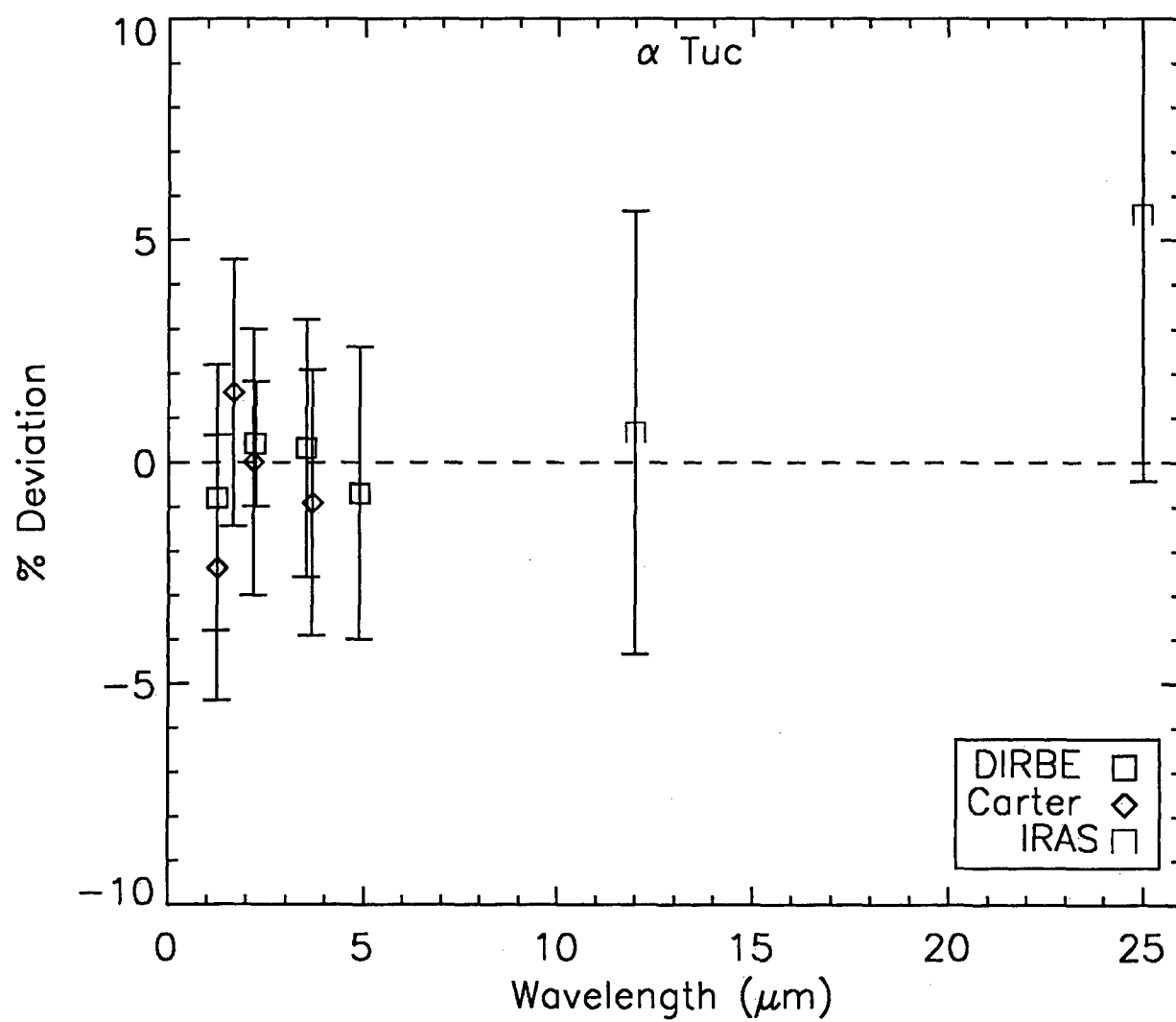
Carter (1993) J: 0.555 (0.03)
 Carter (1993) H: -0.140 (0.03)
 Carter (1993) K: -0.282 (0.03)
 Carter (1993) L: -0.389 (0.03)

IRAS 12: -0.48 (0.04)
 IRAS 25: -0.55 (0.05)

Uncertainty: In shape: 5% near 1 μm , 3% near 2 μm ,
 1% from 2.5 μm to 12 μm , 1.5% beyond
 In normalization relative to Sirius: 1.0%
 In absolute flux of Sirius: 1.2%

Adjustments:

SWS:	1A	$0.946\times$
	1B	$0.947\times$
	1D	$0.955\times(\lambda/3.1)^{0.1}$
	1E	$0.970\times$
	2A	$1.00\times$
	2B	$0.9855\times$
	2C	$1.012\times(\lambda/7.0)^{0.037}$
	3A	$0.95\times(\lambda/15.5)^{-0.35}$



Star: λ Gru
HD 209688, HR 8411, IRAS 022031-3947
K3 III
CWW template star

Fit Parameters: $T_{\text{eff}} = 4200 \text{ K}$, $\theta = 2.82 \text{ mas}$

Spectral Data: SWS TDT: 53904837 (2.36 μm to 11 μm)

Photometry (with Sirius defined as -1.36):

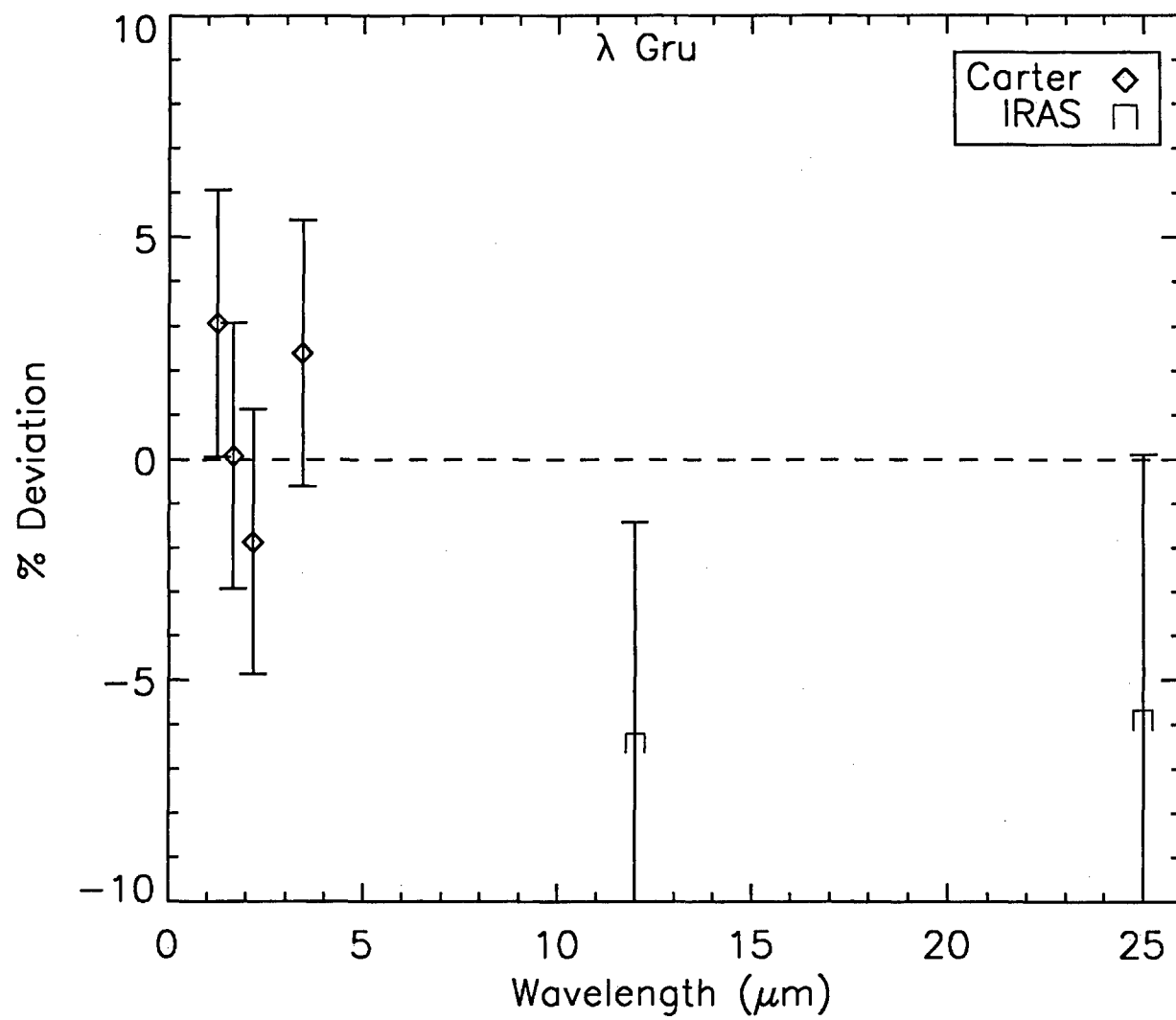
Carter (1990) J: 2.201 (0.03)
Carter (1990) H: 1.581 (0.03)
Carter (1990) K: 1.444 (0.03)
Carter (1990) L: 1.334 (0.03)

IRAS 12: 1.29 (0.05)
IRAS 25: 1.28 (0.06)

Uncertainty: In shape: 5% near 1 μm , 3% near 2 μm ,
1% from 2.5 μm to 12 μm , 1.5% beyond
In normalization relative to Sirius: 2.5%
In absolute flux of Sirius: 1.2%

Adjustments:

SWS: 1A 0.944 \times
1B 0.944 \times
1C $1.01 \times (\lambda/3.6)^{0.24}$
1E 1.005 \times
2A 0.993 \times
2B 0.95 \times
2C $1.02 \times (\lambda/7.5)^{-0.30}$



Star: σ Oph
HD 157999, HR 6498, IRAS 17240+0410
K2 II
CWW template

Fit Parameters: $T_{\text{eff}} = 4100 \text{ K}$, $\theta = 3.518 \text{ mas}$

Spectral Data: SWS TDT: 10200835 (2.36 μm to 9.5 μm)

Photometry (with Sirius defined as -1.36):

DIRBE1: 1.821 (0.024)	lightcurve ampl: 0.04 (0.04)
DIRBE2: 0.978 (0.011)	lightcurve ampl: 0.05 (0.04)
DIRBE3: 0.828 (0.022)	lightcurve ampl: 0.10 (0.07)
DIRBE4: 1.036 (0.023)	lightcurve ampl: 0.10 (0.12)

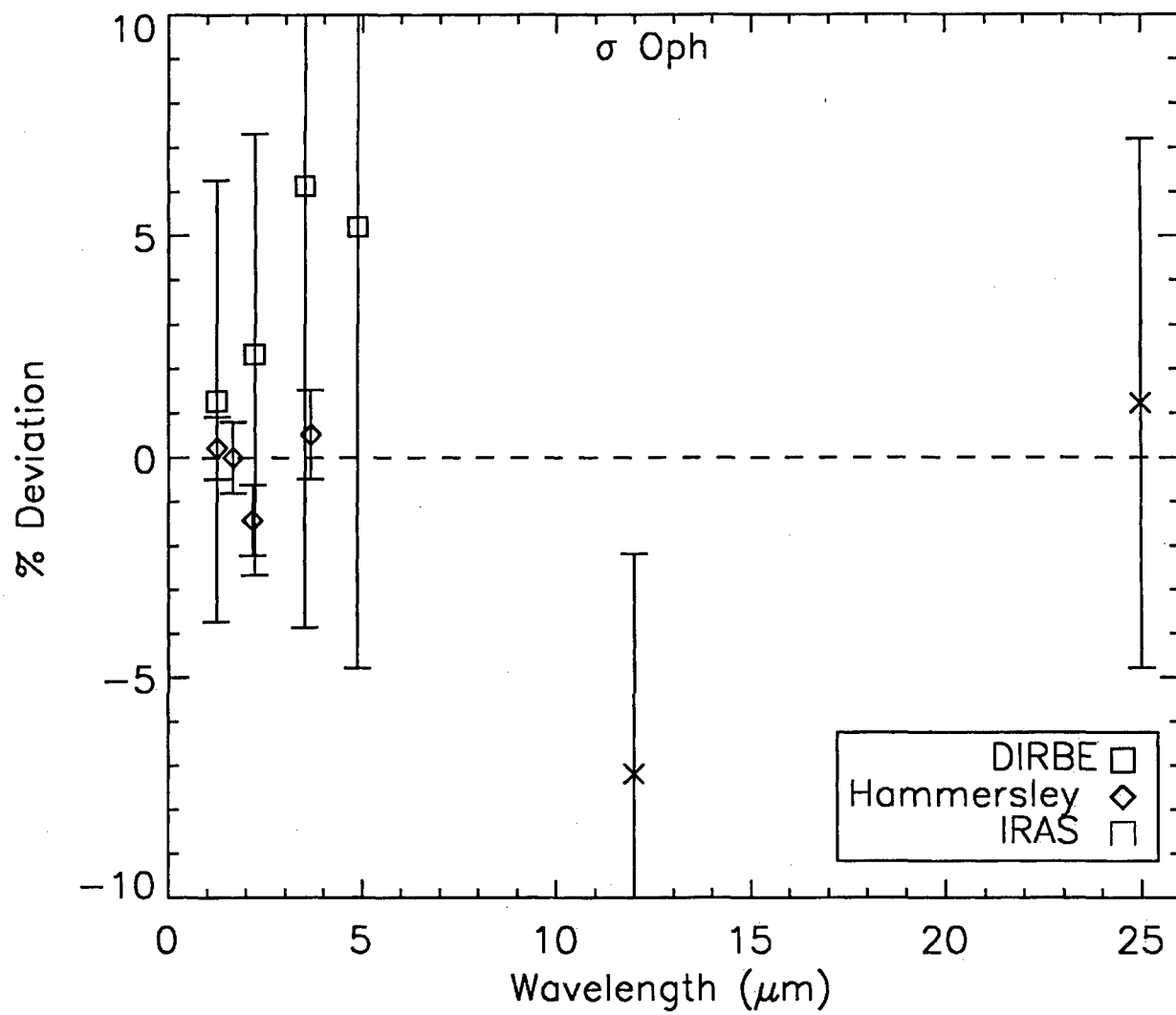
Hammersley et al. (1998) J:	1.832 (0.03)
Hammersley et al. (1998) H:	1.155 (0.03)
Hammersley et al. (1998) K:	1.003 (0.03)
Hammersley et al. (1998) L:	0.867 (0.03)

IRAS 12: 0.85 (0.05)
IRAS 25: 0.75 (0.06)

Uncertainty: In shape: 5% near 1 μm , 3% near 2 μm ,
1% from 2.5 μm to 12 μm , 1.5% beyond
In normalization relative to Sirius: 2.0%
In absolute flux of Sirius: 1.2%
Variable?

Adjustments:

SWS:	1A	1.003 \times
	1B	1.019 \times
	1C	1.009 \times
	1E	1.019 \times
	2A	1.00 \times
	2B	$0.99 \times (\lambda/7)^{-0.05}$
	2C	$1.79 \times (\lambda/7)^{-0.25}$



Star: δ Psc
HD 4656, HR 224, IRAS 00460+0718
K5 III
CWW template star

Fit Parameters: $T_{\text{eff}} = 4050 \text{ K}$, $\theta = 3.746 \text{ mas}$

Spectral Data: SWS TDT: 39502401 (2.36 μm to 12 μm)

Photometry (with Sirius defined as -1.36):

DIRBE1: 1.696 (0.06)	lightcurve ampl: 0.08 (0.04)
DIRBE2: 0.816 (0.05)	lightcurve ampl: 0.06 (0.03)
DIRBE3: 0.697 (0.05)	lightcurve ampl: 0.07 (0.05)
DIRBE4: 0.899 (0.10)	1 lightcurve ampl: 0.14 (0.10)

Selby et al. (1988) J: 1.775 (0.02)
Selby et al. (1988) K: 0.832 (0.02)
Selby et al. (1988) L: 0.692 (0.03)

van der Blik et al. (1996):

H_0 : 1.152 (0.005)
 K_0 : 0.865 (0.005)
 L_0 : 0.736 (0.005)

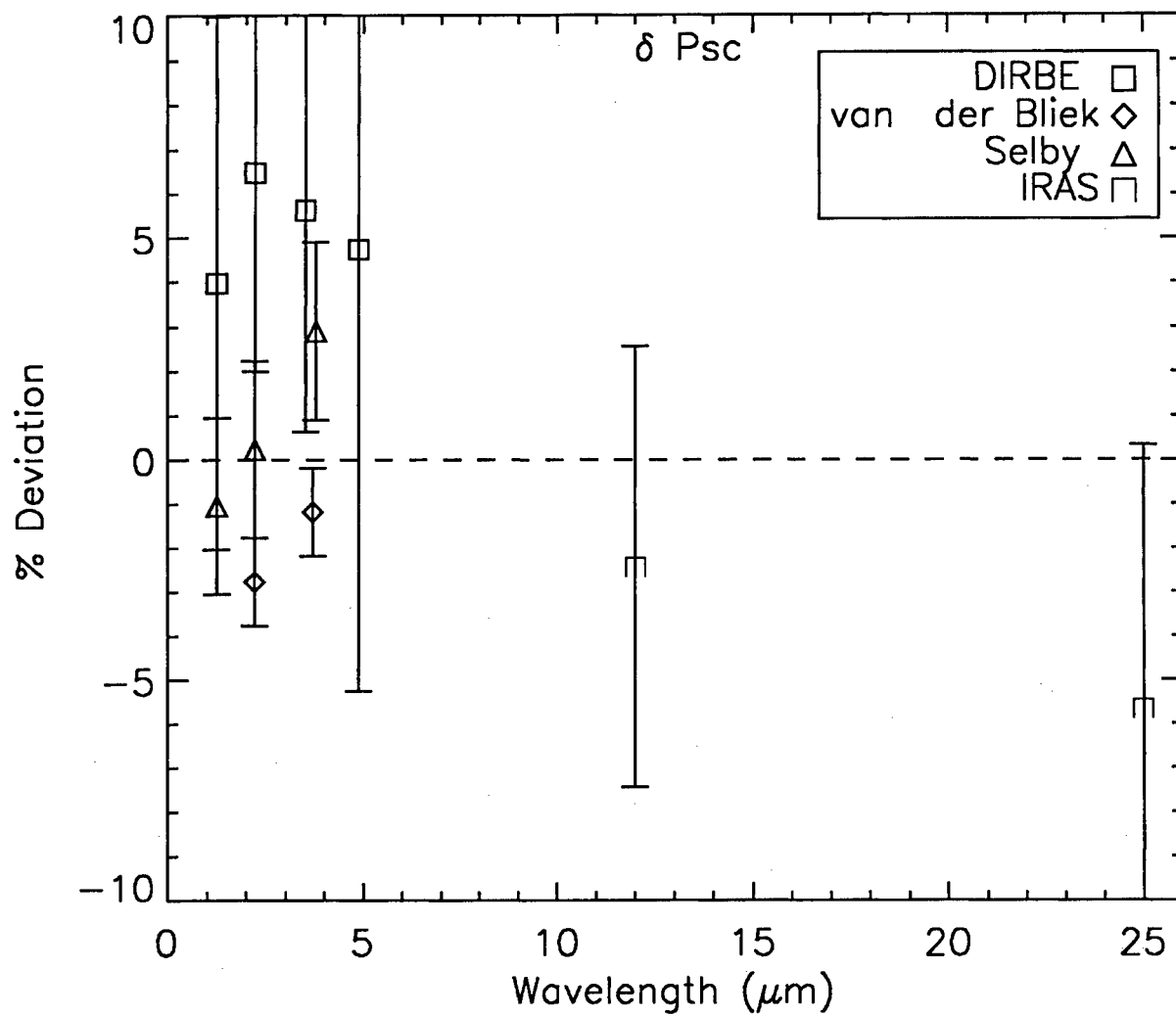
IRAS 12: 0.68 (0.05)
IRAS 25: 0.70 (0.06)

Uncertainty: In shape: 5% near 1 μm , 3% near 2 μm ,
1% from 2.5 μm to 12 μm , 1.5% beyond
In normalization relative to Sirius: 2%
In absolute flux of Sirius: 1.2%
5-10% variability?

Adjustments:

SWS: 1A 1.01 \times
1B 1.02 \times
1D $1.06 \times (\lambda/3.4)^{0.05}$
1E 1.06 \times

2A 0.985×
 2B 1.008×
 2C $1.06 \times (\lambda/7.0)^{0.01}$



Star: γ Phe
HD9053, HR429, IRAS 01261-4334
K4/5III
CWW template star

Fit Parameters: $T_{\text{eff}} = 3950 \text{ K}$, $\theta = 6.76 \text{ mas}$

Spectral Data: SWS TDT: 54901434 (2.36 μm to 9.5 μm)

Photometry (with Sirius defined as -1.36):

DIRBE1: 0.597 (0.027)	lightcurve ampl: 0.04 (0.03)
DIRBE2: -0.356 (0.014)	lightcurve ampl: 0.04 (0.02)
DIRBE3: -0.489 (0.025)	lightcurve ampl: 0.04 (0.03)
DIRBE4: -0.272 (0.031)	lightcurve ampl: 0.06 (0.04)

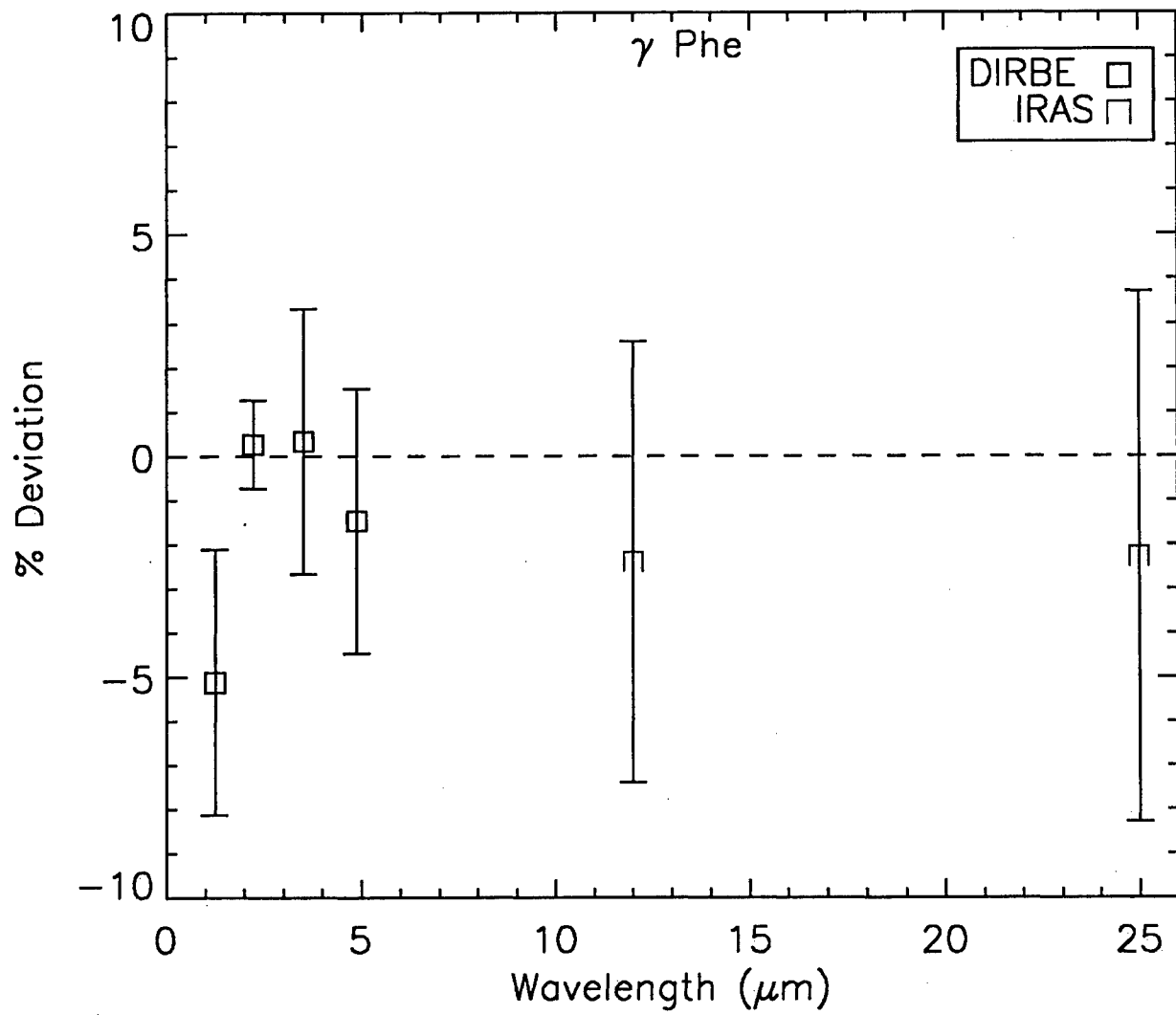
IRAS 12: -0.581 (0.05)

IRAS 25: -0.588 (0.06)

Uncertainty: In shape: 5% near 1 μm , 3% near 2 μm ,
1% from 2.5 μm to 12 μm , 1.5% beyond
In normalization relative to Sirius: 1.0%
In absolute flux of Sirius: 1.2%

Adjustments:

SWS:	1A	0.93 \times
	1B	0.93 \times
	1D	0.93 \times
	1E	0.93 \times
	2A	0.972 \times
	2B	$0.949 \times (\lambda/5.5)^{-0.05}$
	2C	$0.958 \times (\lambda/7.5)^{0.05}$



Star: H Sco
HD149447, HR6166, IRAS 16330-3509
K5 III
CWW template star

Fit Parameters: $T_{\text{eff}} = 3850 \text{ K}$, $\theta = 4.90 \text{ mas}$

Spectral Data: SWS TDT: 84700107 (2.36 μm to 11 μm)

Photometry (with Sirius defined as -1.36):

DIRBE1: 1.360 (0.03)	lightcurve ampl: ---
DIRBE2: 0.409 (0.08)	lightcurve ampl: ---
DIRBE3: 0.223 (0.10)	lightcurve ampl: 0.19 (0.11)
DIRBE4: 0.449 (0.03)	lightcurve ampl: 0.10 (0.13)

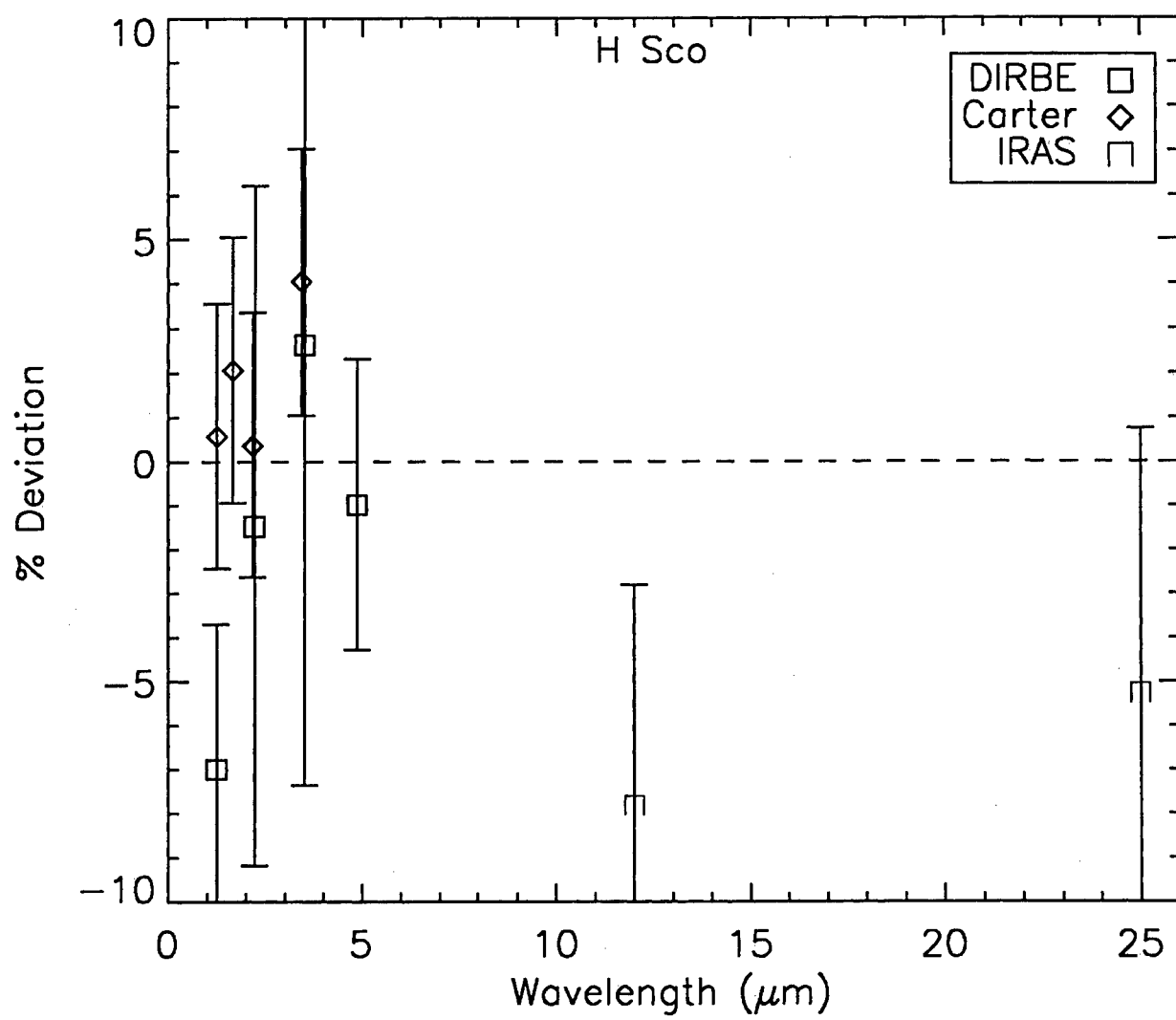
Carter (1990) J: 1.320 (0.03)
Carter (1990) H: 0.550 (0.03)
Carter (1990) K: 0.375 (0.03)
Carter (1990) L: 0.257 (0.03)

IRAS 12: 0.212 (0.05)
IRAS 25: 0.174 (0.07)

Uncertainty: In shape: 5% near 1 μm , 3% near 2 μm ,
1% from 2.5 μm to 12 μm , 1.5% beyond
In normalization relative to Sirius: 5%
In absolute flux of Sirius: 1.2%

Adjustments:

SWS:	1A	$0.95\times$
	1B	$0.957\times$
	1D	$0.965\times(\lambda/3.05)^{0.15}$
	1E	$0.978\times(\lambda/3.6)^{0.08}$
	2A	$1.045\times(\lambda/4.2)^{0.13}$
	2B	$1.043\times(\lambda/5.5)^{0.15}$
	2C	$1.11\times(\lambda/7.5)^{0.16}$



Star: δ Oph
 HD146051, HR6056, IRAS16117-0334
 M1 III
 CWW template star

Fit Parameters: $T_{\text{eff}} = 3850 \text{ K}$, $\theta = 10.23 \text{ mas}$

Spectral Data: SWS TDT: 8201231 (2.36 μm to 12.5 μm)

Photometry (with Sirius defined as -1.36):

DIRBE1: -0.261 (0.03)	lightcurve ampl: ---
DIRBE2: -1.223 (0.01)	lightcurve ampl: 0.01 (0.01)
DIRBE3: -1.353 (0.03)	lightcurve ampl: 0.04 (0.03)
DIRBE4: -1.126 (0.02)	lightcurve ampl: 0.01 (0.02)

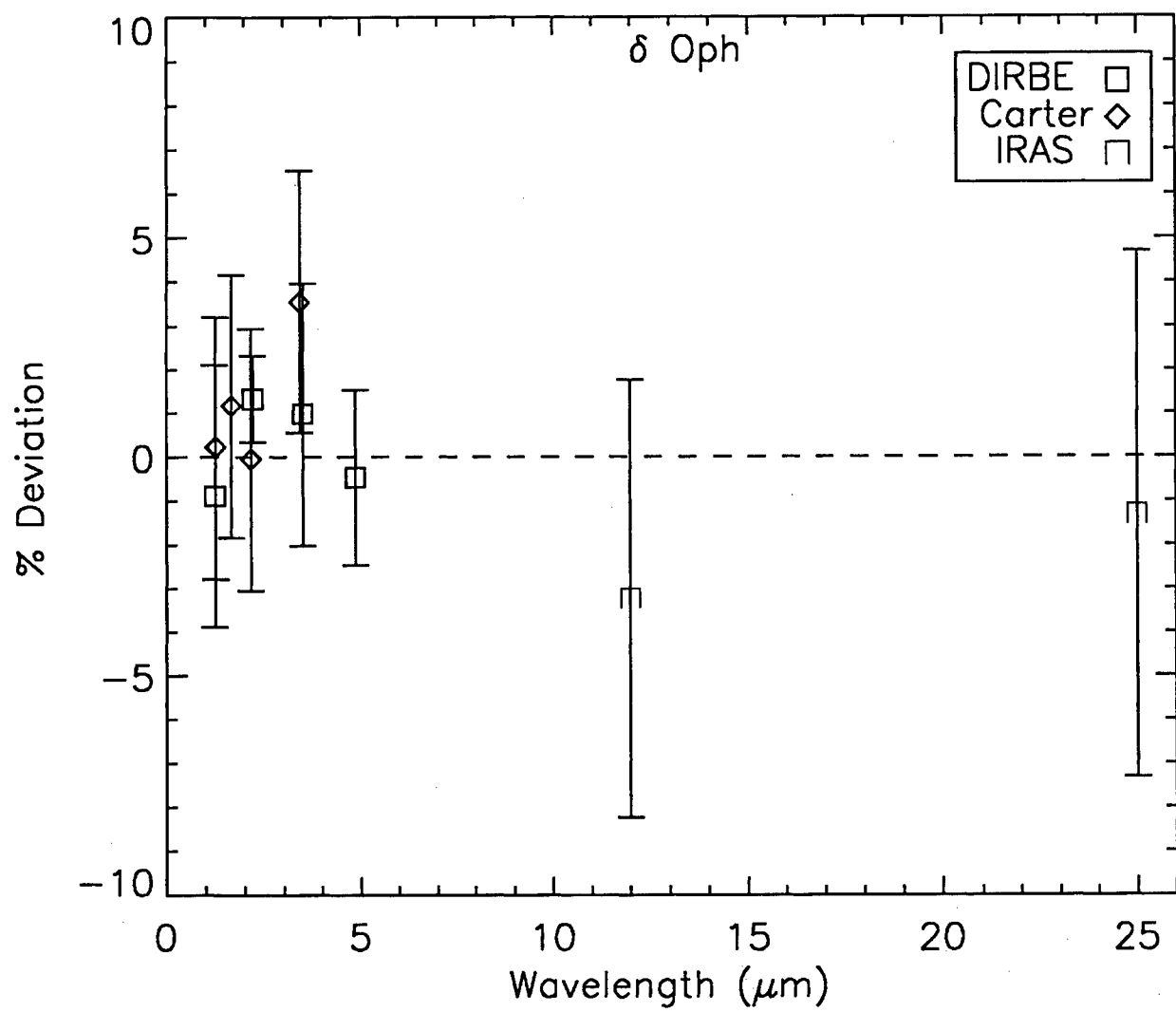
Carter (1990) J: -0.273 (0.03)
Carter (1990) H: -1.039 (0.03)
Carter (1990) K: -1.221 (0.03)
Carter (1990) L: -1.335 (0.03)

IRAS 12: -1.44 (0.05)
IRAS 25: -1.47 (0.06)

Uncertainty: In shape: 5% near 1 μm , 3% near 2 μm ,
 1% from 2.5 μm to 12 μm , 1.5% beyond
 In normalization relative to Sirius: 1.0%
 In absolute flux of Sirius: 1.2%

Adjustments:

SWS:	1A	$0.953\times$
	1B	$0.945\times$
	1D	$0.97\times$
	1E	$1.00\times$
	2A	$1.02\times$
	2B	$0.98\times$
	2C	$1.04\times(\lambda/7.5)^{0.17}$
	3A	$0.99\times(\lambda/15.5)^{0.1}$



Star: AE Cet
HD1038, HR48, 00121-1912
M1 III
CWW template star

Fit Parameters: $T_{\text{eff}} = 3850 \text{ K}$, $\theta = 5.186 \text{ mas}$

Spectral Data: SWS TDT: 55502138 (2.36 μm to 11 μm)

Photometry (with Sirius defined as -1.36):

DIRBE1: 1.233 (0.03)	lightcurve ampl: 0.03 (0.03)
DIRBE2: 0.218 (0.02)	lightcurve ampl: 0.02 (0.02)
DIRBE3: 0.082 (0.05)	lightcurve ampl: 0.09 (0.06)
DIRBE4: 0.279 (0.04)	lightcurve ampl: 0.03 (0.05)

Feast et al. (1990) H: 0.399 (0.01)

Feast et al. (1990) K: 0.212 (0.01)

Feast et al. (1990) L: 0.077 (0.02)

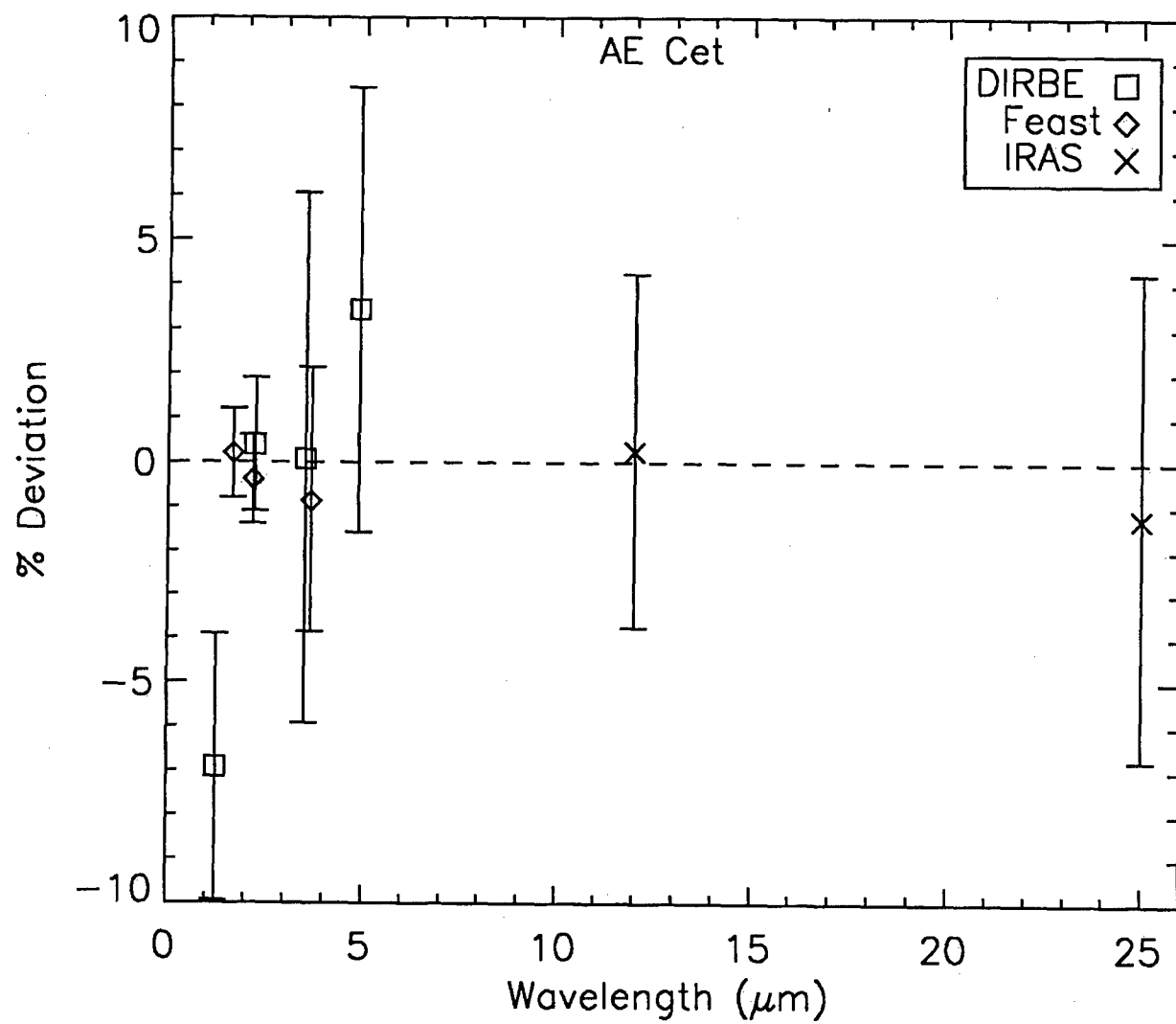
IRAS 12: -0.05 (0.06)

IRAS 25: -0.04 (0.07)

Uncertainty: In shape: 5% near 1 μm , 3% near 2 μm ,
1% from 2.5 μm to 12 μm , 1.5% beyond
In normalization relative to Sirius: 1.0%
In absolute flux of Sirius: 1.2%

Adjustments:

SWS:	1A	$0.89\times$
	1B	$0.90\times$
	1D	$0.90\times(\lambda/3.6)^{-0.10}$
	1E	$0.90\times$
	2A	$0.945\times$
	2B	$0.920\times(\lambda/5.9)^{0.01}$
	2C	$0.965\times(\lambda/7.0)^{-0.04}$



Star: δ Vir
HD112300, HR4910, IRAS 12530+0340
M3 III
CWW template star

Fit Parameters: $T^{\text{eff}} = 3660 \text{ K}$, $\theta = 10.71 \text{ mas}$

Spectral Data: SWS TDT: 24201225 (2.36 μm to 11 μm)

Photometry (with Sirius defined as -1.36):

DIRBE1: -0.196 (0.03)	lightcurve ampl: 0.03 (0.03)
DIRBE2: -1.214 (0.01)	lightcurve ampl: 0.01 (0.01)
DIRBE3: -1.366 (0.03)	lightcurve ampl: 0.02 (0.02)
DIRBE4: -1.129 (0.04)	lightcurve ampl: 0.02 (0.02)

Kenyon (1988) H: -1.011 (0.02)

Kenyon (1988) K: -1.229 (0.02)

IRAS 12: -1.50 (0.05)

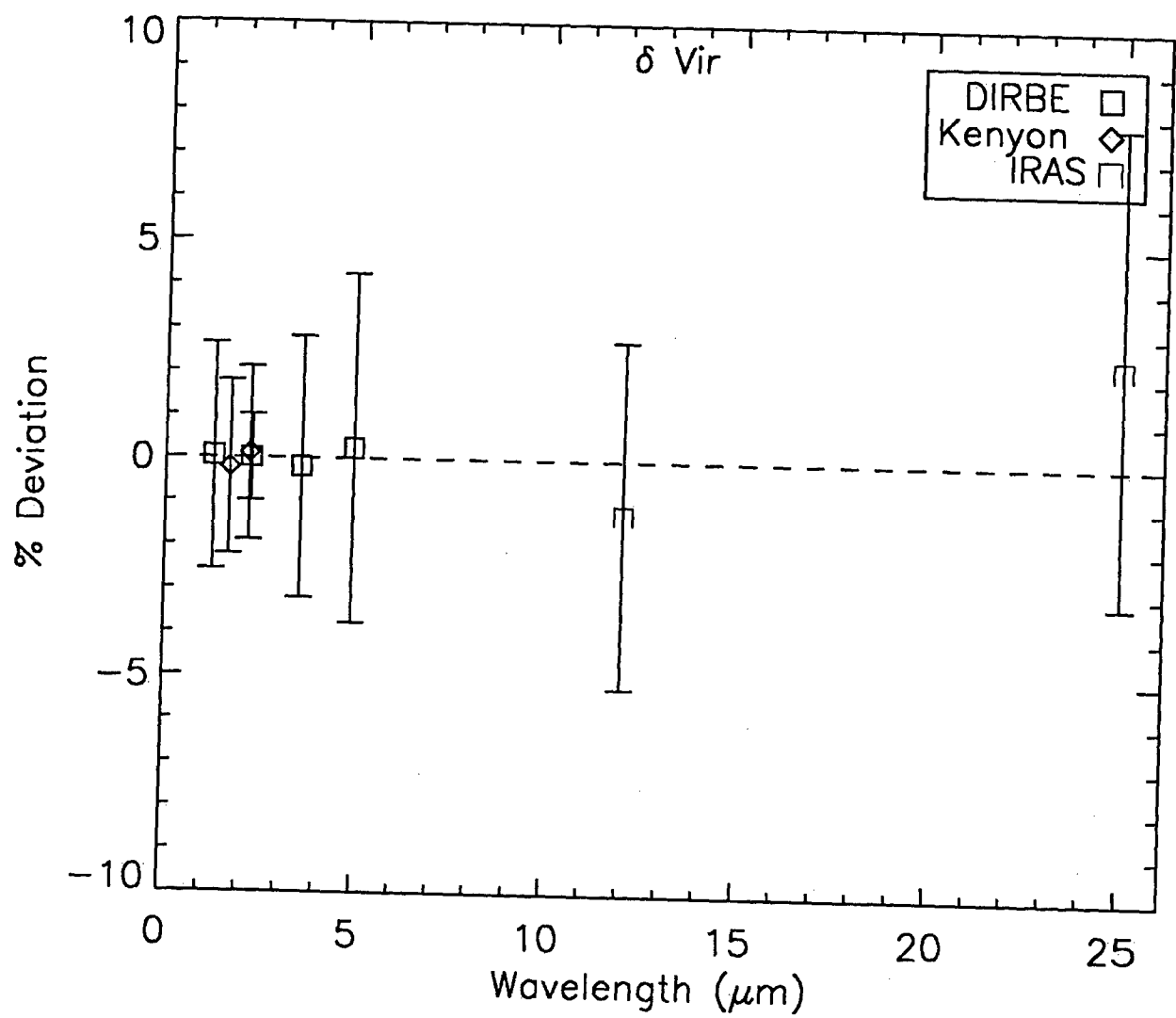
IRAS 25: -1.55 (0.06)

Uncertainty: In shape: 5% near 1 μm , 3% near 2 μm ,
1% from 2.5 μm to 12 μm , 1.5% beyond
In normalization relative to Sirius: 0.5%
In absolute flux of Sirius: 1.2%

Adjustments:

SWS:

1A	$0.985\times$
1B	$1.01\times$
1D	$0.987\times(\lambda/3.6)^{-0.10}$
1E	$0.987\times$
2A	$1.00\times$
2B	$0.990\times(\lambda/5.9)^{0.1}$
2C	$1.00\times(\lambda/7.5)^{-0.10}$



Star: ρ Per
 HD 19058, HR 921, IRAS 03019+3838
 M4 II
 CWW template star

Fit Parameters: $T_{\text{eff}} = 3540 \text{ K}$, $\theta = 15.50 \text{ mas}$

Spectral Data: SWS TDT: 79501105 (2.36 μm to 18.5 μm)

Photometry (with Sirius defined as -1.36):

DIRBE1: -0.901 (0.03)	lightcurve ampl: ----
DIRBE2: -1.951 (0.02)	lightcurve ampl: 0.01 (0.01)
DIRBE3: -2.109 (0.03)	lightcurve ampl: 0.05 (0.02)
DIRBE4: -1.916 (0.02)	lightcurve ampl: 0.04 (0.02)

Alonso et al. (2000) H: -1.731 (0.04)

Alonso et al. (2000) K: -1.979 (0.04)

Alonso et al. (2000) L: -2.128 (0.04)

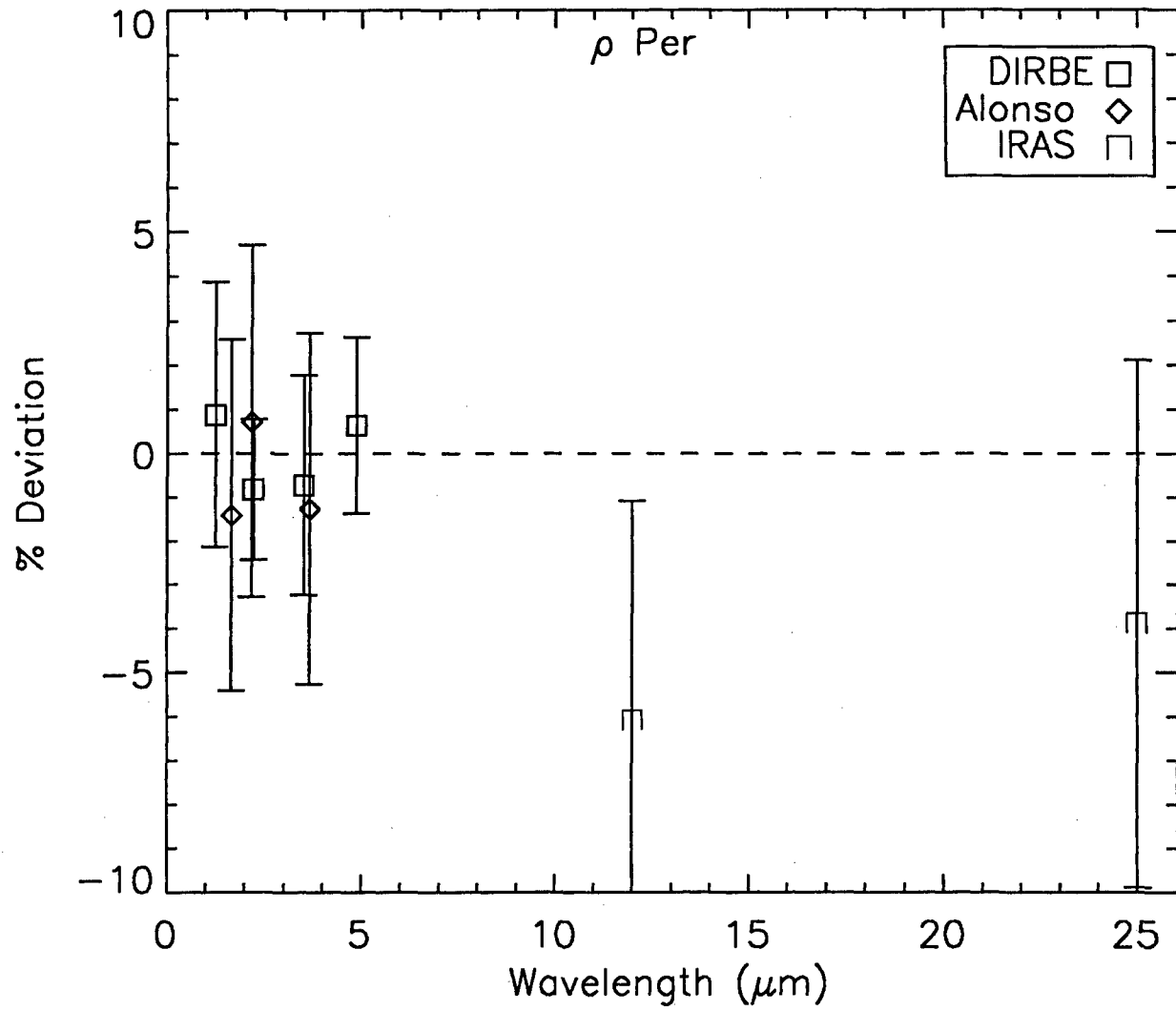
IRAS 12: -2.21 (0.05)

IRAS 25: -2.25 (0.06)

Uncertainty: In shape: 5% near 1 μm , 3% near 2 μm ,
 1% from 2.5 μm to 12 μm , 1.5% beyond
 In normalization relative to Sirius: 1.0%
 In absolute flux of Sirius: 1.2%
 Variable?

Adjustments:

SWS:	1A	$1.00\times$
	1B	$0.99\times$
	1D	$0.948\times(\lambda/3.6)^{-0.15}$
	1E	$0.940\times(\lambda/3.6)^{-0.15}$
	2A	$0.935\times(\lambda/4.2)^{0.12}$
	2B	$0.934\times(\lambda/5.9)^{0.10}$
	2C	$0.928\times(\lambda/7.5)^{0.02}$
	3A	$0.913\times(\lambda/15.5)^{-0.08}$
	3C	$0.915\times(\lambda/19.3)^{-0.15}$



Star: π Aur
HD 40239, HR 2091, IRAS 05562+4556
M3 II
CWW template star

Fit Parameters: $T_{\text{eff}} = 3500 \text{ K}$, $\theta = 9.05 \text{ mas}$

Spectral Data: SWS TDT: 83802031 (poor quality spectrum) (2.36 μm to 9.9 μm)

Photometry (with Sirius defined as -1.36):

DIRBE1:	0.283 (0.02)	lightcurve ampl: ---
DIRBE2:	-0.818 (0.01)	lightcurve ampl: ---
DIRBE3:	-1.000 (0.06)	lightcurve ampl: 0.12 (0.06)
DIRBE4:	-0.743 (0.04)	lightcurve ampl: 0.05 (0.03)

Kenyon (1988) H: -0.581 (0.02)

Kenyon (1988) K: -0.819 (0.02)

IRAS 12: -1.10 (0.05)

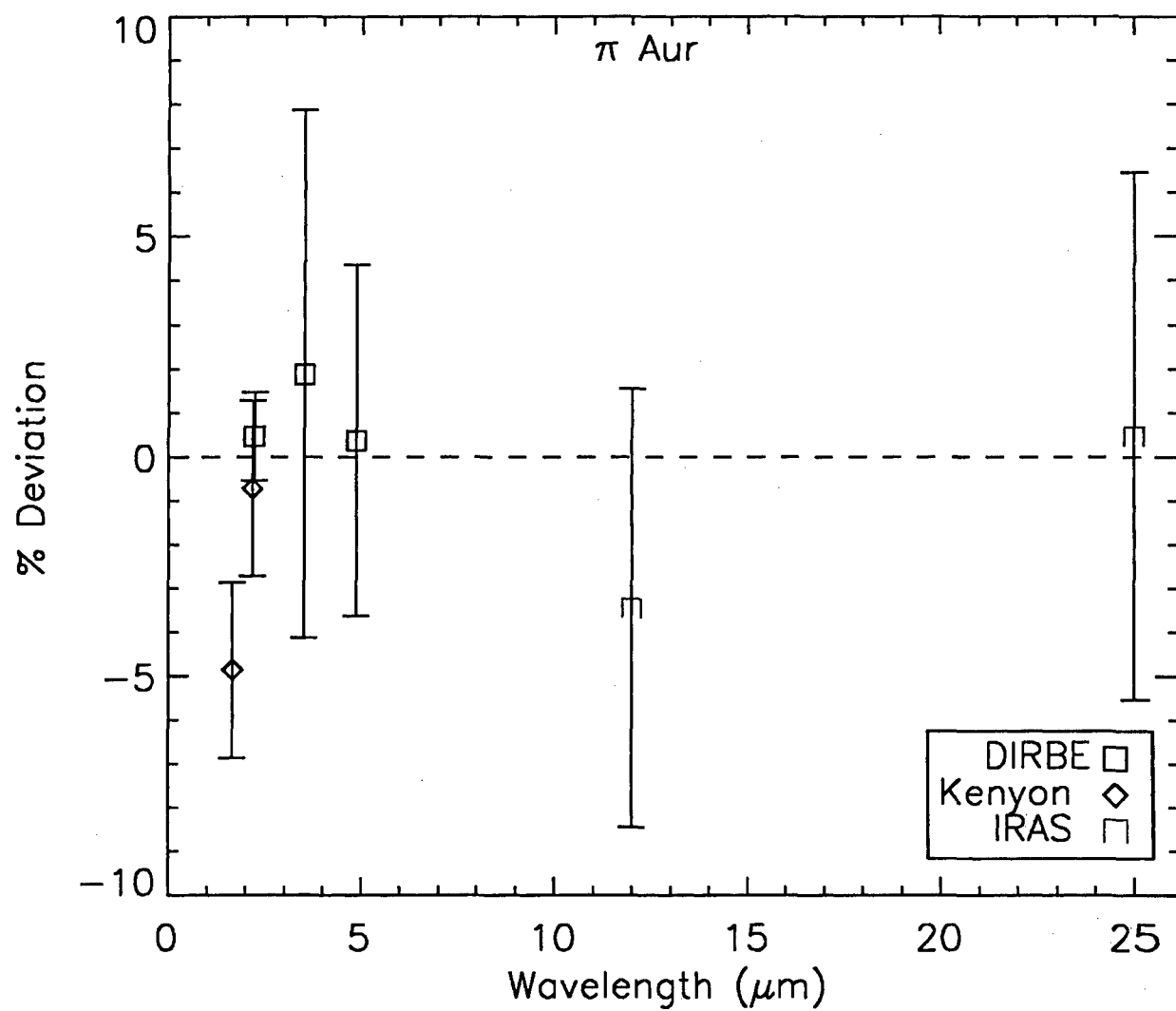
IRAS 25: -1.16 (0.05)

Uncertainty: In shape: 5% near 1 μm , 5% near 2 μm ,
5% from 2.5 μm to 12 μm , 5% beyond
In normalization relative to Sirius: 3.0%
In absolute flux of Sirius: 1.2%
Variable?
SWS seems abnormally low relative to photometry

Adjustments:

SWS:

1A	$1.45\times$
1B	$1.43\times$
1D	$1.54\times$
1E	$1.55\times(\lambda/3.6)^{0.30}$
2A	$1.82\times(\lambda/4.2)^{0.30}$
2B	$1.86\times$
2C	$2.00\times$



Star: β Peg
HD217906, HR8775, IRAS23013+2748
M2.5 III
CWW composite star

Fit Parameters: $T_{\text{eff}} = 3490$ K, $\theta = 17.88$ mas

Spectral Data: SWS TDT: 55100705 (2.36 μm to 35 μm)
SEW used 1.22 μm to 2.3 μm

Photometry (with Sirius defined as -1.36):

DIRBE1: -1.200 (0.01)	lightcurve ampl: 0.05 (0.03)
DIRBE2: -2.224 (0.01)	lightcurve ampl: 0.03 (0.01)
DIRBE3: -2.373 (0.02)	lightcurve ampl: 0.04 (0.02)
DIRBE4: -2.174 (0.02)	lightcurve ampl: 0.04 (0.01)

Hammersley et al. (1998) J: -1.204 (0.01)	Selby et al. (1988) J: -1.17 (0.01)
Hammersley et al. (1998) H: -2.087 (0.01)	
Hammersley et al. (1998) K: -2.305 (0.01)	Selby et al. (1988) K: -2.30 (0.01)
Hammersley et al. (1998) L: -2.388 (0.01)	Selby et al. (1988) L: -2.48 (0.01)

MSX A: -2.466 (0.02)	MSX C: -2.567 (0.02)
MSX B1: -2.319 (0.02)	MSX D: -2.577 (0.02)
MSX B2: -2.263 (0.02)	MSX E: -2.630 (0.02)

Uncertainty: In shape: 5% near 1 μm , 3% between 2 μm and 3 μm ,
1% from 3 μm to 12 μm , 1.5% beyond
In normalization relative to Sirius: 1.0%
In absolute flux of Sirius: 1.2%
8% variability observed by MSX

Adjustments:

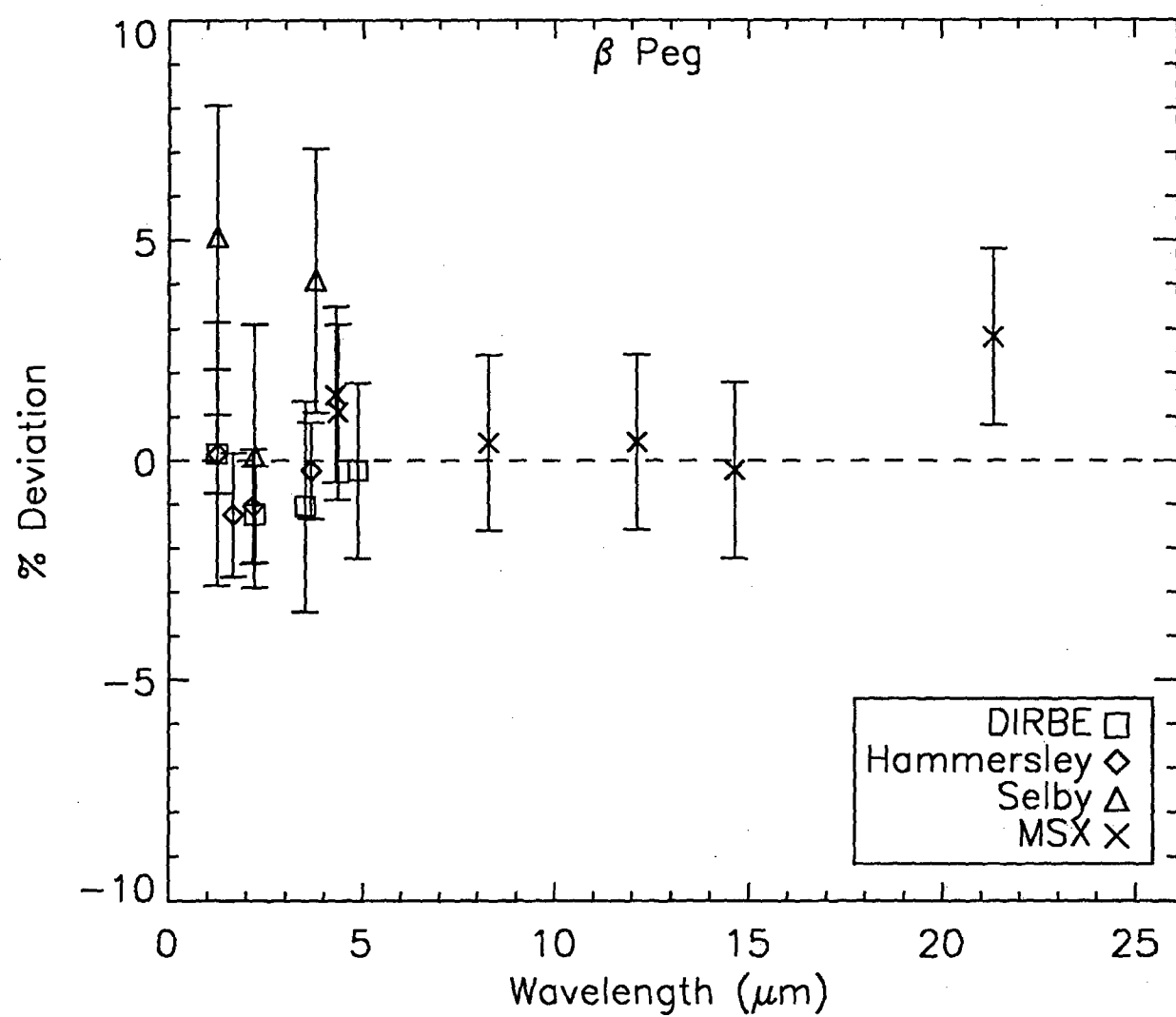
SWS:

1A	0.96 \times
1B	0.96 \times
1D	0.972 \times
1E	$0.97 \times (\lambda/3.2)^{-0.02}$
2A	1.075 \times
2B	1.135 \times
2C	0.950 \times

3A	0.978x
3C	0.975x
3D	0.96x
3E	1.07x

4	0.78x
---	-------

SEW	1.02x
-----	-------



Star: β Gru
HD214952, HR8636, IRAS22396-4708
M5 III
NO CWW template or composite

Fit Parameters: $T_{\text{eff}} = 3480 \text{ K}$, $\theta = 27.80 \text{ mas}$

Spectral Data: SWS TDT: 53802302 (2.36 μm to 26 μm)

Photometry (with Sirius defined as -1.36):

DIRBE1: -2.188 (0.04)	lightcurve ampl: 0.06 (0.03)
DIRBE2: -3.189 (0.01)	lightcurve ampl: 0.02 (0.01)
DIRBE3: -3.354 (0.03)	lightcurve ampl: 0.04 (0.02)
DIRBE4: -3.109 (0.02)	lightcurve ampl: 0.02 (0.01)

Thomas normalized through γ Cru photometry:

Thomas H: -3.098 (0.02)
Thomas K: -3.233 (0.02)
Thomas L: -3.391 (0.01)
Thomas M: -3.094 (0.02)
Thomas 8.4: -3.401 (0.02)
Thomas 10: -3.508 (0.02)
Thomas 12: -3.519 (0.02)

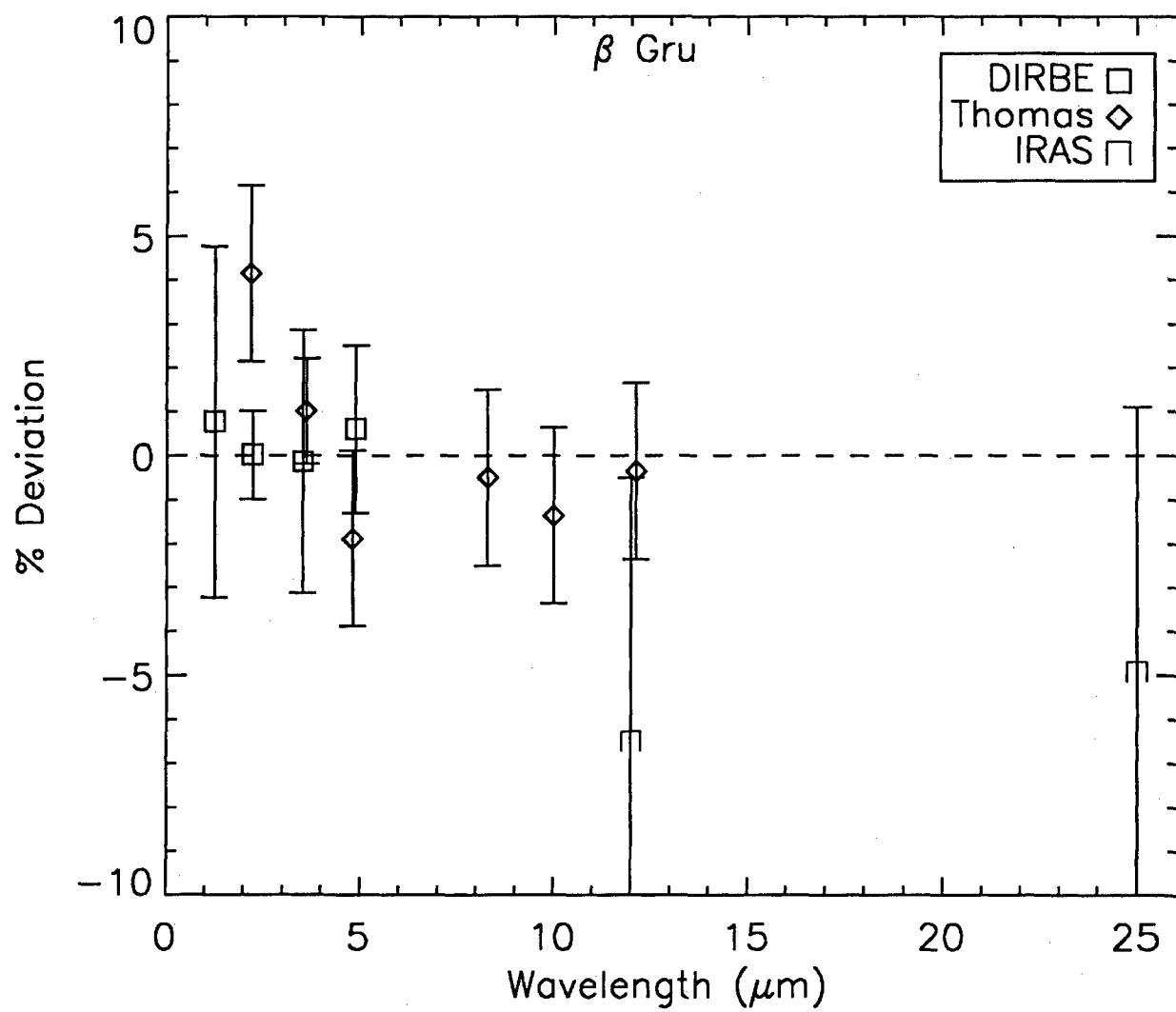
IRAS 12: -3.45 (0.06)
IRAS 25: -3.47 (0.06)

Uncertainty: In shape: 5% near 1 μm , 3% 2-3 μm ,
1% from 3 μm to 12 μm , 1.5% beyond
In normalization relative to Sirius: 1.0%
In absolute flux of Sirius: 1.2%

Adjustments:

SWS:	1A	$0.97 \times$
	1B	$0.99 \times (\lambda/2.7)^{-0.05}$
	1D	$0.985 \times (\lambda/3.3)^{-0.20}$
	1E	$0.967 \times (\lambda/3.9)^{-0.03}$
	2A	$0.903 \times$
	2B	$0.920 \times (\lambda/5.5)^{-0.10}$

2C	$0.780 \times (\lambda/7.0)^{0.28}$	$\lambda < 10.7 \mu\text{m}$
2C:	$0.865 \times$	$\lambda > 10.5 \mu\text{m}$
3A	$0.910 \times$	
3C	$0.930 \times$	
3D	$0.905 \times$	



Star: GZ Peg (57 Peg)
HD218634, HR8815, IRAS 23070+0824
M4 III + A2V
CWW template star

Fit Parameters: $T_{\text{eff}} = 3450 \text{ K}$, $\theta = 7.82 \text{ mas}$

Spectral Data: SWS TDT: 37600306 (2.36 μm to 12 μm)

Photometry (with Sirius defined as -1.36):

DIRBE1: 0.693 (0.03)	lightcurve ampl: -----
DIRBE2: -0.428 (0.01)	lightcurve ampl: 0.02 (0.02)
DIRBE3: -0.603 (0.04)	lightcurve ampl: 0.06 (0.05)
DIRBE4: -0.361 (0.03)	lightcurve ampl: -----

Kerschbaum & Hron (1994) H: -0.120 (0.04)
Kerschbaum & Hron (1994) K: -0.420 (0.04)
Kerschbaum & Hron (1994) L': -0.645 (0.04)
Kerschbaum & Hron (1994) M: -0.320 (0.04)

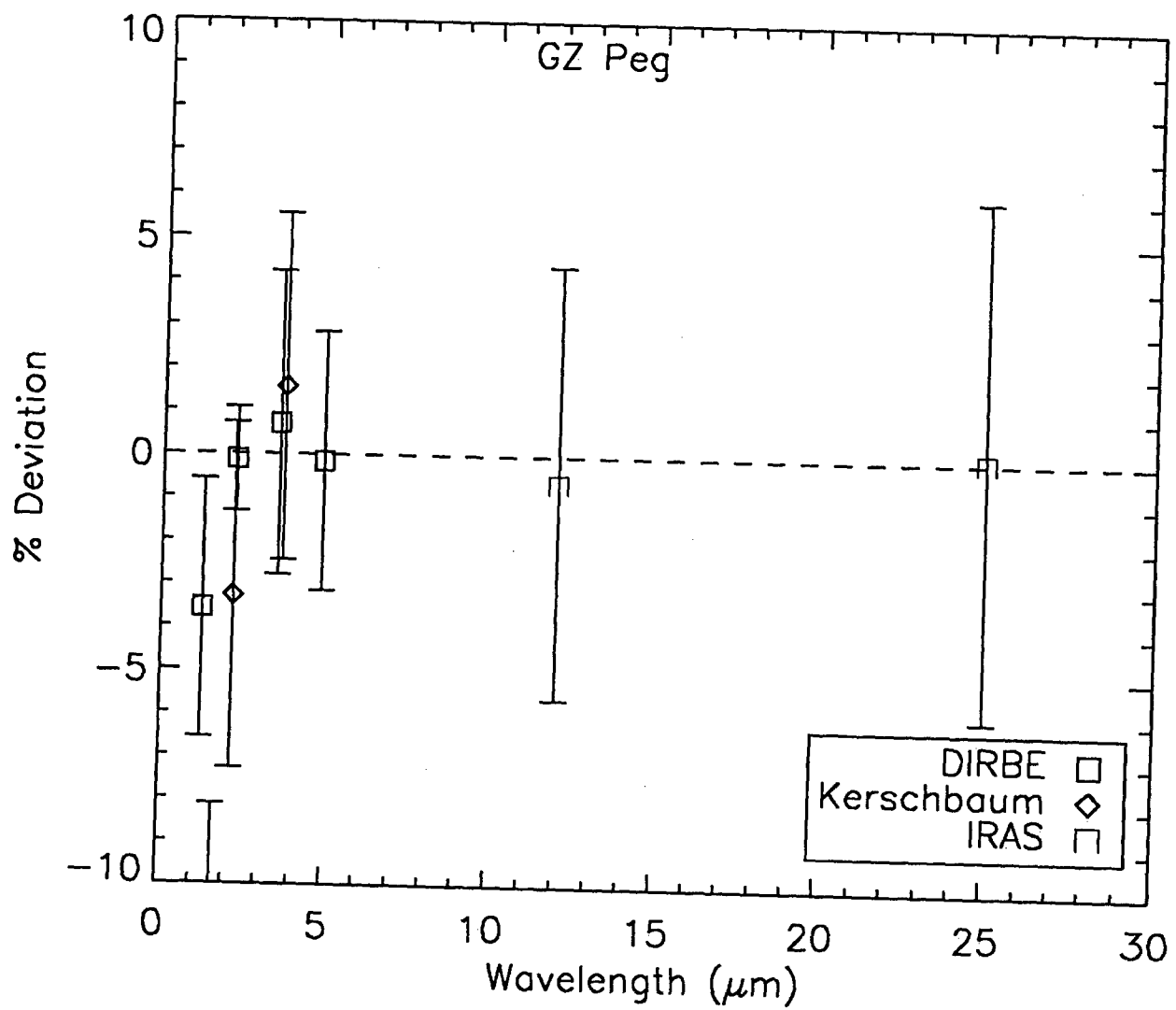
IRAS 12: -0.74 (0.05)
IRAS 25: -0.79 (0.06)

Uncertainty: In shape: 10% near 1 μm , 4% near 2 μm ,
1.5% from 2.5 μm to 12 μm , 1.5% beyond
In normalization relative to Sirius: 1.5%
In absolute flux of Sirius: 1.2%

Adjustments:

SWS:

1A	$0.94\times$
1B	$0.94\times$
1D	$0.945\times$
1E	$0.955\times(\lambda/3.6)^{0.05}$
2A	$0.96\times(\lambda/4.2)^{0.01}$
2B	$0.942\times$
2C	$0.95\times(\lambda/7.0)^{-0.03}$
3A	$0.87\times(\lambda/15.5)^{-0.1}$



Star: δ^2 Lyr
HD175588, HR7139, IRAS18527+3650
M4 II
Walker & Cohen IR Bright Star template

Fit Parameters: $T_{\text{eff}} = 3300 \text{ K}$, $\theta = 11.50 \text{ mas}$

Spectral Data: SWS TDT: 10200126 (2.36 μm to 26.9 μm)

Photometry (with Sirius defined as -1.36):

DIRBE1: -0.070 (0.02)	lightcurve ampl: 0.02 (0.02)
DIRBE2: -1.172 (0.01)	lightcurve ampl: 0.02 (0.01)
DIRBE3: -1.368 (0.03)	lightcurve ampl: 0.04 (0.03)
DIRBE4: -1.083 (0.03)	lightcurve ampl: 0.03 (0.02)

IRAS 12: -1.45 (0.08)

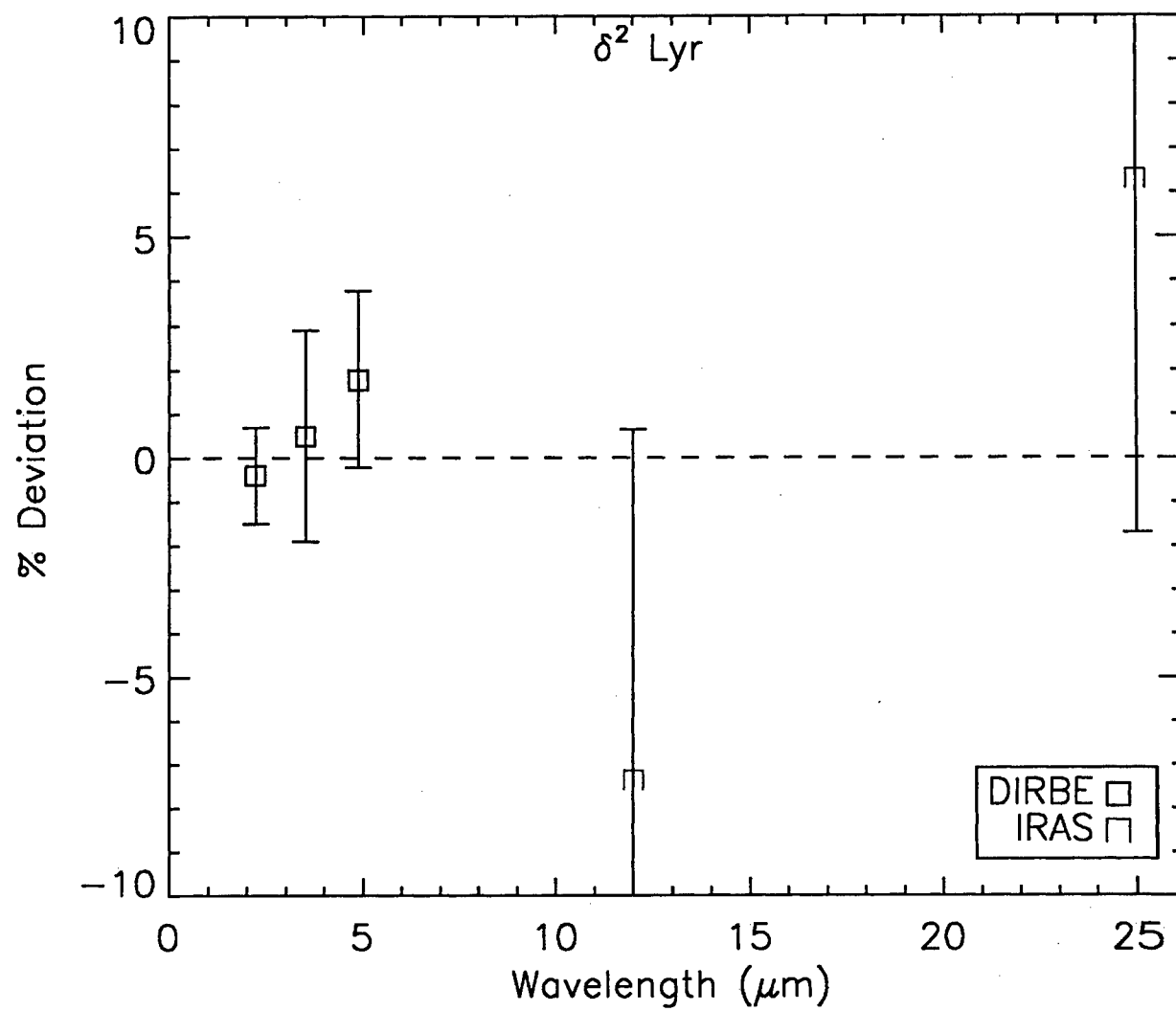
IRAS 25: -1.65 (0.08)

Uncertainty: In shape: 5% near 1 μm , 5% near 2 μm ,
5% from 2.5 μm to 12 μm , 5% beyond
In normalization relative to Sirius: 1.0%
In absolute flux of Sirius: 1.2%

Adjustments:

SWS:

1A	$0.935 \times$
1B	$0.936 \times$
1D	$0.936 \times$
1E	$0.921 \times (\lambda/3.7)^{-0.03}$
2A	$0.961 \times (\lambda/4.05)^{-0.13}$
2B	$0.857 \times (\lambda/5.7)^{-0.05}$
2C	$0.904 \times (\lambda/7.0)^{-0.07}$
3A	$0.907 \times$
3C	$0.857 \times (\lambda/18.0)^{-0.4}$
3D	$0.834 \times$



Star: α Aur
HD 34029, HR 1708, IRAS 05130+4556
G4 III
NO CWW template or composite

Fit Parameters: $T_{\text{eff}} = 5450 \text{ K}$, $\theta = 10.23 \text{ mas}$

Photometry (with Sirius defined as -1.36):

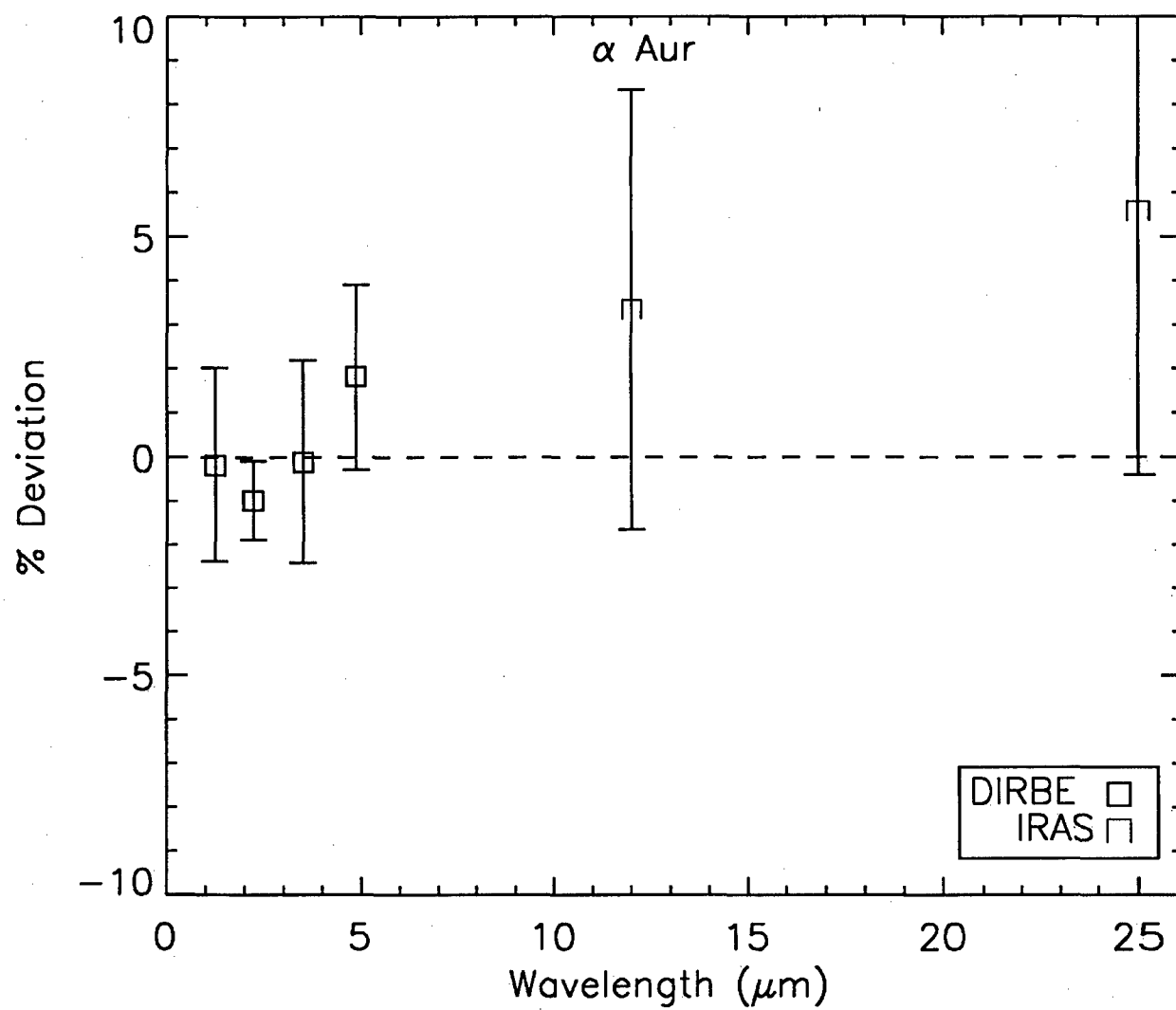
DIRBE1: -1.297 (0.022)	lightcurve ampl: 0.01 (0.03)
DIRBE2: -1.788 (0.009)	lightcurve ampl: 0.00 (0.01)
DIRBE3: -1.850 (0.023)	lightcurve ampl: 0.02 (0.02)
DIRBE4: -1.815 (0.021)	lightcurve ampl: 0.02 (0.01)

IRAS 12: -1.91 (0.05)

IRAS 25: -1.93 (0.06)

Uncertainty: In shape: 5% near 1 μm , 3% near 2 μm ,
1% from 2.5 μm to 12 μm , 1.5% beyond
In normalization relative to Sirius: 0.5%
In absolute flux of Sirius: 1.2%

RS CVn variable star, but DIRBE and other photometry is consistent



Star: α Hya
HD 81797, HR 3748, IRAS 09251-0826
K3 II
CWW composite star

Fit Parameters: $T_{\text{eff}} = 4150 \text{ K}$, $\theta = 9.588 \text{ mas}$

Photometry (with Sirius defined as -1.36):

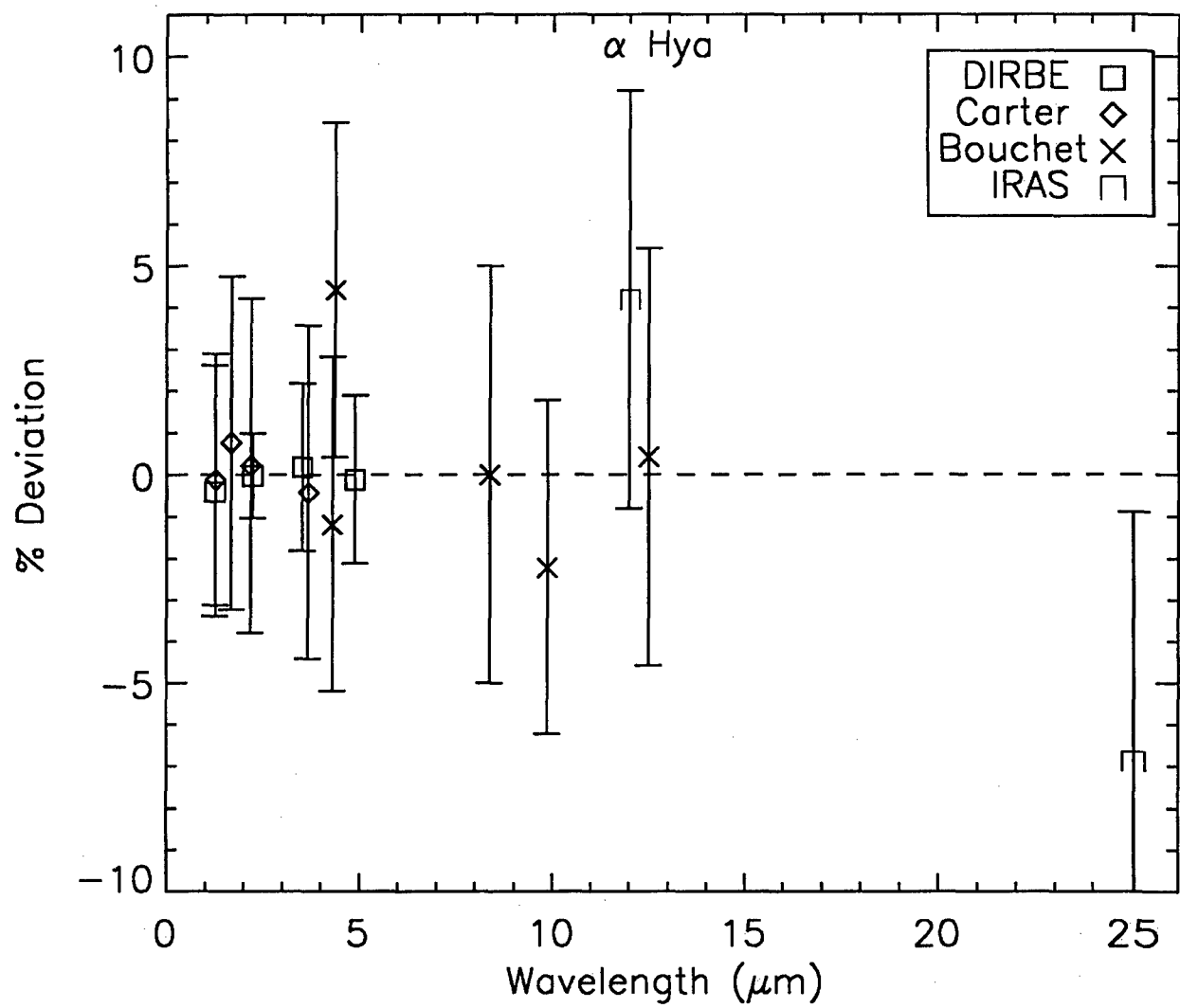
DIRBE1: -0.378 (0.03)	lightcurve ampl: 0.02 (0.03)
DIRBE2: -1.199 (0.01)	lightcurve ampl: 0.01 (0.01)
DIRBE3: -1.320 (0.02)	lightcurve ampl: 0.02 (0.03)
DIRBE4: -1.122 (0.02)	lightcurve ampl: 0.02 (0.02)

Carter (1003) J:	-0.381 (0.03)
Carter (1993) H:	-1.056 (0.04)
Carter (1993) K (2.17 μm):	-1.214 (0.04)
Carter (1993) L (3.43 μm):	-1.329 (0.04)

Bouchet et al. (1989, 1991) M (4.7 μm):	-1.166 (0.04)
Bouchet et al. (1989, 1991) N1 (8.37 μm):	-1.290 (0.05)
Bouchet et al. (1989, 1991) N2 (9.86 μm):	-1.324 (0.05)
Bouchet et al. (1989, 1991) N3 (12.55 μm):	-1.434 (0.05)

IRAS 12: -1.47 (0.05)
IRAS 25: -1.35 (0.06)

Uncertainty: In shape: 5% near 1 μm , 3% near 2 μm ,
1% from 2.5 μm to 12 μm , 1.5% beyond
In normalization relative to Sirius: 0.5%
In absolute flux of Sirius: 1.2%



Star: γ Aql
HD 186791, HR 7525, IRAS 19438+1029
K3 II
CWW template star

Fit Parameters: $T_{\text{eff}} = 4050 \text{ K}$, $\theta = 7.29 \text{ mas}$

Photometry (with Sirius defined as -1.36):

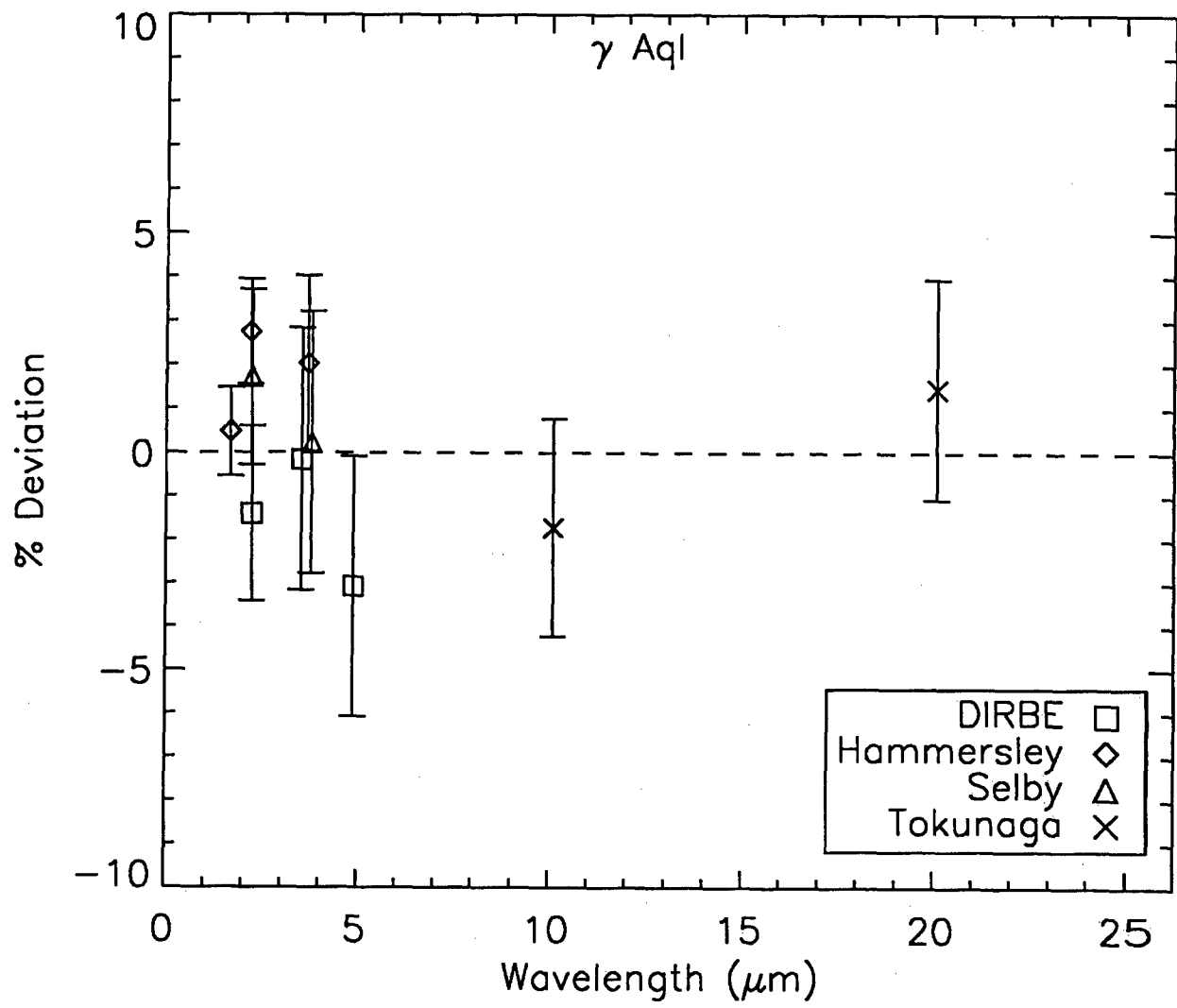
DIRBE1: 0.292 (0.03)	lightcurve ampl: 0.04 (0.04)
DIRBE2: -0.545 (0.02)	lightcurve ampl: 0.00 (0.02)
DIRBE3: -0.684 (0.03)	lightcurve ampl: 0.03 (0.04)
DIRBE4: -0.442 (0.03)	lightcurve ampl: 0.05 (0.04)

Hammersley et al. (1998) J: 0.268 (0.01)	Selby et al. (1988) J: 0.295 (0.02)
Hammersley et al. (1998) H: -0.441 (0.01)	
Hammersley et al. (1998) K: -0.603 (0.01)	Selby et al. (1988) K: -0.629 (0.02)
Hammersley et al. (1998) L: -0.723 (0.02)	Selby et al. (1988) L: -0.724 (0.03)

Tokunaga (1984) 10.1: -0.74 (0.02)
Tokunaga (1984) 20.1: -0.82 (0.02)

IRAS 12: -0.68 (0.05)
IRAS 25: -0.78 (0.06)

Uncertainty: In shape: 5% near 1 μm , 3% near 2 μm ,
2% from 2.5 μm to 12 μm , 2% beyond
In normalization relative to Sirius: 3%
In absolute flux of Sirius: 1.2%



Star: α TrA
 HD 150798, HR 6217, IRAS 16433-6856
 K2 II
 CWW composite star

Fit Parameters: $T_{\text{eff}} = 4000 \text{ K}$, $\theta = 9.81 \text{ mas}$

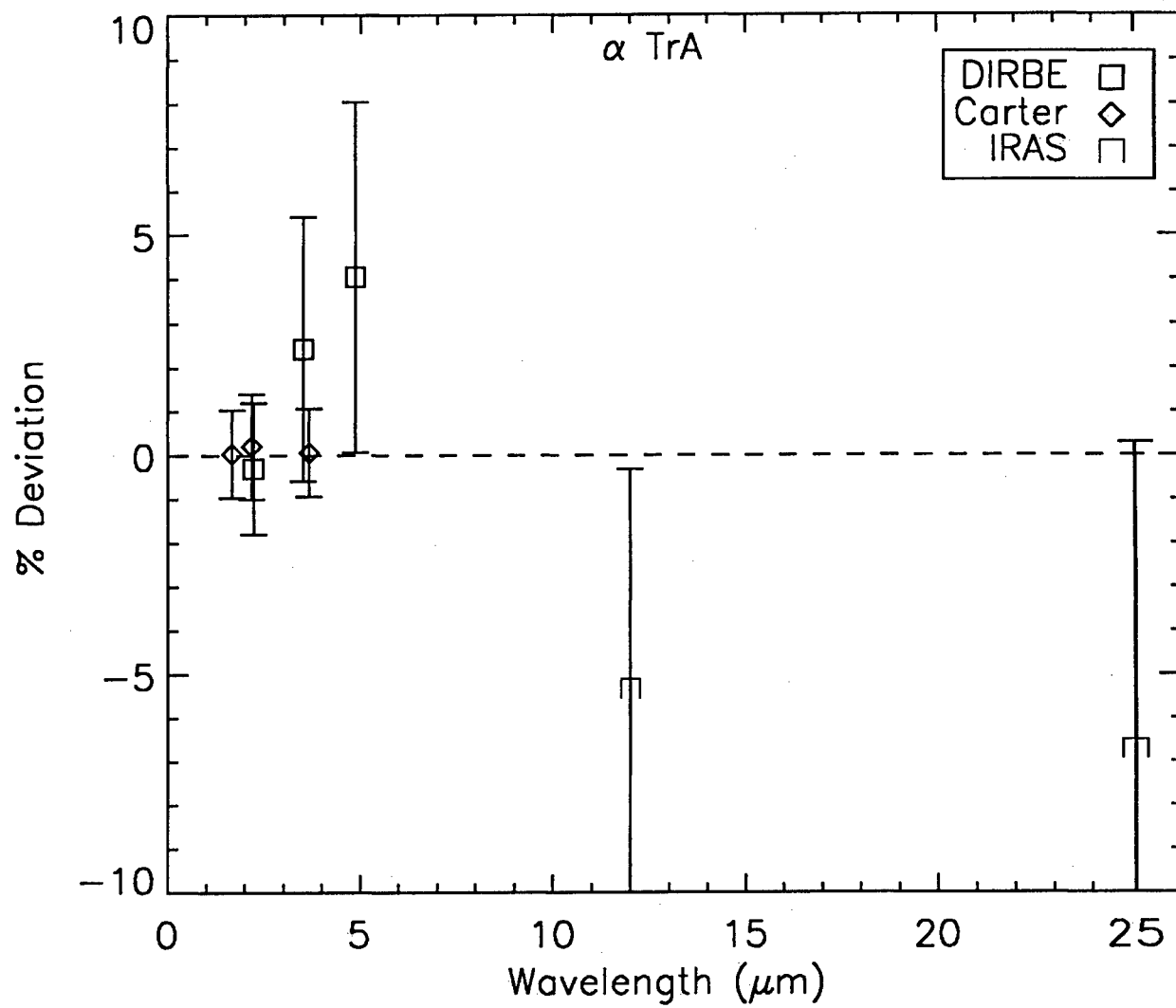
Photometry (with Sirius defined as -1.36):

DIRBE1: -0.384 (0.02)	-----
DIRBE2: -1.180 (0.02)	lightcurve ampl: 0.001(0.02)
DIRBE3: -1.338 (0.03)	lightcurve ampl: 0.06 (0.03)
DIRBE4: -1.139 (0.04)	lightcurve ampl: 0.05 (0.02)

Carter (1993) H:	-1.055 (0.005)
Carter (1993) K:	-1.199 (0.009)
Carter (1993) L:	-1.328 (0.008)

IRAS 12: -1.368 (0.05)
IRAS 25: -1.36 (0.06)

Uncertainty: In shape: 5% near 1 μm , 3% near 2 μm ,
 1% from 2.5 μm to 12 μm , 1.5% beyond, 3% in molecular bands
 In normalization relative to Sirius: 1.0% for average
 In absolute flux of Sirius: 1.2%



Star: ϵ Car
HD 71129, HR 3307, IRAS 08214-5920
K3 III (+B2V?)
CWW composite star

Fit Parameters: $T_{\text{eff}} = 3300 \text{ K}$, $\theta = 14.59 \text{ mas}$

Photometry (with Sirius defined as -1.36):

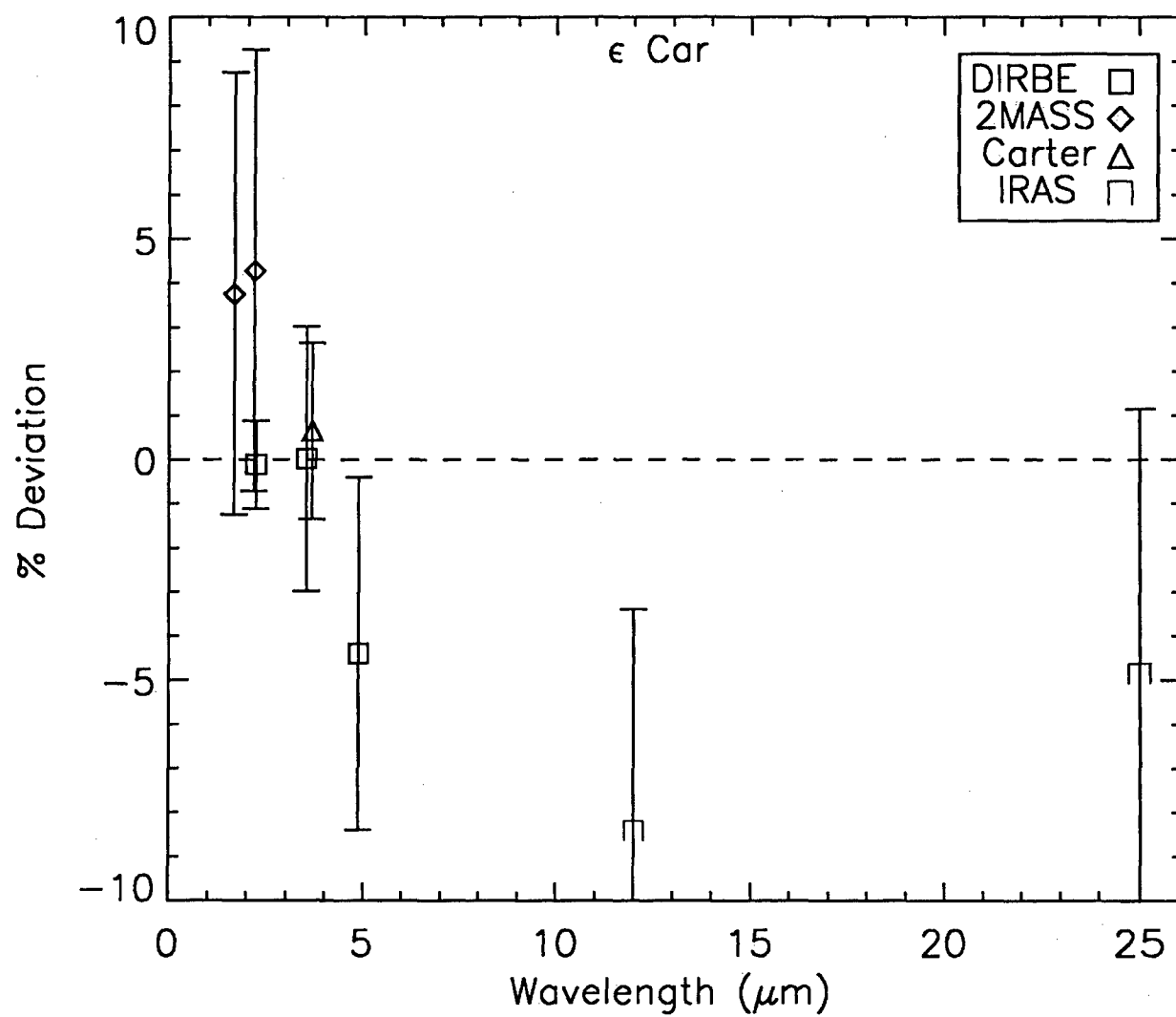
DIRBE1: -0.79 (0.03)	lightcurve ampl: 0.03 (0.03)
DIRBE2: -1.69 (0.01)	lightcurve ampl: 0.01 (0.01)
DIRBE3: -1.88 (0.03)	lightcurve ampl: 0.03 (0.03)
DIRBE4: -1.56 (0.04)	lightcurve ampl: 0.04 (0.04)

2MASS J: -0.756 (0.05)
2MASS H: -1.532 (0.05)
2MASS K: -1.752 (0.05)

Carter(1993) L: -1.904 (0.02)

IRAS 12: -1.95 (0.05)
IRAS 25: -2.02 (0.06)

Uncertainty: In shape: 5% near 1 μm , 5% near 2 μm ,
5% from 2.5 μm to 12 μm , 5% beyond
In normalization relative to Sirius: 5%
In absolute flux of Sirius: 1.2%



Appendix B Additional Templated Spectra

This appendix contains the photometry, *autoshape* fit parameters, and final photometric fit plots for four additional stars that were templated after the main section of this Technical Report was finished. The information and format are identical to Appendix A. The four stars are β Oph, α Ser, β Cnc, and δ Vir, and were tertiary standards in the Cohen et al. network.

Table B-1: Additional Templated Standard Stars

Star	Sp. Type	T_{eff} (K)	θ (mas)	Spectra	Photometry
α Ser	K2 IIIb	4700	4.75	A[35]	DIR, H, S, IRAS
β Oph	K2 III	4650	4.55	A[35]	H, CS, IRAS
β Cnc	K4 III	3950	5.44	A[35]	DIR, IRAS
ν Vir	K4 III	3750	5.73	A[35]	DIR, Fk, IRAS

The uncertainty on T_{eff} is ± 7 percent and that on θ is ± 4 percent. Note that the uncertainties in T_{eff} and θ are not independent. The overall absolute flux uncertainty is typically close to that cited for θ . Photometry sources defined in Tables 20 and 21 with the addition of CS= Castor & Simon. (1983, *Astroph. J.*, 265, 304) and Fk=Fluks et al. (1994, *Astron. & Astroph. Supp.*, 105, 311)

Star: α Ser
HD 140573, HR 5854, IRAS 15418+0634
K2 IIIb
CWW template star

Fit Parameters: $T_{\text{eff}} = 4700 \text{ K}$, $\theta = 4.75 \text{ mas}$

Photometry (with Sirius defined as -1.36):

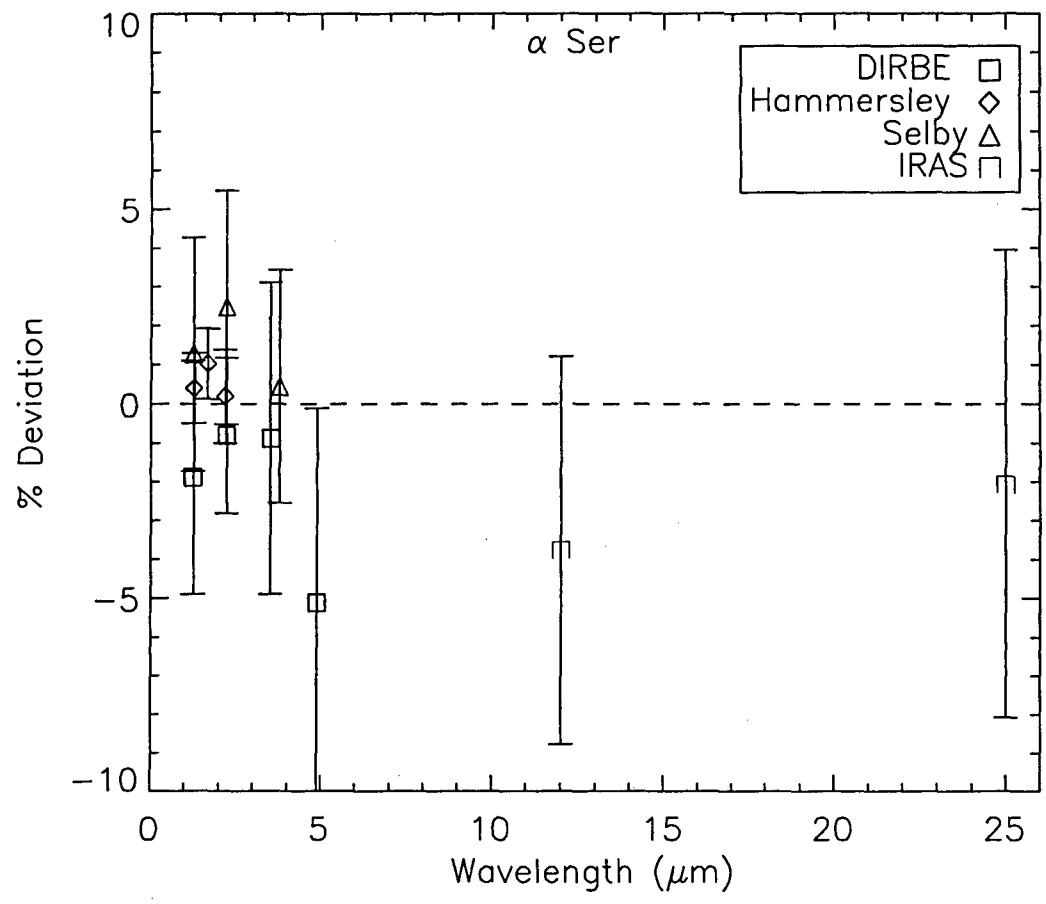
DIRBE1: 0.772 (0.03)	lightcurve ampl: 0.01 (0.03)
DIRBE2: 0.119 (0.02)	lightcurve ampl: 0.03 (0.02)
DIRBE3: 0.033 (0.04)	lightcurve ampl: 0.07 (0.05)
DIRBE4: 0.185 (0.05)	lightcurve ampl: 0.06 (0.06)

Hammersley et al. (1998) J: 0.747 (0.01)
Hammersley et al. (1998) H: 0.208 (0.01)
Hammersley et al. (1998) K: 0.108 (0.01)

Selby et al. (1988) J: 0.295 (0.03)
Selby et al. (1988) K: 0.051 (0.03)
Selby et al. (1988) L: -0.009 (0.03)

IRAS 12: 0.00 (0.05)
IRAS 25: -0.02 (0.06)

Uncertainty: In shape: 5% near 1 μm , 3% near 2 μm , 5% near 5 μm
1% from 2.5 μm to 12 μm , 1.5% beyond
In normalization relative to Sirius: 0.5%
In absolute flux of Sirius: 1.2%



Star: β Oph
HD 161096, HR 6603, IRAS 17403+0435
K2 III
CWW template star

Fit Parameters: $T_{\text{eff}} = 4650 \text{ K}$, $\theta = 4.55 \text{ mas}$

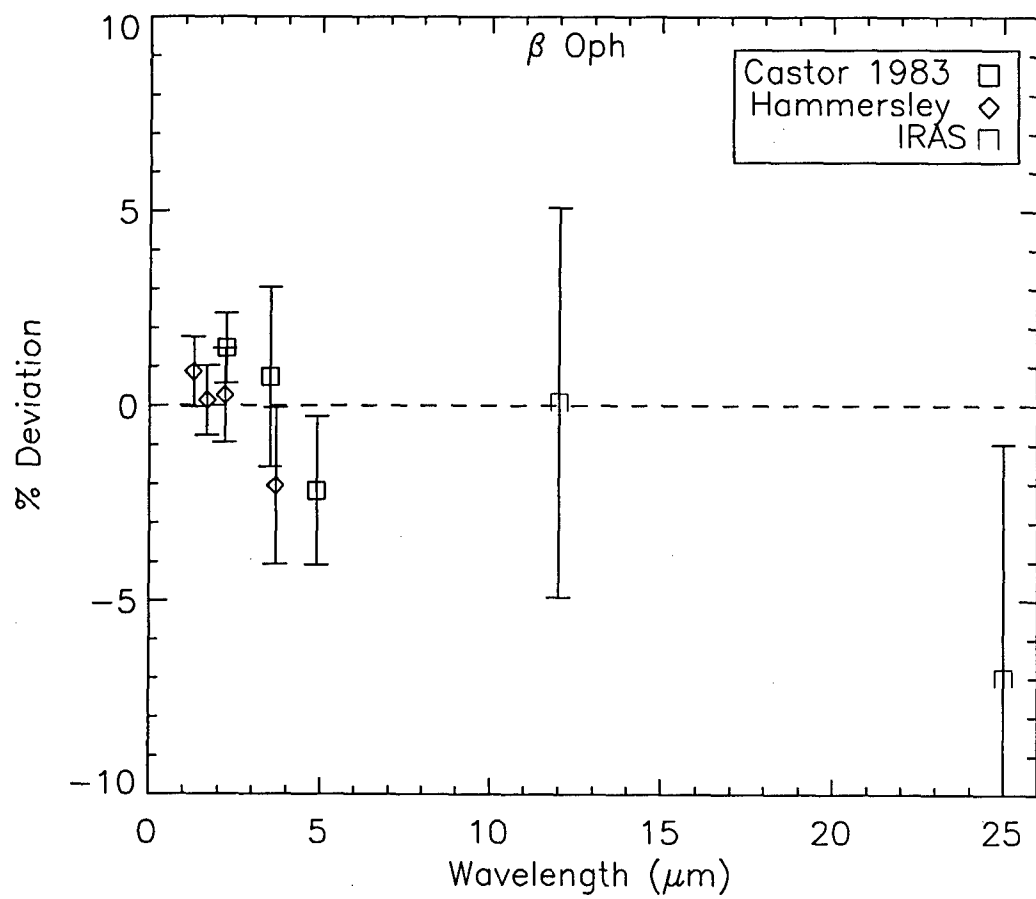
Photometry (with Sirius defined as -1.36):

Hammersley et al. (1998) J: 0.876 (0.01)
Hammersley et al. (1998) H: 0.336 (0.01)
Hammersley et al. (1998) K: 0.220 (0.01)
Hammersley et al. (1998) L: 0.142 (0.01)

Castor & Simon (1983) H: 0.322 (0.02)
Castor & Simon (1983) K: 0.207 (0.02)
Castor & Simon (1983) L: 0.125 (0.02)
Castor & Simon (1983) M: 0.295 (0.02)

IRAS 12: 0.062 (0.05)
IRAS 25: 0.141 (0.06)

Uncertainty: In shape: 5% near 1 μm , 3% near 2 μm , 4% near 5 μm
1% from 2.5 μm to 12 μm , 1.5% beyond
In normalization relative to Sirius: 0.5%
In absolute flux of Sirius: 1.2%



Star: β Cnc
HD 69267, HR 3249, IRAS 08138+0920
K4 III
CWW template star

Fit Parameters: $T_{\text{eff}} = 3950 \text{ K}$, $\theta = 5.44 \text{ mas}$

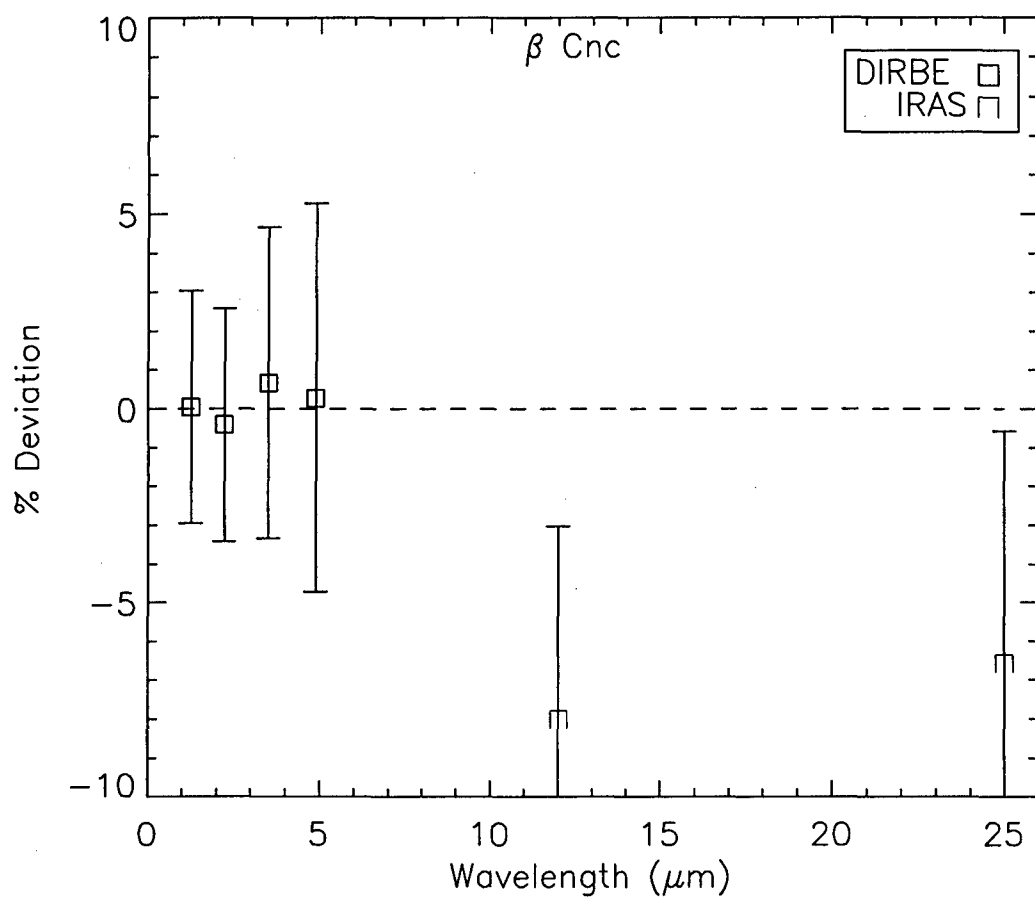
Photometry (with Sirius defined as -1.36):

DIRBE1: 1.000 (0.03)	lightcurve ampl: ---
DIRBE2: 0.120 (0.03)	lightcurve ampl: 0.03 (0.02)
DIRBE3: -0.024 (0.04)	lightcurve ampl: 0.05 (0.03)
DIRBE4: 0.178 (0.05)	lightcurve ampl: 0.05 (0.05)

IRAS 12: -0.05 (0.05)

IRAS 25: -0.07 (0.06)

Uncertainty: In shape: 5% near 1 μm , 3% near 2 μm , 3% near 5 μm
1% from 2.5 μm to 12 μm , 1.5% beyond
In normalization relative to Sirius: 0.5%
In absolute flux of Sirius: 1.2%



Star: ν Vir
 HD 102212, HR 4517, IRAS 11432+0648
 K4 III
 CWW template star

Fit Parameters: $T_{\text{eff}} = 3750 \text{ K}$, $\theta = 5.73 \text{ mas}$

Photometry (with Sirius defined as -1.36):

DIRBE1: 1.08 (0.03)	lightcurve ampl: 0.00 (0.03)
DIRBE2: 0.120 (0.03)	lightcurve ampl: 0.01 (0.02)
DIRBE3: -0.024 (0.04)	lightcurve ampl: 0.05 (0.04)
DIRBE4: 0.167 (0.05)	lightcurve ampl: 0.04 (0.05)

Fluks et al. (1994) H: 0.28 (0.01)
Fluks et al. (1994) K: 0.08 (0.01)
Fluks et al. (1994) L: -0.06 (0.01)
Fluks et al. (1994) M: 0.176 (0.05)

IRAS 12: -0.05 (0.05)
IRAS 25: -0.07 (0.06)

Uncertainty: In shape: 5% near 1 μm , 3% near 2 μm , 3% near 5 μm
 1% from 2.5 μm to 12 μm , 1.5% beyond
 In normalization relative to Sirius: 0.5%
 In absolute flux of Sirius: 1.2%

